UNIVERSIDAD AUTONOMA DE MADRID

FACULTAD DE CIENCIAS
DEPARTAMENTO DE FÍSICA DE MATERIALES

Preparation and Development of CdTe and CdZnTe Detectors for Gamma Ray Radiation Applications

PhD Dissertation

Qian Zheng

Supervisor

Prof. Ernesto Diéguez

Thesis Tribunal

Prof. Luisa Eugenia Bausá
Prof. Jose Francisco Fernández
Dr. José Manuel Pérez
Dr. Andrea Zappettini
Dr. Matthias Strassburg

Madrid, October 2012

ACKNOWLEDGMENTS

First and foremost I would like to express my deepest appreciation to my supervisor, Prof. Ernesto Diéguez, for not just giving me the opportunity to start my PhD, but supporting me throughout my thesis with his patience and knowledge.

I am deeply grateful to Prof. Peter Wellmann for giving me the opportunity of three months research stay in his group at Material for Electronic and Energy Technology (IMEET) in University of Erlangen-Nuremberg. Many thanks to all the members in the group for their help, especially Felix Oehlschläger, Ulrike Künecke, Martin Wilhelm, and Dr. Andres Osvet.

I would like to acknowledge the collaborations of several groups where the measurements for the scientific investigations have been carried out. I am thankful to Dr. José-Manuel Pérez and Oscar Vela from the Centro de Investigation Energéticas Medioambientales y Tecnológicas (CIEMAT) in Madrid for their help in the gamma ray measurements. I am grateful to Dr. Victoria Corregidor and Prof. Eduardo Alves from the Instituto Tecnológico e Nuclear (ITN) in the Unidade de Física e Aceleradores in Portugal for the RBS measurement. I would like to acknowledge Prof. Jan Franc from Charles University in Prague for PL measurement. I would like to thank Eduardo Ruiz from Laboratorio de Microelectrónica in UAM for the evaporation investigations.

I would like to thank the people from El Servicio Interdepartamental de Investigación (SIDI) in UAM for the scientific investigations. Especially thanks to Ramon Fernández- Ruiz for TXRF measurement, César Pastor for HRXRD measurement, Esperanza Salvador, Isidoro Poveda, and Enrique Rodríguez for SEM and EDX measurements, Inmaculada Rivas for ICP-MS measurement, and Pascual Torres for FTIR measurement.

Many thanks to Dr. Mohamed Ayoub from Kromek in United Kingdom and Dr. Adriano Cola from Istituto Per La Microelettronica e Microsistemi (CNR-IMM) in Italy for their help and advice.

I would also like to thank my colleagues from Crystal Growth Laboratory (CGL) in UAM for their support and good memories: Dr. Jerome Crocco, Dr. Verónica Carcelén, Hakima Bensalah, Andrés Black, Juan Medina, Axa Pinneiro, Sandra Rubio, and Dr. José Luis Plaza.

My sincere thanks to my colleagues from Departamento de Física de Materiales in UAM: Martina Dobrinčić, Jon Martinez, Mariano Jubera, and Iñigo Aguirre.

Finally, I would like to thank my family for always giving me encouraging words and keeping me strong to pursue my interests. Most especially to my husband Fabrice, who had supported and understood me all the time. Special thanks are extended to my parents in law, papy et mamie, and Benjamin for their constant support.

ABSTRACT

This thesis presents the results of preparation and development of CdTe/CZT detectors for gamma ray radiation applications.

In the first part of the thesis, the processes for fabricating CdTe/CZT detectors including the preparation of surface and lateral edges have been investigated. A complete process of surface preparation including ingot slicing and dicing, wafer lapping, mechanical polishing, and chemical etching have been described and emphasized by the surface characterization for each step. The selection of the best etchant, the choice of the optimal concentration of the etchant, and the study of the cleaning of the surface after etching stage will be characterized in terms of surface roughness, contamination and morphology. The important influence of the different preparation methods for the lateral edges of the detectors has been studied in the last section.

In the second part of this work, the properties of the contacts on CdTe/CZT crystals in terms of deposition methods, metallization parameters, and electrical performance have been investigated. In the first section, different deposition methods using sputtering, evaporation, and electroless techniques have been investigated. In the second section, different parameters which are associated with the quality of the contacts have been studied. In the third section, single layer deposited on CdTe/CZT materials with the best deposition method have been investigated. Finally, the feasibility of the deposition of multi-layers has been researched.

In the last part, the results of the characterization of detectors prepared with different crystal growth processes have been presented, and more specifically, the commercial CZT detectors from eV products, and the detectors fabricated from the ingots grown with different growth conditions. The investigation is mainly focused on the influence of the presence of Te inclusions, the homogeneity of the alloy and doping, the luminescence behaviour, the surface properties of the sample, and the electrical properties of the detectors.

RESUMEN

Esta tesis presenta los resultados de preparación y el desarrollo de CdTe/CZT detectores para aplicaciones de radiación de rayos gamma.

En la primera parte de la tesis, se han investigado los procesos para la fabricación de CdTe/CZT detectores incluyendo la preparación de la superficie y los bordes laterales. Se ha investigado el proceso completo de preparación de la superficie, incluyendo el corte del lingote, lapping de las obleas, pulido mecánico, y ataque químico, poniendo énfasis en la caracterización de la superficie obtenida en cada paso. Se ha estudiado la selección del mejor ataque químico, su concentración óptima, y la limpieza de la superficie después del ataque químico, investigándose en términos de rugosidad de la superficie, contaminación, y morfología. En la última sección se ha estudiado la influencia de los diferentes métodos de preparación para los bordes laterales de los detectores.

En la segunda parte de este trabajo, se han investigado las propiedades de los contactos sobre cristales CdTe/CZT, los parámetros de metalización, y el rendimiento eléctrico. En la primera sección, se han estudiado los diferentes métodos de deposición utilizando sputtering, evaporación, y técnicas electrolíticas. En la segunda sección, se han investigado los diferentes parámetros que están asociados con la calidad de los contactos. En la tercera sección, se estudia la capa única depositada sobre CdTe/CZT, investigándose en la viabilidad de la deposición de capas múltiples.

En la última parte, se han estudiado los resultados de la caracterización de los detectores preparados con materiales procedentes de diferentes procesos de crecimiento de cristales, y más en concreto, detectores CZT comerciales de eV products, y detectores preparados a partir de lingotes crecidos con diferentes condiciones de crecimiento. La investigación se centra principalmente en la influencia de la presencia de inclusiones de Te, la homogeneidad de la aleación y el dopaje, el comportamiento de luminiscencia, propiedades de la superficie de la muestra, y las propiedades eléctricas de los detectores.

CONTENTS

CHAPTER 1. INTRODUCTION OF CDTE/CZT

1.1. Introduction of Semiconductor Materials

In this chapter, first of all, the physical and electrical properties of CdTe/CdZnTe will be introduced. Then, the different mechanisms of interactions of radiation inside detectors will be described. In addition, the transport phenomena in semiconductor materials will be presented. Moreover, the principle of operation and detector properties will be explained. Futhermore, the geometry of the detectors will be simulated and discussed. Finally, the different main applications of CdTe and CdZnTe (CZT) radiation detectors will be described.

The material properties are essential to be known for the realization of high performance spectrometers providing both good spectral resolution and high counting efficiency. High atomic number (Z) is required for efficient radiation-atomic interactions, while large enough bandgap and high intrinsic $\mu\tau$ product are needed for achieving high resistivity and low leakage current materials. Moreover, for high-sensitivity and efficiency, large detector volumes are required to ensure that maximal incident photons have the opportunity to interact in the detector volume. The demand of homogeneous and low defect density is the objective for obtaining good charge transport properties, low leakage currents, and also no conductive short circuits between the detector contacts.

Considering all requirements described above, several materials appear to be especially well suited for this application, such as Si, Ge, GaAs, HgI_2, TlBr, CdTe, CdZnTe (CZT), being the summary of their properties shown in Table 1.1. In fact, the advantage of using compound semiconductors is the possibility to develop materials with a wide range of physical properties making them adequate to almost any detection application. Furthermore, interests in radiation detectors operating at room temperature give rise to development of compound semiconductors with wide band gaps, in comparison to Si and Ge.

In recent years, X-ray and Gamma ray spectrometers have been developed to demonstrate that they can reliably produce high resolution spectra over a wide energy range [1]. This performance has been achieved through both improved material properties and through the development of a number of device geometries which take the best advantage of the material properties [2].

Table 1.1. The properties of semiconductors used for radiation detectors [8].

	Si	Ge	GaAs[3]	HgI_2[4]	TlBr	CdTe[5-6]	$Cd_{0.9}Zn_{0.1}Te$[6-7]
Crystal Structure	Cubic	Cubic	Cubic(ZB)	Tetragonal	Cubic(CsCl)	Cubic(ZB)	Cubic(ZB)
Growth Method	C	C	CVD	THM	THM,HPB	VAM	BM
Atom number	14	32	31, 33	80, 53	81,35	48, 52	48,30, 52
Density (g/cm^3)	2.33	5.33	5.32	6.4	7.56	6.20	5.78
Band gap (eV)	1.12	0.67	1.43	2.13	2.68	1.44	1.57
E_{Pair} (eV)	3.62	2.96	4.2	4.2	6.5	4.43	4.6
Resistivity (Ωcm)	10^4	50	10^7	10^{13}	10^{12}	10^9	10^{10}
$\mu_e\tau_e$ (cm^2/V)	>1	>1	10^{-5}	10^{-4}	10^{-5}	10^{-3}	10^{-3} - 10^{-2}
$\mu_h\tau_h$ (cm^2/V)	~1	~1	10^{-6}	10^{-5}	10^{-6}	10^{-4}	10^{-5}

As one example, for incident radiation energy of 60 keV, Figure 1.1 gives the useful information about the thickness in which 90% of radiation is absorbed for different materials. Of all the shown listed materials, CdTe/CZT is the material requiring the lowest thickness (0.5 mm) for an applied voltage of a hundred volts, which is very close to the ideal detector material. For this reason, the properties of CdTe and CZT will be further introduced.

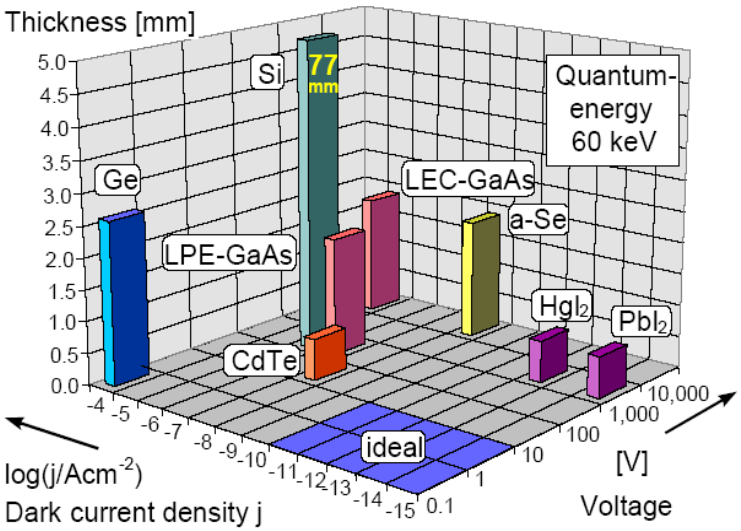

Figure 1.1. Thickness required for stopping 90% of radiation incident energy at 60 keV for different semiconductor materials including CdTe/CZT [9].

1.2. Physical properties of CdTe/CZT

1.2.1. Crystal Structure

CdTe/CZT material has zinc blende structure, which belongs to the cubic space group $F\bar{4}3m$ and consists of two interpenetrating face centered cubic (fcc) lattices offset from each other by one-quarter of a unit cell body diagonal [10]. Each sub-lattice is occupied by the Cd (or Zn depending on the composition) atoms or Te atoms, respectively, being the structure of the zinc blende of CdTe/CZT material shown in Figure 1.2. It is important to mention that all atoms in the lattice are identical, each atom is surrounded by four close neighbours belonging to the other fcc sub-lattice. They are arranged in a tetrahedron and each atom shares its four outer (valence) electrons with those of the neighbours, thus forming covalent bonds.

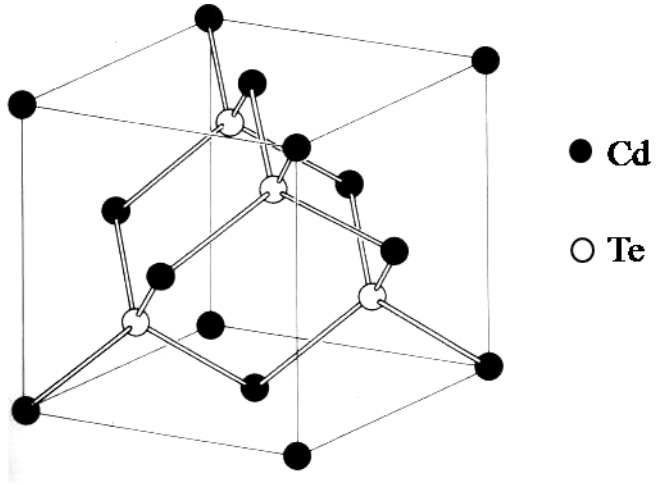

Figure 1.2. Zinc blende structure of CdTe/CZT.

CdTe/CZT crystals have a fcc lattice with a two-points basis σ1=(0,0,0) and σ2=(1/4*a*,1/4*a*,1/4*a*). The geometry factor can be expressed by:

$$S(q) = \sum_{i=1}^{2} f_i e^{j(\sigma_i \cdot q)} \quad \text{Eq. 1-1}$$

where *q* is the scattering vector, *f1* and *f2* are the atomic form factors for Cd (or Zn) and Te, respectively. The Bragg peak *q* is equals to the reciprocal lattice vector, *K*, thus the structure factor can be written as:

$$S(K) = \sum_{i=1}^{2} f_1 + f_2 e^{j(\sigma_i \cdot q)} \quad \text{Eq. 1-2}$$

Indeed, f_1 and f_2 are different in zinc blende structure, therefore, the structure factor never equals to 0.

The alloy $Cd_{1-x}Zn_xTe$ can be considered as the Zn atoms randomly substitute the Cd atoms of the CdTe crystal in fraction of *x*. In fact, the lattice constants for CdTe and ZnTe are 6.482 Å and 6.104 Å, respectively [11]. The difference in the lattice constants of CdTe and ZnTe indicates that the zinc substitution of Cd atoms can lead to small changes in average unit cell dimensions.

In this way, it is known that the lattice constant of CZT material can be expressed by using Vegard's Law [12]:

$$a(x) = a_1(1-x) + a_2 x \quad \text{Eq. 1-3}$$

where a_1 and a_2 are the lattice constants of CdTe and ZnTe, respectively, and *x* is the composition. With this law, the lattice constant of $Cd_{0.9}Zn_{0.1}Te$ can be estimated at 6.441 Å by using the lattice constant of CdTe and ZnTe [13].

In fact, the effects of incorporating Zn into the CdTe crystal can decrease the lattice constant of the material whereas increase the bandgap energy. Nevertheless, larger bandgap energy can bring about the probability for achieving higher resistivity detector materials. Moreover, due to the higher binding energy of ZnTe with regards to CdTe, the lattice is strengthened which resulting in a higher shear modulus.

1.2.2. Band Structure

In order to study the band structure of CZT, the band structure of CdTe and ZnTe are essential to be known. CdTe and ZnTe are direct-bandgap semiconductors with the bandgaps at room temperature 1.5 eV and 2.2 eV, respectively [14]. The direct-bandgap means that the momentum of electrons and holes is the same in both the conduction band and the valence band, hence an electron can directly emit a photon. The band structure of CdTe based on the pseudopotential calculations is exhibited in Figure 1.3, which is qualitatively similar to the band structure of ZnTe [15].

There are four valence bands contains eight valence electrons per unit cell. The high-hole and light-hole bands and the degeneracy at k=0 of the split-off band are rejected by the spin-orbit interaction [16]. The effective masses of holes and electrons, *m*, can be described by [12]:

$$\frac{1}{m*} = \frac{2\pi^2}{h^2}\frac{\partial^2 E}{\partial k^2} \quad \text{Eq. 1-4}$$

Considering that the constant energy surface is spherical, the value can be achieved from the reciprocal of the curvature of the energy band in k-space at k=0. As reported by *Peyghambarian et al.*, CdTe and ZnTe have relatively low effective masses for electrons at around 0.11 m_0 and 0.15 m_0, respectively [14]. *Kanzer* demonstrated that the effective hole masses are 0.70 for heavy holes and 0.103 for light holes, indicating that more effective masses can be achieved due to the separation in the valence band [17].

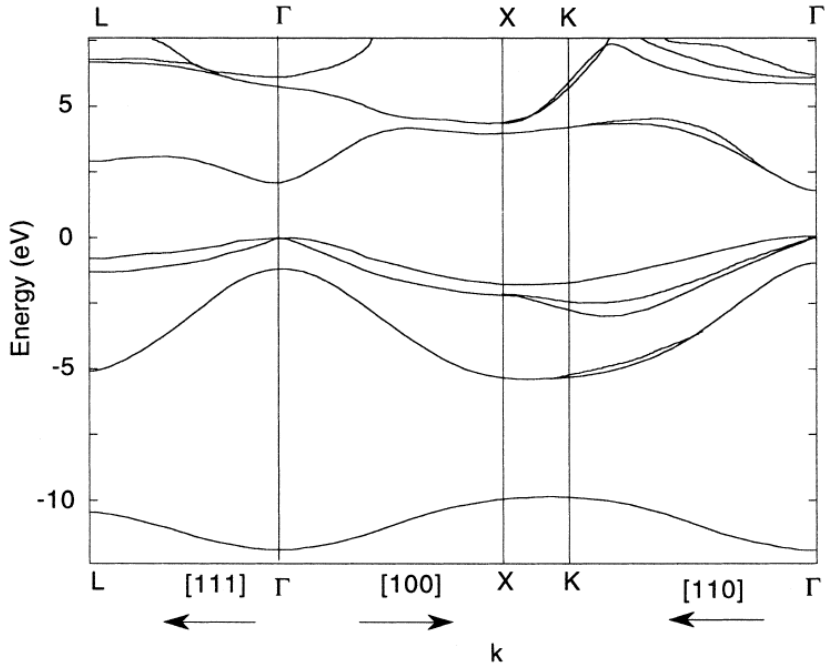

Figure 1.3. Band structure of CdTe calculated by the pseudopotential method [16].

It is difficult to obtain the band structure of $Cd_{1-x}Zn_xTe$, due to the fact that the entire band theory of solids is based on the assumption of periodicity, which does not exist in an alloy because of the local composition fluctuations. Generally, the approximation for the CZT band structure is related with the structure of two binary semiconductors (CdTe and ZnTe) as a linear interpolation between these two compounds.

However, this approximation is not very effective in the definition of the relationship between the band gap and composition. *Singh et al.* reported that for direct-bandgap

semiconductors in the tight-binding approximation, the band edges are linear sums of the matrix elements, revealing that the bandgap varies linearly with *x* [18]. Actually, quadratic curvature is always found to fit well with the measured dependence of the bandgap as a function of composition ($E_g(x)$).

1.2.3. Methods of Crystal Growth

For the CdTe/CZT crystals grown from the melt, the first solids formed from the melt will incorporate more zinc than the average melt content in accord with the phase diagram. The variation of zinc in the crystal has been investigated and presented big difference considering the position of the samples in the ingot, which is due to the segregation coefficient of zinc at 1.3 [12]. In fact, the commercially available Cd, Zn, Te starting materials are normally greater than 6N pure, purer starting materials are demanded for nuclear detectors. It is important to note that the thermal dissociation pressure at the melting point causes the cadmium evaporating at a higher rate than tellurium leading to the non-stoichiometry and precipitation of tellurium in the crystal [12].

Several methods have been successfully employed in the growth of $Cd_{1-x}Zn_xTe$ for detector applications. The crystal growth techniques for CdTe/CZT material include the Bridgman method (BR), Vertical Gradient Freeze (VGF) method, Travelling Heater method (THM), Physical Vapour Transport (PVT) method, and Liquid Phase Epitaxy (LPE) method [19-24]. In the next paragraph, a brief description of each method will be given.

Bridgman (BR) growth method is a controlled freezing process occurring at the liquid-solid equilibrium condition. The growth happens under a temperature gradient in order to produce a single nucleus from which a single crystal will propagate and grow. In the growth stage, the starting materials are melted and cooled to solidify into a crystalline form by allowing the solid-liquid to move slowly until the whole molten charge is solidified.

Different modifications to BR method containing High Pressure Bridgman (HPB) and Low pressure Bridgman (LPB) have been reported. High pressure BR is the most commonly used method for commercial production of CZT, where the material is typically grown under Te-rich conditions [25]. In the HPB method, a high pressure of 10-150 atm of an inert gas over the melt to suppress the loss of cadmium in the molten materials [1]. In the LPB method, the CZT crystal is grown without the use of high gas pressure, which can be achieved in the horizontal or vertical configuration.

For the BR method, it is difficult to obtain long term stability at the growth interface owing to that the charge and the furnace move relatively to each other and the temperature profile is not modified during the whole process. Therefore, the radiative heat transport is continuously modified even for a constant thermal gradient, leading to a non uniform process.

This effect can be eliminated by the Vertical Gradient Freeze (VGF) method, where the heat transport can be stabilized, and the variation of temperature across the melt is operated by temperature programming in a multi-zone furnace [2]. Using this method, several heaters are carried out to achieve the desiring temperature profile along the ampoule. The temperature profile is gradually displaced when the ampoule and the heaters are fixed, moving the solid-liquid interface (SLI) upwards across the charge [3]. The challenge of obtaining a stable growth arises from the continuous variations in the temperature profile with the probability of varying the temperature gradient during the crystal growth [4].

Physical vapour transport (PVT) method has been successfully used to grow several binary compounds used in radiation applications, such as HgI_2 and CdTe [26]. The advantages of PVT growth method are the lower growth temperature and minimal contact area with walls of the ampoule that results in reduction of impurities stress related imperfections. Meanwhile, it is easier to control the stoichiometry and obtain greater uniformity [5-7].

The travelling heater method (THM) is a seeded growth process that operates by precipitation of grown material from a solution. The CdTe/CZT seed is placed in the growth crucible and molten Te is added as solvent while polycrystalline CdTe/CZT is supplied as a feed material. In consequence, the polycrystalline CdTe/CZT dissolves into molten tellurium. When the travelling heater is moved, the CdTe/CZT crystal precipitates from Te solvent and then grows onto the CdTe/CZT seed, therefore, homogenous single grains of CdTe/CZT crystal are achieved.

The advantage of THM method is the possibility to grow at lower temperature compared with the BR and VGF methods due to the use of Te as solvent. Generally, the crystals are grown at a rate of around 4-5 mm-day^{-1}, and exhibit better crystalline quality and homogeneity in Zn concentration than the crystals grown by BR or VGF methods [27]. Furthermore, low levels of impurities are exhibited in as grown ingots, the impurities can be slowly eliminated with each subsequent pass of the heater [25]. One disadvantage of this method is the difficulty to scale large diameter crystals, which have large macro defects exhibited in the last-to-freeze region of the ingot [28].

1.2.4. Crystalline Defects

An ideal crystal has every atom in a perfect, exactly repeating pattern. However, in reality, most crystalline materials have a variety of crystallographic defects, places where the crystal's pattern is interrupted. The types and structures of these defects may have a profound effect on the properties of the materials and the performance of semiconductor devices. The most common crystallographic defects presented in our material are described below.

A. Grain Boundaries

Grain boundaries play an important role in controlling the electrical and mechanical properties of the polycrystalline crystal. It is believed that these properties are affected by the atomic structure of the grain boundaries, as well as by the dislocations and ledges. Generally, grain boundaries have different atomic configurations and local atomic densities from the perfect crystal, which act as sinks for impurity atoms with tendency to segregate to interfaces.

The grain boundaries can be formed during crystal growth at high temperature gradients or high growth speeds. Normally, the grain boundaries are introduced at the very early stage of crystal growth when the nucleation of numerous grains appears, or resulting from the instabilities at the growth interface. In fact, the grain boundaries have an impact on the limitation of the charge transport properties in the detectors, which may be ascribable to the high concentration of impurities and dislocations appearing at the grain boundaries [29]. In conclusion, the trapping effect along the grain boundaries can bring about nonuniform charge transport which can lead to the degradation of the detector performance.

B. Twins

When two or more crystals grow together symmetrically parallel to each other, some parts share the crystallographic direction or plane, the other parts are in a reversed orientation, and this phenomenon is called twinning**.** In general, the lattice points in the crystal with twinning behaviours are shared with another crystal adding apparent symmetry to the crystal pairs. Due to the addition of symmetry, this behaviour never happens in connection with the existing symmetry of the crystal.

The twins are generally introduced into the crystal by the temperature fluctuations during the cooling phase, or other parameters related with the growth parameters. As reported by some authors, the twins in CdTe/CZT are normally in groups of 3 – 6 micro-twins parallel to each

other, with twinning planes lying entirely in CdTe/CZT {1 1 1} planes [30]. *Kestigan et al.* demonstrated that the number of micro-twins can be substantially diminished by improving the cooling profiles during the crystal growth [31].

C. Cracks

Cracks are resulting from the thermal and mechanical stresses brought by the ampoule, or during the crystal cooling down period. The cracks are typically a few cm in length and around 25 μm in width, and they originate at the edges of the ingot near the ampoule wall, and propagate through the ingot [20].

In addition, cracks may also result from the mechanical stresses produced in the crystal during slicing, lapping, and polishing process. Therefore, these defects can be removed by suitable choices of thermal profiles, crucible materials, cooling, and surface treatment.

D. Dislocations

Dislocations are normally produced in the crystal growth process, which is probably due to the thermal stress during solidification and cooling down. *Szeles et al* reported that the dislocations were introduced into CdTe/CZT crystal by deformation which is associated with a localized defect level with ionization energy of 0.27 eV [2].

The density of dislocations can be characterized by using Etch Pit Density (EPD) technique. This technique is an important indicator of material quality as the appearance of dislocations deteriorates the detector performance. For a good quality crystal, the EPD value is reported at the range of $10^{-3} \sim 10^{-4}$ cm^{-2} [2]. The dislocations crossing the polished surface with <111> orientation in CdTe/CZT crystal can be revealed by appropriate etching methods. The EPD process obtained by Nakagawa etch was generally used as the standard solution to measure the dislocation density in CdTe/CZT materials [32].

In fact, this phenomenon is typically observed when the crystal is grown at a high temperature gradient where the dislocations introduced into the crystal undergo polygonalization or cellular structures [2]. The dislocations can also be produced at the ampoule wall by the thermally induced stress or formed during the solidification and cooling down stages in the growth process.

E. Te Precipitates /Inclusions

Te precipitates and inclusions have an important impact on the performance of CdTe/CZT devices. The average size of Te precipitates is between 10 nm and 30 nm, whereas the typical diameter of Te inclusions is at the range of 10 ~ 100 μm [33].

Precipitates are created during the cooling process and originated from the retrograde slope of the solidus line, and it has been reported that the nucleation and growth of Te precipitates can be controlled by the atomic diffusion [34].

Te inclusions generally are originated from the morphological instabilities at the growth interface, while the Te-rich melt droplets are captured from the boundary layer before the interface. Te inclusions can be created at the growth interface and embedded into the crystal grains, which can migrate during the cool-down stage of the CdTe/CZT ingot with the effect of temperature gradients [34].

It is important to note that the impurities usually trapped at Te inclusions are segregated at the first-to-freeze and last-to-freeze section of the ingots [2]. It has been accepted that the nonuniform distribution of Te inclusions can significantly affect the charge transport properties and deteriorate the spectroscopic performance of CdTe/CZT nuclear radiation detectors [2].

1.3. Electrical Properties of CdTe/CZT

1.3.1. Electrical Compensation

X-ray and gamma-ray radiation detector applications require the materials have high resistivity and a minimum quantity of carrier traps that contribute to incomplete charge collection and broadening or ‘tailing’ in the photopeak [12]. Most materials achieve high resistivity by purifying the material or electrically active dopants added in low or high level concentration. Therefore, it is necessary to introduce dopants to compensate the impurities existing in the materials.

For CdTe/CZT materials, the compensation is obtained by the presence of deep levels, which can act as carrier trapping centers, hence it is essential to understand the mechanism of compensation. It is known that the high resistivity CdTe/CZT can be achieved through the

pinning of the Fermi-level near the midgap by compensation of the shallow and deep level defects rather than through the growth of intrinsic material [12].

Doty demonstrated that the use of high pure starting material to grow intrinsic high resistivity CZT material is unsuccessful, whereas introduce Al as a dopant into CZT starting material can achieve high resistivity CZT crystal [35]. Generally, when the deep levels locate near the intrinsic Fermi-level, the large changes in the occupancy of the level can be obtained by small variations in the Fermi-level. Consequently, the extra free holes or electrons created by the introduction of shallow acceptors or donors can be neutralized by further ionization of deep level.

Figure 1.4 exhibits the position of energy levels of ionizations of the native defects, impurities and complexes presented in $Cd_{1-x}Zn_xTe$. Cd vacancies (V_{Cd}), which exist in the CZT crystals can be reduced by the Cd over-pressure in the growth process and enhanced by low Cd partial pressure [36]. In fact, Cd vacancies are the dominant native shallow acceptor defects with a concentration of 10^{11} — 10^{15} cm^{-3}, which is critical in the electrical compensation and carrier trapping in CZT [37].

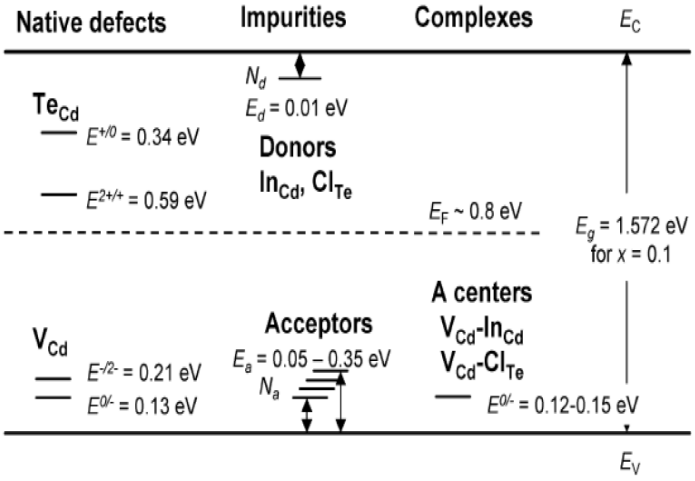

Figure 1.4. Position of energy levels of ionization of certain defects in $Cd_{1-x}Zn_xTe$ (x=0.1) [39].

For the In-doped CdTe materials, it has been reported that the concentration of Cd vacancies increase with [In], which is consistent with the self-compensation of In with V_{Cd} by the formation of In-V_{Cd} complexes [38]. For the group III elements act as donors at the Cd site, there is significant evidence of self-compensation involves the vacancy complexes (A-centers), particularly for In [13].

In the complexes part, one can observe the presence of A-centers, which is formed when the V_{cd}- native defects coupled with the shallow donors such as In_{Cd} or Cl_{Te}.

For the compensation model, for the case of CdZnTe doped with In, *Barnes and Zanio* supposed that the doubly charge Cd vacancy, V_{Cd}^{2-}, forms two types of complexes: $[V_{Cd}^{2-} In_{Cd}^{+}]^{-}$, a singly ionized acceptor, and $[V_{Cd}^{2-} 2In_{Cd}^{+}]^{0}$, a fairly neutral entity, which can bind electrons or holes weakly [40]. The compensation between In donors and Cd vacancies could be expressed in the example by:

$$V_{Cd}^{2-} + In \Leftrightarrow In_{Cd}^{+} + 3e^{-} \qquad \text{Eq. 1-5}$$

$$V_{Cd}^{2-} + In_{Cd}^{+} \Leftrightarrow [V_{Cd}^{2-} In_{Cd}^{+}]^{-} \qquad \text{Eq. 1-6}$$

$$[V_{Cd}^{2-} In_{Cd}^{+}]^{-} + In_{Cd}^{+} \Leftrightarrow [V_{Cd}^{2-} 2In_{Cd}^{+}]^{0} \qquad \text{Eq. 1-7}$$

where In_{Cd}^{+} is an ionized shallow donor, formed by the compensation with Cd vacancy (Eq. 1-5). The shallow donor In_{Cd}^{+} attracts one V_{Cd}^{2-} shallow acceptor, thereby the singly negative donor-vacancy complex (A-centers) can be formed ($[V_{Cd}^{2-}In_{Cd}^{+}]^{-}$) (Eq. 1-6). The complex A-centers can further recombined with the extra accumulated In donors, In_{Cd}^{+}, forming the neutralentity ($[V_{Cd}^{2-} 2In_{Cd}^{+}]^{0}$), which is caused by self-compensation (Eq. 1-7).

1.3.2. Resistivity

The conductivity of CdTe/CZT bulk material is proportional to the total free carrier density, which is depending on the density of free electrons and holes and also the densities of the ionized impurity. The density can be modified by applying a bias producing an electric field within the material, while small regions of the material can be located in a state where all the carriers be eliminated by the electric field as applying appropriate bias, therefore, the remaining charge density within the material is only associated with the density of ionized purity [41].

The conductivity of the material is determined by the current density, *J*, which is a function of the electric field, *E*:

$$J = \sigma E = q(n\mu_e + p\mu_h)E \qquad \text{Eq. 1-8}$$

where σ is the conductivity of the material, μ_e and μ_h are the mobility of the electrons and holes, respectively, q is the electric charge ($1.6 \cdot 10^{-19}$ C), and n and p are the density of free electrons and free holes, respectively.

Therefore, the conductivity σ equals the product of the charge of the mobile carriers, their density and velocity, can be described by [41]:

$$\sigma = q(p\mu_h + n\mu_n) \qquad \text{Eq. 1-9}$$

The electrical resistivity, ρ, is equivalent to the inverse of the conductivity of the material, σ [41]:

$$\rho = \frac{1}{\sigma} = \frac{1}{q(p\mu_h + n\mu_n)} \qquad \text{Eq. 1-10}$$

Indeed, in the n-type semiconductor, if the mobile carriers are depleted within the depletion region, the density of charges in that region is only related with the ionized donors. Therefore, the resistivity is higher for the depleted region than the un-depleted zone.

1.3.3. Electrical Contacts

Electrical contacts are generally used for collecting the electric charges created by radiation. Gold and Platinum are the most commonly used for contacts, which can be operated by sputtering, evaporation, and electroless deposition methods. The metal/semiconductor interface is important for understanding the interdiffusion of the metal and semiconductor, the chemical species formation, the defect formation and their interactions [42].

The surface preparation for the detector fabrication plays an important role to determine the contact characteristics and the leakage current for detectors. The surface leakage current is always one dominant factor to influence the detector performance. Some authors have reported the contact-related problems remaining in the development of CdTe/CZT devices.

One common problem is the active volume of the detector of high resistivity and large applied bias is not equal to its geometric volume even at full depletion. High electric field near the cathode can be explained by the presence of injecting contacts and space-charge effects [43].

Thermal annealing of the contacts during or after the deposition process was found to be beneficial, notwithstanding the physical mechanisms responsible for this improvement are

essential to be understood. The surface oxides both on the lateral sides and the metal/semiconductor interface of the CdTe/CZT crystal also play an important role.

The I-V characteristic of the metal/semiconductor junction is determined by the barrier height at the interface. The simple Schottky-Mott theory of the metal/semiconductor contacts reveals that high work function metals (eg. Au) can form Ohmic (injecting) contacts on p-type material and Schottky (blocking) contacts on n-type material, whereas low work function metals (eg. In) is the opposite case [44].

1.3.3.1. Work Function

It is been accepted that the Fermi level of any two solids in contact must be equal in thermal equilibrium. The difference between the Fermi level and the vacuum level is defined as work function, W_M, can be expressed by:

$$W_M = E_{vac} - E_F \qquad \text{Eq. 1-11}$$

where E_F and E_{vac} are the energy of Fermi level and vacuum level, respectively.

The work function varies by using different materials. A contact metal and a semiconductor can have different work functions, termed Φ_M and Φ_S, respectively. When the metals are deposited on the semiconductor materials, electrons will flow from the one with lower work function until the Fermi levels to equilibrate. Consequently, the material with lower work function will attribute to a slight positive charge while the one with higher work function will turn to slightly negative.

The metals have the work functions around the electron affinity of semiconductors easier to form ohmic contacts. Indeed, the metals with low work functions form the best contacts to n-type semiconductors whereas those with high work functions create the best contacts to p-type semiconductors. However, in realistic conditions, the contact metals may react with the surfaces of the semiconductors to produce a compound with new electronic properties. As a result, the contamination layer at the interface may effectively broaden the barrier.

Figure 1.5 presents the position of the Fermi level in the metal given by the work function $W_M = - e\Phi_M$. The work function shows the atomic shell structure and the minima of the work function exists for group-I elements [45]. Due to the high electron density in the metal

conduction band, the position of the Fermi level does not change substantially when the charge is exchanged between metal and semiconductors.

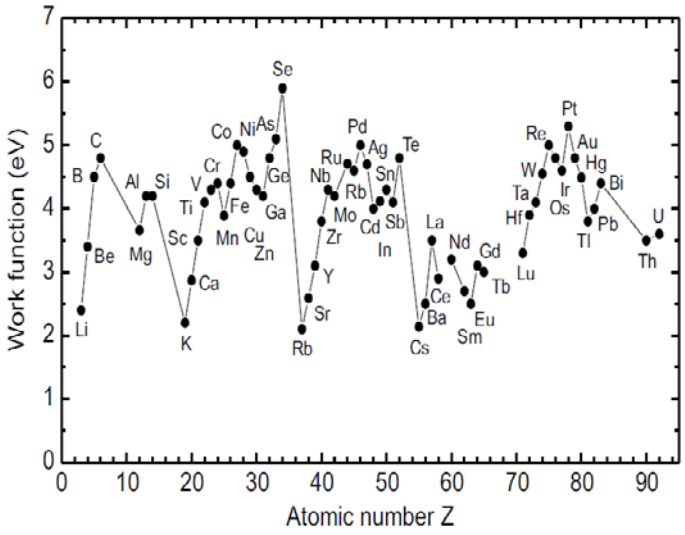

Figure 1.5. Work function of various metals [45].

1.3.3.2. Ohmic Contact

Whenever a gamma photon is absorbed within the detector, it will generate electrons and holes that flow in opposite directions along the field lines towards the contacts. The charge in the detectors will redistribute the electric field within it and the current will stabilize to a steady state. The amount of photo-generated charge is proportional to the photon energy, hence this energy will be measurable if the charge is fully collected [46].

In the ohmic contact detectors, there is an extra flow of electrons from the negative contact towards the holes, in addition to the flow of the gamma generated holes and electrons. Since the flow velocity of the electrons are ten times faster than the holes, the electrons will flow from the negative contact towards the holes faster than holes flow the same way in the opposite direction. The extra electron flow transforms the detector into a fast response device, and there will be little difference if the holes do not move at all, hence the detector is not sensitive to hole trapping.

The current density, *J*, within the detector, is the sum of the carrier and displacement currents which can be presented by [47]:

$$J = n\mu eE + \frac{\varepsilon}{4n}\frac{dE}{dt} \quad \text{Eq. 1-12}$$

where n is the electron density, μ is the mobility, e is the electron charge, ε is the dielectric constant, E is the electric Field, dE/dt is its time derivative.

Indeed, at the ohmic contact surface, there is only the carrier current and the displacement current is zero, then $dE/dt = 0$. Consequently, the electric field induced by the external bias voltage at the contact can be described by $E = V/d$. The electric field will be time independent without considering any event occur within the detector [46]. The current through any cross section within the detector, or the detection circuit is the same. Since there is no displacement current at the negative contact, the carrier current there will be equal to the overall current at any other cross section.

Normally the ohmic contact has a small resistance for both current directions. The voltage across the contact is smaller than the voltage in the active layer. The contact resistance, R_c, is denoted as the differential resistance at $V=0$ [45],

$$R_C = \left(\frac{\partial I}{\partial V} \right)^{-1}_{V=0} \quad \text{Eq. 1-13}$$

At low doping, in our case, the transport is determined by the thermionic emission, the equation can be expressed by:

$$R_C = \frac{k}{eA^*T} \exp\left(-\frac{e\Phi_B}{kT} \right) \quad \text{Eq. 1-14}$$

A small barrier height will result in small contact resistance.

For high doping, the contact resistance, R_c, is dominated by the tunnelling current, which decreases exponentially with the doping, then Eq. 1-14 can be described by [45]:

$$R_C \propto \exp\left(-\frac{e\Phi_B}{E_{00}} \right) \quad \text{Eq. 1-15}$$

where E_{00} is the characteristic energy parameter, and can be given by:

$$E_{00} = \frac{e\hbar}{2} \left(\frac{N_D}{m^* \varepsilon_S} \right)^{1/2} \quad \text{Eq. 1-16}$$

The two mechanisms with low barrier height or high doping for the formation of Ohmic contacts on semiconductors are summarized schematically in Figure 1.6. Indeed, the barrier height of the detector can only be modified by changing the metal or the doping density.

The high doping region is depending on the carrier type. Since the transmission coefficient in tunnelling depends exponentially on the particle mass, the semiconductors with lower effective masses are more easily contacted. Moreover, semiconductors with smaller bandgaps more promptly to form ohmic contacts owing to their lower electron affinities (and thus barrier heights).

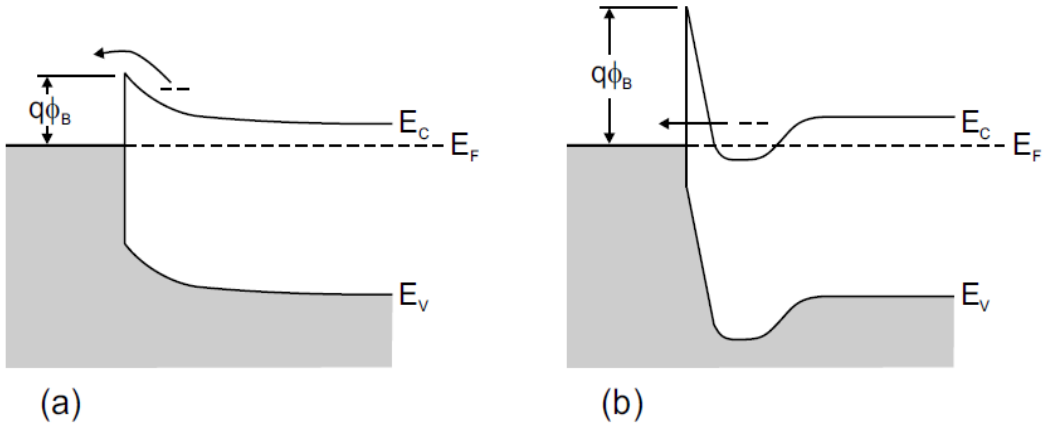

Figure 1.6. Schematic diagram of the formation of an Ohmic contact, (a) low barrier height, (b) high doping (thin depletion layer) [45].

1.3.3.3. Schottky Contact

In opposition to the Ohmic contact, if the I-V characteristic is non-linear and asymmetric, the contact is a blocking or Schottky contact instead of Ohmic contact. Schottky contact can be created by bringing a very thin metal layer in contact with a semiconductor material, which can form a junction near the surface of the semiconductor. It is important to note that the layer must be as thin as possible in order to assure high transparency of the metal layer to the photons.

The Schottky-Mott theory of metal-semiconductor contacts implies that high work function metals, such as Au, can form Ohmic contacts on p-type material and Schottky contacts on n-type material, while for low work function metals, such as In and Al, the opposite is true. The Schottky barrier having a large barrier height and low doping concentration that is less than the density of states in the conduction band or valence band.

The potential barrier between the metal and the semiconductor can be identified on an energy band diagram, as exhibited in Figure 1.7. To build such a diagram, the energy band diagram of the metal and the semiconductor has been considered, and align them with the same vacuum level as presented in Figure 1.7 (a) (c). When the metal and semiconductor are

connected together, the Fermi energies of the two materials must be equal at thermal equilibrium, as shown in Figure 1.7 (b) (d).

Whenever a metal and a semiconductor are in intimate contact, there exists a potential barrier between the two that prevents most charge carriers (electrons or holes) from passing from one to the other. The barrier height, Φ_B, is defined as the potential difference between the Fermi energy of the metal and the band edge where the majority carrier resides. For n-type semiconductors, $\Phi_B = \Phi_M - \chi_S$, where χ_S is electron affinity of the semiconductors, expressed by the difference between the vacuum level and the conduction band level.

For n-type material, the barrier height Φ_B can be described by:

$$\Phi_B = \Phi_M - \chi_S \qquad \text{Eq. 1-17}$$

where Φ_M is the work function of the metal, χ_S is the electron affinity of the semiconductors. In the ideal contact, the Schottky barrier height can be stabilized by modifying the work function of the deposited metal.

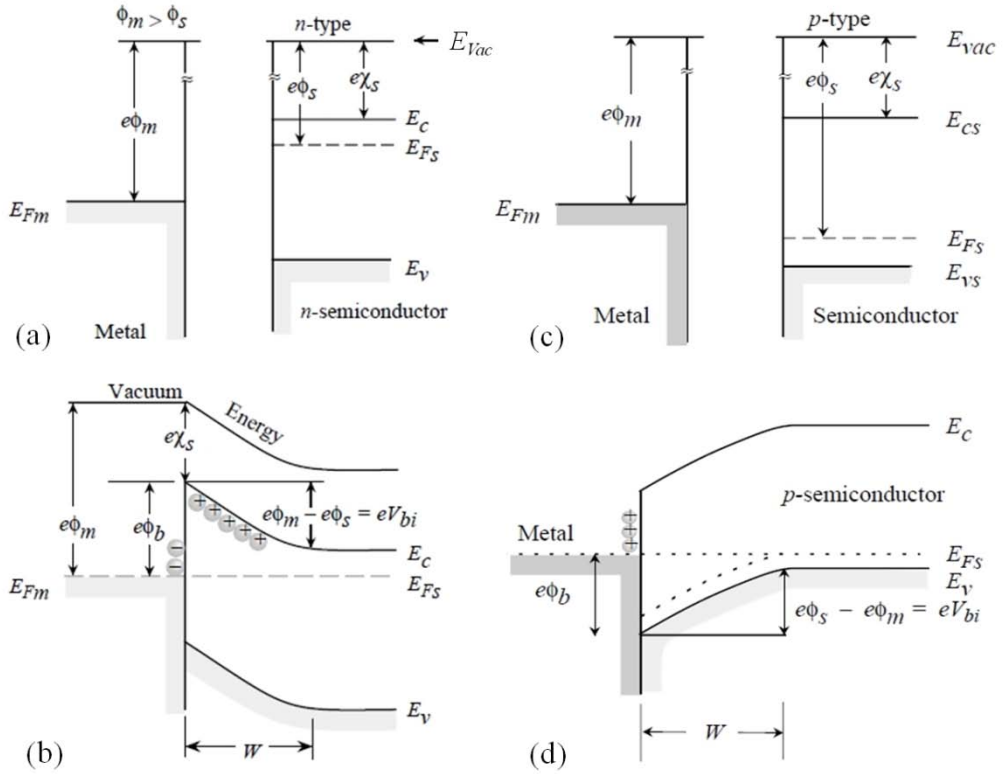

Figure 1.7. (a) Energy band diagram of a metal and the n-type semiconductor before contact, (b)Formation of a Schottky junction for n-type materials, (c) Energy band diagram of metal and p-type semiconductor before contact, (d) Formation of a Schottky junction for p-type materials.

For p-type semiconductors, the barrier height Φ_B can be defined as:

$$\Phi_B = E_g - (\Phi_M - \chi_S) \quad \text{Eq. 1-18}$$

The built in potential, V_{bi}, can be described by the difference between the work function of the metal and the work function of the semiconductors:

$$V_{bi} = \Phi_M - \Phi_S \quad \text{Eq. 1-19}$$

If $\Phi_M > \Phi_S$, the contact is supposed to be blocking contact, while Ohmic contact can be obtained when $\Phi_M < \Phi_S$.

The ideal case of leakage current of the Schottky contact taking in account the thermionic emission and the diffusion is [48]:

$$J = A^* T^2 \exp\left(-\frac{q\Phi_B}{kT}\right)\left(\exp\left(\frac{nqV}{kT}\right)-1\right) \quad \text{Eq. 1-20}$$

where n is the realization factor which is around 1 ~ 2 for good detectors, V is the applied bias, and A^* is the effective Richardson constant, which can be written as:

$$A = \frac{4\pi m_n^* k^2}{h^3} \quad \text{Eq. 1-21}$$

Several effects can modify the actual Schottky barrier Metal/Semiconductor junction current from the theoretical value described by Eq. 1-20. When consider a large doping concentration in the semiconductor region, the tunnelling current becomes prominent, and Schottky effect induced lowering of the barrier height should also be included.

Szeles et al. demonstrated a method to calculate the resistivity by using I-V characteristics, the thermionic emission theory can be modified to [49]:

$$I = I_S(\exp(\frac{q(V_B - IR_S)}{kT} - 1)) \quad \text{Eq. 1-22}$$

where I_S is the reverse saturation current, R_S is the semiconductor series resistance and can be written as:

$$R_S(I \to 0) = \frac{V_B}{I} - \frac{kT}{qI_S} \quad \text{Eq. 1-23}$$

1.3.4. Space Charge Limited Current

For structures where carriers can promptly enter the insulator and freely flow through the insulator one finds that the resulting current and carrier densities are much higher. The high density of these charged carriers causes a field gradient, which can limit the current density. Transport of the charges under the effect of this non-uniform electric field is known as space charge limited current (SCLC). SCLC measurement can provide information about the mobility and the concentration of the charge carriers, and the energy distribution of localized defects or carrier trapping states [50]. If injecting contacts can be produced, SCLC is very sensitive to characterize semi-insulating or insulating materials.

Figure 1.8 shows a simply energy-band diagram for an insulator, with a discrete trap level, in Ohmic contact with thermal and electrical equilibrium [51]. When apply bias to the insulator, this reservoir will inject electrons into the bulk material, as presented in Figure 1.7 (B). Therefore, the metal is tightly coupled to the reservoir and readily supplies it while the current is lower than its saturation value for the special contact at the given temperature.

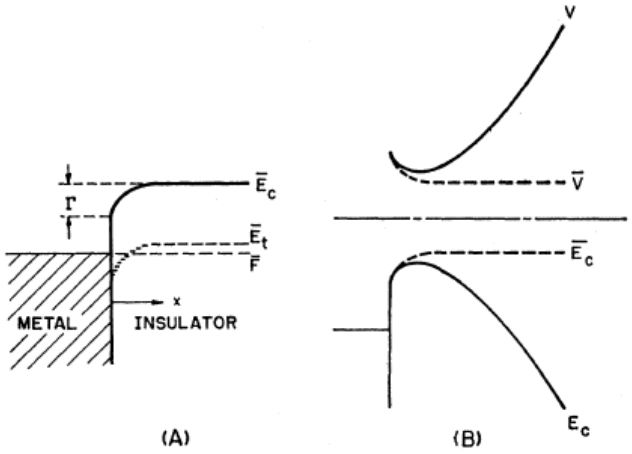

Figure 1.8. Simplified energy-band diagrams for an injecting contact of an insulator with a metal. (A) the contact in the thermal and electrical equilibrium, (B) the contact in steady state under an applied bias [51].

The simplified SCLC theory to model the *I-V* characteristics in semiconductor devices is based on two dominant approximations [52]: (i) the diffusion currents are ignored to describe the current flow, (ii) the Ohmic contact is regarded as an infinite reservoir of charges which is available for injection.

The approximation considering only the drift current can be written as:

$$J = q\mu nE = q\mu n\frac{V}{d} = const \quad \text{Eq. 1-24}$$

where J is the current density, q is the electronic charge, μ is the carrier mobility, n is the charge carrier density, E is the electric field, V is the applied voltage and d is the thickness of the semiconducting layer.

Then the current-flow equation containing the first current and the diffusion current can be expressed by [53]:

$$J = qn\mu E - qD(dn/dx) = const \quad \text{Eq. 1-25}$$

where J is the current density, q is the unit charge, μ is the electron mobility, n is the free charge carrier density, E is the electric field, D is the electron diffusion constant which is associated with the carrier mobility by D = (kT/q)μ. In fact, the drift current is opposing the diffusion current and the electric field will drive the holes back to the metal.

Generally, SCLC occurs when the electron density is small or when the mobility of the carriers is small, especially when the charge-density gradient dn/dx is large. By integrating the Eq. 1-25 from x = 0 to x = d with V(0) = V and V(d) = 0, the current-voltage characteristic can be obtained as:

$$J = \frac{9}{8}\varepsilon\mu\frac{V^2}{d^3} \quad \text{Eq. 1-26}$$

The Eq. 1-26 is defined as the trap-free square law, the Mott-Gurney square law or Child's law for solids. In this regime, the current is proportional to the square of the electric field.

In the case of trap-limited SCLC, the equation of trapped limited can be modified as:

$$J = \frac{9}{8}\varepsilon_r\varepsilon_0\mu\theta\frac{V^2}{d^3} \quad \text{Eq. 1-27}$$

The magnitude of current differs approximately by a factor of θ, called trap factor and reflects the extent to which the traps reduce the effective mobility between the two cases and is given as:

$$\theta = \frac{N_v}{N_t}\exp(-\frac{E_t}{kT}) \quad \text{Eq. 1-28}$$

where N_t is the density of traps, N_v is the effective density of states in the valance band and Et is the energy of trap level.

At the trap-filled limit, the onset of trap filled voltage (V_{TFL}) results in the density of traps, can be expressed as:

$$N_t = \frac{3}{2}\frac{\varepsilon_r \varepsilon_o V_{TFL}}{qd^2} \quad \text{Eq. 1-29}$$

Figure 1.9 summarizes the SCLC as a function of applied bias. For low applied bias in the device with Ohmic contacts, the number of injected charge carriers is smaller or comparable to the thermally generated intrinsic charge carriers, and the $I-V$ characteristics display linear behaviour (Eq. 1-24). For increased bias, the density of holes becomes larger than the negatively charged acceptors and the device enters the SCLC regime. The effective mobility can still be limited by traps (Eq. 1-27). For a certain voltage all traps get filled (Eq. 1-29) and the device enters the trap-free SCLC regime (Eq. 1-26).

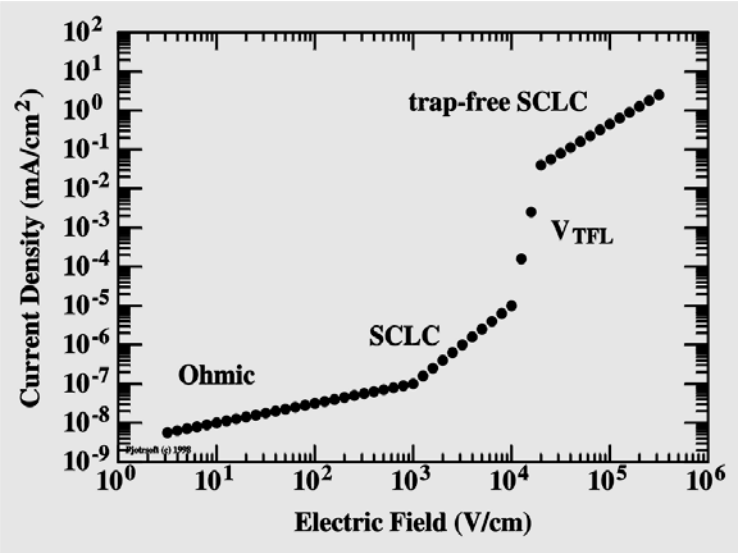

Figure 1.9. Space-charge-limited current as a function of bias [54].

1.4. Interactions of Radiation with Detectors

The operation of the detectors is based on the collection of charges which are produced by the photon interactions through the application of an external electric field. The principally methods of X-ray and gamma-ray interactions are including photoelectric absorption, Compton scattering, and pair production.

In the process of photoelectric absorption, all of the energy of an incident photon is transferred to one of the orbital electrons of the atoms in the detector material to an electron

of the K-shell. The photoelectron then loses its kinetic energy via Coulomb interactions with the semiconductor lattice by forming many electron-hole pairs. The photoelectron has a kinetic energy (E_e-) equal to incident photon energy ($h\nu$) minus the atomic binding energy (E_b) of the ejected electron in the original shell, can be described by:

$$E_{e^-} = h\nu - E_b \qquad \text{Eq. 1-30}$$

The interaction also leaves one of the absorber atom's shell empty leading to the rearrangement of electrons in the atom or the absorption of a free electron.

Photoelectric absorption is predominant at low photon energies and in materials with high atomic number. A rough approximation for the probability, τ, of the photoelectric absorption per atom over all ranges of energy (E_γ) and atomic number (Z) can be expressed by [55]:

$$P(\gamma, e^-) \propto \frac{Z^n}{E_\gamma^{3.5}} \qquad \text{Eq. 1-31}$$

where n varies between 4 and 5 depending on the gamma-ray energy.

Compton scattering is a collision between an incident photon and an orbital electron through an angle regarding its original angle, and the partial transfer energy to the recoil electron. The incident photon energy is divided between the recoil electron and the scattered photon dependent on the scattering angle, θ. The scattered photon energy, $h\nu'$, in terms of its scattering angle is given by:

$$h\nu' = \frac{h\nu}{1 + \left(\frac{h\nu}{m_0 c^2}\right) + (1 - \cos\theta)} \qquad \text{Eq. 1-32}$$

where m_0c^2 is the rest mass of the electron (511 keV). For small scattering angle θ, very little energy is transferred. Some of the original energy is always retained by the incident photon, even in the extreme of $\theta=\pi$.

The kinetic energy of the recoil electron is therefore written as:

$$E_{e^-} = h\nu - h\nu' = h\nu \left(\frac{(\frac{h\nu}{m_0 c^2})(1 - \cos\theta)}{1 + (\frac{h\nu}{m_0 c^2})(1 - \cos\theta)} \right) \qquad \text{Eq. 1-33}$$

In normal circumstances, all scattering angles will occur in the detector. Therefore, a continuum of energies can be transferred to the electron.

Pair production is the process that results in the conversion of the photon energy into an electron-positron pair. This process is energetically possible only when the gamma-ray energy exceeds twice the rest mass energy of an electron (1.02 MeV). Indeed, the probability of this interaction remains very low until the gamma-ray energy approaches several MeV and hence this process is predominantly limited to high-energy gamma rays. The positron has a very short lifetime causing the annihilation with an electron in the material to create two photons of energy 0.511 MeV.

The linear attenuation coefficient is the sum of individual contributions with respect to different photon interactions described above:

$$\beta = \beta_{PE} + \beta_{C} + \beta_{PP} \qquad \text{Eq. 1-34}$$

where β_{PE} is the attenuation coefficient of photoelectric absorption, β_{C} is the attenuation coefficient of Compton scattering, and β_{PP} is the attenuation coefficient of pair production.

Each interaction process can remove the photon from the beam away either by absorption or scattering away from the detector direction and can be characterized by a fixed probability of occurrence per unit path length in the absorber [55]. The probability of different types of X-ray and gamma-ray interactions in the detector is related with the atomic number Z, which is proportional to Z^n ($4<n<5$) for photoelectric absorption, Z for Compton scattering, and Z^2 for pair production.

For the attenuation of the intensity of a beam of photons as they pass through an absorbing medium follows an exponential law, the Beer's law:

$$\frac{I}{I_0} = e^{-\beta x} \qquad \text{Eq. 1-35}$$

where I_0 is the incident photon intensity (s^{-1}), I is the intensity of the primary photons at a depth of x (in cm) in the absorber, and β is the linear attenuation coefficient in cm^{-1}.

The attenuation coefficients of CdTe/CZT material for photoelectric absorption, Compton scattering and pair production are summarized in Figure 1.10. For the photon energy below 0.26 MeV, the photoelectric absorption is the dominant process, whereas the pair production process becomes dominate when the photon energy at above 6.4 MeV. As can be seen that

the Compton scattering is predominating in determining the amount of charges deposited within the detectors at the energy between 0.26 MeV and 6.4 MeV. It is been accepted that one most important interaction is the electron-hole pairs which are generated in the detector and can be detected by an external electronic circuit.

Figure 1.11 presents the attenuation coefficients as a function of low photon energies up to 10 MeV for different radiation detector materials (Si, Ge, GaAs, HgI_2, CdTe). The much higher effective atomic numbers of HgI_2 and CdTe translate into significantly higher X-ray and gamma-ray photoelectric absorption than Si, Ge, and GaAs. CdTe material has the advantages of stability and less toxicity than HgI_2. Furthermore, CdTe detector is more stable in air than HgI_2, which requires encapsulation to inhibit the deterioration of the detector under air exposure for a long period.

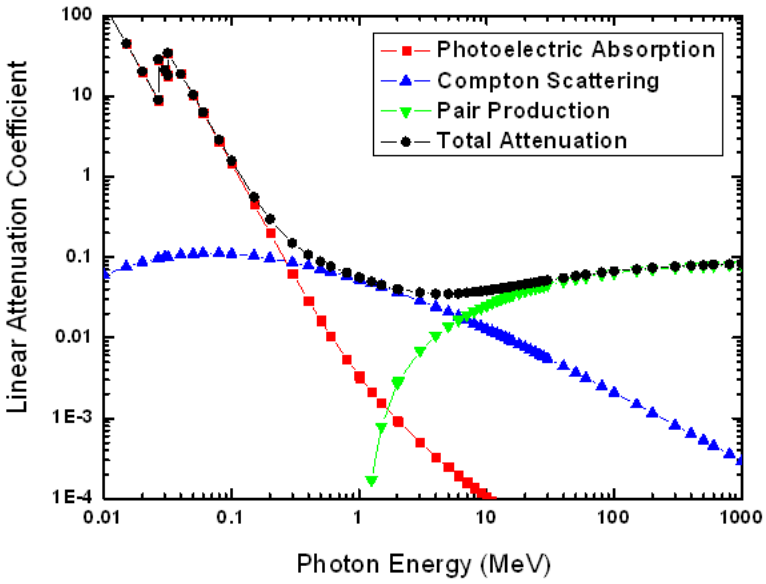

Figure 1.10. The behaviours of the attenuation coefficient of CdTe/CZT for photoelectric absorption, Compton scattering, and pair production.

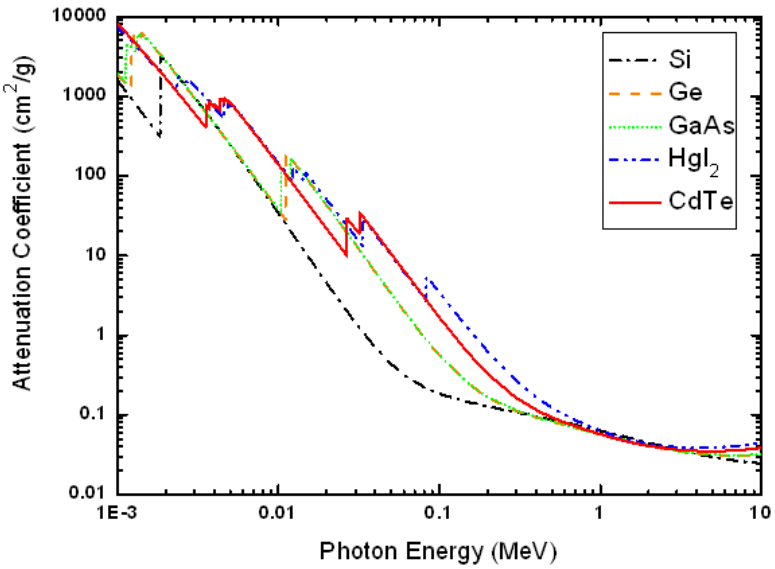

Figure 1.11. Attenuation coefficients as a function of photon energy for different materials.

In fact, CdTe combines comparatively high atomic numbers (48 and 52) with large bandgap energy (1.47 eV) for operating at room temperature. The probability of photoelectric absorption per unit path-length is approximately 4-5 times higher in CdTe than in Ge, and 100 times larger than in Si for typical gamma-ray energies. Si and Ge detectors must always be operated at low temperatures in order to reduce thermally generated leakage current.

In principle, semiconductor material with larger bandgap (higher than 1.5 eV) can reduce the leakage current which can also operate at room temperature. However, wider bandgap semiconductors require greater energies to excite an electron-hole pair [55]. For the X-ray and gamma-ray applications, the cooling treatment can reduce the leakage current and thereby improve the energy resolution. It has been reported that the HgI_2 detectors require cooling until 0 °C to obtain leakage current less than 0.1 pA in typical cases [56]. For CdTe, further cooling to -40 °C can significantly enhance the energy resolution.

1.5. Transport in Semiconductor Materials

Charge transport is generally characterized by two parameters for each carrier type: mobility μ, and mean trapping lifetime, τ. The commonly used technique to study charge transport properties in detectors is based on their response to alpha-particles. The induced signal due to

the alpha particle irradiation is dominated by the drift of the charge carrier single polarity which is resulting from the penetration depth of the alpha particles (~ 20 μm) compared with the thickness of the detector [57].

The mean carriers drift length, λ, is directly associated with the mobility-lifetime products, which can be described by:

$$\lambda = \mu\tau E \quad \text{Eq. 1-36}$$

where E is the electric field applied to the detector.

The charge carriers drift length (λ) should be larger than the thickness of the detectors in order that all photo-generated carriers can be collected at the electrode, thereby to prevent incomplete charge collection. The mobility of charge carriers (μ) in a semiconductor is depending of the crystalline quality of the material, can be characterized by time of flight (TOF) [58]. The lifetime of charge carriers (τ) is related with the presence of recombination centres in the bandgap of the semiconductors, can be measured by transient charge techniques.

Consequently, for the alpha particle spectra, the mobility-lifetime product ($\mu\tau$) is a primary indicator of the charge transport properties and the performance of the detectors [59]. The charge carriers will be accelerated if the applied electric field increases, hence improve the charge collection efficiency (CCE). However, the homogeneity of electric field in the thickness of the detector is influenced by the appearance of crystalline defects.

When an electric field is applied, the electrons will undergo migration ascribable to both random thermal velocity and a drift velocity parallel to the direction of the field. At low values of electric field, the drift velocity is proportional to the field. Then the mobility of electrons and holes can then be expressed by:

$$\nu_h = \mu_h E \quad \text{Eq. 1-37}$$

$$\nu_e = \mu_e E \quad \text{Eq. 1-38}$$

where ν_e and ν_h are the drift velocity of electrons and holes, respectively, μ_e and μ_h are the mobility of electrons and holes, respectively, E is the electric field magnitude.

At higher electric field, a saturation velocity will reach a certain value which stabilizes even when increasing the electric field strength. The saturated drift velocity is around 10^7 cm/s for

the thickness at 0.1 cm hence takes approximately 10 ns to collect the carriers, which makes the detectors one of the fastest responding radiation detectors.

For CdTe and CZT detectors, hole trapping is a especially strong effect resulting from the limited hole mobility. The charge collection efficiency (CCE) is ratio of the charge induced at the sensitive electrode (Q) and the charge produced due to the radiation interaction (Q_0). For a detector of thickness *L mm* in planar configuration, an approximated expression for CCE can be described by the Hecht equation [59]:

$$CCE = \frac{Q(x)}{Q_0} = \frac{\lambda_e}{L}[1-\exp(\frac{L-x}{\lambda_e})] + \frac{\lambda_h}{L}[1-\exp(\frac{x}{\lambda_h})] \quad \text{Eq. 1-39}$$

where x is the interaction depth, L is the thickness of the detector, λ_e and λ_h are the mean drift lengths for electrons and holes, respectively.

Whenever extra charge is generated in the detector, thermal equilibrium is disturbed, thus the detector returns to equilibrium by means of recombination which may lead to trapping sites [60]. Generally, traps are formed by deep impurities in a lattice which relates to impurities that form energy levels near the middle of the bandgap. Trapping and recombination can lead to shorter lifetimes for charge carriers.

For working efficiently, a detector requires collecting a large fraction (ideally 100%) of charge carriers, then has much shorter collection time than the charge carrier lifetime is a desirable characteristic. For CZT, typical lifetimes might be 10^{-6} s for electrons and 0.5×10^{-7} s for holes. For CdTe, the hole lifetime is typically 2×10^{-6} s which is an order of magnitude larger than in CZT. Accordingly, the trapping restricts the size and the energy resolution of CdTe/CZT gamma-ray and X-ray detectors.

Without trapping, holes and electrons are completely collected regardless of position at which they are created in the detector, hence the gamma spectrum can be illustrated by a sharp line or peak at full collection. However, when the trapping phenomenon occurs, the entire electrons (holes) cloud does not reach the positive (negative) electrode. Therefore, the photopeak or pulse height will shift downward. A spread in pulse height occurs even through the concentrations of the trapping of electrons and holes are uniform. If the drift length of the electrons and holes are equal, then the maximum pulse height will occur when electron-hole pairs are created in the center between two electrodes, while the minimum pulse height will appear when the interaction occurs at either one of the two electrodes.

For the case of nonuniform trapping, the pulse height distribution will broaden even further. In low resistivity material, good charge collection also occurs for both electrons and holes because the drift lengths of electrons and holes are much greater than depletion width [20]. Several groups have researched the effect of trapping of electrons and holes on the shape of the photopeak [21]. A precise calculation is not possible because of nonuniform material, detrapping and the dependence of the mobility and trapping time on the electric field, especially at high electric fields [22]. The shapes agree reasonably well with actual spectra. Further details will be discussed in section 1.7.

1.6. Operation Principle and Detector Properties

The interaction is a two-step process where the electrons created in the photoelectric or Compton process lose their energy through electron-hole ionization. The most important feature of the photoelectric absorption is that the number of the electron-hole pairs is proportional to the photon energy. Figure 1.12 exhibits the sketch overview of the operation principle of radiation detectors.

When the energy (E_0) of high energy irradiation is absorbed by the material, the electrons from the valence band jump to the conduction band. Therefore, additional electrons are created in the conduction band and holes are left in the valence band, creating the electron-hole pairs. Under an applied electric field, electron-hole pairs drift to the two electric polarities respectively, which would induce currents in two electrodes. All radiation detection is based on the ionizing radiation generating free electrons and ions (or holes) in the medium of where the interaction occurs.

The generated charge is proportional to the energy deposited (E_0), the energy of the electron-hole pair, N_0, can be expressed by:

$$N_0 = \frac{E_0}{E_{pair}} \qquad \text{Eq. 1-40}$$

where E_{pair} is the energy required for producing electron-hole pairs, which is about three or four times larger than the bandgap. With an external electric field, electron-hole pairs drift to the two electric polarities respectively, which would induce currents in two electrodes.

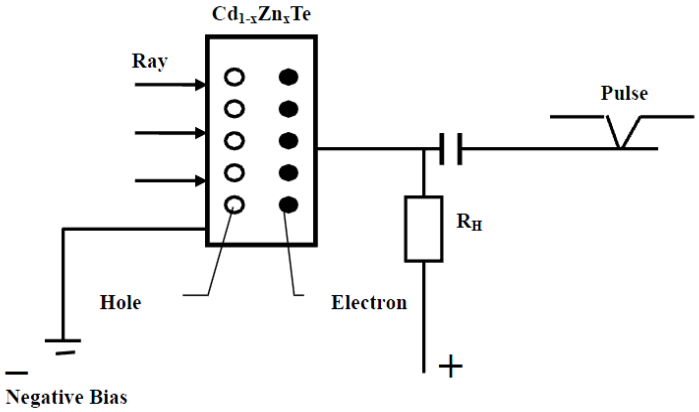

Figure 1.12. Sketch map for the operating principle of radiation detectors.

The time stability of the detectors is one of the most important factors for the practical application of CdTe/CZT detectors. The instability phenomenon is always considered as a polarization phenomenon and characterized by a progressive degradation of energy resolution and a shifting of the photopeak toward low energies with time after applying the voltages. The polarization of the space charge distribution causes the disturbance of electric field in crystal-type detectors.

In fact, when a radiation interaction occurs, the electrons and holes travel towards the contacts on both sides, as shown in Figure 1.13. Some of these charges maybe trapped in the appearance of trapping sites, hence can reduce the internal electric field induced by the charge carriers. If the trapping lifetime is long, the distribution of electric field in CdTe material decreases slowly, resulting in the decrease of the carriers drift velocity and more carriers to be trapped.

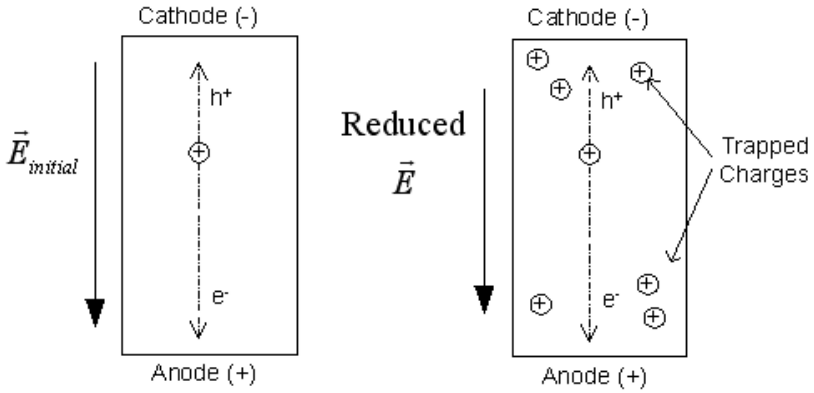

Figure 1.13. Sketch diagram of polarization in CdTe diodes.

If the radiation detectors are produced from the same region of an ingot containing two crystals in polycrystalline ingot, the detectors may contain more defects and a shorter lifetime than monocrystalline ingot. In a polycrystalline detector, the electric field will not be uniform and constant. Furthermore, the conductivity is larger along the ingot with grain boundaries, which can change the electric field. Due to the thermal gradients, the Cd to Zn ratio can vary radially in the crystal, causing the bandgap alters over the volume of the detector, resulting in a distinct peak broadening. Spatial variations in the trap density lead to the fluctuations in the lifetime and tailing.

In the photoelectric absorption process, a characteristic X-ray is often emitted by the absorber atom, which can be reabsorbed near the original interaction site. However, the X-ray photon may escape when the photoelectric absorption occurs near a surface of the detector. In this event, the energy deposited in the detector is decreased by an amount equal to the X-ray photon energy. Without the X-ray escape, the original gamma ray would have been fully absorbed and the resulting pulse would have contributed to the photopeak. With escape, a new category of events is created in which an amount of energy is equal to the original gamma-ray energy minus the characteristic X-ray energy is repeatedly deposited in the detector. Consequently, a new peak will appear in the response function and placed at a distance equal to the energy of the characteristic X-ray below the peak, which is prominent at low incident gamma-ray energies for large surface-to-volume ratio detectors.

1.7. Geometry Simulation of Detectors

The poor transport properties of CdTe and CdZnTe materials are a critical issue in the development of X-ray and γ-ray detectors. Hole trapping can reduce the charge collection efficiency of the detectors and produces an asymmetric long tail in the photopeaks of the measured spectra (hole tailing).

Some techniques concern the particular irradiation configuration of the detectors have been used in order to minimized this effect. These techniques are based on a single charge collection. In this section, three different configurations including planar detectors, pixel detectors, and hemisphericals detectors have been investigated.

1.7.1. Planar Detectors

The simplest configuration is a planar detector, i.e. a slab of a semiconductor material with metal electrodes on the opposite faces of the semiconductor. The photo-interaction is a two-step process where the electrons created in the photoelectric or Compton process lose their energy through electron-hole ionization, producing electron-hole pairs in the semiconductor volume.

The most important feature of the photoelectric absorption is that the number of electron-hole pair N is equal to E/w, where w is the average pair creation energy (5.00 eV for CZT). The generated charge cloud can be expressed by [61]:

$$Q_0 = Ne = eE / \omega \quad \text{Eq. 1-41}$$

Figure 1.14 presents the schematic of simple planar detector geometry. The electrons and holes move toward the opposite electrodes, anode for electrons and cathode for holes, respectively. One can observe that, there are three different interaction sites in the detector: close to the cathode (1), at a depth interaction x inside the detectors (2), and close to anode (3).

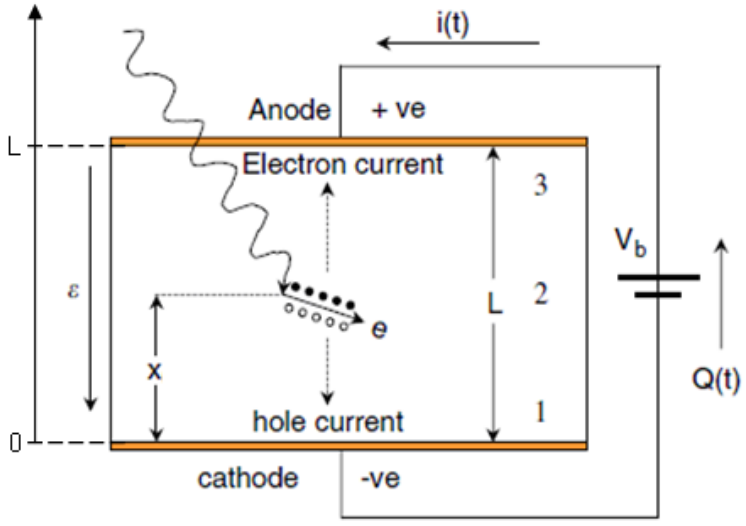

Figure 1.14. The schematic of a simple planar detector showing a photoelectric interaction [61].

When applying an electric field across the detector, the liberated carriers drift towards the anode and cathode with drift velocities v_e and v_h, which can be defined by: $v_e = \mu_e E$ and $v_h = \mu_h E$ with E the applied electric field and μ_e and μ_h are the respective mobilities of the

electrons and holes (more details in section 1.5). For electron, the mobility is generally between 1000-1100 $cm^2/V{\cdot}s$ for CdTe and 1000-1300 $cm^2/V{\cdot}s$ for CZT. For hole, the mobility is about 100 $cm^2/V{\cdot}s$ for CdTe and 50-80 $cm^2/V{\cdot}s$ for CZT.

The movement of the electrons and holes creates a variation of induced charge ΔQ on the electrodes. The theorem of Shockley-Ramo allows calculating this induced charge concerning the concept of weighting potential incorporated [62]. The weighting potential (φ) is defined as the potential that occurs in the detector with the collecting electrode held at unit potential when containing all the other electrodes at zero potential.

For a planar detector, the weighting potential φ at the anode is a linear function of the distance x from the cathode, which can be written as:

$$\varphi(x) = \frac{x}{L} \qquad 0 \le \frac{x}{L} \le 1 \qquad \text{Eq. 1-42}$$

where x is the position of the interaction, and L is the thickness of the detector.

For the planar geometry detector irradiated with a radiation source at the absorbed energy $d\varepsilon$ can be given by the motion of a positive charge through the potential difference ($d\varphi$):

$$d\varepsilon = -Q_0 d\varphi \qquad \text{Eq. 1-43}$$

Regarding the electric field $E(x)=-d\varphi/dx$, Eq. 1-43 can be modified as:

$$\frac{d\varepsilon}{dx} = -Q_0 E(x) = Q_0 \frac{V_0}{L} \qquad \text{Eq. 1-44}$$

where V_0 is the applied bias, and L is the thickness of the detector.

The Figure 1.15 illustrates the simulation of the weighting potential and electric field inside a planar detector with a thickness of 4 mm and biased at 400 V by using the equations Eq. 1-42 and Eq. 1-44. As one can observe, the weighting increases linearly from cathode (-) at 0 of potential to anode (+) at 1 of potential. Moreover, we can see that the electric field is always constant for all positions in the planar detector.

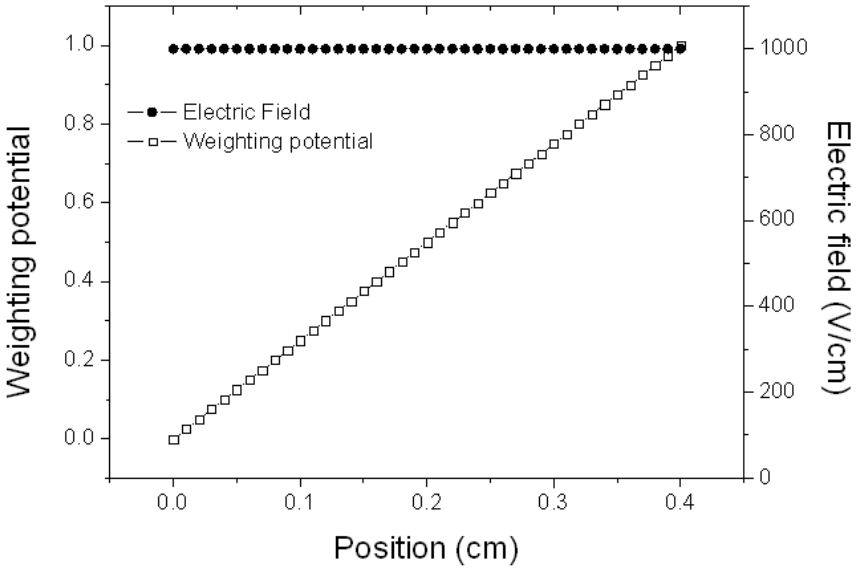

Figure 1.15. Simulation of the weighting potential and electric field as a function of the position (*x*) inside a planar detector.

If now we suppose that an interaction occurs at a position *x* inside the planar detector. After the integration between the point *x* where the charge are generated and the point x_0 where the latter are collected, the drifting charges result in an induced charge on the electrodes which reduce the device voltage of ΔV_R from the applied value *V*. The signal voltage will be described as:

$$\Delta V_R = Q_0 \cdot \frac{V}{L} = \frac{Q_0}{C} \cdot \frac{(x - x_0)}{L} \quad \text{Eq. 1-45}$$

where C is the constant, and L is the detector thickness. Q_0 is the charge total bring by an interaction, hence during the drift of the charges, the total induced charge go from 0 to Q_0. When there is no trapping, Q_0 is constant, however, while there is trapping, Q_0 is no more constant and depend of mu tau of the charges.

Therefore, the induced charge can be expressed as:

$$\Delta Q_0 = C\Delta V_R = Q_0 \cdot \frac{(x - x_0)}{L} \quad \text{Eq. 1-46}$$

In consequence, the signal pulse can be described by using a time constant dependent of the drift velocity of the induced charge. By neglecting the charge loss during the transit time of the carriers, the total charge induced on the anode electrode by N electrons-hole pairs can be

separated in two contributions, the hole and the electron part and can be summarized by the following formula:

$$Q(t) = Q_h + Q_e \quad \text{Eq. 1-47}$$

$$Q_e = Q_0 \frac{v_e}{L} t \quad t < t_e \qquad Q_e = Q_0 \frac{v_e}{L} t_e \quad t > t_e \quad \text{Eq. 1-48}$$

$$Q_h = Q_0 \frac{\upsilon_h}{L} t \quad t < t_h \qquad Q_h = Q_0 \frac{\upsilon_h}{L} t_h \quad t > t_h \quad \text{Eq. 1-49}$$

where t_e is the transit time of electrons, and t_h is the transit time of holes, which can be written as:

$$t_e = \frac{x}{\mu_e E} \quad \text{Eq. 1-50}$$

$$t_h = \frac{L - x}{\mu_h E} \quad \text{Eq. 1-51}$$

Depending of the localization of the interactions sites, three different cases can occur (as presented in Figure 1.14):

1) If the interaction sites are closed to the cathode, the total induced charge is only due to the contribution of the electrons. The previous equations can be modified:

$$Q(t) = Q_0(\frac{v_e}{L} t) \text{ if } t < t_e \qquad Q(t) = Q_0(\frac{v_e}{L} t_e) = Q_0 \text{ if } t > t_e \quad \text{Eq. 1-52}$$

$$\text{with } t_e = \frac{L}{\mu_e E} \quad \text{Eq. 1-53}$$

Figure 1.16 displays the simulation of the induced charge of the electrons versus time for different electric field ranging from 1000 V/cm to 4000 V/cm, with a mobility of electrons of 1000 $cm^2/V{\cdot}s$ and a detector thickness of 4 mm (the voltage is varied between 400 V and 1600 V).

We can observe that as the electric field increases, the drift velocity of the electrons increases, and hence the collection time of electrons is reduced. The slope of the induced charge ratio $Q(t)/Q_0$ at the electric field of 4000 V/cm is the steepest, while the most gentle slope can be seen at around 45° for the induced charge ratio $Q(t)/Q_0$ at the electric field of 1000 V/cm. In conclusion, a higher applied voltage can help to obtain a faster collection of electrons.

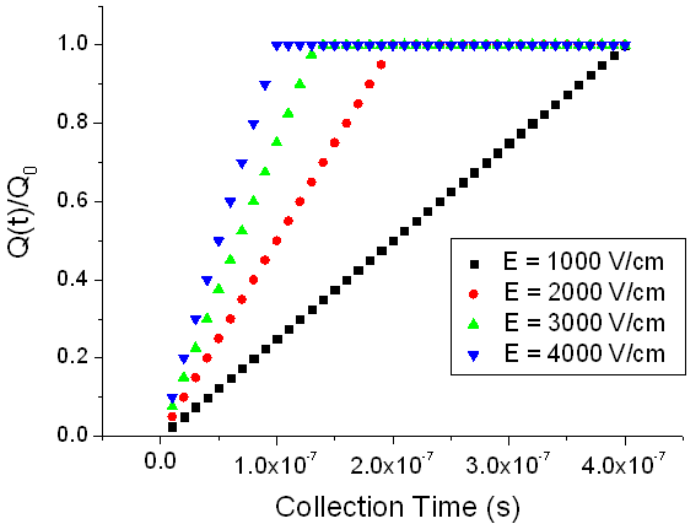

Figure 1.16. Time dependence of the induced signal for three different interaction sites in the detector in the absence of trapping (positions 1, 2 and 3) if the interaction sites are closed to the cathode.

2) If the interaction sites are closed to the anode, the total induced charge is only due to the contribution of the holes. In this condition, the previous equations can be modified as:

$$Q(t) = Q_0(\frac{v_h}{L}t) \quad t < t_h \qquad Q(t) = Q_0(\frac{v_h}{L}t_h) = Q_0 \quad t > t_h \qquad \text{Eq. 1-54}$$

$$\text{with } t_h = \frac{L}{\mu_h E} \qquad \text{Eq. 1-55}$$

Figure 1.17 presents the simulation of the induced charge of the holes as a function of collection time at different electric field from 1000 V/cm to 4000 V/cm. It is important to mention that the mobility of the holes is 100 $cm^2/V{\cdot}s$, which is 10 times lower than the electrons. In addition, the detector thickness was chosen as 4 mm that is the same with the simulation in Figure 1.16. Therefore, the time of collection is varied in the same range with the electrons for comparison.

As can be seen, when the electric field increases, the induced charge ratio ($Q(t)/Q_0$) of the holes increases, but stay 10 times lower than the only contribution of the electrons for the same collection time (see Figure 1.16). This behaviour shows that holes go slower than electrons for the detectors based of CdTe and CdZnTe.

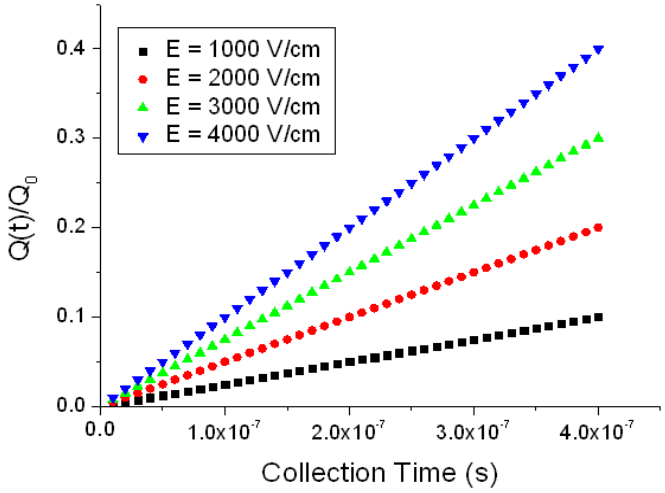

Figure 1.17. Time dependence of the induced signal for three different interaction sites in the detector in the absence of trapping (positions 1, 2 and 3) if the interaction sites are closed to the anode.

3) If the interaction sites are situated between the cathode and anode, the total induced charge is shared between the contribution of the electrons and holes. The simulations can use the equations (Eq. 1-52 and Eq. 1-54) for the two conditions previously described.

We can observe that when the interaction occurs between the cathode and anode, the total induced charge can be clearly divided into two components. The fast increases of the charge of the electrons in addition of the holes contribution, followed by a slow increase of charge contribute by only the holes. These behaviours display in the same way that the poor transport properties of the holes which will have a strong influence in the radiation responses.

Furthermore, as the interaction occurred deeper from the cathode side and therefore closer to the anode side, we observe the rise of collection time decreases, which is significantly related to the lower transport properties of holes in comparison of electrons.

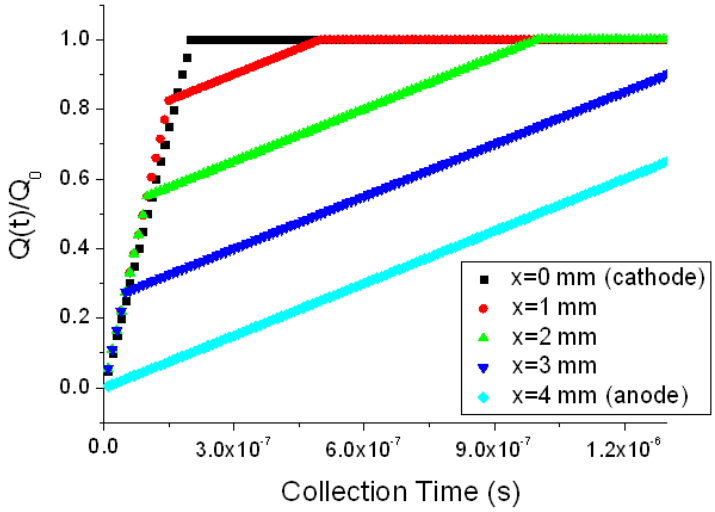

Figure 1.18. Time dependence of the induced signal for three different interaction sites in the detector in the absence of trapping (positions 1, 2 and 3) if the interaction sites are at a depth interaction *x* inside the detectors.

If we suppose that the interaction occurred in the middle of the detector, that is to say *x*=2 mm. Then we can simulate the total induced charge at different electrical field between 1000 V/cm and 4000 V/cm, as displayed in Figure 1.19. One can observe that, the curves can be divided into two parts: (1) a fast increase of induced charge resulting from the electrons, (2) follow by a slow increase of total charge coming from the holes.

When the electric field (applied bias) increases, the total charge collection is faster due to the higher carrier velocity of the charge. Moreover, it is possible to observe that the velocity of the holes increases drastically with voltage in comparison of the electrons.

The component due to electrons is faster when the electrical field increases from 1000 V/cm to 2000 V/cm. At 3000 or 4000 V/cm, the collection time of the electrons is nearly the same than 2000 V/cm. It is not the same case for holes, one can observe a faster collection when the electric field go from 1000 to 2000 V/cm. Moreover, by increasing the electric field at 3000 or 4000 V/cm, the time of collection can be reduced.

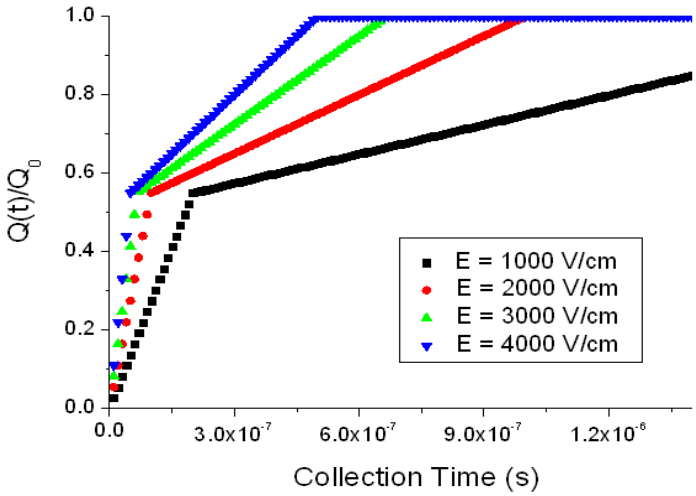

Figure 1.19. Time dependence of the induced signal for three different interaction sites in the detector in the absence of trapping (positions 1, 2 and 3) if the interaction sites are at a depth x=2 mm inside the detectors.

In fact, an accurate determination of the energy absorbed in the volume of a semiconductor detector, requires that all the electron and hole charge carriers are collected. In practice, the semiconductor materials contained imperfections that may be introduced during the crystal growth stage, the device fabrication stage, or during irradiation.

These structural defects in the crystal, impurity atoms, vacancies, or structural irregularities (e.g. dislocations) introduce states into the crystal that can trap charge carriers. These trapping phenomena usually occur for both carriers. The charge trapping is characterized by a carrier lifetime τ, which is the average time a charge carrier can "survive" in a crystal before the trapping occurs.

It is possible that the trapped carriers may be released from the trap, drift in the field and be trapped again, if we suppose that only trapping process exists inside the detectors. A model, which describes the behaviour of the charge trapping phenomena can be given by an exponential decay of the initial charge (Q_0) with a time constant divided by the lifetime τ, can be expressed by [66]:

$$Q(t) = Q_0 \exp(-\frac{t}{\tau}) \quad \text{Eq. 1-56}$$

where t is the elapsed time, the charge traversed a distance of x with a carrier speed $v = \mu E$, then the elapsed time can be described as:

$$t = \frac{x}{v} = \frac{x}{\mu E} \qquad \text{Eq. 1-57}$$

Assuming a uniform material being used, the remaining charge after traverse a distance *x* can be written as:

$$Q(x) = Q_0 \exp(-\frac{x}{\mu \tau E}) \qquad \text{Eq. 1-58}$$

This simple model describes well the charge trapping phenomena. If includes the charge trapping within the detector provided by Eq. 1-58, and one can assume that no de-trapping effects occur, then the change in induced charge, ΔQ_{ind}, on an electrode can be given as [66]:

$$\Delta Q_{ind,e} = Q_e \cdot \frac{1}{L} \exp(-\frac{x}{\mu_e \tau_e E}) dx \qquad \text{Eq. 1-59}$$

$$\Delta Q_{ind,h} = Q_h \cdot \frac{1}{L} \exp(-\frac{x}{\mu_h \tau_h E}) dx \qquad \text{Eq. 1-60}$$

where *x* is the depth of interaction, *L* is the detector thickness, Q_e and Q_h are the initial charges of electrons and holes, respectively.

Integration of ΔQ_{ind} occuring with electrons and holes, and supposing that no de-trapping effects are presented, lead to a total induced charge on the collecting electrodes as a function of interaction position [63]:

$$Q(x) = Q_0 \left[\frac{\mu_e \tau_e E}{L} \cdot \left(1 - e^{(-\frac{L-x}{\mu_e \tau_e E})} \right) + \frac{\mu_h \tau_h E}{L} \cdot \left(1 - e^{(-\frac{x}{\mu_h \tau_h E})} \right) \right] \qquad \text{Eq. 1-61}$$

This equation is well known as Hecht equation, which is well known to describe the signal formation in the conventional planar detectors.

For CdZnTe grown by the high pressure Bridgeman technique, typical lifetimes are $\tau_e = 3 \times 10^{-6}$ s and $\tau_h = < 0.5 \times 10^{-6}$ s [65]. Due to the much shorter lifetime of holes than the transit time, the induced charge is significantly reduced and is depending of the interaction depth (*x*).

In an ionization event, an equal number of electrons and holes are created, with respective initial charges of $-Q_0$ and $+Q_0$. The total charge induced on an electrode due to the collection of these carriers can be obtained by integrating the Ramo equation [62]. The effect of trapping is taken into account by making *Q* a decreasing quantity in the integration.

The charge collection efficiency (CCE) is widely used to indicate the total charge induced at an electrode normalized to the charge created initially in the detector. The CCE is directly calculated by the Hecht equation, shown in Eq. 1-39, more details are presented in section 1.5.

CCE depends not only on the mean drift length λ_h and λ_e, but also the incoming photon interaction position. The random distribution of the interaction points increases the fluctuations on the induced charge and can provoke peak broadening in the energy spectrum. A plot of CCE versus the position of initial charge creation can provide an indication of the non uniformity of charge induction in the detector.

Figure 1.20 shows the calculated CCE as function of position for a planar detector at different mobility-lifetime values of electrons and holes ($\mu_h\tau_h$ and $\mu_e\tau_e$) at an electric field of 1000 V/cm.

If hole collection is absent ($\lambda_e = 0$), which means that the mobility-lifetime value of holes is 0 cm^2/V, then the signal is determined only by the distance of electrons travelled in the detector. Therefore, the CCE value is only depending of the charge induced by the electrons therefore it varied linearly from cathode to anode (red curve). Moreover, the CCE shows an overall increase from the case of $\tau_h = 0$ s (red curve) due to the contributions from the hole collection to the case of $\mu_h\tau_h = 5\times10^{-5}$ (black line).

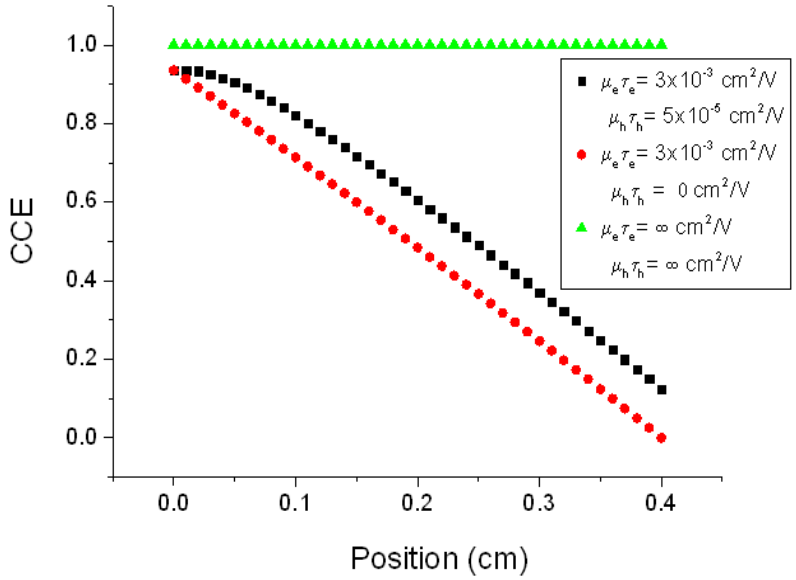

Figure 1.20. Simulation of the charge collection efficiency as a function of position in a planar detector.

As can be seen, the slight downward curvature towards the cathode is due to electron trapping (black line). When collections of the both charges are infinitely fast ($\mu_h \tau_h = \infty$ and $\mu_e \tau_e = \infty$), the CCE is independent of the position and full collection can occur at every position in the detector (green curve). As can be seen, a constant *CCE=1* can be obtained when the carrier collection is ideally happened.

When a beam of energetic photons travels through the materials, the interaction processes can be characterized by a probability of occurrence per unit path length in the absorber [67]. The entire probabilities of the individual processes are the total probability per unit length that the photon is removed from the beam, which is termed as linear attenuation coefficient, β, (in cm^{-1}).

The number of primary photons transmitted through the material with a thickness can be expressed by [67]:

$$I_{trans} = I_0 e^{-\beta x} \qquad \text{Eq. 1-62}$$

where I_0 is the incident photon intensity (s^{-1}), and I_{trans} is the intensity of the transmitted primary photons at a depth of x (in cm) in the absorber. (see Eq. 1-34 in section 1.4)

The number of primary photons interacting in the material, I_{in}, can be described by:

$$I_{in} = I_0[1 - e^{-\beta x}] \qquad \text{Eq. 1-63}$$

The interaction mechanisms are energy dependent, thus the linear attenuation coefficient (μ) is strongly depending on the energy. For example, for CZT with the photon energy of 122 keV, the linear attenuation coefficient is 6.22 cm^{-1} (see section 1.4).

If we suppose that the detector is irradiated with 122 keV incident photons, then the CCE and the number of events versus the position inside the detector with the mobility-lifetime values of $\mu_h \tau_h = 5 \times 10^{-5}$ cm^2/V and $\mu_e \tau_e = 3 \times 10^{-3}$ cm^2/V for the irradiation at the cathode side can be shown in Figure 1.21.

One can observe that the CCE and counts decrease when the interaction travel through the detector from the cathode side to the anode side. The solid line described the CCE versus position is the same presented in Figure 1.20, which shows a slight convex structure for the specified parameters of the simulation. For the number of events versus the position, one can see that the curve exhibits a concave structure, which represents the number of photons

interacting inside the detector at different volumes spaced by a distance of 0.002 cm in our simulation.

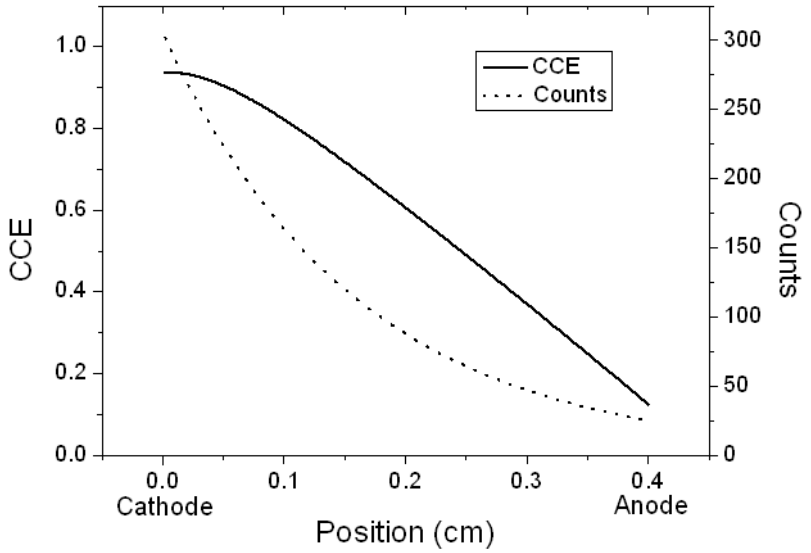

Figure 1.21. CCE and the number of events as a function of position in the detector with the photon energy of 122 keV.

It is necessary to remark that, for the photons interact at a position of *x* (in mm), only a part of photons can be collected which is depending of the CCE at this position (*x*). From these curves, the histogram of pulse heights can be determined by supposing that the detector is irradiated with a deeply penetrating 122 keV gamma-ray radioactive source with a noise free photopeak.

The histogram of pulse height is simulated, to put in evidence the difference of the planar detector irradiated on the cathode side and on the anode side, radiation responses are simulated and presented in Figure 1.22.

For the simulations, the number of collected counts is plotted versus the CCE. The number of collected counts represents the number of photons interacting at the distance *x* multiplied by the CCE at this same distance. Concequencely, a histogram representing the total number of collected versus CCE is use to simulate the response of the detector under irradiation.

The CCE is divided into different bins from 0 to 1 with an interval of 0.01. In fact, the CCE and histograms of pulse height for $\mu_h \tau_h = 5 \times 10^{-5}$ cm^2/V and $\mu_e \tau_e$ varying between 3×10^{-5} cm^2/V and 3×10^{-2} cm^2/V are plotted in this figure.

One can observe that the simulated spectra show a peak at a CCE situated between 0.93 and 0.94, and a number of collected counts close to 3200 for the detector irradiated at the cathode side.

As can be seen, when the detector is irradiated on the anode side, the main contributor to the spectra is coming from the holes, at this moment the peak/valley ratio of the main peak located at the CCE of 0.93 – 0.94 decreases drastically.

Indeed, only 300 counts can be observed for the irradiation of the anode side in comparison of 3200 counts seen with the irradiation at cathode side. This behaviour shows clearly that the planar detector always requires to be irradiated at the cathode side to enhance the number of counts and resolution of the detector.

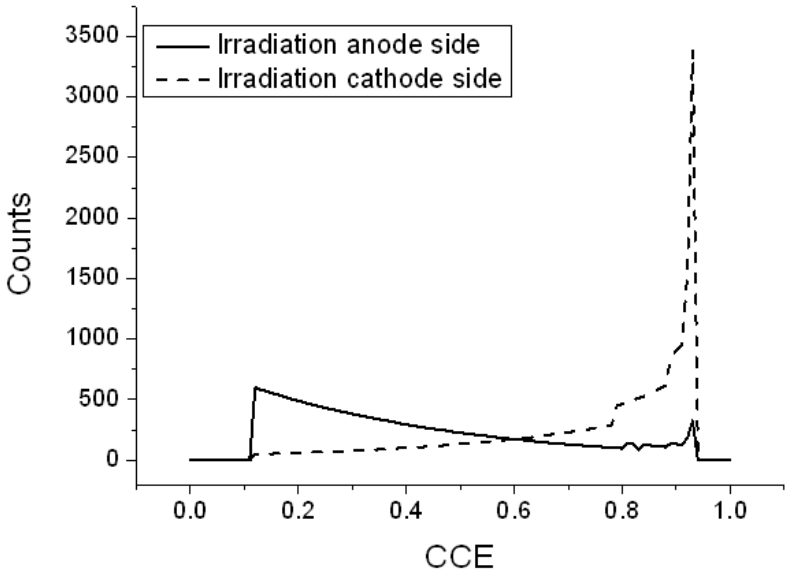

Figure 1.22. Simulated charge collection efficiency of the planar detector irradiated at two sides.

Figure 1.23 displays the simulation of the CCE versus position of the planar detector with different mobility-lifetime of the electrons (Eq. 1-62). When the $\mu_e \tau_e$ decreases and comes closer to the value of the $\mu_h \tau_h$ (5×10^{-5} cm^2/V), one can observe in this figure that the slope of the CCE decreases and tendency to 0°, indicating that the CCE becomes more independent of the position in the detector. Moreover, the CCE and the number of counts are drastically reduced when the mobility-lifetime of the electrons is similar to the holes mobility-lifetime.

In the contrary, one can see that, when $\mu_e \tau_e$ is significantly larger than $\mu_h \tau_h$ (black line), the CCE maximal at the position of 0 cm (cathode side) is dramatically increased. Nevertheless, the CCE becomes more dependent of interaction position, revealing that a stronger CCE at the cathode side is directly associated to the electron contribution.

It is necessary to remark that the parameters both $\mu_e \tau_e$ and $\mu_h \tau_h$ are directly related to the materials properties and crystal growth processes, therefore, these parameters are very complicated to modify.

Figure 1.24 exhibits the results of simulations for the planar detector at different $\mu_e \tau_e$ values (The same than before $\mu_h \tau_h$ (5×10^{-5} cm^2/V). It should be mention that only full energy events were considered, Compton and electron escape effects are not included [68].

When the mobility-lifetime of the electrons is closer to the value of the mobility-lifetime of the holes, one can observe that the spectra shift to the lower CCE value and the number of total collected counts is larger for the case of $\mu_e\tau_e = 3\times10^{-3}$ and $\mu_e\tau_e = 3\times10^{-4}$ cm^2/V than the others. The histograms of pulse height show that when the $\mu\tau$ product of the electrons increases, less trapping effect occurs and hence the CCE shift to a higher value.

In the case of $\mu_e\tau_e = 3\times10^{-3}$ cm^2/V, one can see that the first 250 microns of the detector have the same CCE of 0.93, implying that the most energetic incident radiations are situated in this region, which have the main contributions to the major peak.

In the case of $\mu_e\tau_e = 3\times10^{-4}$ cm^2/V, we can observe that a larger part (500 microns) inside the detector has a constant CCE of 0.59. This large part of constant CCE is the reason of the large peak at around 3300 counts. It is necessary to remark that the judicious choices of values $\mu_e\tau_e$ and $\mu_h\tau_h$ can give a constant CCE in 500 microns.

However, due to the fact that the CCE is more dependent on the position with a higher mobility-lifetime for electrons (as presented in Figure 1.23), the collected carriers are situated closer to the cathode. In the case of $\mu_e\tau_e = 3\times10^{-2}$ cm^2/V (black line), one can observe the collected counts at a higher CCE value when the irradiation is very close to the cathode side.

One can conclude that the gamma response of the planar detector depends strongly on the shape and value of the CCE along the detector, which is primarily related to the values of $\mu_e \tau_e$ and $\mu_h \tau_h$ for the charge carriers.

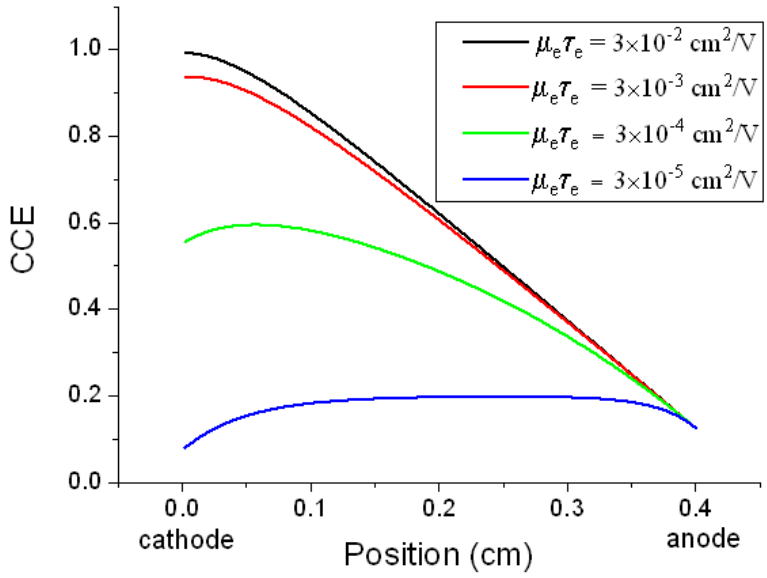

Figure 1.23. Simulation of the CCE versus position with different mobility-lifetime products of electrons for planar detector.

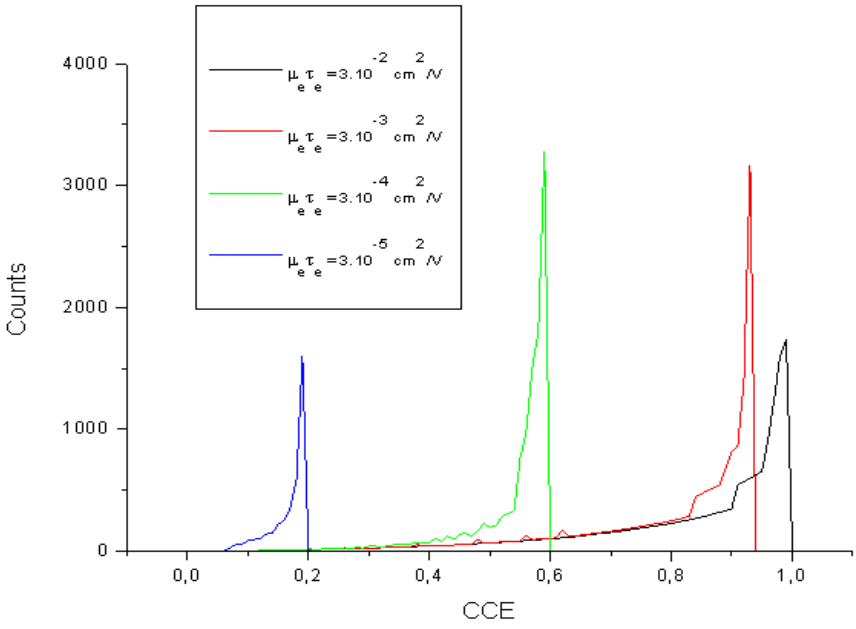

Figure 1.24. Calculated pulse height distributions for the planar detector with different $\mu_e\tau_e$ value.

1.7.2. Pixel Detectors

Due to trapping, the total charge induced depends on the depth at which the gamma ray is absorbed. As a result, the pulse height spectra show a tail or plateau, with a large fraction of the events occurring in this tail instead of the desired photopeak. Since events in the tail convey little useful energy information, some of the advantages of the semiconductor detectors are neglected by hole trapping. In order to remediate to this point, improve the sensitivity and spatial resolution of the detector, it is essential to use pixels with an adapted pixel size.

Indeed, all the electrons produced by an incident photon will be collected by the pixel contacts with 100% efficiency. The idealistic situation is when the semiconductor surface is a good dielectric. However, if the conductivity of the thin metallic layer on the subsurface is different from the bulk, the field distribution inside the material will be modified. Therefore, the signal electrons moving along the field lines may be trapped in the surface layer.

One should note that if the charge gets trapped at the subsurface, the fraction of trapped charges should depend on both the size of contacts and surface preparation process. In consequence, the requirement of contacts for the pixels must be small enough to minimize the spectral "tailing" resulting from the signals induced by uncollected holes, which can minimize the input capacitance to the readout electronics [69].

The small pixel effect can be conceptualized by using Shockley-Ramo theorem [70]. The calculations of the induced current pulses are related with the weighting field approach. The current pulse $I_j(t)$ induced at the electrode (j) is as a function of time (t), which can be described by the formula [71]:

$$I_j(t) = e\overrightarrow{E_{wj}}(\vec{x})\overrightarrow{v_i}(t) \quad \text{Eq. 1-64}$$

where $E_{wj}(x)$ is the weighting field at a position x, and $v_i(t)$ is the velocity of the charge i.

In the one-dimensional case, where the charge is drifting along the pixel axis (x axis), the following expressions can be used to calculate the weighting potential and weighting field as a function of distance x along the symmetry axis of the pixel [71][72]:

$$\Phi_{wj}(x) = -\sum_{k=-\infty}^{\infty} \frac{x + 2kL}{\left[(x + 2kL)^2 + \left(\frac{D}{2} \right)^2 \right]^{\frac{1}{2}}} \quad \text{Eq. 1-65}$$

$$E_{wj}(x) = \left(\frac{D}{2} \right)^2 \sum_{k=-\infty}^{\infty} \frac{1}{\left[(x + 2kL)^2 + \left(\frac{D}{2} \right)^2 \right]^{\frac{3}{2}}} \quad \text{Eq. 1-66}$$

where k is an integer, D is the pixel width, and L is the detector thickness.

In fact, for the pixel detectors geometries of D/L ≈ 0.1, the weighting potential at small depth x is greatly increased compared to that of an infinite electrode device [71]. Therefore, the current pulse induced in a pixellated electrode is dominated by the movement of charge near the electrode, and almost uninfluenced by the charge movement deeper in the bulk of the detector.

To solve the weighting potential, one pixel has a bias of 1 V while all other pixels and the cathode have bias of zero [15]. Figure 1.25 presents the simulation of the weighting potentials as a function of distance x along the symmetry axis for a pixel detector compared with a planar detector (by Eq. 1-42). The pixellated detector with different pixel size on the anode side (where D/L is the ratio between the pixel size and the detector thickness), as well the planar detector have been simulated. It should be noted that the distance between two pixels is assumed to be nil.

One can see that from cathode to anode, the weighting potential increases gradually from the interaction position of 0 cm to 0.4 cm when the D/L is 1/2, while the weighting potential stay at 0 at the interaction depth before 0.4 cm and a sharp increase occur at the anode side for the D/L at 1/40.

We can observe that in contrast with the planar where the weighting potential increases linearly with the distance, in the case of the pixel, the weighting potential is close to 0 near the cathode side, but greatly increases when the depth of interaction is close to the anode. The increase of weighting potential at the anode is particularly stronger when the size of the pixel decreases, that is to say when the D/L ratio is lower.

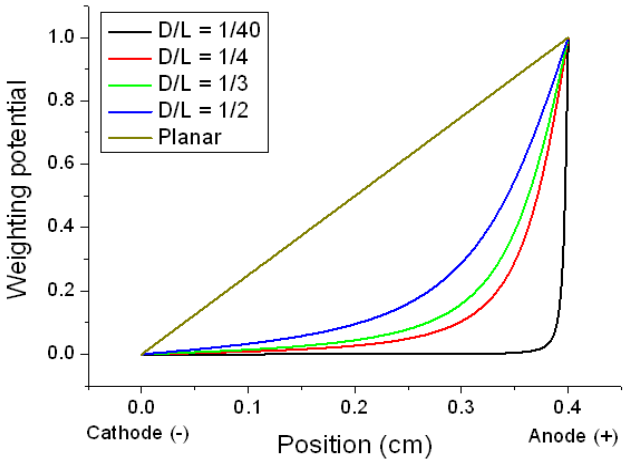

Figure 1.25. Simulation of the weighting potential for pixel detectors and a planar detector as a function of the normalized interaction depth.

Hamel et al. demonstrated that the weighting potential for the small pixel with D/L ratio of 1/10 at the pixel surface fall off quickly, and the positive charge drifting away from the small pixel is seen to induce 70 % if an electronic charge during the first 10 % of its transit [73].

In fact, the weighting field that surrounds a small pixel is only of considerable magnitude close to the pixel. Hence, the charge carriers will only induce a significant signal on a pixel when they are in close proximity to the pixel. In this case, the carriers drift to the pixel will induce charge, whereas the holes in the cathode side will be collected without producing a significant charge on the pixel. However, the limit of small pixel detectors is that the increase in quantity of charge sharing occurs between pixels as the size of pixel decreases according to the thickness of the detectors.

Sordo et al. reported that it is possible to improve the unipolar properties of the pixel detectors by reducing the D/L ratio [61]. Indeed, we can observe the weighting potential and the detector signals are more unipolar as the D/L ratio decreases, which is in agreement with the theory of the small pixel effect.

Single-polarity charge sensing with room temperature semiconductor detectors eliminates the requirements to collect the severely trapped holes. In a pixellated detector, the induced charge essentially depends on the number of electrons collected on the pixel [74].

If trapping is present, the induced charge on the electrode can be described by using the theorem of Ramo [70]. When the theorem states without taking into account the presence of

space charge, the change in the induced charge (ΔQ_{ind}) at an electrode brought about by a charge (Q) moving from the position x_i to x_f can be described by [63]:

$$\Delta Q_{ind} = \int_{x_i}^{x_f} Q \cdot \vec{E}_\omega(x) \cdot \vec{d}x = -Q \cdot [V_\omega(x_f) - V_\omega(x_i)] \quad \text{Eq. 1-67}$$

where $V_\omega(x)$ and $E_\omega(x)$ are the weighting potential and weighting field at the position x, respectively. Q is the total induced charge, which is the sum of the induced charges by the electrons and holes.

By knowing the weighting potential at different pixel size (Eq. 1-65), and using the theorem of Ramo to calculate ΔQ_{ind}, it is possible to obtain the total induced charge on the collecting electrodes and thus the CCE as a function of interaction position. (Eq. 1-67)

Figure 1.26 shows the simulation of the calculated CCE as a function of position for the pixellated detector with different values of ratio D/L. It is necessary to mention that the parameters for simulation have been selected as: $\mu_e\tau_e = 3.10^{-3}$ cm^2/V, $\mu_h\tau_h = 5.10^{-5}$ cm^2/V, and the electric field at 1000 V/cm.

One can observe the drastic modification of the CCE by using pixellization in comparison of planar geometry. When irradiate from the cathode side, more charges will be collected at the cathode, thereby we observe the linear decrease of charge collection from the cathode to the anode. Nevertheless, for the pixellated detectors, the charge collection is significantly associated with the pixels. In consequence, different D/L ratio can determine different CCE behaviours.

Indeed, a small D/L ratio can allow an increase of CCE along the interaction position compared with planar geometry, which will have a degradation effect on the gamma response, as we will see in Figure 1.26. In the extreme case, the pixel with a very low D/L ratio (e.g. 1/40) permits a recovery of the CCE, indicates that the CCE becomes flatter from the cathode to the anode. One can conclude that the pixellated detector requires the irradiation to be carried out at the cathode in order to achieve better charge collection.

By using the CCE described in Figure 1.26 and by supposing that the number of events generated inside the detector is similar to the Figure 1.21, the histogram of pulse heights can be simulated. The detector is irradiated with a deeply penetrating 122 keV gamma-ray source

with a noise free photopeak on the cathode side, the simulate response is exhibited in Figure 1.27.

In general, as we can observe, when the ratio D/L decreases, the CCE maximal shift to higher value and the intensity of the peak increases considerably in comparison of the planar detector from a factor 2 to 4.5 depending of the size of the pixels.

As can be seen, the lowest value of D/L (1/40) does not show the highest intensity. An optimal ratio seems to exist and situate close to 1/4 of D/L, which corresponds to a flatter CCE along the interaction depth, implying that the events come to the same CCE when irradiate on the cathode side, therefore enhance the gamma response coming at this bin.

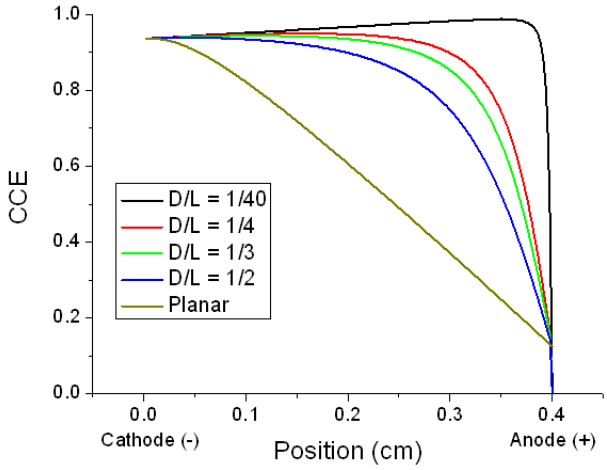

Figure 1.26. Simulation of the CCE for the pixel detectors with different D/L ratio and a planar detector as a function of the normalized interaction depth.

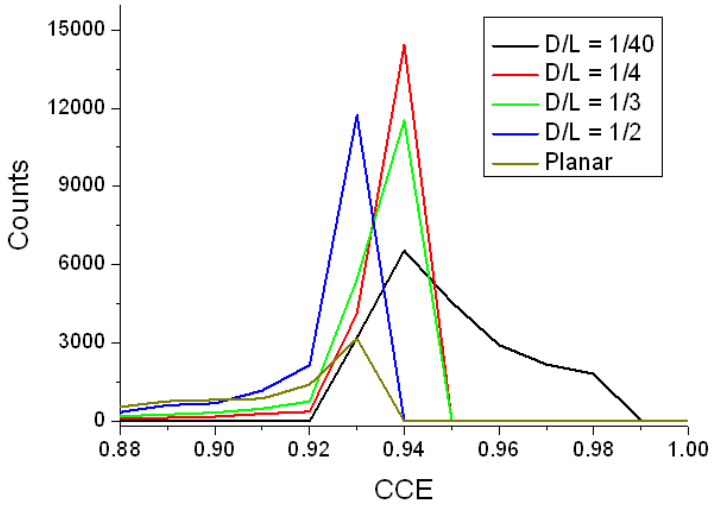

Figure 1.27. Simulation of the pulse height distribution with a deeply penetrating 122 keV gamma-ray source.

Finally, the simulations of the CCE of the pixellated detectors with the irradiation at the cathode side at a deeply penetrating 122 keV gamma-ray source are carried out, the pixels located at the anode side and the cathode side are compared in Figure 1.28. For the simulations, the pixels are considered to give a D/L ratio of 1/4.

One can observe that the intensity of the peak is close to 14400 counts when the pixels are fabricated on the anode. However, only 1400 counts are observed when the pixels are fabricated on the cathode, which is already inferior by a factor of 10 compared to the pixels at the anode side.

This behaviour exhibits that in the case of pixellated detector, the pixels need to be fabricated on the anode and the irradiation needs to be carried out at the cathode. Moreover, in order to give the best resolution and performance of the pixellated detectors, the size of the pixels required to be optimized to a D/L ratio near 1/4.

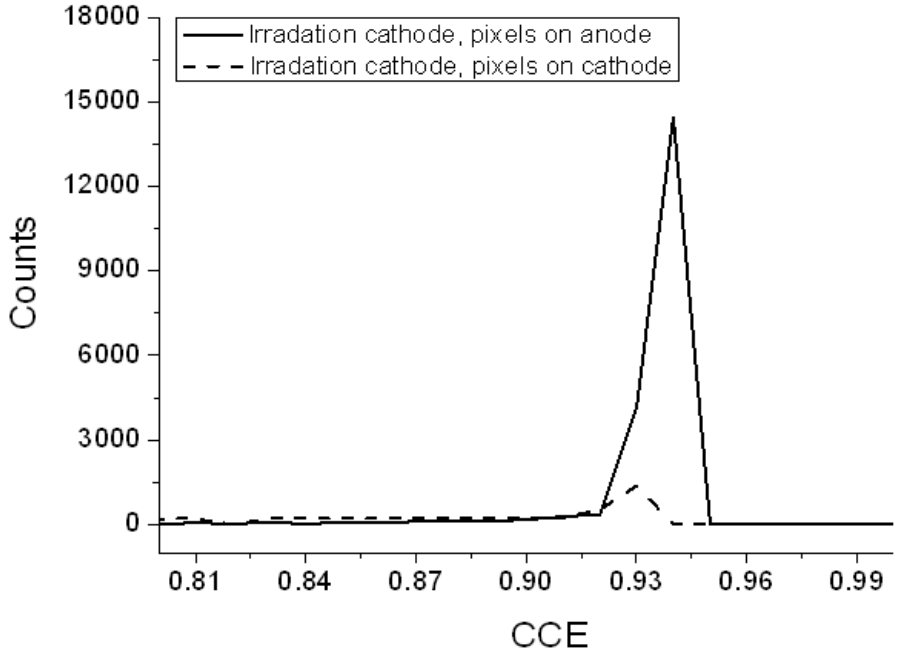

Figure 1.28. Simulation of the CCE with pixels at different electrode side.

1.7.3. Hemispherical Detectors

For more penetrating photons where half thickness of the photon is comparable or higher than the electrode separation, better performance can be achieved by choosing an optimum field shape with different parameters. The basic idea is to increase the electric field in the region of the crystal where the trapping is excessive [76].

For instance, if the hole μτ products are much less than the electron μτ products, more trapping will occur at the anode electrode, where a higher electric field will increase the drift velocity of holes in this region and leading to more uniform charge collection.

Figure 1.29 displays the penetrating photons in CdTe where the electron collection dominated. For the hemispherical geometry, the density of electron-hole pairs is proportional to the radius square, and the weighing field is localized near the anode, and therefore, the charge transport of the bulk is mainly due to the electrons [77].

With a hemispherical configuration, the drift length of an electron is related with its radial position in the detector due to the nonuniform electric field. In such a nonuniform field, most of the induced charge can be produced by the carrier traversal across the high field region [78].

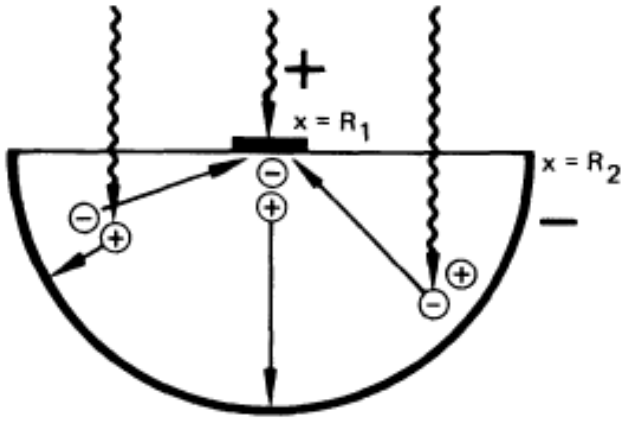

Figure 1.29. Penetrating photons in CdTe where electron products are much higher than the hole products [77].

In the hemispherical detector, the electric field (*E*) can be given by [76]:

$$E = V / \{r^2[(1/r_1) - (1/r_2)]\} \quad \text{Eq. 1-68}$$

where V is the applied voltage, r, r_1, and r_2 are the radial depth of interaction, the radius of the small (pixel) contact, and the radius of the outer contact, respectively. In the case of a quasi hemispherical detector which was investigated in our work, r_2 is the outer contact that is equal to the thickness of the detector [76].

Figure 1.30 displays the simulation of the electric field inside the quasi hemispherical detectors with different radius of the small pixel contact (r_1). Meanwhile, the electric field inside the planar detector with different interaction position is exhibited for comparison.

In fact, for a hemispherical detector simulated, the radius of the outer contact is selected as 0.4 cm (r_2=0.4 cm). Actually, the experimental work was carried out following the simulations with the same r_2 value, which is not presented in this Chapter. It should be mentioned that the simulation was done by using Eq. 1-68 with the applied voltage of 400 V. It can be seen that the electric field is depending of the interaction position (r) and the radius of the pixel contact (r_1) [78].

Actually, for the quasi hemispherical detector, since the electric field varies as the radial depth of interaction (r), a high field exists near the anode side and a low field close to the cathode. Thus the drift length of the electron is changing as a function of its radial distance from the anode. One can observe that the electric field increases drastically near the anode side, leading to an acceleration of the charges and less trapping.

With the same detector thickness (r_2), the electric field decreases as the radius of the pixel contact (r_1) decreases. We can observe that, the electric field of the detector increases close to the cathode and decreases close to the anode when r_1 increases, implying that the detector becomes closer to a case where the electric field is constant when r_1 increases, such as the planar geometry.

However, the electric field stays the same with various interaction positions for the planar detector, which is extremely different from the case of the hemispherical detector. This behaviour demonstrates that the charge collection, which is linked to the electric field, is significantly related with the detector geometry.

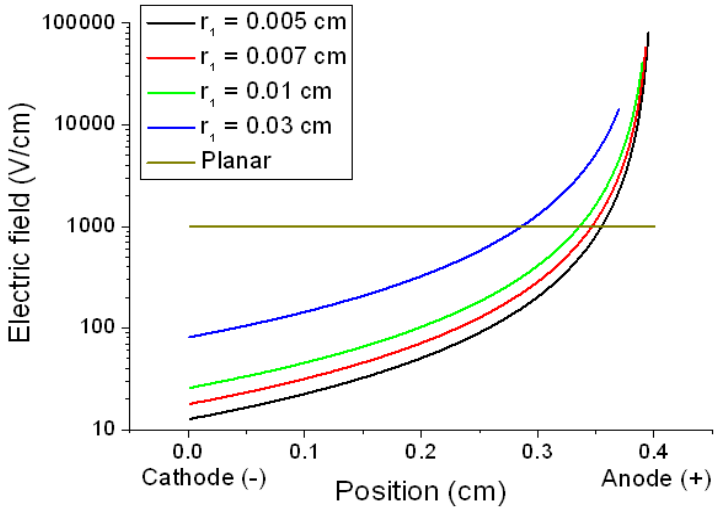

Figure 1.30. Simulation of the electric field as a function of interaction position with different r_1 value for the quasi hemispherical detector.

Carriers generated near the cathode have to traverse a predominantly low field. As the lifetime for the electrons is typically far larger than that of the holes, the electrons have a high probability of traversing this region and arriving in the high field region.

Once in the high field, the carriers will induce a charge *dQ* on the anode, can be written as [79]:

$$dQ_{ind} = (q/V)E(r)dr \qquad \text{Eq. 1-69}$$

where *E(r)* is the electric field at the distance *r*, *V* is the applied voltage, and *dr* is the displacement.

Indeed, the induced charge comes from the localized weighing field close to the anode, the induced charge on the cathode is negligible, which leads to good spectral resolution and high detector efficiency [76].

By using the electric field depending of the radial position and by calculating the induced charge, the CCE of the charges collected can be simulated by assuming that $\mu_h\tau_h = 5.10^{-5}$ cm^2/V and $\mu_e\tau_e = 3.10^{-3}$ cm^2/V (by Eq. 1-68, Eq. 1-69).

Figure 1.31 illustrates the simulation of the CCE versus the depth of interaction (*r*) with different the radius of the small contact r_1 on the anode. The CCE of a planar detector is exhibited in this figure for comparison.

As can be seen, when the radius of the small contact r_1 at the anode is decreased, the CCE close to the anode increases. In opposition, the CCE near the cathode increases as the radius of the anode increases. For the planar detector, we can observe that the CCE almost linearly decreases with the interaction depth from the cathode (0 cm) to the anode (0.4 cm).

One can observe that the CCE is close to a certain value or varied very slightly near the anode for the hemispherical detectors with different sizes of small contacts. For instance, when r_1 is set as 0.007 cm, the CCE is around a value of 0.85-0.90 near the anode side. This behaviour implies that the hemispherical detector requires to be irradiated at the anode side in order to obtain the best charge collection, which is in contrast with the pixellated detector (Pixel=Anode and irradiation on cathode).

By irradiating at the anode side and considering the CCE inside the detector, the histogram of pulse heights can be determined by supposing that the detector is irradiated with a deeply penetrating 122 keV gamma-ray source with a noise free photopeak, as exhibited in Figure 1.32.

It should be noted that the histograms of pulse height simulated in this figure is considering that $\mu_h \tau_h = 5 \times 10^{-5}$ cm^2/V and $\mu_e \tau_e = 3 \times 10^{-2}$ cm^2/V for different radii of the anode. The simulation of the planar detector irradiated at cathode side is plotted in the same figure for comparison.

As we can observe, when the radius of the small contact (r_1) decreases, the photopeak shift to the higher CCE. Moreover, one can see that less tailing due to the holes occur with the smaller r_1, meaning that the bad collection of the events are transferred to higher CCE which is in agreement with the feature of a single charge collection configuration.

Meanwhile, a higher number of counts can be observed for the quasi hemispherical detector with a radius of 0.007 cm in comparison with the planar detector, which corroborates the observations of the CCE presented in Figure 1.31.

Although the simple design hemispheric shaped detectors are difficult to fabricate, the shape can be approximated by a cubic detector, in which the cathode covers five sides and the anode is a small pad located in the center of the sixth side.

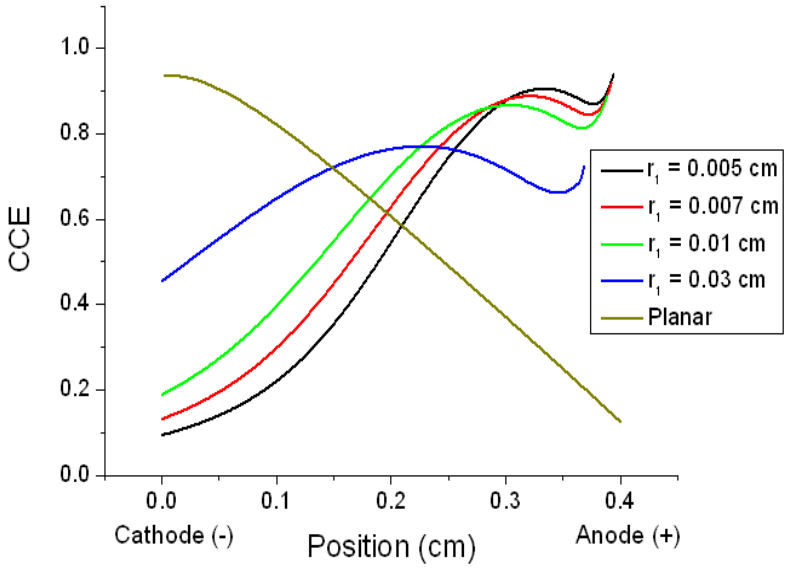

Figure 1.31. Simulation of the CCE as a function of interaction position with different different r_1 value for the quasi hemispherical detector.

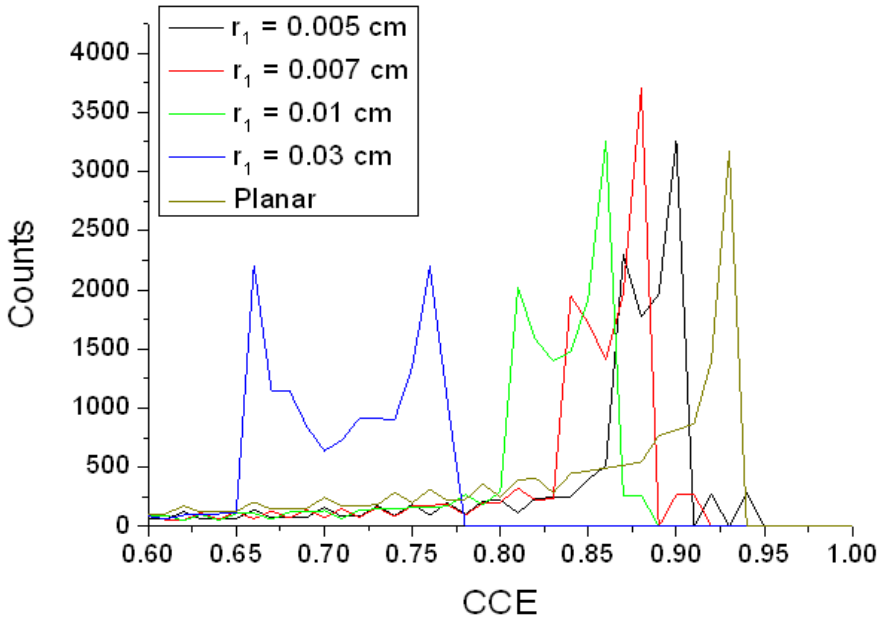

Figure 1.32. Calculated pulse height distributions for the quasi hemispherical detector with different r_1 value. The pulse height distribution for the planar detector is presented for comparison.

1.8. Applications of CdTe/CZT Radiation Detectors

II-VI semiconductor materials such as CdTe and CZT have a combination of desirable properties, such as high average atomic number, large band-gap, and good mobility-lifetime product (μτ), which have made them of great importance for room temperature X-ray and gamma-ray spectrometer, nuclear medicine, safeguards and homeland security, industrial gauging and non-destructive testing, and other applications [80].

1.8.1. X-ray and Gamma-ray Spectrometer

Gamma-ray and X-ray are differentiated by their source: while the γ-rays come from a nuclear transformation, X-rays are extra-nuclear origin. Apart from their origin, nothing can differentiate an X-ray from γ-ray. The X-ray radiation are more energetic than light. They have enough energy to eject an electron during their absorption or their deviation in the matter, which is defined as ionization. The ionization of the constituent atoms of organic matter may have adverse effects on the structure and cell viability. The electromagnetic radiations from more than 10 keV are ionizing radiation and are, as such, regarded as dangerous. The imaging studies using X-rays (radiographs and computed tomography) and γ-rays (scintigraphy) are accompanied by safety precautions and are supervised by regulations to limit the risks to health. Figure 1.33 shows the CdTe and CZT X-ray and gamma ray spectrometers.

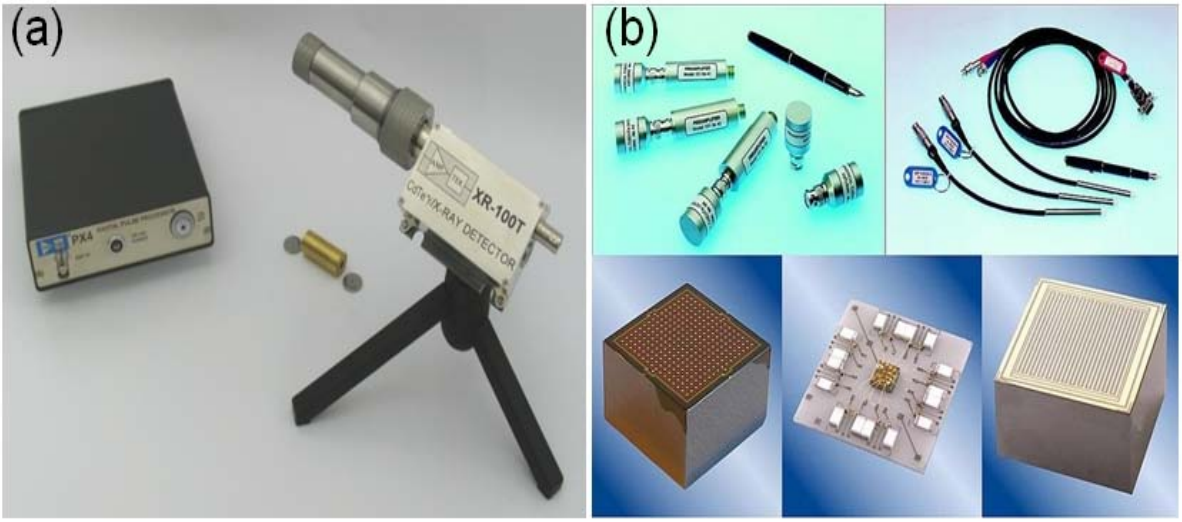

Figure 1.33. (a) XR-100T-CdTe X-ray and Gamma ray spectrometer, (b) CZT detector for gamma spectrometer [81].

1.8.2. Nuclear Medicine

Semiconductor arrays are an attractive alternative to scintillators for use in gamma camera. The importance of semiconductor detectors for nuclear medicine imaging has been reported and numerous different detector configurations and read-out schemes have been proposed [82]. However, the main disadvantages of semiconductor arrays used for nuclear medicine are the high cost of semiconductor detector material and the requirement for large amounts of readout electronics. Silicon and germanium are excellent semiconductor detectors but neither is practical for nuclear medicine due to their low gamma-ray stopping power or the requirement of expensive cryogenics. The other detector materials, such as CdTe, CdZnTe or HgI_2, which have good gamma-ray stopping power are favourable for the nuclear medicine applications.

It has been reported that the CdTe imaging sensor is suitable for the digital radiography. The foremost advantages of using CdTe sensor are the simple structure of CdTe facilitating down-sizing, high sensitivity and high S/N ratios, the reduced scattered radiation fraction by fan-beams, electrical signals converted directly by X-ray photons, and energy information acquired associating with the incident X-ray photons [83]. One important objective of nuclear medicine is to image the organs and other parts of the body with finer spatial resolution and faster velocities.

Computed tomography (CT) has always been considered as a valuable tool in radiotherapy treatment planning due to the increased accuracy offered in tumour localisation and tissue inhomogeneity corrections. Single-photon emission computed tomography (SPECT) is a nuclear medicine tomographic imaging technique using gamma rays [83]. SPECT produces computer-generated images of local radiotracer uptake, while CT produces 3-D anatomic images of X ray density of the human body. Combined SPECT/CT imaging provides sequentially functional information from SPECT and the anatomic information from CT, accurately obtained in a single examination [84].

The single detector system with pixellated CdZnTe array was favourable designed to acquire simultaneous data which is currently evaluated [85]. The photograph of a prototype CdTe X-ray image scanner for dental imaging and a SPECT/CT scanner for full body tomography in Siemens are presented in Figure 1.34.

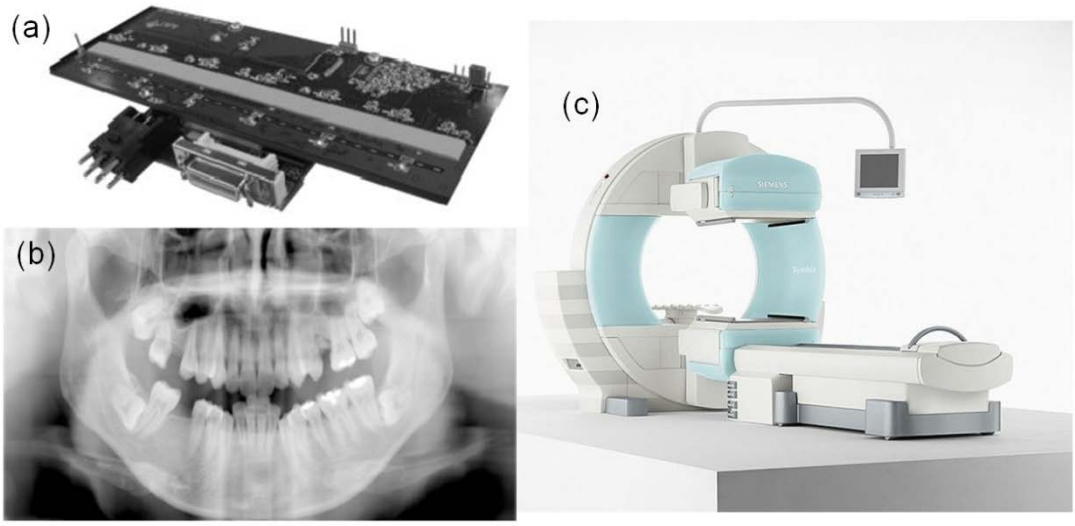

Figure 1.34. (a) A full size COMS-CdTe panoramic camera, (b) A panoramic projection image of a human skull acquired by the Ajat COMS-CdTe panoramic camera, (c) The Siemens Symbia SPECT/CT scanner [85].

1.8.3. Safeguards

Room temperature semiconductor detectors have been used in International Safeguards for more than 10 years [86]. The small size and high intrinsic efficiency is vital for the verification of spent fuel. Shielded and collimated detection systems can be set near the irradiated item (e.g. a CANDU bundle) and picking up its specific signature. Access space is often limited and some items can only be observed with small size detection probes. In addition, small size and light-weight detection probes with high efficiency are required for portable measurement systems.

The using of these detectors is beneficial for enhancing the efficiency and effectiveness of Non-Destructive Assay (NDA) Techniques for safeguards applications. NDA techniques can be applied to a broader range than the nuclear safeguards alone, which historically indicates that the accountancy of declared quantities of nuclear materials by safeguards inspection organizations. The burden on operators and inspectors was reduced by allowing access and verification with the NDA detector rather than the removal from storage for verification [87]. Los Alamos National Laboratory has developed several NDA techniques that are presently used for domestic and international safeguards which includes neutron coincidence counting, segmented gamma-ray scanning, Cf-252 shuffler, and neutron multiplicity counting [88].

The advantage of using CdTe and CZT detectors is to provide a nuclear material gamma spectrum with a higher resolution than that of classical NaI and liquid nitrogen cooled Ge detectors. *Carchon et al.* mentioned that the development of HgI_2 and GaAs has not yet obtained results in agreement with the requirements for safeguards applications, while $LaBr_3$ detectors seem very promising concerning the sensitivity and resolution [89].

In addition, the standard NaI detectors have high efficiency but show low resolutions requiring stabilization. Meanwhile, the Peltier-cooled CdTe detectors have an adequate resolution to perform the measurement of Pu samples using FRAM and can replace HpGe detectors when proven sufficiently reliable. Moreover, the tested CZT technologies is limited by the lacking of availability of large crystals, the reference CZT500 and CZT1500 detectors have performed significantly better than the other tested prototypes (Figure 1.35) [89].

Figure 1.35. Photography of CdZnTe spectrometric detectors CZT/500 and CZT/1500.

1.9. Bibliography

[1] M. Fiederle, T. Feltgen, J. Meinhardt, M. Rogalla, K.W. Benz, State of the art of (Cd,Zn)Te as gamma detector. *Journal of Crystal Growth*, Vol **197**, No. 3, 635-640 (1999).

[2] C. Szeles, S.E. Cameron, J.O. Ndap, W. Chalmers, Advances in the Crystal Growth of Semi-insulating CdZnTe for Radiation Detector Applications, *IEEE Trans. Nucl. Sci.*, Vol **49**, No. 5, 2535-2540 (2002).

[3] T. Asahi, O. Oda, Y. Taniguchi, A. Koyama, Growth and Characterization of 100 mm Diameter CdZnTe Single Crystals by the Vertical Gradient Freezing Method, *Journal of Crystal Growth*, Vol **161**, No. 14, 20-27, (1996).

[4] J. Franc, P. Moravec, Hlidek, E. Belas, P. oschl, R. Grill, A. Sourek, Development of Inclusion Free CdZnTe Substrates from Crystals Grown by the Vertical Gradient Freeze Method, *Journal of Electronic Materials*, Vol **32**, No. 7, 761-765 (2003).

[5] O.S. Babalola, Growth and Characterization of Cr^{2+}: CdSSe crystals, Master Thesis, Fisk University, Nashville, TN (2004).

[6] U.N. Roy, O.S. Babalola, J.Jones, Y. Cui, T. Mounts, A. Zavalin, S. Morgan and A. Burger, Uniform Cd^{2+} Doping of Physical Vapor Transport Grown CdS_xSe_{1-x} Crystals, *J. Elect. Mater.*, Vol **34**, No.1, 19 (2005).

[7] U.N. Roy, O.S. Babalola, Y. Cui, T. Mounts, A. Zavalin, S. Morgan and A. Burger, Vapor Growth and Characterization of Cr-doped $CdS_{0.8}Se_{0.2}$ Single Crystals, *J. Crys. Growth.*, Vol **265**, Issues 3-4, 453-458 (2004).

[8] A. Owens, Semiconductor Materials and Radiation Detection, *J. Synchrotron Rad.*, Vol **13**, 143-150 (2006).

[9] M. Hoheisel, L. Bätz, Requirements on Amorphous Semiconductors for Medical X-Ray Detectors, *Thin Solid Films*, Vol **383**, 132-163 (2001).

[10] K. Zanio, Willardson, Beer, Teatise (Eds.), Cadmium Telluride, *Semiconductors and Semimetals*, Academic Press, San Diego, Vol **13**, 53 (1978).

[11] N. Romčević, M. Romčević, R. Kostić, D. Stojanović, B. Abolmasov, G. Karczewski, R. Galazka, Resonant Raman Spectra of CdTe/ZnTe Self Assembled Quantum Dots, *Acta Physica Polonica A*, Vol **116**, 88 (2009).

[12] T.E. Schlesinger, T.E. Toney, H. Yoon, E.Y. Lee, B.A. Brunett, L. Franks, R.B. James, Cadmium Zinc Telluride and Its Use as A Nuclear Radiation Detector Material, *Materials Science and Engineering*, Vol **32**, 103-189 (2001).

[13] P. Capper, Properties of Narrow Gap Cadmium-based Components, *London: Institution of Electricla Engineers*, (1997).

[14] N. Peyghambarian, S.W. Koch, A. Msyrowicz, Introduction to Semiconductor Optics, Prentice-Hall, Englewood Cliffs, (1993).

[15] M.L. Cohen, J.R. Chelikowsky, Electronic Structure and Optical Properties of Semiconductors, *Springer*, New York, (1988).

[16] B.K. Ridley, Quantum Processes in Semiconductors, *Oxford University Press*, New York, (1982).

[17] D. Kanzer, Hall and Drift of Polar p-type Semiconductors. II. Application to ZnTe, CdTe, and ZnSe, *J. Phys. C: Solid State Phys.*, Vol **6**, 2977 (1973).

[18] J. Singh, Physics of Semiconductors and their Heterostructures, McGraw-Hill, New York, (1993).

[19] P. Cheuvart, U. El-Hanani, D. Schneider, R. Triboulet, CdTe and CdZnTe Crystal Growth by Horizontal Bridgman Technique, *J. Cryst. Growth.*, Vol **101**, 270 (1990).

[20] H.L. Glass, A.J. Socha, C.L. Parfeniuk, D.W. Bakken, Improvements in Production of CdZnTe Crystals Grown by the Bridgman Method, *J. Cryst. Growth.*, Vol **184-185**, 1035-1038 (1998).

[21] F.P. Doty, J.F. Butler, J.F. Schetzina, K.A. Bowers, Properties of CdZnTe Crystal Grown by a High Pressure Bridgman Method, *J. Vac. Sci. Technol. B.*, Vol **10**, 1418-1422 (1992).

[22] W. Palosz, K. Grasza, D. Gilles, G. Jerman, Growth of Cadmium-Zinc Telluride Crystals by Controlled Seeding 'Contactless' Physical Vapor Transport, *J. Cryst. Growth.*, Vol **169**, 20-26 (1996).

[23] L. Ben-Dor, Vertical Unseeded Vapor Growth and Characterization of $Cd_{0.95}Zn_{0.05}Te$ Crystals, *J. Cryst. Growth.*, Vol **71**, 519 (1985).

[24] L. Chibani, M. Hage-Ali, J.P. Stoquert, P. Siffert, Carbon and Silicon in Travelling Heater Method Grown Semi-insulating CdTe, *Mater. Sci. Eng. B.*, Vol **16**, 202-206 (1993).

[25] A. Koyama, A. Hichiwa, R. Hirano, Recent progress in CdZnTe crystals, *Journal of Electronic Materials*, Vol **28**, No. 6, 683-687.

[26] K. Grasza, U. Zuzga-Grasza, A. Jedrzejczak, R. Galazka, J. Maajewski, A. Szadkowski, E. Grodzicka, A Novel Method of Crystal Growth by Physical Vapour Transport and Its Application to CdTe, *J. Cryst. Growth.*, Vol **123**, 519 (1992).

[27] M. Fiederle, V. Babentsov, J. Franc, A. Fauler, J.P. Konrath, Growth of high resistivity CdTe and (Cd,Zn)Te crystals, *Crystal Research and Technology*, Vol **38**, 588-597(2003).

[28] H. Chen, S.a. Awadalla, J. Mackenzie, R. Redden, G. Bendley, A.E. Bolotnikov, G.S. Camarda, G. Carini, R.B. James. Characterization of Traveling Heater Method (THM) Grown $Cd_{0.9}Zn_{0.1}Te$ Crystals, *IEEE Trans. Nucl. Sci.*, Vol **54**, No. 4, 811-816 (2007).

[29] A.E. Bolotnikov, G.S. Camarda, G.A. Carini, Y Cui, K.T. Kohman, L Li, M.B. Salomon, R.B. James, Performance-limiting Defects in CdZnTe Detectors, *IEEE Trans. Nucl. Sci.*, Vol **54**, 821-827 (2007).

[30] G. Li, S. Shih, Y. Huang, T. Wang, W. Jie, Nanostructures of Defects in CdZnTe Single Crystals, *J. Cryst. Growth*, Vol **311**, 85-89 (2008).

[31] M. Kestigan, A.B. Bollong, J.J. Derby, H.L. Glass, K. Harris, H.L. Hettich, P.K. Liao, P. Mitra, P.W. Norton, H.Wadley, Cadimum Zinc Telluride Substrate Growth, Characterization, and Evaluation, *J. Elec. Mater.*, Vol **28**, 726 (1999).

[32] K. Nakagawa, K. Maeda, S. Takeuchi, *Appl. Phys. Lett.*, Vol **34**, 574 (1979).

[33] M. Fiederle, Crystal Growth and Characterization of Detector Grade (Cd,Zn)Te Crystals, *IEEE Trans. Nucl. Sci.*, Vol **54**, 769-772 (2007).

[34] H.R. Vydyanath, J. Ellsworth, J.J. Kennedy, B. Dean, C.J. Johnson, G.T. Neugebauer, J. Sepich, P.K. Liao, Recipe to Minimize Te Precipitation in CdTe and (Cd,Zn)Te Crystals, *J. Vac. Sci. Technol.*, Vol **B10**, 1476-1484, (1992).

[35] F.P. Doty, in: Progress of the Presentation at the 1998 US Workshop on the Physics and Chemistry of II-VI Semiconductors, Charleston, SC, 21-22 (1998).

[36] F. Bissani, S. Tatarenko, K. Saminadayar, N. Magnea, R.T. Cox, A. Tardot, C. Grattepain, *J. Appl. Phys.*, Vol **72**, 2927 (1992).

[37] C. Szeles, Advances in the Crystal Growth and Device Fabrication Technology of CdZnTe Room Temperature Radiation Detectors, *IEEE Trans. Nucl. Sci.*, Vol **51**, 3, 1242-1249 (2004).

[38] R. Krause-Rehberg, H.S. Leipner, T. Abgarjan, A. Polity, Review of Defect Investigation by Mean of Positron Annihilation in II-VI Compound Semiconductors, *Appl. Phys. A*, Vol **66**, 599614 (1998).

[39] J.F. Butler, F.P. Doty, C. Lingren, $Cd_{1-x}Zn_xTe$ Gamma Ray Detectors, *IEEE Trans. Nucl. Sci.*, Vol **39**, 605-609 (1992).

[40] C.E. Barnes, K. Zanio, Photoluminescence in High-Resistivity CdTe:In, *J. Appl. Phys.*, Vol **46**, 3959-3964 (1975).

[41] I. Kuvvetli, Development of CdZnTe Detector Systems for Space Applications, Thesis, Denmark, (2003).

[42] A. Burger, H. Chen, K. Chattopadhyay, D. Shi, S.H. Morgan, W.E. Collins, R.B. James, Characterization of Metal Contacts on and Surfaces of Cadmium Zinc Telluride, *Nucl. Instr. Meth. A.*, Vol **428**, 8-13 (1999).

[43] H. Walter Yao, R.J. Anderson, R.B. James, Optical Characterization of the Internal Electric Field Distribution under Bias of CdZnTe Radiation Detectors, *Proc. SPIE.*, Vol **3115**, 62 (1997).

[44] W. Monch, Semiconductor Surfaces and Interfaces, 2nd Version, Vol **347**, Springer, Berlin (1995).

[45] M. Grundmann, The Physics of Semiconductors: An Introduction Including Devices and Nanophysics, Springer, 1st edition (2006).

[46] U. Lachish, The Role of Contacts in Semiconductor Gamma Radiation Detector, *Nucl. Instr. Meth. A.*, Vol **403**, 417-424 (1998).

[47] U. Lachish, CdTe and CdZnTe Semiconductor Gamma Detectors Equiped with Ohmic Contacts, *Nucl. Instr. Meth. A.*, Vol **436**, 146-149 (1999).

[48] S.M. Sze, Physics of Semiconductor Devices, Wiley-Interscience, 2nd edition (1981).

[49] M. Prokesch, C. Szeles, Accurate Measurement of Electrical Bulk Resistivity and Surface Leakage GaAs Wafer Resistivity Using the Time-dependent Charge Measurent, *Semiconductor Science and Technology*, Vol **6**, 995 (2006).

[50] P. Mark, W. Helfrich, Space-Charge-Limited Currents in Organic Crystals, *J. Appl. Phys.*, Vol **33**, 205-215 (1962).

[51] M.A. Lampert, Simplified Theory of Space-Charge-Limited Currents in an Insulator with Traps, *Physical Review*, Vol **103**, No. 6, 1648 (1956).

[52] R. W. Smith, A. Rose, Space Charge Limited Currents in Single Crystals of Cadmium Sulfide, *Phys. Rev.*, Vol **97**, 1531-1537 (1955).

[53] M. Koehler, I. Biaggio, Influence of Diffusion, Trapping, and State Filling on Charge Injection and Transport in Organic Insulators, *Phys. Rev. B*, Vol **68**, 075205 (2003).

[54] P. Stallinga, Electrical Characterization of Organic Electronic Materials and Devices, 1st Edition (2009).

[55] G.F. Knoll, Radiation Detection and Measurement, 3rd Edition, John Wiley and Sons (2000).

[56] J.S. Iwanczyk, B.E. Patt, Y.J. Yang, A.Kh. Khusainov, Comparison of HgI_2, CdTe and Si (p-i-n) X-ray Detectors, *Nucl. Instr. Meth. A*, Vol **380**, 186 (1996).

[57] M.C. Veale, P.J. Sellin, A. Lohstroh, A.W. Davies, J. Parkin, P. Seller, X-ray Spectroscopy and Charge Transport Properties of CdZnTe Grown by the Vertical Bridgman Method, *Nucl. Instr. Meth. A.*,Vol **576**, 90-94 (2007).

[58] M.C. Veale, P.J. Sellin, J. Parkin, A. Lohstroh, A.W. Davies, P. Seller, Ion Beam Induced Charge Studies of CdZnTe Grown by Modified Vertical Bridgman Method, *IEEE Trans. Nucl. Sci.*, Vol **55**, No. 6, 3741 (2008).

[59] P. Sellin, A.W. Davies, S. Gkoumas, A. Lohstroh, M.E. Özsan, J. Parkin, V. Perumal, G. Prekas, M. Veale, Ion Beam Induced Charge Imaging of Charge Transport in CdTe and CdZnTe, *Nucl. Instr. Meth. B.*, Vol **266**, 1300-1306 (2008).

[60] S.M. Sze, Physcis of Semiconductor Devices, Wiley & Sons (1981).

[61] S.D. Sordo, L. Abbene, E. Caroli, A.M. Mancini, A. Zappettini, P. Ubertini, Progress in the Development of CdTe and CdZnTe Semiconductor Radiation Detectors for Astrophysical and Medical Applications, *Sensors*, Vol **9**, 3491-3526 (2009).

[62] Z. He, Review of the Shockley-Ramo Theorem and its application in Semiconductor Gamma Ray Detectors, *Nucl. Instrum. Meths. A.*, Vol **463**, 250-267 (2001).

[63] A. Owens, A.G. Kozorezov, Single Carrier Sensing Techniques in Compound Semiconductor Detectors, *Nucl. Instrum. Meths. A.*, Vol **563**, 31-36 (2006).

[64] D.S. McGregor, H. Hermon, Room Temperature Compound Semiconductor Radiation Detector, *Nucl. Instrum. Meths. A.*, Vol **395**, 101-124 (1997).

[65] K. Suzuki, A. Iwata, S. Seto, T. Sawada, K. Imai, Drift Mobility Measurements on Undoped Cd0.9Zn0.1Te Grown by High-Pressure Bridgman Technique, *J. Cryst. Growth.*, Vol **204/205**, 909-912 (2000).

[66] I. Kuvvetli, Thesis, Development of CZT Detector Systems for Space Applications, Technical University of Denmark (2003).

[67] http://www.amptek.com/pdf/cztapp1.pdf

[68] H.L. Malm, D. Litchinsky, C. Canali, Single Carrier Charge Collection in Semiconductor Nuclear Detectors, *Rev. Phys. Appl.*, Vol **12**, 303-310 (1977).

[69] H.H. Barrett, J.D. Eskin, H.B. Barber, Charge Transport in Arrays of Semiconductor Gamma-Ray Detectors, *Phys. Rev. Lett.*, Vol **75**, 156 (1995).

[70] S. Ramo, *Proc. IRE*, Vol **27**, 584 (1939).

[71] P.J. Sellin, Modelling of the Small Pixel Effect in Gallium Arsenide X-Ray Imaging Detectors, *Nucl. Instrum. Meths. A.*, Vol **434**, 75-81 (1999).

[72] A. Zumbiehl, Modelling and 3D optimization of CdTe Pixels Detector Array Geometry - Extension to Small Pixels, *Nucl. Instrum. Meths. A.*, Vol **469**, 227-239 (2001).

[73] L. Hamel, S. Paquet, Charge Transport and Signal Generation in CdTe Pixel Detectors, *Nucl. Instrum. Meths. A.*, Vol **380**, 238-240 (1996).

[74] J.D. Eskin, H.H. Barrett, H.B. Barber, Signals Induced in Semiconductor Gamma Ray Imaging Detectors, *J. Appl. Phys.*, Vol **85**, 647 (1999).

[75] M.E. Myronakis, M. Zvelebil, D.G. Darambara, Computational Modelling of Pixilated CZT Detectors for X- and γ- Ray Imaging Applications, *Journal of Instrumentation*, Vol **7**, 3004 (2012).

[76] M. Sowinska, G. Hennard, D. Feder, M. Hage-Ali, J.M. Koebel, A. Zumbiehl, A. Myoub, P. Siffert, Spectral Characteristics of Small and Large Volume CdTe Detectors: Comparison Among Hemispheric, Planar and Pixellated Structure, *IEEE Trans. Nucl. Sci.*, Vol **49**, 3306 (2002).

[77] K. Zanio, Use of Various Device Geometries to Improve the Performance of CdTe Detectors, *Rev. Phys. Appl.*, Vol **12**, 343-347 (1977).
[78] D.S. Bale, C. Szeles, Design of High Performance CZT Quasi-Hemispherical Gamma Ray CAPture Plus Detectors, *Proc. SPIE*, Vol 6319, **63190B** (2006).
[79] H.L. Malm, Gamma-ray Spectroscopy with Single Carrier Collection in High Resistivity Semiconductors, *Appl. Phys. Lett.*, Vol **26**, 344 (1975).
[80] A. Burger, H. Chen, K. Chattopadhyay, J.O. Ndap, S.U. Egatievwe, R.B. James, Cadmium Zinc Telluride High-Resolution Detector Technology, *Proc. SPIE.*, Vol **3446**, 154 (1998).
[81] http://www.amptek.com/xr100cdt.html.
[82] L. Kaufman, D.C. Price (Eds.). Semiconductor Detectors in Medicine, U.S. Atomic Energy Commission, CONF- 730321, NTIS, U.S. Department of Commerce, Washington, DC. (1973).
[83] C. Scheiber, New Developments in Clinical Applications of CdTe and CdZnTe Detectors, *Nucl. Instr. Meth. A.*, Vol **380**, 385-391 (1996).
[84] C. Scheiber, CdTe and CdZnTe Detectors in Nuclear Medicine, *Nucl. Instr. Meth. A.*, Vol **448**, 513-524 (2000).
[85] T. Schulman, Si, CdTe and CdZnTe Radiation Detectors for Imaging Applications, Thesis, University of Helsinki, Finland, IBSN 952-92-0428-0 (2006).
[86] R. Arlt, K.H. Czock, D.E. Rundquist, Overview of the Use of CdTe Detectors for the Verification of Nuclear Material in Nuclear Safeguards, *Nucl. Instr. Meth. A.*, Vol **322**, 575-582 (1992).
[87] J. Arenas Carrasco, V. Bytchkov, A. Dubreuil, S. Yim, R. Arlt, K. Esmailpour, Use of Improved Spent Fuel Attribute Tester (SFAT) for Verification of Spent Fuel, Session 5A of IAEA Symposium on International Safeguards, Vienna, Austria, 13-17 October, (1997).
[88] T.H. Prettyman, T. D. Reilly, M. C. Miller, C. L. HoIlas, M. M. Pickrell, J. M. Prommel, and J. S. Dreicer, Advances in Nuclear Instrumentation for Safeguards, Conference: European Safeguards R&D Association/Institute of Nuclear Materials Management (ESARDA/INMM) workshop on science and modern technology in safeguards, Arona (Italy), 28-31 Oct (1996).
[89] R. Carchon, M. Moeslinger, L. Bourva, C. Bass, M. Zendel, Gamma Radiation Detectors for Safeguards Applications, *Nucl. Instr. Meth. A.*, Vol **579**, 380-383 (2007).

CHAPTER 2.

CHARACTERIZATION

TECHNIQUES

Different techniques have been used to characterize the materials and detectors. These technques can be classified in three groups, compositional and structural, optical, and electrical characterizations. Generally, the bulk of the materials are characterized by structural and optical techniques. The interface between the contact the detector is characterized by compositional and optical techniques and the detector properties by electrical techniques.

2.1. Compositional and Structural Characterization Techniques

2.1.1. Total reflection X-ray Fluorescence

Total reflection X-ray Fluorescence (TXRF) is a technique which has been previously used to evaluate compositions of new materials [1][2]. It is an instrumental analytical technique used for the simultaneous determination of elements down to concentrations of one part per billion (ppb). It is also a microanalytical technique for analysis of small sample amounts placed on a flat carrier, for contaminants on flat sample surfaces, and stratified near-surface layers.

TXRF is essentially an energy dispersive XRF technique in a special geometry. An incident beam impinges upon a specimen at angles below the critical angle of external total reflection for X-rays leading to the reflection of almost 100 % of the excitation beam photons. Due to its unique configuration, the main advantage of TXRF over conventional XRF is reduced measurement background contributions by elimination of sample scattering resulting in increased elemental measurement sensitivity.

Figure 2.1 presents a schematic view of TXRF system. In the procedure of the TXRF measurement, the sample was placed in the form of a thin layer on a sample carrier with a smooth surface, where it is excited to x-ray fluorescence. It is achieved by letting a primary beam hit the sample carrier at an angle of a few minutes of arc, from which it is totally reflected, thus causing effective excitation of the sample. The X radiation emitted by the specimen can be detected by energy dispersive spectrometers.

The advantages of this technique are extremely rapid qualitative information of the sample composition (~ 1 min), limiting of detection as low as the picogram range, absence of matrix effects, simultaneous determination of approximately 30 elements, simple quantification by

the addition of a single standard reference element, and requirement of a minimal amount of sample in the μg or μl range.

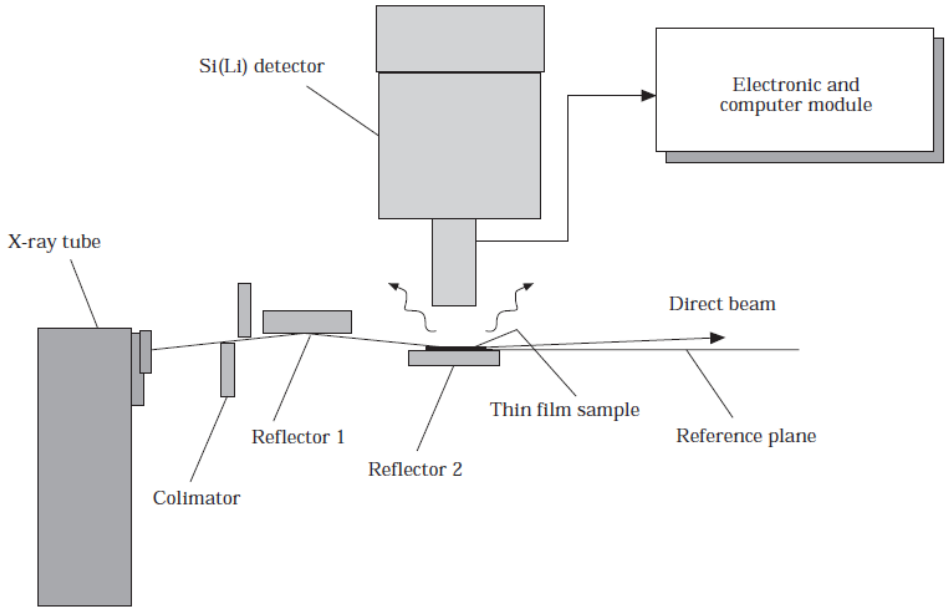

Figure 2.1. Schematic diagram of the TXRF technique.

The analysis in this work were performed by means of an Atomika TXRF 8030C spectrometer, equipped with a 3 kW X-ray tube with a Mo/W alloy anode with a double-W/C multilayer monochromator, adjusted to obtain an optimum excitation energy of 35 keV, and a Si (Li) detector with an active area of 80 mm^2 with a resolution of 150 eV at 5.9 keV. The measurements were performed working at 50 kV and the intensity was adjusted automatically so that a count rate of about 8500 cps was achieved. A fixed acquisition time of 500 seconds was used. Figure 2.2 shows the TXRF equipment used in SIDI at UAM.

Figure 2.2. TXRF equipment at Universidad Autónoma de Madrid.

The detection limits (DL) associated with the evaluated elements, were calculated according to Prange [3]:

$$DL = \frac{3M}{A}\sqrt{\frac{B}{\tau}} \quad \text{Eq. 2-1}$$

where M is the evaluated element mass, A and B are the areas of the peak and background associated with each element, respectively, and τ is the acquisition time in seconds.

2.1.2. Induced Coupled Plasma – Mass Spectroscopy

Induced Couple Plasma couple with Mass Spectroscopy (ICP-MS) has been carried out to determine the chemical compositional and analyze the impurities of CZT material. The ICP-MS implement employs plasma as the ionization source and a mass spectrometer (MS) analyzer to detect the ions generated. It can simultaneously characterize most of the elements in the periodic table and determine the element chemical concentration down to part-per trillion (ppt) levels.

The principle of this technique is that ionized or excited atoms created by the application of plasma to the specimen are separated and can be identified according to their mass and charge ratio (m/z). The whole system is comprised of inductive coupled plasma, interface, mass spectrometry, data processing, and display section. The specimen in the form of aerosol carried out by argon is passed through the central tube.

Auxiliary argon is passed at a rate around 1 $Lmin^{-1}$ through the middle tube and plasma gas is passed at a rate 10^{-15} $Lmin^{-1}$ through the second or middle tube which maintains the plasma. Seeded free electrons are accelerated by the radio-frequency (RF) field and absorb sufficient energy form the coil to maintain constant higher plasma temperature (6000-10000K). When the atoms pass through the plasma torch, they eventually obtain enough energy to lose an electron and become single ionized, and thus display positive charge [4][5].

A special interface is necessary to be introduced for single charged ions entering the quadropole, and transfer from the extremely hot plasma into the mass spectrometer, which requires a high vacuum (10^{-6} Torr) to avoid collisions between ions and background gas molecules which divert the ions from their trajectory in a magnetic field. The quadropole filters the ions regarding to their mass so only atoms with desired mass can trench the detector. By modifying the settings of the quardropole, different mass-to-charge ratios can be

tested and allow for the spectroscopic analysis. Figure 2.3 displays the schematic of the ICP-MS system used in our work in SIDI at UAM.

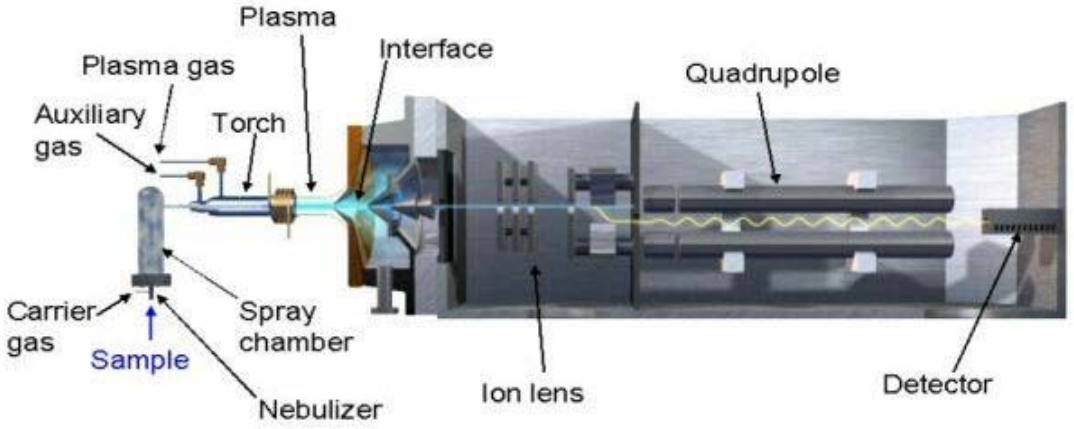

Figure 2.3. Schematic illustration of an ICP-MS instrument.

The equipment is maintained inside of a class 100 K cleanroom environment, at a temperature of 20^{o}C, with a HEPA filtration system used to provide positive overpressure. A micropipette is used to measure the volumes while analytical scale accurate to 0.00001gis used for measuring mass. The sample is required to digest in an aqueous solution before to do the chemical analysis. The sample was treated in aqua regia (~ 100 ºC) using hot PTFE material to prevent possible contamination.

In this work, the chemical solution is prepared by using approximately 3 μg of CdZnTe, 1 mL of aqua regia for digestion, and 2 mL of water, then the solution is warmed until 80 ºC to complete the dissolution. The reactions can be expressed as following:

$$10HNO_3 + 12ZnTe \rightarrow 12ZnO + 6Te_2O_3 + 5H_2 + 5N_2 \qquad \text{Eq. 2-2}$$

$$10HNO_3 + 12CdTe \rightarrow 12CdO + 6Te_2O_3 + 5H_2 + 5N_2 \qquad \text{Eq. 2-3}$$

The equipment is used for analyzing only positive ions, therefore, the low Z elements such as Carbon, Oxygen, Boron, the halogens, and the other lighter elements cannot be quantified by this technique. In addition, due to using Aqua Regia as a dissolution regent, Nitrogen and Chlorine are undetectable for the specimen. Moreover, as this method is a mass spectrometer, there is interference between stable molecules O_2 and S which have the same mass. Furthermore, Iron is not detectable by the system due to the interferences.

2.1.3. Energy Dispersive X-ray Spectroscopy

Energy Dispersion X-Ray (EDX) spectroscopy is an analytical technique that qualitatively and quantitatively identify the elemental composition of the surface area top to 2 microns of the specimen with a spatial resolution of 1 micron. This technique is based on the characteristic X-rays that are generated when the specimen is bombarded with a focused beam of electrons in an electron beam instrument (SEM) to obtain a localized chemical analysis. The equipment used in this work is coupled to the Hitachi S-3000N Scanning Electron Microscope with an INCAx-sight model.

The principle of EDX spectroscopy is that each element has a unique atomic structure allowing that the atomic structure of different elements can be identified different from each other, as exhibited in Figure 2.4. The incident beam excites an electron in an inner shell, while the electron in this shell might be ejected and generate an electron hole where the electron was, then an electron from an outer shell (higher-energy shell) fills the hole. The difference of energy between the higher-energy shell and the lower energy shell may be released in the form of an X-ray.

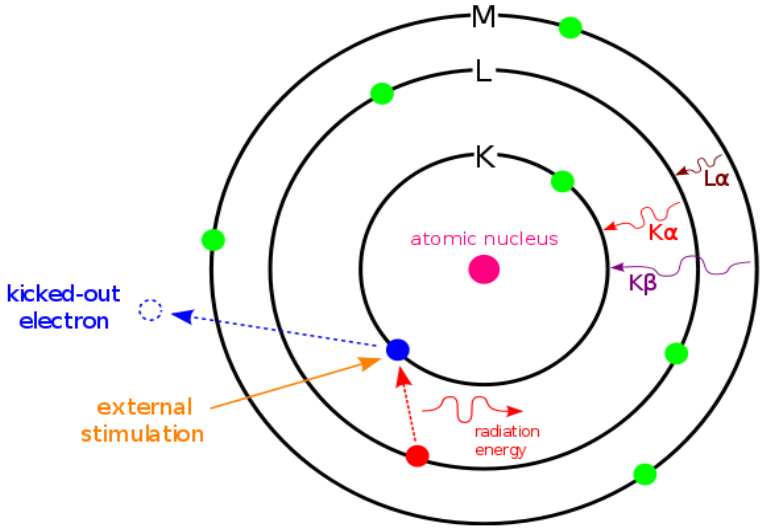

Figure 2.4. Principle of EDX technique.

The characterized X-ray that is emitted by atoms can be described by the Moseley's law:

$$\lambda = \frac{K}{(Z-\sigma)^2} \quad \text{Eq. 2-4}$$

where λ is the wavelength of a spectral line, Z is the atomic number, and K and σ are constants for a given spectral line. The constant σ is equal to 1 for the K-lines and 7.4 for more shielded L-lines. For the energy E, this equation can be approximately equivalent to:

$$E = K(Z-1)^2 \quad \text{Eq. 2-5}$$

where K is constant of 1.042×10^{-2} for K-shell, 1.494×10^{-3} for L-shell, and 3.446×10^{-4} for the M-shell, respectively. Moseley's determination of this relationship gave a simple evaluation of the atomic number of the elements. The characteristics X-ray energies calculated by using Moseley's law for several materials studied in our work (in SIDI) are shown in Table 2.1.

Table 2.1. The chacteristics X-ray energies of principal K- and L- emission lines for several materials investigated in our work.

Material	Z	K-shell (keV)	L-shell (keV)
Carbon	6	0.277	—
Oxygen	8	0.525	—
Aluminium	13	1.486	—
Zinc	30	8.638	1.011
Cadmium	48	23.173	3.133
Tellurium	52	27.472	3.769
Platinum	78	66.832	9.442
Gold	79	68.803	9.713
Ruthenium	44	19.279	2.558

2.1.4. Rutherford Backscattering Spectrometry

Rutherford backscattering spectrometry (RBS) is used to determine the structure and composition of materials by measuring the backscattering of a beam of high energy ions impinging on the specimen [6][7]. There are three concepts in backscattering and each gives an analytical capability: (1) the kinematic number enables mass analysis, (2) the differential

scattering cross section allows quantitative analysis, (3) the energy loss makes possible the depth analysis.

The schematic diagram of the experimental geometry of RBS technique is presented in Figure 2.5. When a projectile with mass M_1 is accelerated with energy E_0 penetrating the substrate material consisting of an atom with mass M_2, it loses energy throughout its trajectory to the electrons of the guest atom by ionization and excitation, and it also loses energy by nuclear collisions. When this projectile encounters a hard, it can change its trajectory into an outward direction in a straight-line path. During its outward path, it also loses energy to the target atoms until the particles emerge from the substrate material. The projectile ion is ricochet off the surface of the atom as backscattering scattering.

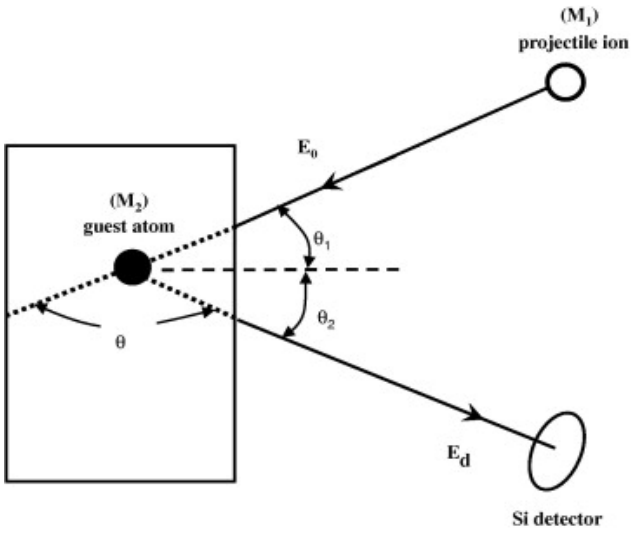

Figure 2.5. Schematic representation of the experimental geometry for the backscattering technique [8].

This scattering process leads to a decrease of kinetic energy for the detected particle, E_d, in contrast with the incident energy, E_0. The energy (E_1) of a backscattered projectile with incident energy (E_0) can be described by:

$$E_1 = k \bullet E_0 \quad \text{Eq. 2-6}$$

where k is the kinematic factor, which is actually the energy ratio of the particle before and after the collision. Since k relies on the masses of the incident particle and guest atom and the scattering angle, the energy of the scattered particle is also determined by these three parameters. Therefore, the kinematic factor k may be defined as:

$$k = \left(\frac{m_1 \cos\theta \pm \sqrt{m_2^2 - m_1^2 (\sin\theta)^2}}{m_1 + m_2} \right)^2 \quad \text{Eq. 2-7}$$

where θ is the scattering angle, M_1 is the mass of the lighter projectile, and M_2 is the mass of the heavier target particle.

RBS includes all types of elastic ion scattering with incident ion energies in the range of 500 keV to several MeV. Different angles or different projectiles are used in special cases. Usually protons, ^{4}He, and sometimes lithium ions are used as projectiles at backscattering angles of typically 150-170°.

RBS allows the quantitative determination of the composition of a material and depth profiling of individual elements. RBS is also quantitative without the need for reference samples, non-destructive, has a good depth resolution of the order of several nm, and very sensitivity to heavy elements with the order of parts-per-million (ppm). The analyzed depth is typically around 2 μm for incident He-ions and 20 μm for incident protons. The drawback of RBS is the low sensitivity for light elements, which often requires the combination of other nuclear based methods like nuclear reaction analysis (NRA) or elastic recoil detection analysis (ERDA).

To carry out the analysis, the instrumentation is shown Figure 2.6. Energetic ions are generated by the accelerator and shaped into a well-defined beam by a beam line and then aim to the sample which is placed in a target chamber. The scattered ions are detected by the detector, which signal is evaluated by the electronics and the PC.

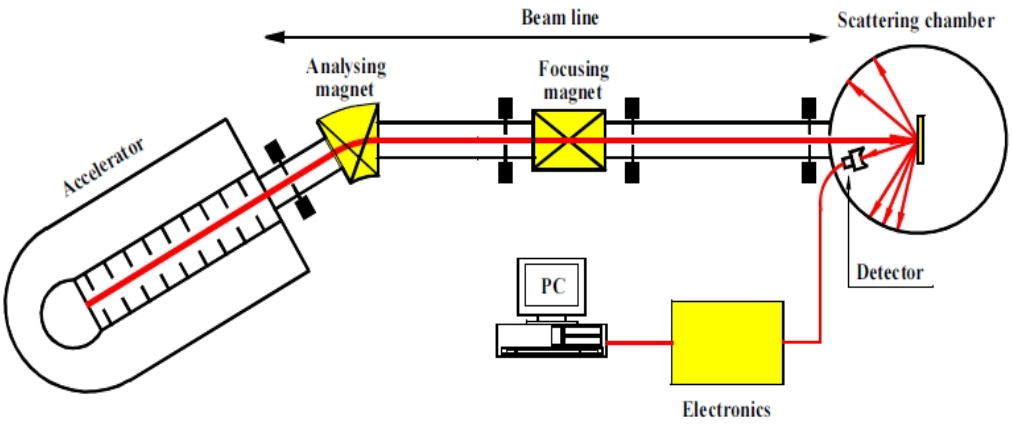

Figure 2.6. Schematic overview of the RBS experimental set-up.

RBS technique is sensitive by the number of atomic layers crossed by the beam, independently of their spacing, which means that RBS alone is not able to determine the real thickness of the layers. The thickness of the layer can be given by:

$$d = \frac{N_t}{\rho} \quad \text{Eq. 2-8}$$

where N_t is the real density of the thin film on the substrate which is given with a unit of 10^{15} at/cm^2 in our work, and ρ is the atomic density of the thin film with a unit of at/cm^3, which is 5.904 at/cm^3, 6.618 at/cm^3, 6.767 at/cm^3, 7.256 at/cm^3, and 7.285 at/cm^3 for Au, Pt, Pd, Ru and Rh, respectively. In addition, the atomic density of TeO_2 and CZT is 3.847 and 3.750 at/cm^3, respectively.

The ion beam (2 MeV $^4He^+$) is produced by the 3.1 MV van de Graaff accelerator at ITN, Lisbon, Portugal. The spectra in our work were recorded simultaneously by two silicon surface barrier detectors at 180° and 160° scattering angles, with 25 and 19 keV FWHM resolution. Different spectra were recorded varying the incidence angle (from normal incidence to 60°) and fitted simultaneously as a single block for a given sample with the IBA Data-Furnace NDF v.9.2.software [9].

2.1.5. High Resolution of X-ray Diffraction

High Resolution of X-ray diffraction (HRXRD) is an important technique for studying individual Bragg peaks of single-crystal and thin-film materials. This technique is used to characterize the thickness, crystallographic structure, composition and the degree of strain / relaxation in thin epitaxial grown films on substrates. High resolution and intensity are achieved using very high quality mirror and monochromator combinations. Typical routine applications of this technique include rocking curves, X-ray reflectivity measurements, coupled scans, and reciprocal space mapping. Particularly, rocking curves can provide information about the defects, layer thickness, superlattice period, strain, composition profile, lattice mismatch, ternary composition, misoritentation, and relaxation.

The characteristics of the diffractometer are operated by four Ge monochromator optimized with the (220) and (440) reflections, equipment with electronic motors, the output of these only obtain photons with the wavelength CuKα1 (λ = 1.540562 Å). The schematic diagram of this technique is exhibited in Figure 2.7.

The experimental setup in SIDI is composed of a rotating anode generator, which allows the monocromatization and collimation of the necessary radiation to achieve high resolution. It incorporates a 4-circles goniometer with large format which can operate at high and low temperatures. The incident angle, ω, is defined between the X-ray source and specimen. The diffracted angle, 2θ, is defined between the incident beam and detector angle. The resolution of ω and 2θ are: (i) Dω = 0.0002º (with optical encoder DOω = 0.00005º), (ii) D2θ = 0.0002º, (iii) DChi = 0.0025º, (iv) DPhi = 0.005º, and v) Dx = Dy = 0.005 mm.

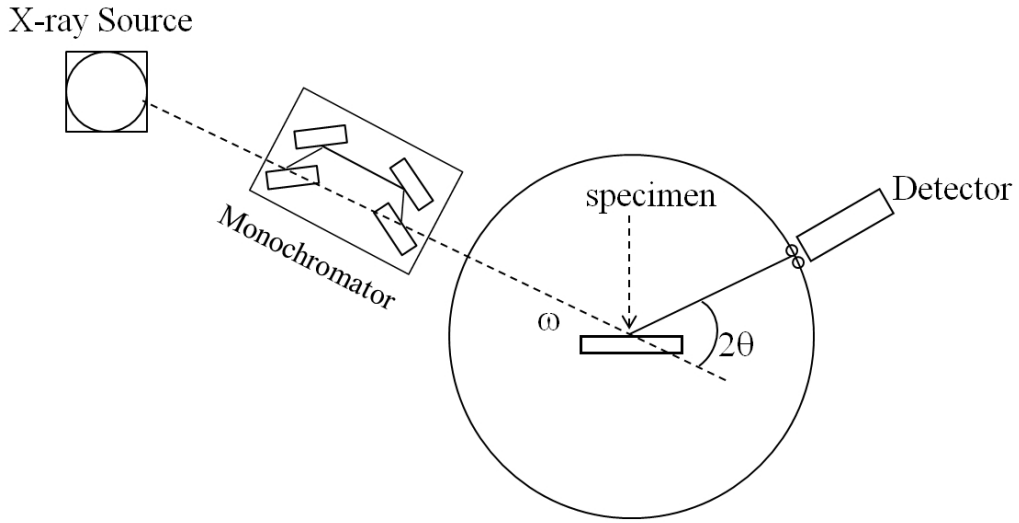

Figure 2.7. Schematic Diagram of a HRXRD.

2.1.6. Fourier Transmission Infrared Spectroscopy

Fourier Transform Infrared Spectroscopy (FTIR) is an analytical technique used to identify the materials, which can measure the absorption of infrared radiation by the specimen versus wavelength. Figure 2.8 presents the FTIR equipment in SIDI at UAM and a spectrometer layout of this equipment.

As shown in Figure 2.8 (b), an interferometer was used to modulate the wavelength from a broadband infrared source, and a detector estimates the intensity of transmitted or reflected light as a function of its wavelength. The signal achieved from the detector is an interferogram which was analyzed with a computer using Fourier transforms to acquire a single-beam infrared spectrum.

The FTIR spectra are usually presented as plots of intensity versus wavenumber (in cm^{-1}), where the wavenumber is the reciprocal of the wavelength. The IR spectra of this work have been obtained with a Bruker FT-IR spectrometer IFS66v, at a wavenumber range of 7000 ~ 500 cm^{-1} with a resolution of 4 cm^{-1} and using as reference the lamp in the instrument itself. This spectral range can provide substantial information regarding free carriers, defects, and dislocations in the material.

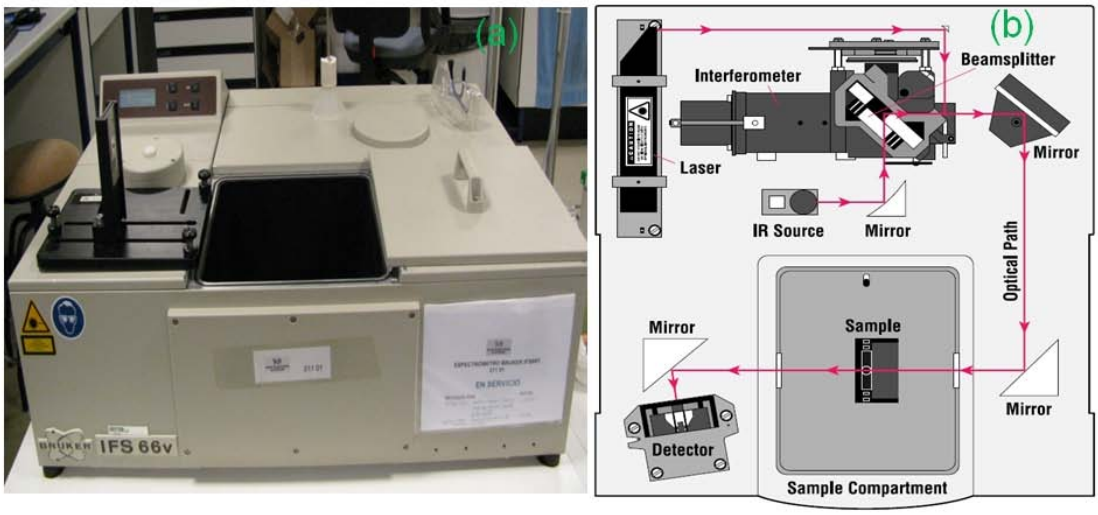

Figure 2.8. (a) FTIR equipment in Universidad Autónoma de Madrid, (b) Spectrometer layout of FTIR equipment.

2.2. Optical Techniques

2.2.1. Infrared and Optical Microscopy

The optical characterization of both bulk and surface properties of CZT materials were carried out with a Nikon 90i Infrared (IR) Microscope. The system is composing of two different light sources for illuminating from the top to the back side of the specimen. Different objectives can be used to describe the surface properties with the magnification of 1 ~ 20 x. Figure 2.9 shows the Nikon 90i IR Microscope used in our laboratory (CGL).

This Microscope is equipped with a 3-axis motorized stage, as well as brightfield (BF), darkfield (DF), and phase-contrastfilter cubes, while also functioning in transmission mode. Characterization in the BF imaging mode are created by the differences in absorption at the surface of the specimen, which is useful for distinguishing different materials or features at the surface. This mode has been operated in conjunction with the phase-contrast filter cube for imaging the surface morphology and surface roughness.

The DF optical configuration is a complementary microscopy technique which is more useful than the BF configuration. The fundamental advantage of the DF technique is ascribable to the arrangement of an opaque disc below the condenser lens within the microscope objective. This opaque disc blocks the light directly reflected by the specimen surface from reaching the condenser lens and finally the CCD. Only light which is scattered at oblique angles is able to pass into the condenser lens and through to the camera or ocular lens.

This technique is very sensitive to the scattered light from scratches, particulates, or other surface non-uniformities. However, for the rough surfaces which present a large degree of scattering, the differences between DF and BF microscopy are not as significant. Furthermore, for more specular surfaces, the DF mode is more sensitive to the scratches and particulate matter.

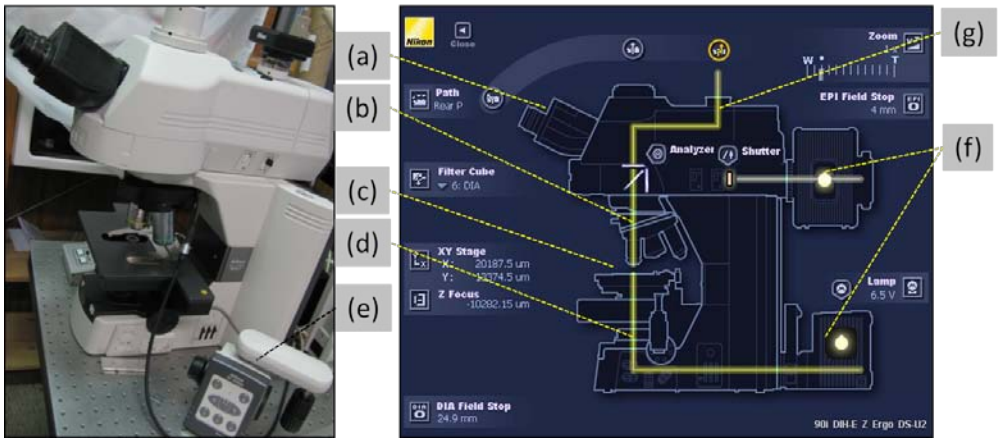

Figure 2.9. Nikon 90i IR microscope in CGL. (a) occular lens, (b) objective turret and objectives, (c) frame, (d) condensor lens, (e) stage controller and focus wheel, (f) light source, (g) external camera.

Nikon's NIS-elements software was used to recognise and sort the objectives in relation with the area, diameter, density, in order to give more information of the surface/transmission of the specimen. This technique has been carried out to characterize and evaluate the CZT material in conjunction with resistivity mapping data for selecting higher quality materials for fabricating nuclear radiation detectors.

2.2.2. Scanning Electron Microscopy

The Scanning Electron Microscopy (SEM) used in this work was a Hitachi S-3000N coupled with energy dispersive X-ray of Oxford Instruments with model INCAx-sight (in SIDI). This technique provides information about the morphology and topography of the surface.

The basic principle of SEM technique is to scan the specimen with a finely focused electron beam with kilovolt energy, while the image can be created by scanning a cathode-ray tube in synchronism with the beam and by modulating the brightness of this tube with beam-excited signals. In consequence, the image is created point-by-point which exhibits the variations in the generation and collection on the specimen. The schematic diagram of the SEM equipment is presented in Figure 2.10.

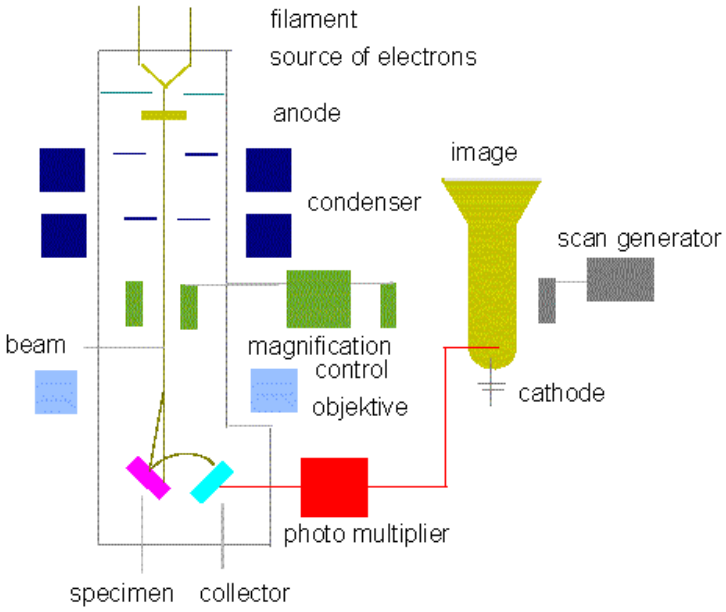

Figure 2.10. The schematic diagram of the SEM equipment.

Figure 2.11 exhibits the schematic diagram of the high resolution scanning electron microscope. The Philips XL 30 S-FEG high resolution SEM equipment has been used to investigate the surface morphology as well as the thickness of the metallic thin film layer on the CZT material. This technique can supply both secondary electron and backscattered electron imaging pictures of the samples.

In the Philips XL-30 S FEG-SEM, electrons are generated by the field emission (electron) gun using a high electrostatic field, then the electrons are accelerated with an energy of around 1 ~ 30 keV down the column towards the specimen. The magnetic lenses adjust the beam to a spot with a diameter of around 1 ~ 10 nm on the specimen, the electron beam overwhelms the surface of the sample by the scanning coils.

The magnified image is produced by relating the detector signal to the position of the beam. Secondary electrons can be formed when loosely bound atomic electrons in the solid are released by the interaction with a primary electron, besides they are required to have small mean free path due to their low energy. It is important to note that the information of the specimen can only be identified with a shallow depth of around 10 nm [10].

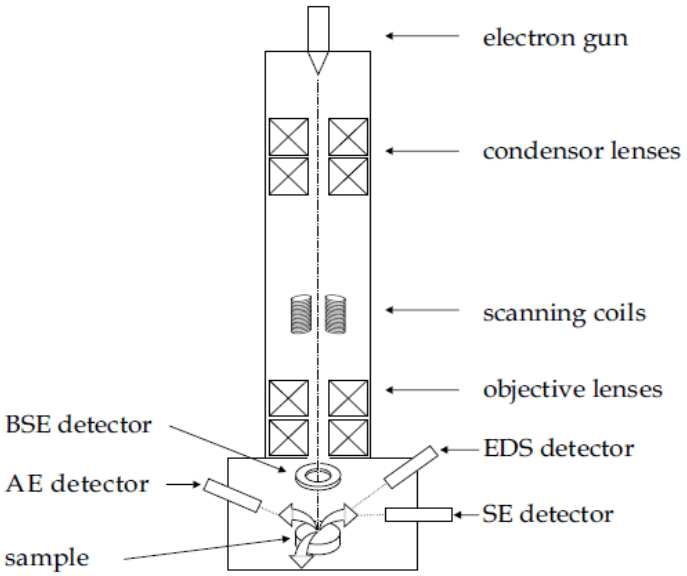

Figure 2.11. Schematic image of the high resolustion SEM equipment.

2.2.3. Atomic Force Microscopy

The atomic force microscope (AFM) can give information of quantitative topographic images of surfaces. The AFM equipment used in the work was a XEI-10 Park System, which can image the samples in contact and non-contact modes.

Contact mode AFM is one of the most widely used scanning probe mode operating by rastering a sharp tip across the specimen. An extremely low force (~ 10^{-9} N) is maintained on the cantilever, hence the tip can be pushed against the sample as it rasters. Either the repulsive force between the tip and sample or the actual tip deflection is recorded relative to spatial variation and then converted into an analogue image of the sample surface.

Non-contact mode AFM is chosen in our work to characterize the polished, etched, and contacted surfaces. The advantages and the superiority of the non-contact mode AFM are including no tip wear, no sample damage, the maintenance of the high resolution imaging, and the accuracy measurement. The tip-sample distance is successfully maintained at a few nm in the net attractive regime of inter-atomic force. The small amplitude of tip oscillation minimizes the sample interaction, leading to tip preservation and negligible sample modification. Figure 2.12 shows the AFM equipment used in this work in CGL at UAM.

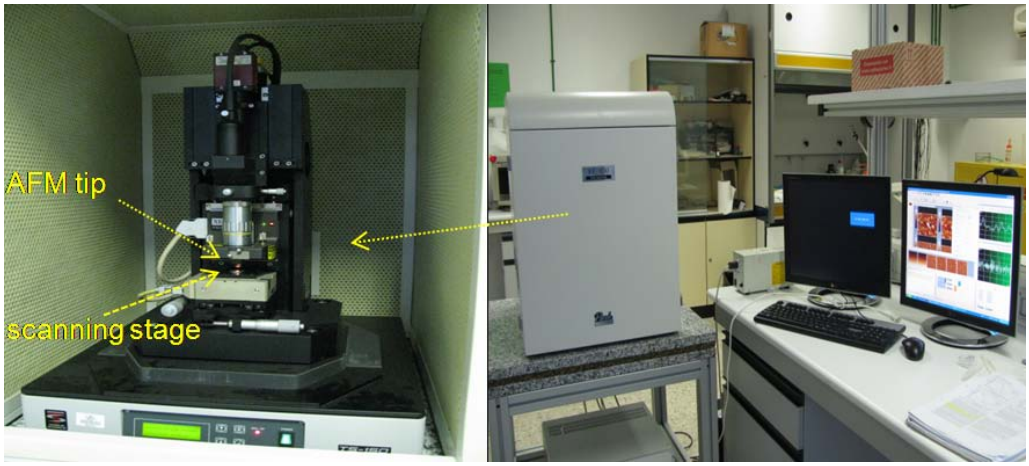

Figure 2.12. Parks XEI-100 AFM equipment of Universidad Autónoma de Madrid.

The average value of the surface roughness is given by R_a, the average deviation of surface height within a given area:

$$R_a = \frac{\sum |(Z_i - Z_{ave})|}{N} \qquad \text{Eq. 2-9}$$

where Z is the topographic height, Z_{ave} the average value of Z within the area, Z_i the value at point i and N the number of points measured within the area [11].

2.2.4. Catholuminescence Spectroscopy

Cathodoluminescence (CL) Spectroscopy is a technique that provides several information of the optical and electronic properties of the semiconductor materials [12][13]. The excitation depth from a crystal is commonly in the range of 2-8 μm, which is depending on the energy of electrons. The energy transfer may occur in a crystal provided by the lattice, interaction of neighbouring lattice defects, or anion groups, and thus the emission site may have a distance from the site of excitation. The CL intensity is proportional to the accelerated voltage and the current density, however, the power level used is limited by the destruction of the specimen or the specific defects including luminescence centres under electron bombardment.

In the SEM and electron microprobe, the sample is bombarded by a focused beam of electrons. Most incident electrons, rather than penetrating the sample in a linear fashion, interact with specimen atoms and are scattered. They follow complicated twisting paths through the sample material and lose energy in the interactions. The scattering events are of two types either elastic or inelastic. In elastic scattering, the electron trajectory changes, but

its kinetic energy and velocity remain essentially constant, which is due to the large difference between the mass of the electron and atomic nuclei. In inelastic scattering, the trajectory of the incident electron may be only slightly perturbed, but energy is lost during the interactions with the orbital electrons of the atoms in the sample.

Figure 2.13 exhibits the schematic diagram of the energies generated from the interaction of electron beam with the solid matter. When the specimen is bombarded by an electron beam, different electromagnetic waves and electrons are produced: CL, X-rays, secondary, and back-scattered electrons. The penetration depth of the incident beam and the excited volume in the sample is depending upon the energy of the incident electrons.

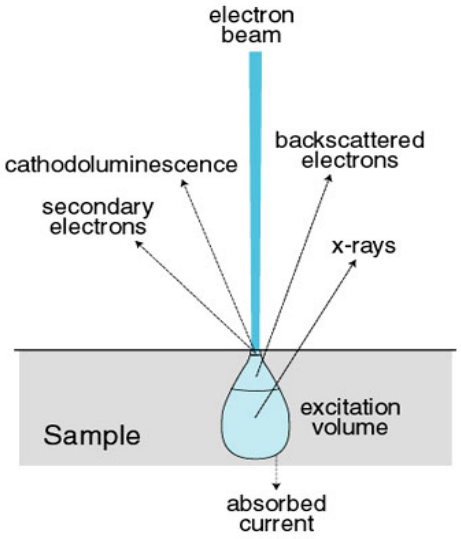

Figure 2.13. Schematic overview of the energies generated from the electron beam interacts with solid matter.

Figure 2.14 presents the process of a set of radiative transitions and luminescence production in the crystals. General properties of these transitions will be described briefly. (a) an intraband transition: excitation of an electron by high-energy particles or photons from the valence band to the conduction band and transition back to the valence band (intrinsic luminescence), (b) excitation of electrons and recombination with an activator and resulting in luminescence emission of a photon with energy $h\gamma$ and trapping of the electrons, Processes (c), (d), and (e) are due to the transitions that start and/or finish on localized states of impurities (e.g. donors and acceptors) or native defects of the material, which lie into the band-gap; these produce extrinsic luminescence.

The recombination processes between free carriers and trapped carriers of the opposite type are named Lambe-Klick model representing donor-to-free-hole transition (c), the Schon-Klasens model representing free-electron-to-acceptor transition (d), the donor-acceptor pair (DAP) recombination model (e), the excitation of several energy levels by absorption of photons and radiative deexcitation of an impurity with incomplete inner shells, (f).

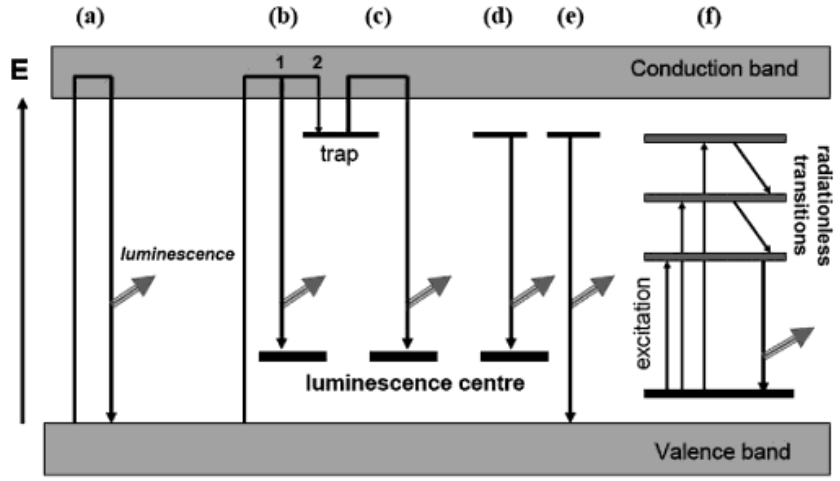

Figure 2.14. Processes of charge transfer and luminescence production in insulator crystals.

The CL spectra used in our investigation were carried out at room temperature with a JEOL JSM 6400 scanning electron microscope, equipped with a Zeiss DSM 940/962 mirror and a waveguide system for light extraction, the experimental setup is shown in Figure 2.15.

For excitation, a focussed electron beam of a SEM is used. The accelerating voltage of the beam is tunable at around 1 ~ 30 keV. Beam current is a function of aperture size and voltage, and can be varied between several pA to nA. The emitted light is detected using a parabolic mirror which is placed a few millimetres above the sample in a way to coincide with the sample. The size of the focus is usually in tens of microns. The mirror is arranged to have a large acceptance angle. The light collected from the focal point is reflected as a parallel beam through a hollow waveguide tube and focussed onto the entrance slits of a monochromator.

The detection range for the setup is between 650 nm and 950 nm, which cover to the spectral range where CZT is emitting light. For light with higher photon energy, a Horiba Jobin Yvon Si-CCD (CCD3000) detection system is available. The work has been done in Institute of Materials Science 6, University of Erlangen-Nürnberg.

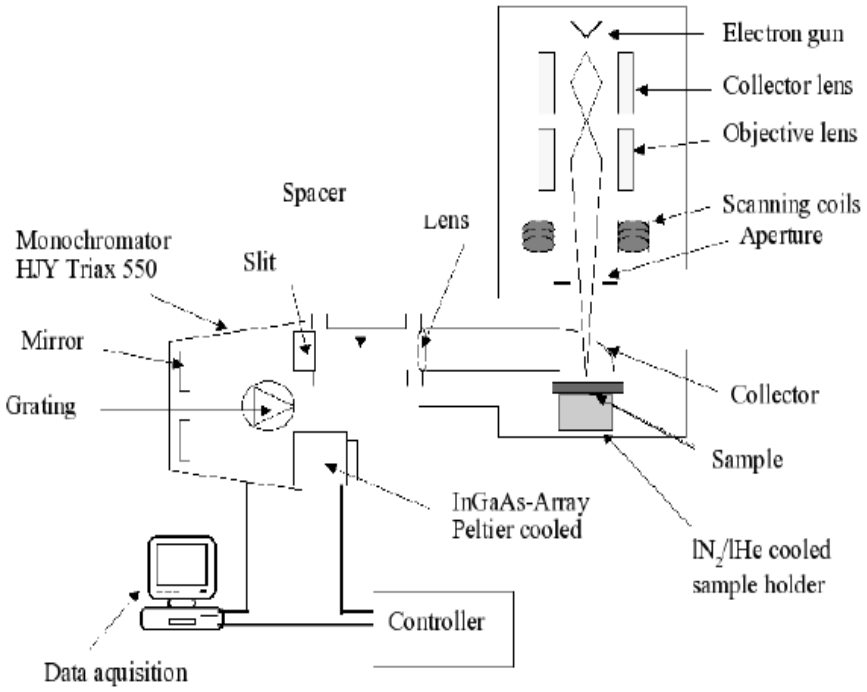

Figure 2.15. CL experimental setup.

2.2.5. Photolominescence Spectroscopy

The phenomenon of photoluminescence (PL) is the spontaneous process of light emission resulting from radiative recombination of electrons or holes from its excited states to their fundamental levels of energy. Potoluminescence spectroscopy is a contactless, non-destructive method of probing the electronic structure of materials. PL spectroscopy is one of the most useful optical method for analyzing the intrinsic and extrinsic properties of semiconductors, with its powerful and sensitive ability to determine impurities and defects in semiconductors specially in group III-V and II-VI semiconductor elements, which significantly influence the materials quality and device performance [14][15].

In the bulk material, translational symmetry can lead to the creation of electronic energy bands. Defects and impurities can break the periodicity of the lattice and perturb the band structure locally. Generally, the disturbance can be represented by a distinct energy level consisting within the bandgap. Depends of the defect or impurity, the state can act as a donor or acceptor with extra electrons in the material. Electrons or holes are attracted to the surplus or deficiency of local charge because of the impurity nucleus or defects, resulting in Coulomb binding. The situation can be termed as a hydrogenic system where the binding energy is

decreased by the dielectric constant of the material. Indeed, donors and acceptors have different binding energies owing to the difference effective masses of electrons and holes.

In fact, the carriers will be trapped at these states at very low the temperature. If these carriers can recombine radiatively, the energy of the emitted light can be examined to ascertain the energy of the defects or impurity levels. Shallow levels, which are located close to the edge of conduction band or valence band, are favourable to participate in the radiative recombination. However, the temperature of the specimen must be sufficiently low to prevent thermal activation of carriers out of the traps. Deep levels incline to facilitate nonradiative recombination by supplying a stop-over for electrons making their way between the conduction band and valence band by emitting phonons. Several intrinsic and impurity transitions are exhibited in Figure 2.16.

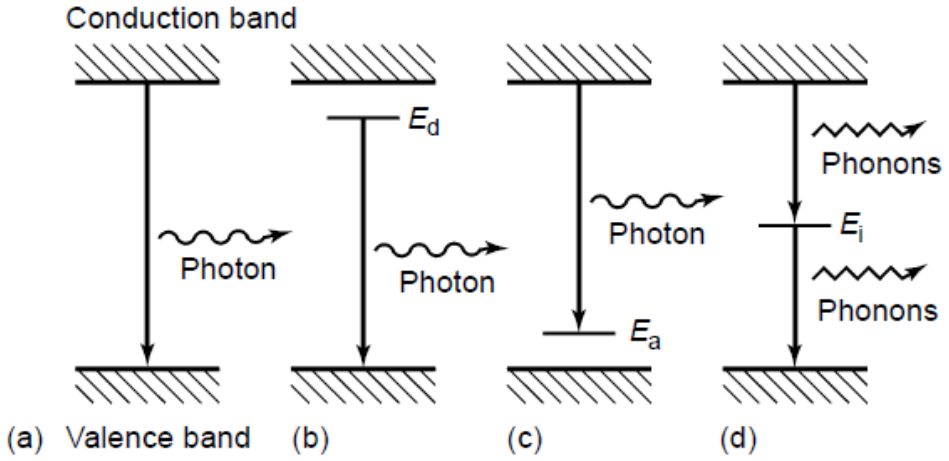

Figure 2.16. (a–c) Radiative recombination paths: (a) band-to-band; (b) donor to valence band; (c) conduction band to acceptor. (d) Nonradiative recombination via an intermediate state [16].

Figure 2.17 shows the diagram of the PL experimental setup. A Argon laser tuned to a wavelength near the bandgap energy of the specimen is directed onto the specimen guided by a set of lenses and mirrors. The specimen can be held in a closed cycle liquid helium cryostat in order to operate at low temperatures.

When the laser beam is incident on the sample, photoluminescence takes place and light is emitted from the specimen at wavelengths dependent on the sample composition. PL signal was focused to the monochromator via lenses, while different filters were required so that unwanted signals and noise can be avoid. The PL signal travels through a single-grating

monochromator which selects a wavelength to transmit to detector. Two types of detectors can be operated at the exit slit of monochromator depending on the detected signal.

Normally at longer wavelengths photomultiplier tube is used and germanium photodiodes are good for the near-infrared range. The digital information is interpreted by the PC, which can exhibit the PL spectrum. The spectrum implies the relative intensities of light with different wavelengths entering the detector. In addition, lock-in amplifier was employed to characterize the amplitude and phase of signals covered by noise. The signal from the detector and lock-in amplifier can be achieved by the data acquisition board.

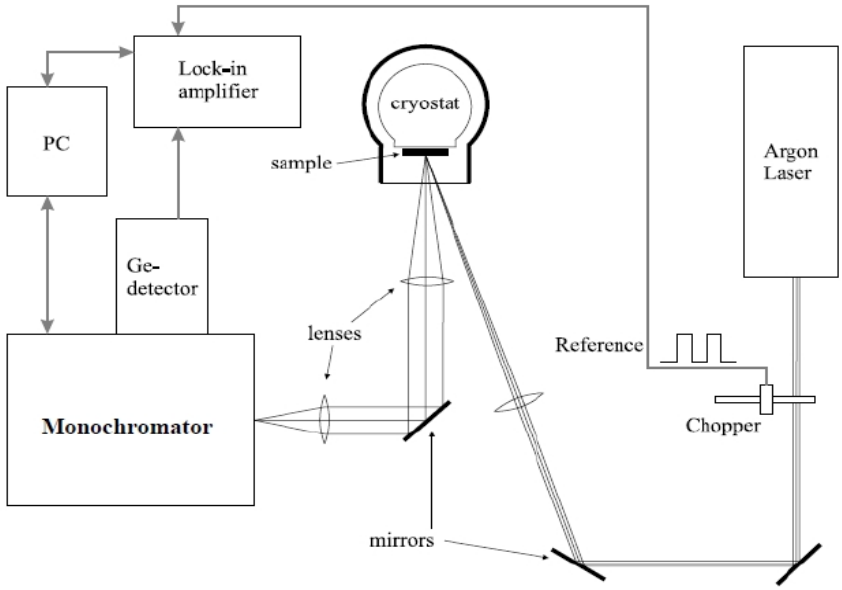

Figure 2.17. Diagram of photoluminescence experimental setup.

In our work, the samples were mounted in a closed-cycle cryostat, cooled to 22 K, and excited with the 488 nm line of an Ar-ion laser. The photoluminescence spectra were recorded with a Hamamatsu R453 photomultiplier and an HRS-2 monochromator (Jobin-Yvon) with a spectral resolution of 0.6 nm. The work was carried out in Institute of Materials Science 6, University of Erlangen-Nürnberg.

2.3. Electrical Characterization Techniques

2.3.1. Contactless Resistivity Mapping

The contact-less resistivity mapping (COREMA) instrument can measure point to point the resistivity of the semiconductor materials. This technique uses a contactless, consequently, non destructive method, termed as Time Domain Charge Measurements (TDCM). The specimen can be placed into a capacitor as a lossy dielectric substance and the resistivity is evaluated by measuring a time dependent charge transient observed after application of a voltage step. The measurement is non-contacting, which prevents the problems connected with the fabrication of Ohmic contacts and also analysis the specimen without degrading surface quality.

Figure 2.18 presents the COREMA mapping instrument in our laboratory (CGL). The specimen is located on the stage serving as back electrode. The top surface of the specimen is approached but not touched by a probe, 2.5mm diameter, measurement electrode surrounded by a guard electrode. The system should be closed during the measurement to avoid free carrier absorption and excitation, which may decrease the resistivity of the bulk material resulting from photoconductivity.

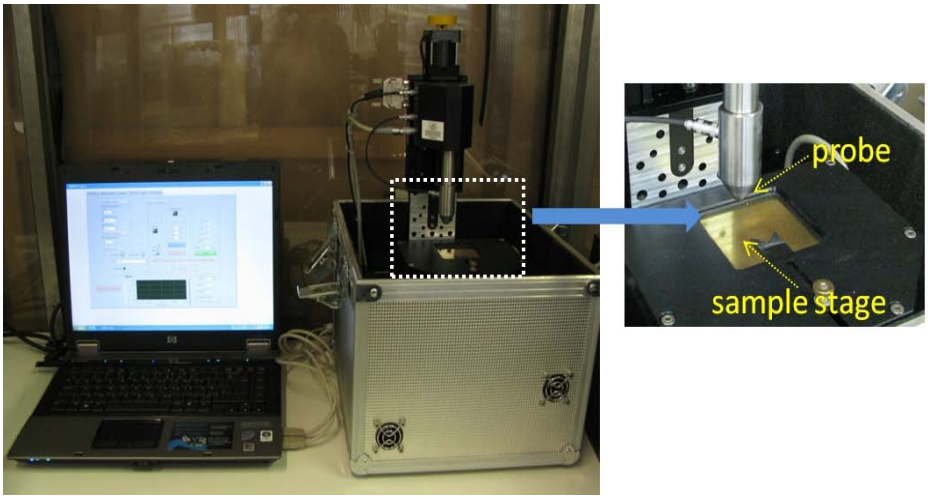

Figure 2.18. COREMA equipment at CGL.

The principle of TDCM measurement and the scheme of the instrument detection probe are shown in Figure 2.19. The semiconductor material can be characterized by the dielectric relaxation, τ.

$$\tau = R_S C_S = \varepsilon\varepsilon_0\rho \quad \text{Eq. 2-10}$$

where ε is the material dielectric constant, ρ is the resistivity of the material, R_S and C_S are the capacity and resistance of the investigated material, respectively.

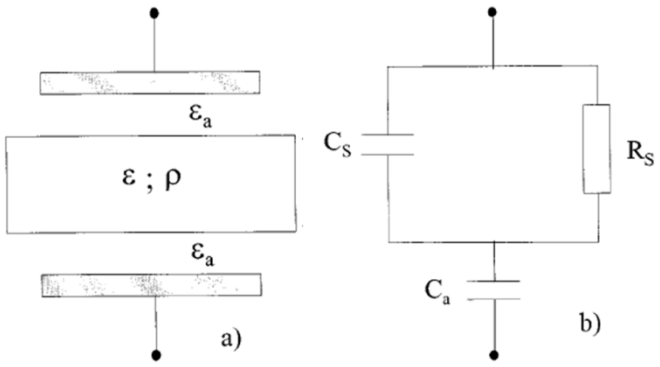

Figure 2.19. TDCM method for resistivity characterization: (a) Schematic image of the capacitor, (b) equivalent circuit. C_a is the two air gap capacitors.

The planar detector is demonstrated by the parallel association of a capacitor:

$$C_S = \varepsilon A / d \quad \text{Eq. 2-11}$$

$$R_S = \rho d / A \quad \text{Eq. 2-12}$$

where A and d are the area and the thickness of the sample, respectively. The quantity, τ, can be measured by characterize the circuit response in the time domain after a step excitation [17]. The capacitors C_S and C_a are supposed to be uncharged. When t = 0, a signal step is applied leading to a charging in the capacitors, while t > 0, the capacitor C_S start to discharge and simultaneously more charge is carried to C_a.

The resistivity can be achieved by testing the charge Q(t) flowing into the capacitors via a charge sensitive amplifier. The relationship between the resistivity and the charge can be expressed by:

$$\rho = \frac{Q(0)\tau_e}{Q(\infty)\varepsilon\varepsilon_0} \quad \text{Eq. 2-13}$$

where ε_0 is the permittivity of vacuum, and $\tau_e = R_S(C_A + C_S)$, which can be received by measure the time dependent charge distribution. The evaluation considers the thickness of specimen and electrode spacing variations.

This procedure is superior to the conventional methods that require the electrical contacts which are time consuming and destructive. The local non destructive characterization only takes few seconds, two-dimensional specimen resistivity mappings can be produced within a resistively short time.

2.3.2. Current-Voltage Characterization

Current-voltage (I-V) characterization was carried out with a Keithley 2400 electrometer in CGL, as shown in Figure 2.20. The characterization was used for examining the detector performance, comparing the influences of different surface preparations on detector resistivity, as well to measuring temporal effects on radiation devices. The system should be closed and protected from light during the characterization in order to prevent free carrier absorption and excitation, which may increase carrier concentration and thus decrease the bulk resistivity due to photoconductivity.

The applied voltages in our work were range from -200 V to +200 V, and the bulk resistivity can be calculated by the following equation:

$$\rho = \frac{R \bullet A}{d} \quad \text{Eq. 2-14}$$

where A is detector area, d is the thickness of the detector, R is the sample resistance determined from I-V curve $\Delta V/\Delta I$.

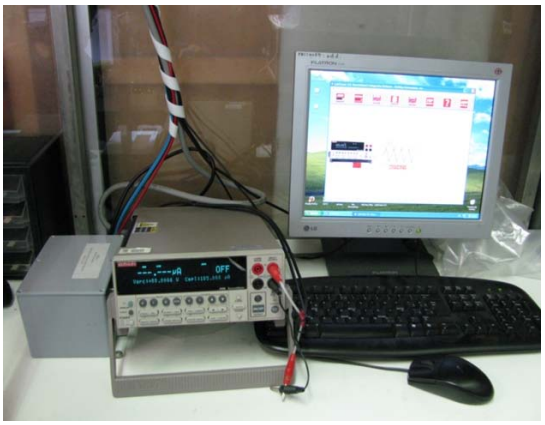

Figure 2.20. Keithley 2000 I-V system in CGL.

2.3.3. Gamma Response

The equipment used for testing the CZT detectors was based on set of A250 charge sensitive preamplifiers from Amptek. Figure 2.21 displays the experimental configuration for testing the CZT radiation detectors in our work at CIEMAT.

As shown in Figure 2.21 (b), the first stage of the preamp circuit shown on the right part is the Amptek A250 integrating amplifier with the 2SK152 Nchannel FET mounted onto the PC250 board. The PC250 board provides a convenient way to test the A250. From the noise performance curves given by Amptek, this FET seems to be the best solution for small capacity detectors. The preamp transfers the charge signal of the test detector into the 1 pF internal feedback capacitor of the A250. The decay time of the A250 circuit is expected to be 300 μs. The PCB boards each contain the FET and A250 charge sensitive pre-amplifier.

The detector was mounted on a Teflon fixture designed by our laboratory, the mounting plate was made of gold and was connected to the anode, and the cathode side is made of a gold cantilever. The cathode of the detector was connected to high voltage, while the anode of the detector was connected to the input of the FET.

Presented on the left part of this figure, the bias voltage across the detector is filtered in the preamp box by a low pass filter with a time constant of 1 s. The values of the default bias voltage circuit are optimised for bias currents up to a few nA. For higher bias currents the bias voltage across the detector will deviate considerately from the bias voltage that is set by the HVPS control.

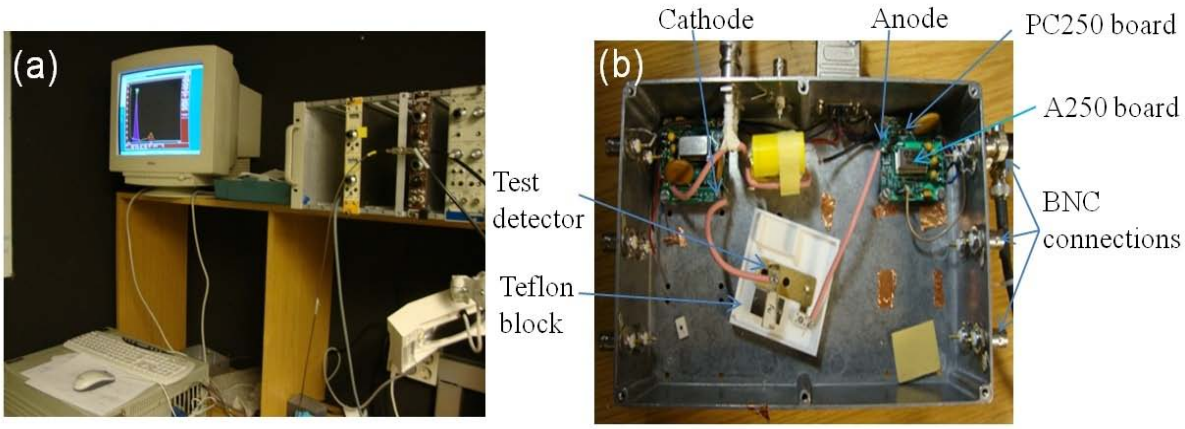

Figure 2.21. Testing equipment (a) and test box with an installed CZT detector (b).

The BNC connections of this configuration are used to connect the cathode to the bias voltage (left) and also connect the output of the A250 pre-amplifier with the input of the Ortec Dual Spec Amp 855 post-amplifier (right). All the BNC connections were made by using 50 Ω coaxial cables with BNC terminations. The measurements were controlled and maintained at 20 °C.

The measurements were carried out in the pulsed detector modes, in contrast to the current modes or mean square voltage (MSV) modes. In order to operate this mode properly, it is necessary to note that the time constant of the charge sensitive preamplifier is substantially larger than the time constant of the detectors.

2.4. Summary of Techniques

	Technique	Preparation	Objective
Compositional & Structural	TXRF	Contacted Sample	Surface and Subsurface Composition
	ICP-MS	Powder Sample	Bulk Composition
	EDX	Contacted Sample	Surface Composition
	RBS	Contacted Sample	Surface and Subsurface Composition, Contact Thickness
	HRXRD	Polished Sample	Crystallinity
	FTIR	Polished Sample	IR Transmission
Optical	IR Microscope	Polished Sample	Te and Cd Inclusions
	SEM	Contacted Sample, Sample Cross Section	Surface Morphology, Contact Thickness
	AFM	Contacted Sample	Surface Roughness
	CL	Polished Sample	Defect Levels
	PL	Contacted Sample	Defect Levels
Electrical	COREMA	Polished Sample	Electrical Resistivity
	I/V	Contacted Sample	Leakage Current, Electrical Resistivity
	Gamma Response	Contacted Sample	Detector’s performance

2.5. Bibliography

[1] R. Klockenkämper, A. von Bohlen, Determination of critical thickness and the sensitivity for thin film analysis by total reflection X-ray fluorescence spectrometry, *Spectrochim. Acta Part B*, Vol **44**, 461-469 (1989).

[2] R. Fernández-Ruiz, J.P. Cabañero, E. Hernández, M. León, Determination of the stoichiometry of CuxInySez by total-reflection XRF, *Analyst*, 2001, 126, 1797-1799.

[3] A. Prange, Total Reflection X-ray Spectrometry: Method and Applications, *Spectrochim. Acta Part B*, Vol **44**, 437-452 (1989).

[4] L. Ebdon, E.H. Evans, A. Fisher, S.J. Hill, An introduction to analytical atomic spectrometry, Wiley NY, 73-134 (1998).

[5] M. Thompson, J.N. Walsh, Handbook of inductively coupled plasma spectrometry, NY: Chapman and Hall, Glasgow: Blackie (1989).

[6] M. Mayer, J. Roth, K. Ertl, 'Rutherford backscattering spectroscopy and elastic recoil detection analysis with lithium ions – The better alternative to helium?', *Nucl. Instrum. Meth. B*, Vol **190**, 405-409 (2002).

[7] N.P. Barradas, C. Jeynes, R.P. Webb, Simulated Annealing Analysis of Rutherford Backscattering Data, *Appl. Phys. Lett.*, **71**, 291 (1997).

[8] D. Shakhvorostov, W.N. Lennard, P.R. Norton, Analytical Solution for Depth Scale Calculations in Rutherford Scattering Spectrometry, *Nucl. Instr. Meth. B.*, Vol **272**, 18-22 (2012).

[9] J.R. Tesmer, M. Nastasi, Handbook of Modern Ion Beam Materials Analysis, *Materials Research Society*, Pittsburgh, PA, (1995).

[10] H. E. Exner, Metallography and microstructures, *Metals handbook*, 9th ed. Vol **9**, 89 (9) (1985).

[11] T. Baum, D.J. Schiffrin, AFM Study of Surface Finish improvement by Ultrasound in the Anisotropic Etching of Si <100> in KOH for Micromaching Applications, *J. Micromech. Microeng.* Vol **7**, 338-342 (1997).

[12] N. Armani, C. Ferrari, G. Salviati, F. Bissoli, M. Zha, L. Zanotti, Crystal defects and optical transitions in high purity, high resistivity CdTe for device applications, *Materials Science and Engineering B*, **91-92**, 353-357 (2002).

[13] M.A. Stevens-Kalceff, S. Prawer, W. Kalceff, J.O. Orwa, J.L. Peng, J.C. McCallum, D.N. Jamieson, Cathodoluminescence microanalysis of diamond nanocrystals in fused silicon dioxide, *J. Appl. Phys.*, Vol **104**, 113514 (2008).

[14] J. Krustok, V. Valdna, K. Hjelt, H. Collan, Deep center luminescence in p type CdTe, *J. Appl. Phys.* Vol **80**, 1757 (1996).

[15] Hwa-Yuh Shin, Cherng-Yuan Sun, The exciton and edge emissions in CdTe crystals, *Materials Science and Engineering B*, Vol **52**, 78-83 (1998).

[16] T.H. Gfroerer, Photoluminescence in Analysis of Surfaces and Interfaces, Encyclopedia of Analytical Chemistry, 15 Sep, (2006).

[17] R. Stibal, J. Windscheif, W. Jantz, Contactless Evaluation of Semi-insulating GaAs Wafer Resistivity Using the Time-dependent Charge Measurement, *Semiconductor Science and Technology*, Vol **6**, 995 (1991).

CHAPTER 3. SURFACE PREPARATION AND DETECTOR FABRICATION

This chapter presents the important process for the fabrication of CdTe/CZT detectors. The investigation is mainly focused on the preparation of surface and lateral edges. Five sections are described in this chapter about the whole preparation of the detector.

In the first section, a complete process of surface preparation including ingot slicing, wafer lapping, mechanical polishing, and etching will be presented followed by the surface characterization for each step. These processes are extremely important for preparing the surface of the detector material before the subsequent electrode deposition.

For the second section, the research of the etching process has been carried out. This section is composed of three parts: the selection of the best etchant, the choice of the optimal concentration of the etchant, and the study of the cleaning of the surface after the etching stage. The surface roughness and morphology have been characterized for each etching process.

In the third section, the characterization of the surface preparation including cutting, polishing, and etching are carried out to determine the importance of the procedures. Therefore, it is necessary to recognise the surface processing steps to identify which steps produce the best surfaces for improving the performance of radiation detectors.

The fourth section involves to the contacts deposition methods (sputtering, evaporation, and electroless), which have been introduced in terms of the theoretical knowledge and the instruments used in our investigation.

In the fifth and last section, the objective is to study the important influence of the different preparation methods for the lateral edges of the detectors. For the whole detector preparation processes, not only the surface preparation by polishing and etching can affect the leakage current and detector performance, but also the preparation of the lateral edges of the detector can determine the quality of the radiation detectors. In this section, the treatments with mechanical polishing and passivation of the edges have been studied.

3.1. Process for the Surface Preparation

Surface processing prior to detector fabrication are known to play an important role in determining the performance of CdTe/CZT radiation detectors. Surface processing can influence the leakage current of the detectors which in turn affects the pulse height resolution of the detector [1].

Several steps have been followed for the preparation of the CdTe/CZT samples, named slicing, lapping, mechanical polishing and chemical polishing before the detector fabrication. These steps always induce surface damage and non-stoichiometric composition on the detector surface. In fact, dangling bonds, surface roughness and non-stoichiometric surface species introduce defects which are responsible for the high surface leakage current.

In consequence, surface properties can influence the electric field inside the device and also can significantly affect the charge transport and signal information. Therefore, it is prominent to study the CdTe/CZT surface process in order to obtain an optimal surface condition that would result in high quality radiation detectors. The following section contains the procedures used for the preparation of the samples studied in this thesis.

3.1.1. Slicing Process

After its removal from the ampoule, the ingot is sliced and diced in small pieces depending of the required geometry of detectors. A Well machine with a diamond wire of 170 μm diameter is used for CdTe/CZT crystals. Two types of wire saws were used for the slicing and dicing processes, the horizontal and vertical slicing machines are shown in Figure 3.1.

Figure 3.1 (a) presents the model well 3032 precision horizontal diamond wire saw, where the wire is travelling horizontally. The sample can be positioned inside the loop thereby allowing for accurate positioning prior to and viewing of the sample during the cutting process. The sample holder is attached to a counter-balanced arm that uses appropriated weights to establish and maintain the proper amount of force throughout the entire cut. Tensioning of the wire is also accomplished through the use of weights. A microscope was mounted on the saw so that accurate positioning of the diamond wire can more readily be accomplished or to watch the cut (or slice) while it is in progress.

Figure 3.1 (b) shows the model 3242 well precision vertical diamond wire saw. A slotted table enables the operator to position the sample in both axis while the sample holder rotates throughout 360 degrees for a proper cutting axis. Two micrometers are supplied standard on this version, one for accurate positioning of the sample, the other for setting the depth of a slice or cut. An adjustable electrical end-switch signal is used when the desired depth of cut is obtained and the motor is automatically shut off.

In order to avoid the cracking of the samples, the wire should be continuously soaked with a solution prepared with 2 L deionised water and 0.5 mL of a lubricant commercial solution. It is also important to note that defects such as dislocations, microcracks, and subsurface damages can be introduced into the bulk material during slicing, which can deteriorate the detector performance. Therefore, lapping and polishing stages are necessary to remove the saw damages and improve the sample planarity.

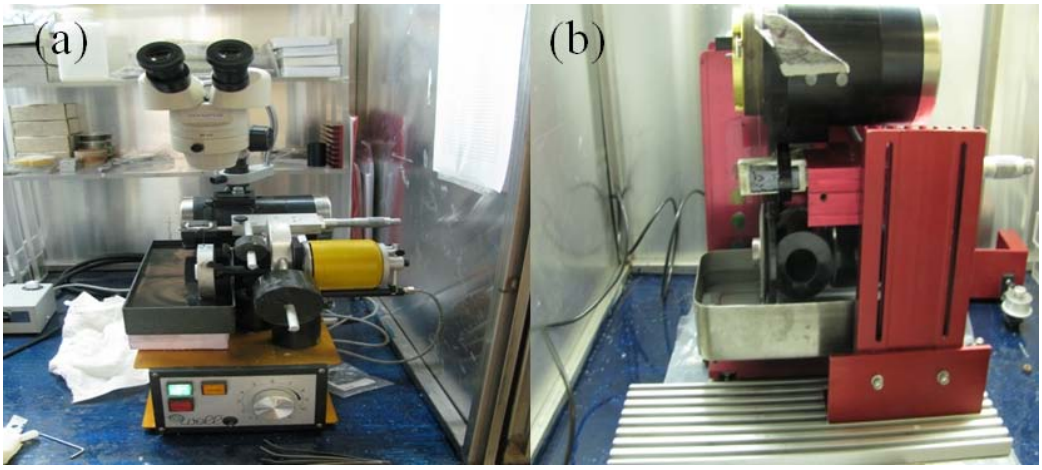

Figure 3.1. Well diamond wire saw for ingot and wafer slicing. (a) Horizontal diamond saw, (b) Vertical diamond saw.

3.1.2. Lapping and Polishing

One important and often overlooked factor that controls the performance of CdTe/CZT detector devices is the interface between the CdTe/CZT bulk crystal and the metal electrodes. Indeed, when the single elements are sliced and diced from the CdTe/CZT ingot, the sawing process introduces a large density of electrically active defects (amorphous layer, microcracks, etc) into the near-surface region of the crystals. To remove this damage layer and produce a clean defect-free surface for electrode deposition, the crystals are typically lapped, polished and chemical etched. Lapping and mechanical polishing can minimize the

defects on the surface and subsurface, but also opens up to other type of defects on the polished surface, such as contamination or chemical modification of the surface, that act as trapping centers and eventually enhance the surface leakage current.

Hossain et al. have studied the effects of the surface processing on the response of CZT gamma detectors by using a collimated synchrotron X-ray beam [2]. The results demonstrated that trapping centers increase when the roughness of the surface increases, therefore the leakage current increases and degrades the detector's quality.

Tepper et al. have investigated the electronic decay in detector grade CdZnTe as function of surface quality and temperature using a contactless pulsed laser microwave cavity perturbation technique [3]. The results indicate that the quality of the CdZnTe surface strongly influence the electronic decay time, and a multitude of charge traps at various energies were introduced by surface damage, which can be eliminated by a Bromine Methanol chemical etching.

Practically, after sawing the ingot into single pieces, the samples were bound with a wax on a glass sacrificial piece by using a hot plate. The samples were first lapped to remove the saw damages, and to obtain flat surfaces with a controlled thickness. This process was carried out using a Logitech PM5 with a standard lapping glass plate operating at 50 rpm, the photos of the Logitech PM5 lapping/polishing machine with lapping pad and polishing pad are shown in Figure 3.2. The abrasive slurries used for this lapping step in this work were generally following the order of 9 μm and 3 μm Al_2O_3 powders.

After lapping process, the objective is to reduce the thickness of the amorphous subsurface damage layer and to improve the surface quality by using a mechanical polishing process. The Al_2O_3 abrasive of 3 μm and 1 μm are used for refinement performed with the same Logitech system, but using a polishing pad (Chemcloth).

In order to improve the surface quality for the detector fabrication, the process is continued by using a fine mechanical polishing, carried out by using a Logitech system with 1 μm diamond slurry at a typical rotary velocity of 50 rpm, shown in Figure 3.3. This step is important to decrease the surface roughness and create a mirror-like surface without degrading the flatness. It is important to note that the choice of polishing pads, slurries, pressure on samples, pad rotational velocity, drip rate of slurries are primordial critiria to optimise the quality, uniformity, and reproductivity of each polishing step. In general, one

can say that the polishing grits create an amorphous layer after each steps of polishing with a thickness about 3-10 times the size of the abrasive particle used.

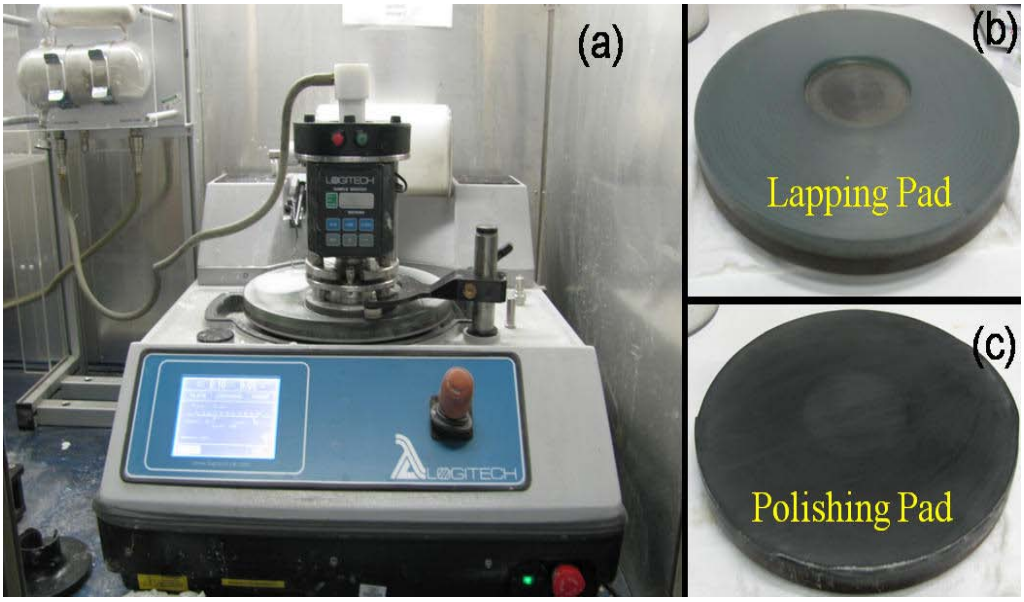

Figure 3.2. Polishing Equipment at CGL: (a) Logitech PM5 Lapping/Polishing machine, (b) Lapping pad, (c) Polishing pad.

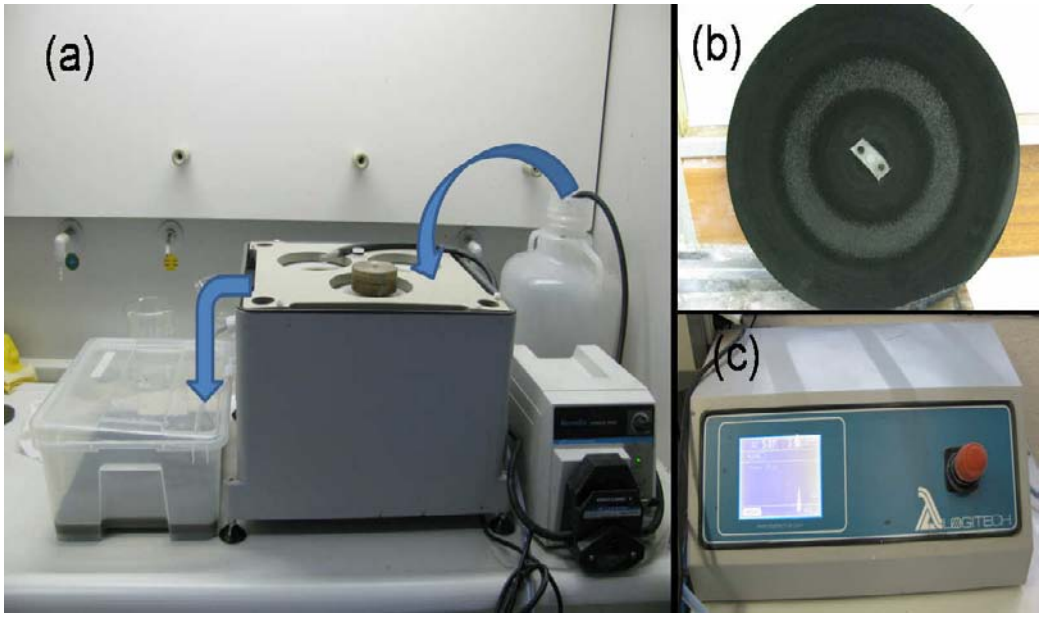

Figure 3.3. Logitech CP3000 Polishing Equipment at CGL: (a) Diamond polish machine, (b) Diamond polishing pad, (c) Logitech polishing control panel.

In order to study the effect of the different cutting and polishing processes on the surface properties, the comparison was done following a subsequent process: 1) first lapped using a 3

μm Al_2O_3 abrasive powder, followed by 2) a polishing step with 1 μm Al_2O_3 powder, and then 3) fine polished with 1 μm diamond slurry. It is necessary to mention that the name of different surface treatments study presented in this section is denoted by the name of the final process, for example, '1 μm diamond polishing' means that the samples has been prepared by the process 1), 2), and 3).

The characterization of these samples was carried out by using an Atomic Force Microscope (AFM), Scanning Electron Microscope (SEM), and Energy Dispersive X-ray Spectroscopy (EDX) to determine surface roughness, surface morphology, and the elemental composition of the surface and subsurface region.

Figure 3.4 shows the AFM 3D images of CZT surfaces with a scale of 2 μm × 2 μm after different mechanical lapping and polishing processes. We can observe a very rough surface after lapping step with the highest roughness than the other polishing steps. After the subsequent polishing processes, one can observe the reduction of roughness and a smoother surface compared with only lapping process considering the height values exhibited in the three AFM images.

In Figure 3.5, one can obtain the line scans of the surface roughness with the analysing scale of 2 μm × 2 μm area, which also gives the information of the maximum, minimum and average values of the surface roughness. For comparison, three different positions on the surface area are exhibited with different colours.

As can be seen in Figure 3.5 (a), the peak to valley depths of the scratches are as deep as about 100 nm and particulates as large as approximately 150 nm present on the surface after only lapping process, with an average surface roughness value of 80-100 nm. In the same figure, we can observe that the average surface roughness after 1 μm Al_2O_3 polishing and after 1 μm Diamond polishing are around 7-10 nm and 1-2 nm, respectively, which is much lower than the previous value obtained after the lapping process.

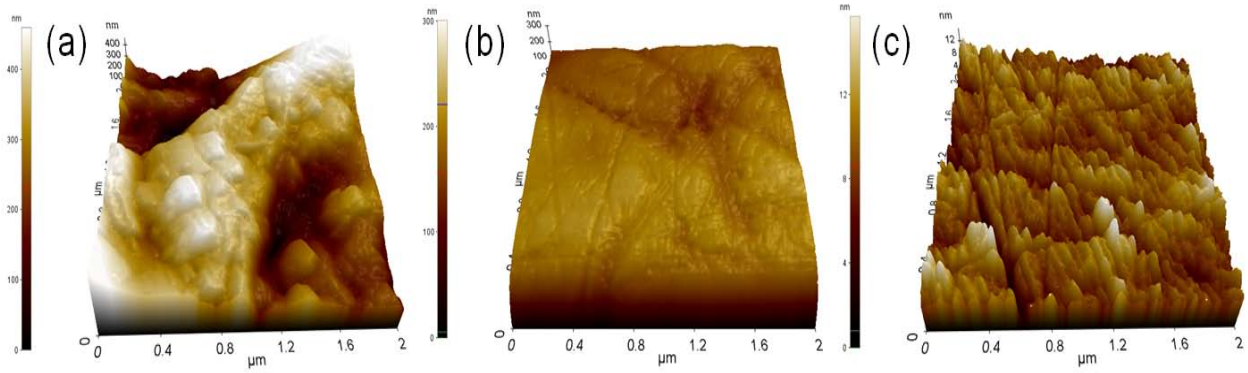

Figure 3.4. The AFM 3D images of CZT samples after different lapping and polishing processes. (a) 3 µm Al_2O_3 lapping; (b) 1 µm Al_2O_3 polishing; (c) 1 µm Diamond polishing.

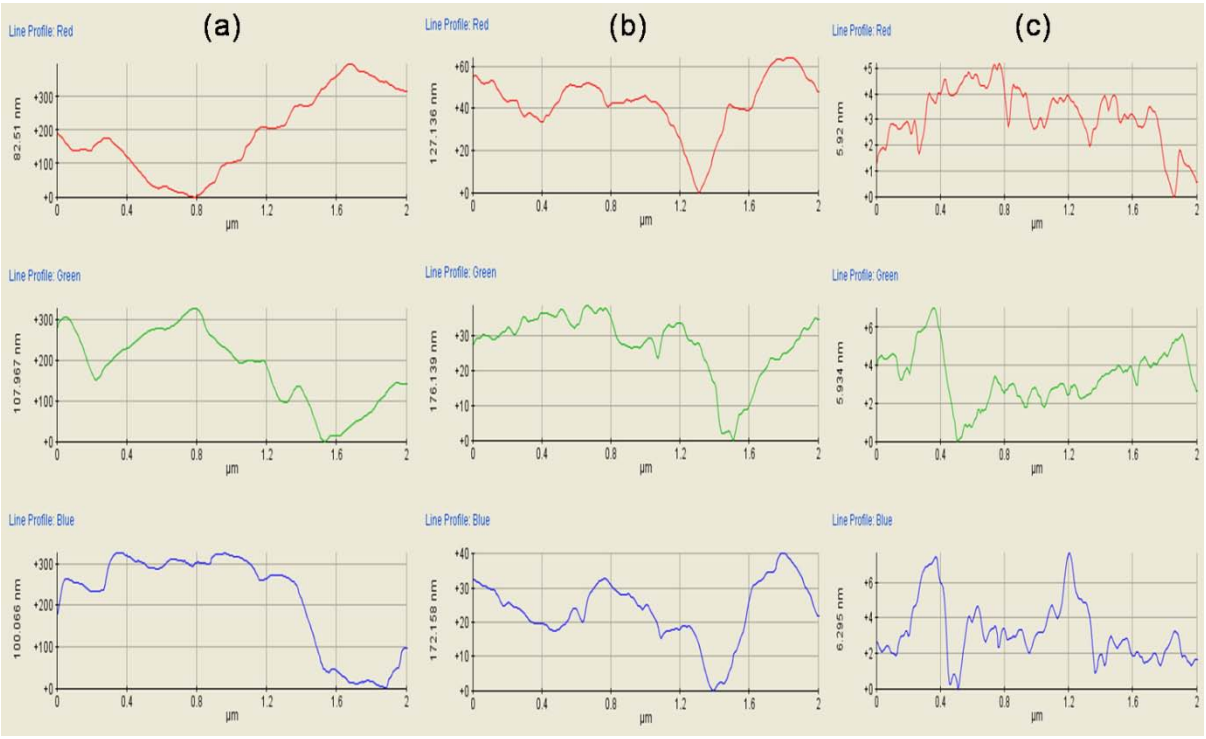

Figure 3.5. Line scale of 2 µm × 2 µm of the surface of CZT samples after different lapping and polishing processes. (a) 3 µm Al_2O_3 lapping; (b) 1 µm Al_2O_3 polishing; (c) 1 µm Diamond polishing.

It is important to note that the AFM technique can not characterize the dead layer in the subsurface which is one reason of the charge trapping of the detector, but allow the characterization of the roughness of the surface and gives information about the flatness, which are a primordial factor for the homogeneity of the devices under irradiation. Moreover, the roughness decreases when the polishing abrasive is finer, hence one can obtain a smoother surface. Particularly, mechanical polishing can remove surface defects, but also opens up

nonuniform defects on the polished surface that can have a catastrophic effect on the detector properties in terms of charge collection and leakage current [2][3].

The morphology of the surface of CZT samples after different lapping and polishing processes were analysed by SEM, as illustrated in Figure 3.6. It is clearly visible that the lapped surface has a very rough surface with high density of scratches. Nevertheless, when a mechanical polishing process with 1 μm Al_2O_3 abrasive was carried out, the sample presents a more reflective surface. For further polishing stage with 1μm Diamond slurries, the surface produces the smoothest by comparison with the other two treatments. Moreover, the density and distribution of particulates and scratches on the surface are the lowest after the Diamond polishing step which generates a more uniform surface.

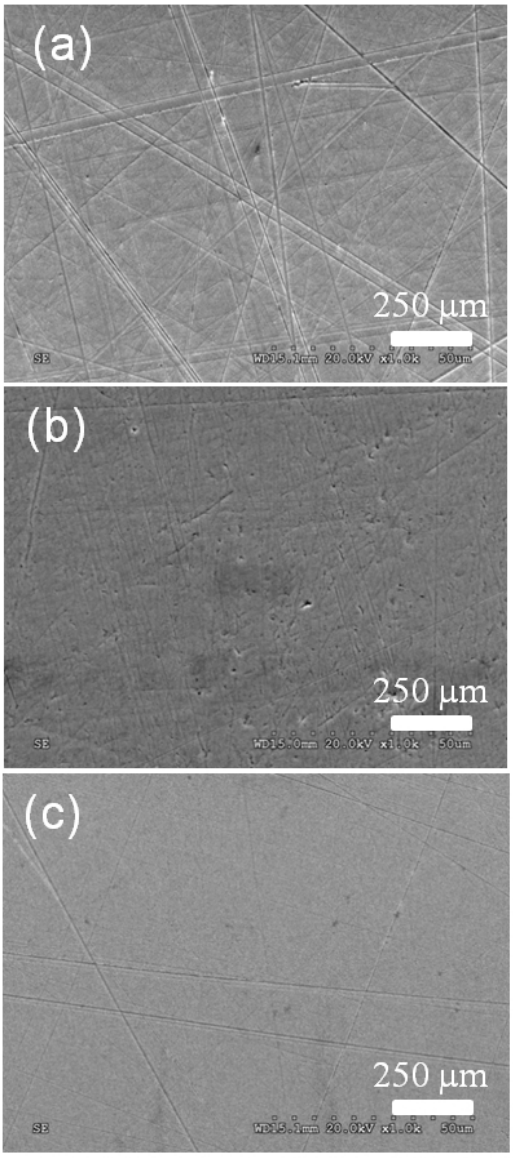

Figure 3.6. SEM surface images of CZT samples after different lapping and polishing steps: (a) 3μm Al_2O_3 lapping, (b) 1μm Al_2O_3 polishing, (c) 1μm Diamond polishing.

The surface composition and the composition of the particulates remaining on the surface, obtained by EDX are exhibited in Figure 3.7. The concentration of each element is proportional to the integral of each peak. Using this technique, the surface composition for each sample with different mechanical processes can be obtained.

As displayed in Figure 3.7, in addition of the presence of the three main elements constituting the matrix Cd, Zn, and Te, different peaks are also observed depending on the stage of surface treatments. As can be seen, after 3 μm Al_2O_3 lapping and 1 μm Al_2O_3 polishing steps, the peaks of Al and O are clearly present, which are obviously due to the residues of Al_2O_3 abrasive contaminating on the surface of the crystals. After the final Diamond polishing step, the peaks of Al_2O_3 disappeared but a new peak of Carbon can be observed, which put in evidence the total removal of the Al_2O_3 particulates and the deposition of fine particulates of diamond at the surface of the crystals.

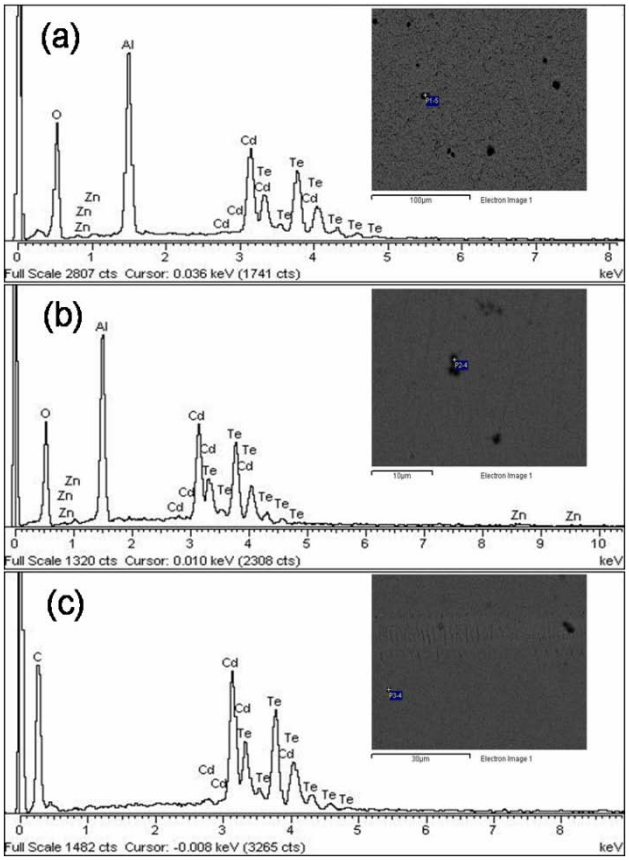

Figure 3.7. EDX analysis spectra of the surface on the sample: (a) 3 μm Al_2O_3 lapping, (b) 1 μm Al_2O_3 polishing, (c) 1 μm Diamond polishing.

Figure 3.8 displays the atomic concentration of the main elements on the surface region of CZT obtained by EDX spectra. One can observe that the atomic concentration of Al and O

decreases while the atomic concentration of Cd and Te increases from 3 μm lap to 1 μm polish stages, which can be explained by the gradual removal of the alumina residues on the surface of CZT. Meanwhile, the appearance of C and disappearance of Al at the surface clearly put in evidence after 1 μm Diamond polishing steps, which is in agreement with Figure 3.7.

Figure 3.9 presents the schematic diagram of the damage layers and defects on the bulk material which were introduced by cutting, lapping and mechanical polishing processes. In fact, the extended thickness of the damage layer can be estimated to be three times deeper than the diameter of the abrasive used, and in consequence the 1 μm polishing process is necessary after 3 μm lapping step.

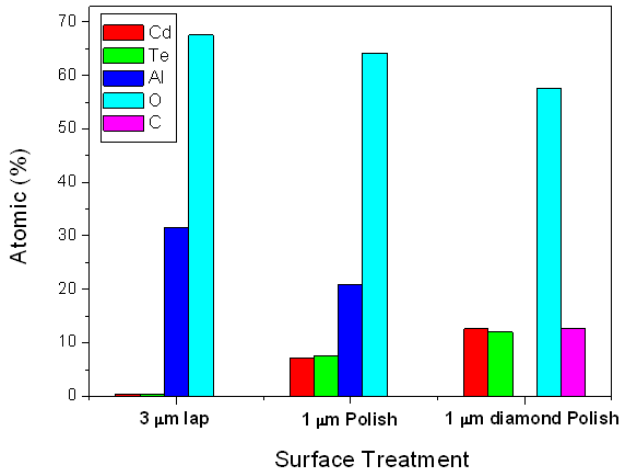

Figure 3.8. Atomic concentration on the surface of CZT samples after different lapping and polishing treatments measured by EDX spectra: 3 μm Al_2O_3 lapping, 1 μm Al_2O_3 polishing, and 1 μm Diamond polishing.

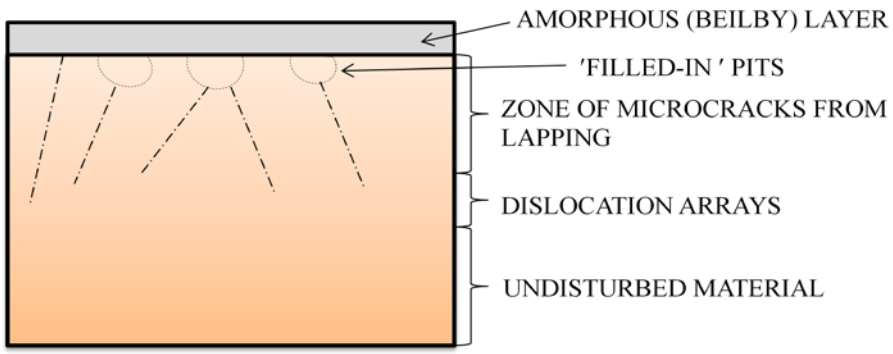

Figure 3.9. Cross-sectional view of the defects remaining after cutting, lapping and mechanical polishing processes.

In mechanical polishing, fine scratches will be introduced into the material and associated with these scratches will be dislocations and plastic deformations of the material. Although finer polishing process may reduce the visibility of these defects, considerable damage can still exist in the form of filled-in scratches, microcracks, pits and dislocations [4]. Therefore, mechanical polishing cannot serve as the final step, and a chemical etching should be done, which will be discussed in the next section.

3.1.3. Chemical Etching Process

Even though after the final polishing the sample surface look optically flat and smooth, the surfaces are already decorated with localized surface states such as impurities, grain boundaries, sub-grains and sub-surface damages induced by mechanical polishing. These defects can decrease the adhesion of the contacts and trap the electrons inside the materials, leading to the deterioration of detector properties [5-7]. Therefore, a chemical etching during detector fabrication is usually done prior to the contacts deposition for the purpose of cleaning the crystal surface.

The chemical etching process can be achieved in a three-step process. The first step involves the transport of the reactants to the surface. The second step is the surface reactions involving electron transfer process, i.e. oxidation of one or more species and simultaneous reduction of the other species, while the third step is the transport of the products from the surface to the solution, leaving a clean material surface thereby reducing the surface states and in consequence the leakage current, and also improving light reflection characteristics of the crystal surface.

The composition of the surface layer depends on the pH, chemical composition and aging of the solutions used [5]. For CdTe/CZT, chemical etching based on a mixture of bromine and alcohol is generally used. This chemical etching is a heterogeneous reaction between liquid and solid, which can be described by the equation:

$$CdTe + 3Br_2 \rightarrow CdBr_2 + TeBr_4 \qquad \text{Eq. 3-1}$$

The $CdBr_2$ compound is preferentially soluble in Br_2, and in consequence the surface is becoming non stoichiometric and richer in Te [8]. If this Te rich layer is exposed to air, depending on the exposition time, some authors observed the growth of a oxide layer at the surface which are TeO_2 and CdO compounds [5][6][9]. Specially the tellurium atoms have

tendency to bind with oxygen coming from air to create tellurates, therefore Te atoms oxidize to TeO_x and in majority to TeO_2. During this evolution, the cadmium concentration stays constant at the surface.

3.2. Improvement of the Etching Process

Chemical etching can remove the amorphous layer on the near surface which can decrease the detector properties. Etching is also used for cleaning, for revelating in which etch pits allow to distinguish the Cd or Te termination, and for surface enrichment by Cd, Te or oxides. It has been accepted that the etching step is extremely important before the electrode deposition of the detectors.

Although in last section, a brief summary of the chemical etching process has been described, a further work has been carried out in this section: the selection of the best etchant, the finding of the optimum etchant concentration, and the different surface cleaning solutions after the etching step.

3.2.1. Selection of the Best Etchant

In the fabrication process of semiconductor devices, surface contamination from impurities can deteriorate the performance of the device. For chemical etching, a standard agent used for CdTe/CZT devices is Br-Methanol, which can remove scratches and help of producing smooth and clean surfaces. However, Br-Methanol etches preferentially cadmium at the surface of CdTe/CZT, leaving a tellurium rich surface. For this reason, this section will have for purpose to determine the best Br-alcohol etchant. High purity ($\geq$ (99.8 %) chemical etchants were used, including bromine in methanol, ethanol, and propanol solutions, being the first three alcohols in the homologous series of linear alcohols.

Considering that AFM is an excellent technique to have quantitative topographic images and a clear evaluation of the surface roughness, this technique has been followed through. Figure 3.10 exhibits the AFM 3D images of CZT crystal surfaces after different etchant treatments with 2 % Bromine. It is necessary to note that the concentration of Bromine used as etchant for different groups are generally chosen within 1-5 % [1][6][10]. In this section 2 % has been selected, and a further investigation for the selection of the optimum concentration will

be presented in next section. The analyzed scanned area is 4 μm^2, which was representative of the topography of the sample.

In Figure 3.10, we can observe a much rougher surface after Br-Propanol etching, indicating that this solvent is not suitable for CZT detector fabrication. By the contrary, we can observe smoother surface obtained after Br-Methanol and Br-Ethanol etching treatment. The average surface roughness for Br-Methanol, Br-Ethanol and Br-Propanol etching are around 3.1 nm, 5.6 nm, and 13.0 nm, respectively, being Br-Methanol the surface treatment which gives the lowest roughness, while Br-Propanol surface treatment given the highest value.

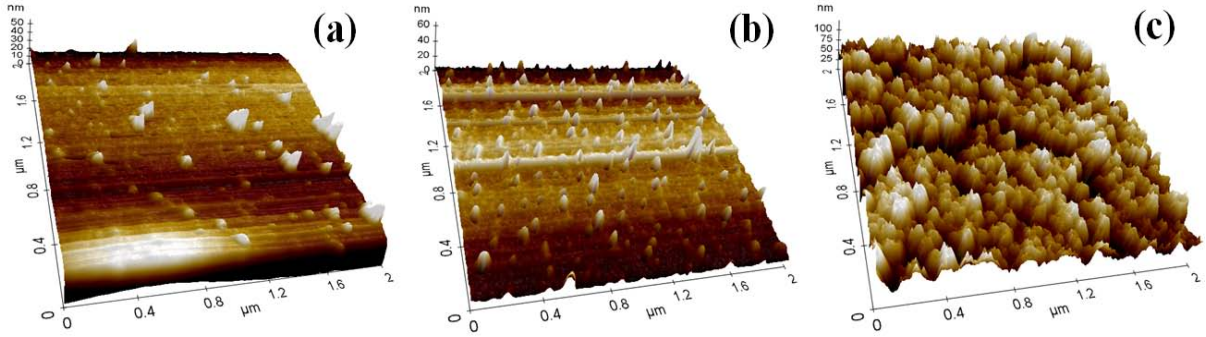

Figure 3.10. The AFM 3D images of CZT samples after three different solvents etching treatments. (a) 2% Br-Methanol, (b) 2% Br-Ethanol, (c) 2% Br-Propanol.

SEM technique has been used to provide information of the morphology and topography on the surface. Figure 3.11 illustrates the SEM image of the CZT surface after different solvents etching treatments. The left part presents the secondary electron micrographs (SE) images on the surface, while the right part exhibits the backscattering electron (BSE) images on the surface of CZT samples.

In fact, this technique provides information regarding the distribution of different elements in the sample, through the interaction between the incident electrons, the variations in the density of the material, and the angle of the collected backscattered electrons. In BSE images, larger atoms (with a greater atomic number, Z) have a higher probability of producing an elastic collision because of their greater cross-sectional area. Consequently, the number of backscattered electrons (BSE) reaching a BSE detector is proportional to the mean atomic number of the sample. Therefore, a "bright" BSE intensity correlates with greater average Z in the sample, and "dark" areas have lower average Z. Indeed, BSE images are very helpful for obtaining high-resolution compositional maps of a sample and for quickly distinguishing different phases.

In the BSE images of Figure 3.11, we observe the presence of small dark dots which are attributed to the presence of elements at low atomic number, such as Al, O, or C, whereas in SE images, these spots do not appear. By comparison of the SE and BSE images, one can see that the etchants can remove the polishing residues on the surface of the specimen with different efficiency. Particularly, a big spot with a diameter of ~150 μm can be seen by SE image after using Br-Methanol etchant, nevertheless, this big spot exhibits "dark" area with BSE images which indicates that it contains low atomic number Z elements such as Al, O, or C. Meanwhile, when Br-Ethanol is used ((b) and (e)), we can observe a large density of small "bright" dots in SE image, which disappear in the BSE image of the sample. This behaviour can be explained by the fact that these spots are due to the topography of CZT but not due to contamination.

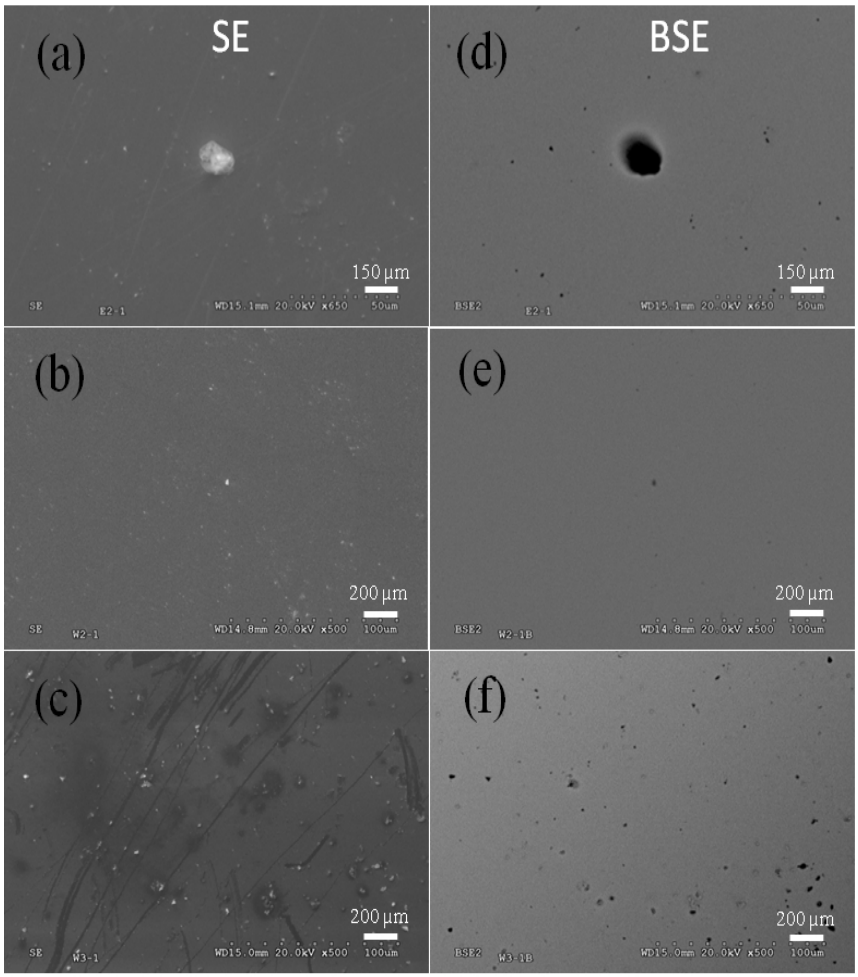

Figure 3.11. SEM figures of CZT samples in SE (left) and BSE (right) images after three different kinds of solvents etching. (a) (d) 2% Br-Methanol, (b) (e) 2% Br-Ethanol, (c) (f) 2% Br-Propanol.

Furthermore, after etching with Br-Propanol solvent we can still see a large density of small dark dots of around 20 μm in diameter (Figure 3.11 (f)), revealing that this etchant is not sufficient enough to eliminate the polishing residues. In contrary, as presented in Figure 3.11 (c), more surface damages and impurities are introduced which may act as trapping centres and deteriorate the detectors performance.

In the meantime, smoother surface with less damages and impurities on the surface are observed with the use of Br-Methanol etchant and Br-Ethanol etchant, which implies that these two solvents can be used to improve the surface after mechanical polishing steps.

In conclusion, the Br-Propanol solvent is not suitable for the chemical etching of CZT surface before contact deposition, while Br-Methanol and Br-Ethanol are more suitable as etchants. By comparison of both AFM and SEM images, Br-Methanol could be considered as the best etchant in our research.

3.2.2. The Choice of the Best Concentration for Br-Methanol Etchant

In order to optimise the chemical etching process, and to achieve smooth clean surfaces for subsequent electrode deposition, the effect of the concentration of Br-Methanol etchant has been studied. The samples were cut from the same wafer of the CZT crystal grown by VGF method, using Br-Methanol solvent as etchant with different Bromine concentration in the range of 1-5 % with the same etching time (2 min).

Figure 3.12 displays the typical AFM 3D images of the surface of CZT material after different concentrations of Br-Methanol etching, being the scanned area of 2 μm × 2 μm. As can be seen, a large density of small particulates appear on the CZT surface after 1 % Br-Methanol etching, indicating that 1 % Br-Methanol for 2 min etching is not sufficient to remove the mechanical polishing residues, supposing that longer time or higher concentration of the etchant is required.

Meanwhile, we observe that the quantity of particulates is reduced gradually when the concentration of the etchant increases from 2 % to 5 %. However, fewer but larger size of particulars presented on the surface at 4 % and 5 % of Br-Methanol etching, as shown in Figure 3.12 (d) (e), which demonstrates that too high etchant concentration with the same etching time (2 min) may etch overwhelmingly the surface of the sample, and create a small density of etch pits with larger particulates. In consequence, when the concentration is too

high, larger particulates appear on the surface which can be attributed to the creation of non dissolved $CdBr_2$ and $TeBr_4$.

The average surface roughness for different concentration of Br-Methanol etching at 1 %, 2 %, 3 %, 4 %, and 5 % are around 3.2 nm, 3.1 nm, 1.8 nm, 2.8 nm, 3.4 nm, respectively, with a minimum value for the concentration at 3 %.

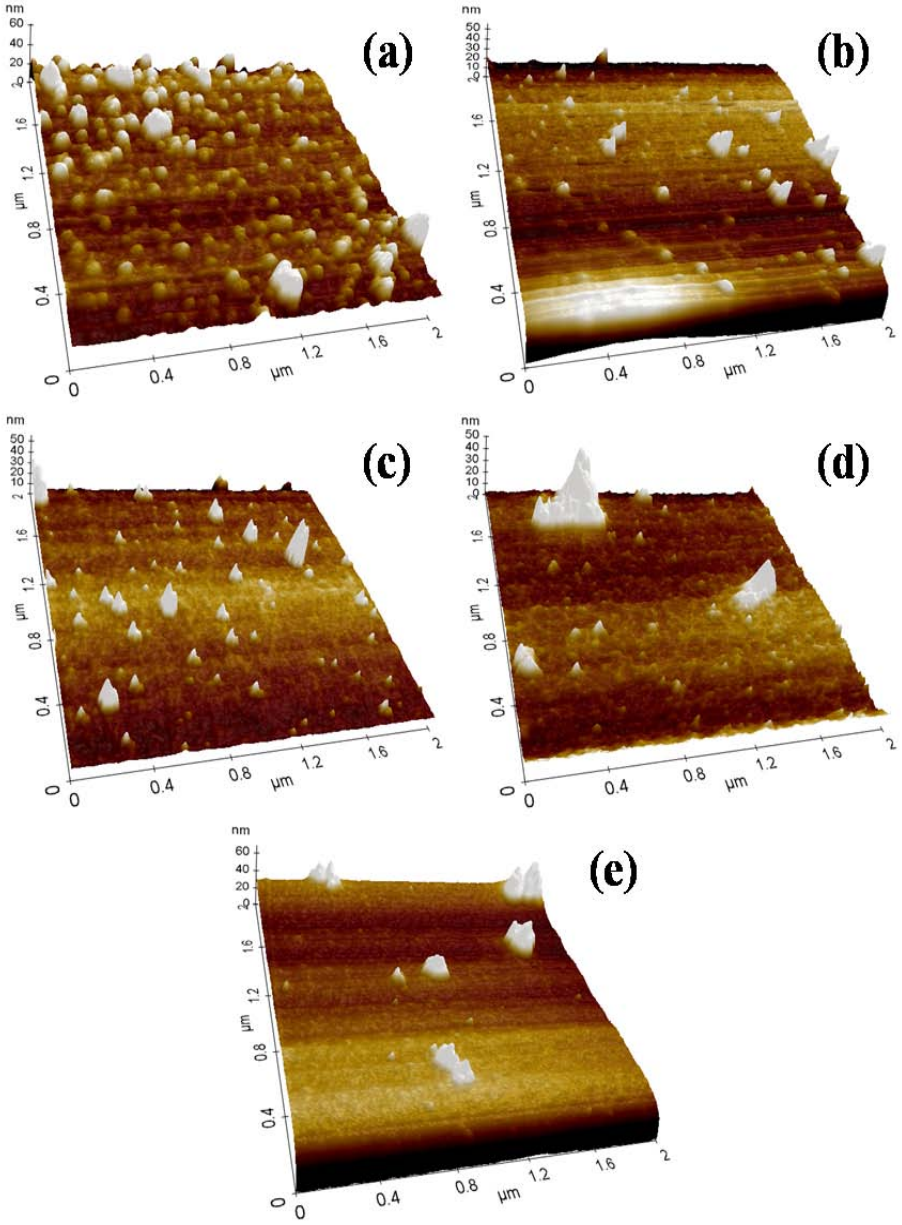

Figure 3.12. AFM figures of CZT samples after (a) 1%, (b) 2%, (c) 3%, (d) 4% and (e) 5% Br-Methanol etching.

To understand the surface structure and the uniformity with different concentration of Br-Methanol etching, the images of the non-contact probe area of AFM technique is exhibited in

Figure 3.13. At lower concentration of Br-Methanol etching, a higher density of small size particulates can be observed on the surface of the samples, whereas a lower density of larger size particulates are presented with higher etching concentration.

In summary, taking into account the images of the scanned surfaces in correspondence with the AFM 3D images, we can conclude that when the concentration of the Br-Methanol solution increases, the amount of native oxide layers are removed as well as the residual particulate matter also increases.

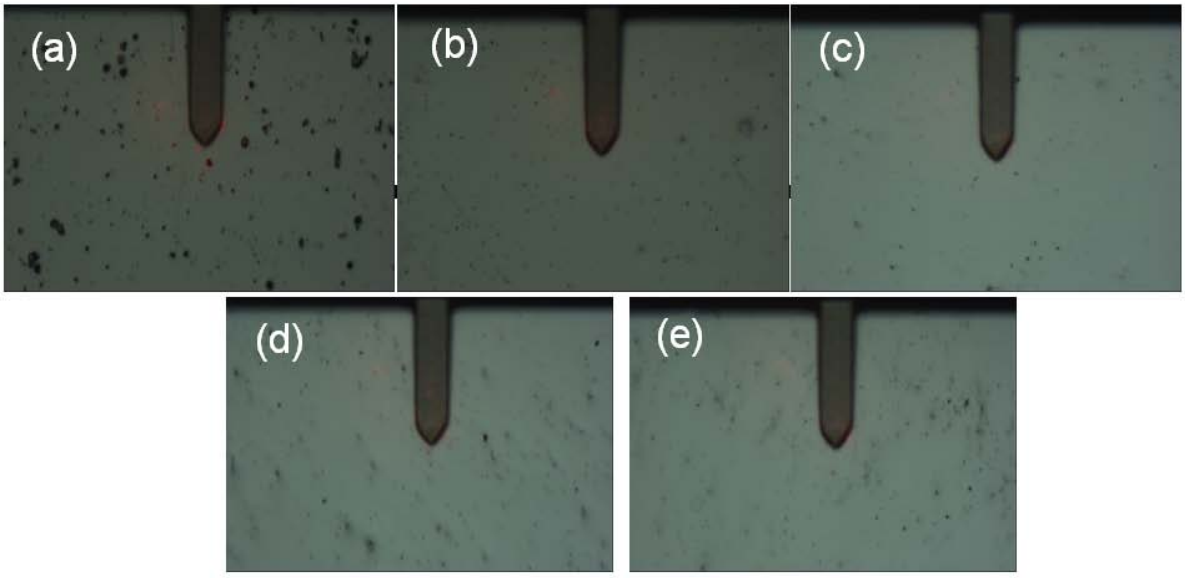

Figure 3.13. AFM probe images of CZT samples after (a) 1%, (b) 2%, (c) 3%, (d) 4% and (e) 5% Br-Methanol etching.

In order to complete the previous information on the morphology, topography, and surface composition, SEM and EDX techniques have been carried out. Figure 3.14 compares the SE and BSE images after different concentration of Br-Methanol etching. By comparing surface etched using different concentrations of Br-Methanol, the effect of etching on surface morphology can be seen.

As can be observed from the SE images presented in Figure 3.14 (a) and (b), a low concentration of etchant creates a "pitting effect" on the surface, while in the BSE images, the objects on the surface have a grayish colour, similar to the background of the image. Due to the fact that the backscattering technique is sensitive to the material quality and related with the atomic number, indicating that the material on the surface shown in SE images is indeed

also CZT (higher atomic number) and the defects may resulting from the morphology after etching treatment.

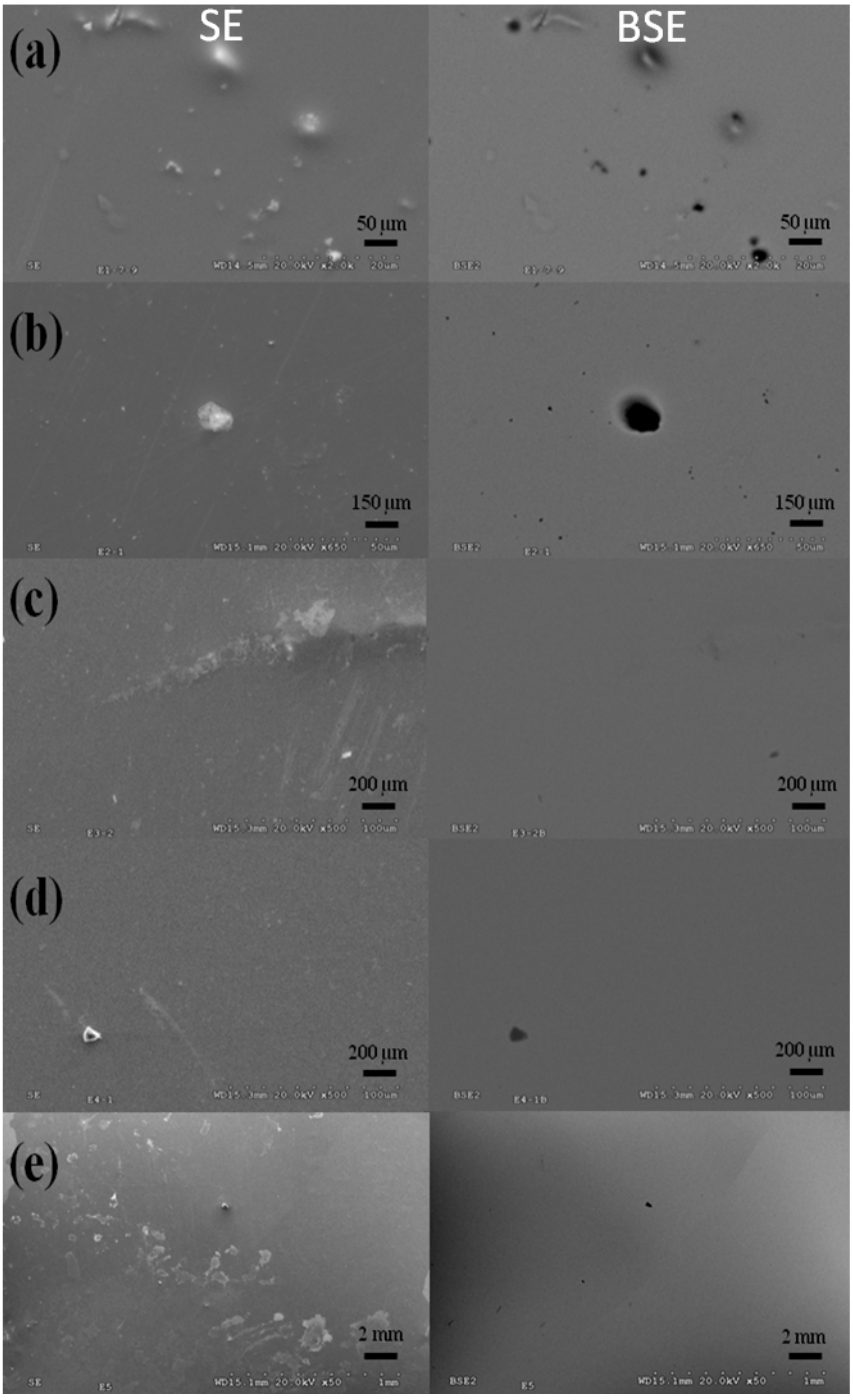

Figure 3.14. SEM surface figures of CZT samples after (a) 1%, (b) 2%, (c) 3%, (d) 4% and (e) 5% BM etching.

In BSE images we also observe two types of dark spots on the surface, small clear spots and large dark spots which appear to vanish from 1 % to 5 % Br-Methanol etching. The small spots can be explained by the presence of residues coming from mechanical polishing steps.

The larger spots are associated with the evaporation of methanol from the surface which tends to leave behind residual surface contamination. As the methanol evaporates, the surface tension of the solvent promotes the formation of small circular shaped droplets on the surface. These droplets eventually break apart into smaller and smaller droplets as the evaporation continues. Finally, it was observed that when the concentration of Br-Methanol etching solution increases, the surface waviness also increases.

Just as one example, the surface of one specimen after 2 % Br-Methanol etching has also been analysed by EDX, as exhibited in Figure 3.15. The polishing residues of C and O can be observed on the surface of the sample. It is important to note that the density of the removal of polishing residues is different with different Br-Methanol concentration, with higher concentration etchant having higher removal rate for the same operation time.

In fact, the action of Br_2 at the surface of the CdTe can be explained by the redox reactions between Bromine and Cd (or Te).

$$Br_2(l) + Cd(s) \rightarrow 2Br^- + Cd^{2+} \qquad \Delta E = +1.469\ V \qquad \text{Eq. 3-2}$$

$$2Br_2(l) + Te(s) \rightarrow 4Br^- + Te^{4+} \qquad \Delta E = +0.498\ V \qquad \text{Eq. 3-3}$$

As can be seen, according to the redox reactions, Br_2 preferentially reacts with Cd, leaving a Te rich layer.

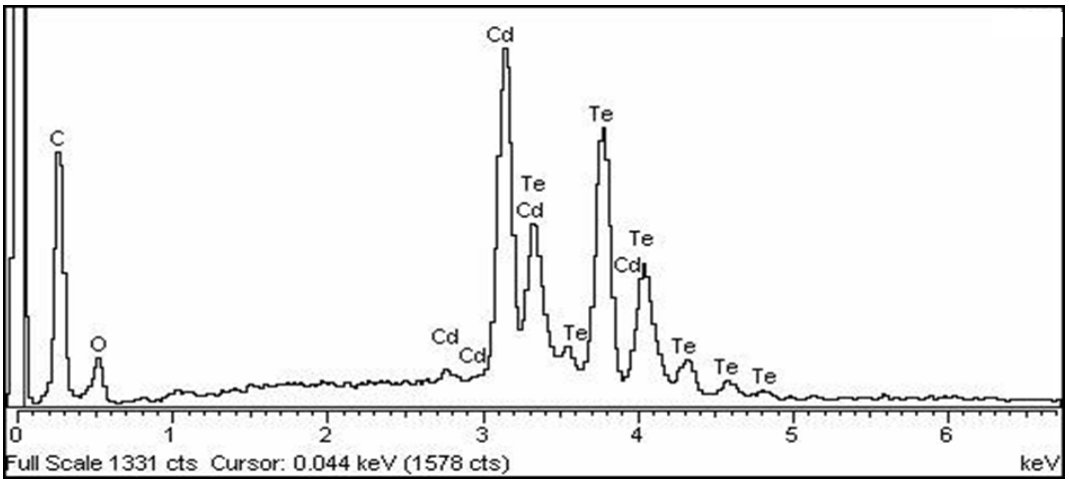

Figure 3.15. EDX spectrum of CZT sample after 2 % Br-Methanol etching treatment.

Figure 3.16 displays the relative atomic concentration of the main elements present on the surface of the samples with different concentration of Br-Methanol etching. At 1 % Br-

Methanol etching, we can observe a high atomic concentration of Al, O, and C, indicating that 1 % Br-Methanol is not sufficient enough to remove the polishing residues on the surface. When the etchant concentration increases, the atomic concentration of Al decreases while the atomic concentration of Cd and Te increases, meaning that less residues are present at the surface of the samples.

It is important to note that the polishing residues remaining on the surface are randomly distributed (can be alumina or carbon), therefore, the relative atomic concentration of Al, O, or C can be considered as the same residues for comparison. As the Br-Methanol concentration increases, the removal of polishing residues increases, the atomic concentration of Cd, Zn and Te are more clearly put in evidence but the surface becomes wavier. Therefore, it is difficult to determine the best concentration of Br-Methanol etching by this technique.

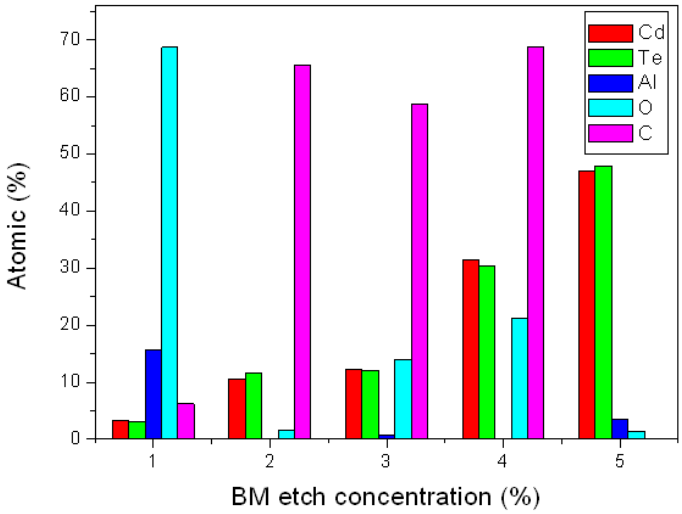

Figure 3.16. Atomic concentration on the surface of CZT samples with different concentration of Br-Methanol (BM) etching measured by EDX spectra.

In summary, by comparison of the different characterization techniques, the medium value (2 % or 3 %) is considered as the best etch concentration regarding the surface roughness and morphology. In this work, 2 % Br-Methanol etching is chosen for the step of chemical etching before electrode deposition.

3.2.3. Cleaning of the Surface

As it has been discussed in previous section 3.1.3, before electrode deposition, chemical etching is a necessary step to improve the surface quality. Moreover, the surface cleaning after etching is also an important technological step to be considered. Therefore, in this section, different surface cleaning treatments by using water, methanol, acetone, and ethanol will be studied in terms of surface roughness and morphology by using AFM and SEM techniques.

Figure 3.17 shows the AFM 3D images of different cleaning treatments after the chemical etching step. As can be seen, a high density of large size particulates remain on the surface after cleaning with water, indicating that water is not sufficient enough to remove the chemical residues. Moreover, $CdBr_2$ and $TeBr_4$ are created at the surface after the chemical etching stage (Eq. 3-1), which could react with water and create oxides on the surface.

In contrary, less density of particulates exists on the surface after cleaning with methanol, acetone, and ethanol, revealing that these solvents are suitable to eliminate the etching residues and to obtain a cleaner surface prior to the electrode deposition. The average roughness for the different cleaning treatment is approximately 21.8 nm, 4.5 nm, 5.3 nm, 5.4 nm, respectively, with a clear indicator that water is an unsuitable cleaning component.

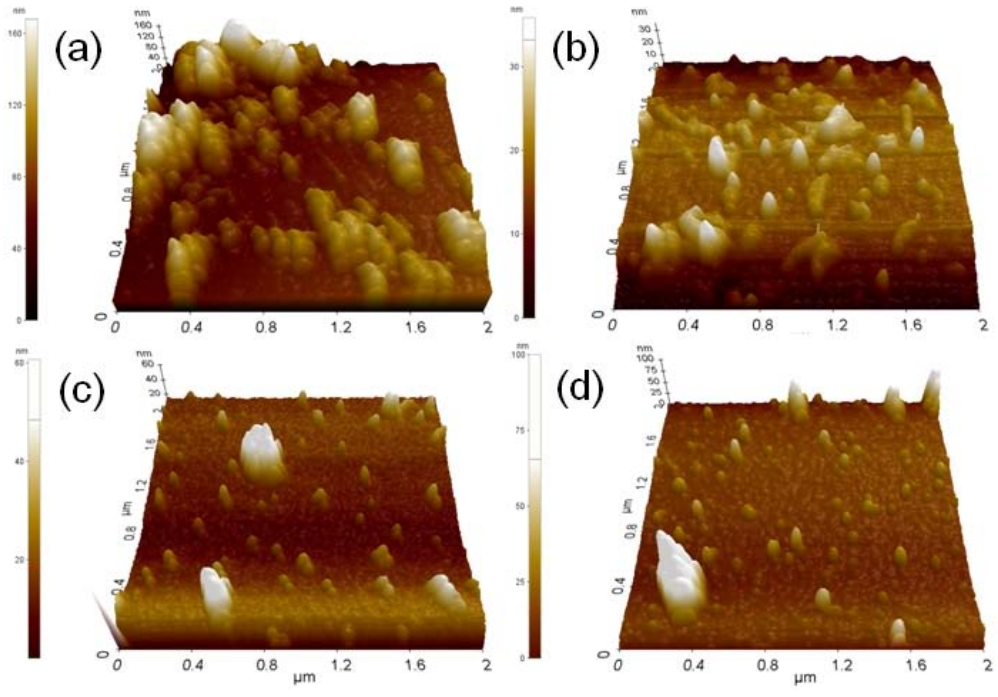

Figure 3.17. The AFM 3D images of CZT samples after different cleaning treatment. (a) with water, (b) with methanol, (c) with acetone, (d) with ethanol.

Figure 3.18 presents the SEM images of the surface after different cleaning treatments. We can observe a dirty surface after cleaning with water with a high density of chemical residues remaining on the surface. Indeed, we observe much cleaner and smoother surface with fewer residues after clean with other solvents. In the BSE images, one can see that much less "dark" spots appear on the surface after cleaning with methanol than the other cleaning processes, indicates that less residues remains on the surface by cleaning with methanol, showing the suitability of this alcohol.

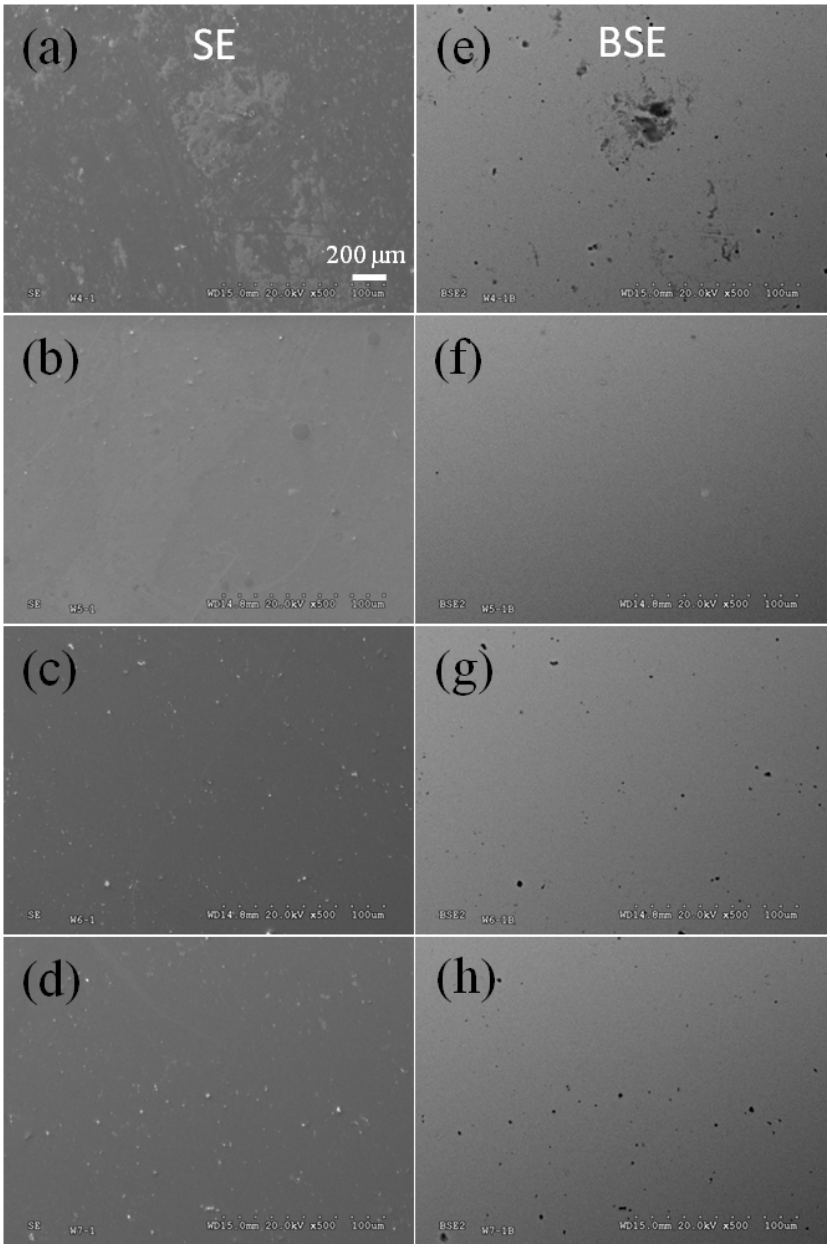

Figure 3.18. SEM surface images of CZT samples with different cleaning processes. SE images (left) and BSE images (right): (a) (e) with water, (b) (f) with methanol, (c) (g) with acetone, and (d) (h) with ethanol.

In conclusion, cleaning with water is not efficient to remove the chemical residues, while cleaning with acetone or ethanol may bring new residues on the surface of the samples. Therefore, cleaning with methanol is much more acceptable to remove the bromine methanol residues, leaving a cleaner surface on CZT material.

3.3. Characterization of the Surface Process

Surface properties can influence the electric field inside the device, and significantly affect charge transport and signal formation [2]. A rough surface enhances leakage current into medium and creates additional trapping centres, thereby adversely affecting the detector's performance [1]. Therefore, it is essential to evaluate the surface processing steps in order to identify the parameters that deliver the best surfaces for improving the quality of radiation detectors.

In this section, the surface properties of the specimen after different surface treatments are investigated. The whole process is following: 1) lapped with 3 μm Al_2O_3, 2) polished with 1 μm Al_2O_3, 3) polished using 1 μm Diamond, finally 4) chemically etched with 2 % Br-Methanol. It is necessary to note that in the next paragraphs the name of the treatments of each sample will follow with the last surface process. For example, '1 μm Diamond polish' means that this sample has been prepared by 1) lapped with 3 μm Al_2O_3, 2) polished with 1 μm Al_2O_3, and 3) polished using 1 μm Diamond.

Even though the characterization techniques discussed in the next paragraphs are generally used for the analysis of the bulk crystals, we have selected the one which could give the information of the influence of the surface process in the preparation of detectors.

3.3.1. High Resolution X-ray Diffraction Analysis

The high resolution X-ray diffraction (HRXRD) technique has been applied for having a general picture about the near-surface quality after the sample has been submitted to different surface processes, although it is known that this technique is generally used for studying the crystallinity of the bulk material. The diffraction curves were recorded on the same (111) oriented samples after different surface treatments [7].

As can be observed in Figure 3.19, HRXRD rocking curves recorded in the same CZT sample after different surface treatment steps exhibit a significant difference. It should be

mentioned that a few samples from the same wafer had been characterized for comparison, and the results were reproducible, thereby only the results of one example are shown in Figure 3.19, where the variations in the full-width-at-half-maximum (FWHM) after each processing step are clear. The most intense HRXRD peak has been obtained with the sample 2 % BM etch, which means that the sample treated with the whole process followed with 1) lapped with 3 µm Al_2O_3, 2) polished with 1 µm Al_2O_3, 3) polished using 1 µm Diamond, finally 4) and chemically etched with 2 % Br-Methanol. The measured FWHM value of the 2 % BM etch sample is 68", significantly lower than the other surface treatments.

The HRXRD results demonstrate the strong influence of the damaged layer produced by the mechanical polishing operations on the crystalline quality at the surface. Indeed, this layer can act as trapping centers for the charges and degrade the detector performance. This leads to the conclusion that chemical etching is a sufficient step to remove the damage layer created by the mechanical polishing operation.

In fact, *Yoon et al.* also investigated the effects of polishing and etching on the structural properties of high pressure Bridgman $Cd_{1-x}Zn_xTe$ crystals using HRXRD technique, and they are in agreement with our work presented here [10].

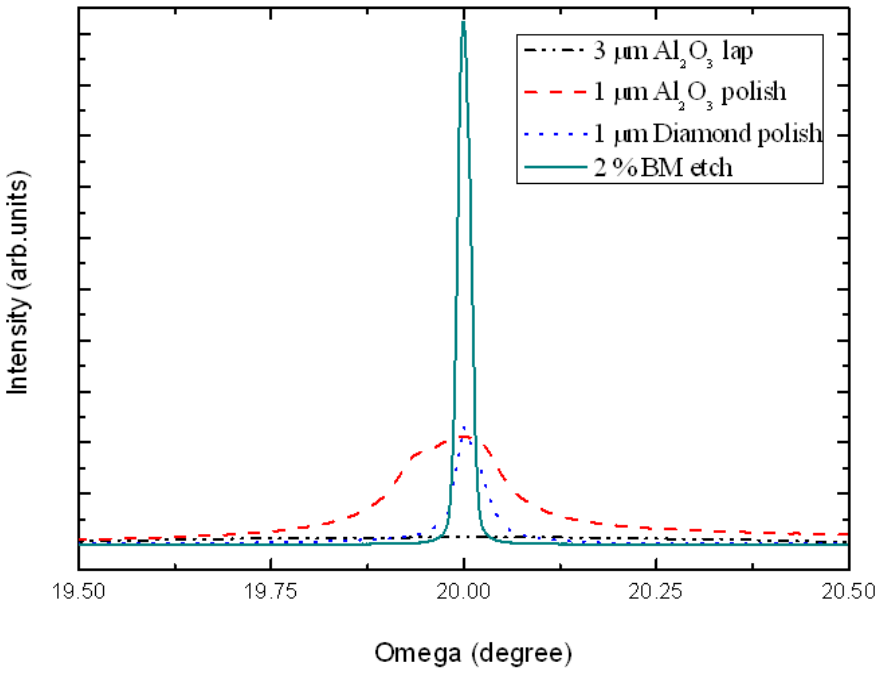

Figure 3.19. Recorded HRXRD pattern of one CZT sample with different surface treatments.

3.3.2. Fourier Transform Infrared (FTIR) spectroscopy

IR transmission measurements are widely used to evaluate the presence of free carriers, defects, and dislocations inside CZT crystals [11]. For a high quality CZT crystal, the IR transmittance is usually constant across throughout the spectra with a transmittance value near 63 % [12]. However, the defects remaining in the CZT material, such as Te precipitates/inclusions, Cd vacancies, impurities, and dislocations can decrease the IR transmission. In this way, the surface process carried out for the preparation of detector could also influence the IR transmission.

The FTIR transmission spectra of one CZT sample after different surface treatments are presented in Figure 3.20. As can be seen, in the wavenumber range from 1000 to 3500 cm^{-1}, the IR transmission was very low and decrease sharply to below 5 % in the sample which was lapped with 3 μm Al_2O_3 abrasive, indicating that a high density of defects are produced after the surface treatment. We can also observe that the IR transmission significantly increase to nearly 60 % when the mechanical polishing was done.

At the wavenumber between 3500 and 7000 cm^{-1}, the IR transmission is stable at a certain value with all the surface treatments. In fact, we can observe the IR transmission slightly higher for the sample after polished with Diamond slurry than with Al_2O_3 abrasive, which means that a fine polishing can remove more defects on the surface of CZT sample.

The IR transmission decreases slightly to round 45 % after further treated with 2 % BM etching follows polishing. It is known that chemical etching can remove the damaged layer caused by mechanical polishing but leave a Te-rich layer, which leads to the absorption of IR [13][14].

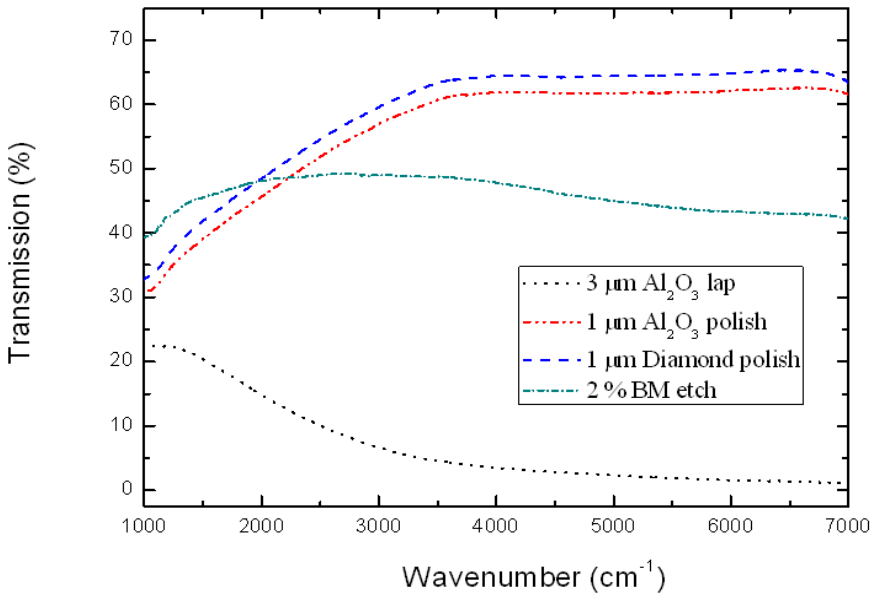

Figure 3.20. IR spectra for CZT sample after different surface treatment.

It is known that the absorption coefficient is mainly influenced by the following factors: (1) free carrier absorption, (2) precipitates absorption, (3) impurity absorption. The precipitates absorption occurs primarily in the longer range, while the impurity absorption occurs mainly at low temperature. Therefore, the free carrier absorption can be explained for the absorption behaviour in the crystals prepared in our work.

The optical transmission, T, is usually calculated by the following equation [15]:

$$T = \frac{(1-R)^2 \exp(-\alpha d)}{1-R^2 \exp(-2\alpha d)} \qquad \text{Eq. 3-4}$$

where α is the absorption coefficient, λ is the wavelength, d is the thickness of the sample, and R is the reflectivity which can be given by:

$$R = (n-1)^2 / (n+1)^2 \qquad \text{Eq. 3-5}$$

where n is the reflective index, which is 2.67 throughout the 2-20 μm range [15]. Therefore, the reflectivity R is equal to 0.21after the calculation by Eq. 3-5 [11][16].

By using Eq. 3-4 and Eq. 3-5, the absorption coefficient α with different surface treatment can be obtained, as shown in Table 3.1. With an IR transmission at 64 % for a sample fine polished with 1 μm Diamond slurry, the absorption coefficient can be calculated at 0.12. When the IR transmission decreases, the absorption coefficient increases.

Table 3.1. The absorption coefficient as a function of IR transmission at the wavenumber of 5000 cm^{-1}.

T	64 %	61 %	45 %	2 %
α	0.12	0.34	1.78	17.24

3.3.3. Photoluminescence Spectroscopy

Photoluminescence Spectroscopy (PL) at low temperature (22 K) has been carried out to investigate the deep and shallow level defects introduced during different surface preparation processes. In this case, three surface processes for the sample preparation have been studied: 3 μm Al_2O_3 lap, 1 μm Al_2O_3 polish, and 2 % Br-Methanol etch. The objective is to compare the $I_{bound\ exciton}/I_{defect}$ intensity ratio, which is supposed to be related with the surface quality of the crystal, as well as the full width at half maximum (FWHM) of the main peak (D^0, X) for the different surface treatments.

Figure 3.21 exhibits the PL spectra after the surface preparation at different stages. As can be seen, no peaks can be observed with the as-grown samples after the lapping step, which means that low surface quality is resulting from the damage during cutting and lapping processes.

However, after the polishing and etching steps, as can be observed in the same figure, in the exciton emission region (1.64 – 1.7 eV), the main neutral donor bound exciton (D^0, X) peak at 1.660 eV and neutral acceptor bound exciton (A^0, X) at 1.647 eV are clearly seen. The shallow donor–acceptor pair recombination DAP at 1.613 eV of the edge emission region (1.57 – 1.64 eV) is present, while the deep level emission region (1.42 – 1.57 eV) which is associated with the crystal imperfection and deeper impurity levels are also presented [17][18]. The band centred at 1.505 eV, named as A-center, is also visible in the samples after polishing and etching treatments, which is attributed to the formation of complexes of cadmium vacancies and In donors, such as $(V_{Cd}\text{- } In_{Cd})^-$ [19][20].

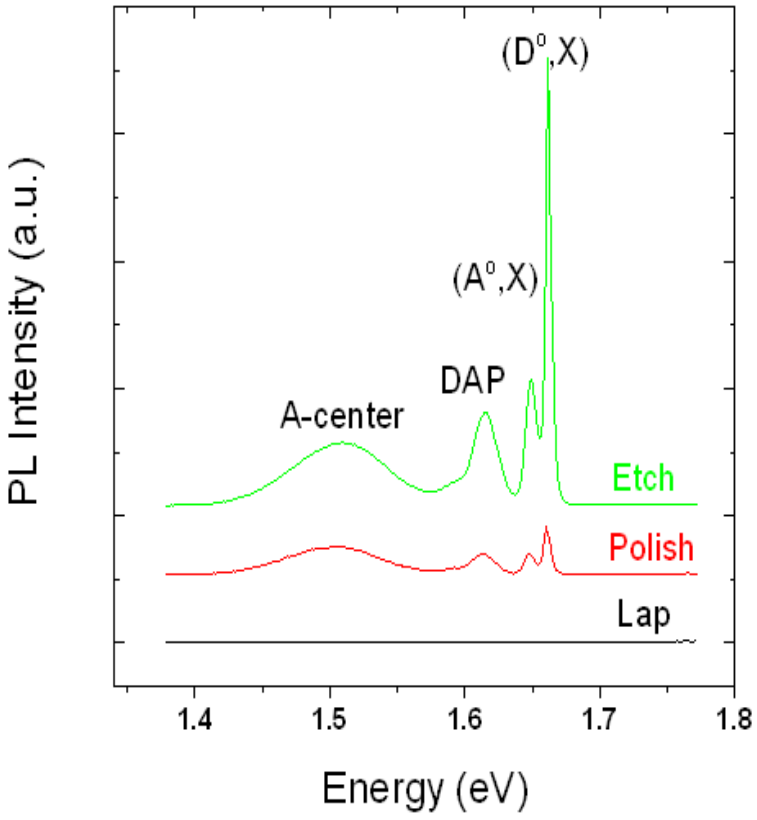

Figure 3.21. Low temperature (22 K) PL spectra of different surface treatment.

As can be observed, the intensities of (D^0, X) peak and (A^0, X) peak become larger from lapping to etching process, which indicates that the surface quality has been improved after polishing and chemical etching processes. The intensity of DAP increases after the chemical etching treatment meaning that this treatment can remove the amorphous layer and deep level defects resulting from the distortion of the lattice. It demonstrates that etching can reduce the density of the impurities and defects on the surface, which can enhance the integrity of the surface lattice.

A summary of the location of the main peaks, the FWHM of the (D^0, X) peak, and the intensity ratio between the (D^0, X) peak and the other main peaks is presented in Table 3.2. It is necessary to note that a larger intensity ratio $I_{bound\ exciton}/I_{defect}$ indicates a lower density of detrimental carrier traps [17]. From Table 3.2, we can observe that etching has higher $I_{(D^0, X)}/I_{A\text{-}center}$ intensity ratio than lapping or polishing treatments, implying that bromine is more effective in removing defects, impurities, and damages which tend to recombine with cadmium vacancies.

Table 3.2. Summary of PL spectra at 22 K on CZT after different surface treatments.

	(D^0, X) (eV)	(A^0, X) (eV)	DAP (eV)	A-center (eV)	$I_{(D^0, X)}/I_{(A^0, X)}$	$I_{(D^0, X)}/I_{DAP}$	$I_{(D^0, X)}/I_{A\text{-center}}$	FWHM (D^0, X) (meV)	Ra (nm)
Lap	1.666	1.647	1.617	1.506	1.18	0.93	1.08	N/A	~90
Polish	1.660	1.647	1.614	1.507	2.30	2.23	1.69	5.9	~7
Etch	1.661	1.649	1.614	1.509	3.50	4.71	6.95	4.6	~3

Furthermore, the Full Width at Half Maximum (FWHM) value of (D^0, X) peak is narrower after chemical etching than before etching (Polishing only), in addition, higher $I_{(D^0, X)}/I_{DAP}$ is also obtained after the etching process. From these results one can conclude that chemical etching can reduce a large density of defects and damages introduced by lapping and polishing steps, and improve the crystalline quality at near-surface region, which is in agreement with the previous investigation carried out by *Chen et al.* [17].

In the same table, the results of the surface roughness obtained in section 3.1.2 have been introduced, showing that the surface roughness of the sample prepared with 3 μ aluminium oxide lapping is very high (~ 90 nm). It means that a large density of defects and impurities exists at the near-surface region of the CZT crystal that may conceal the signal of Photoluminescence, which may explain why the intensity of all the emission regions is too low to be identified.

3.3.4. Current-Voltage Characteristics

The current-voltage (I-V) characteristics have been investigated with the samples after different surface treatment in order to reveal how the surface treatment influences the leakage current. The samples were prepared with three steps described previous: 3 μm Al_2O_3 lap, 1 μm Al_2O_3 polish, and 2 % Br-Methanol etch. After the surface preparation, Au contacts were deposited by electroless deposition method. It is important to note that due to the crystal is n-type, after the deposition of Au as contacts on both sides of the CZT samples, blocking contacts are formed on CZT material due to the barrier height between the contact and CZT.

In Figure 3.22, the comparison of the leakage current with different surface preparation processes only at the forward bias (0 V ~ +170 V) is presented due to the symmetrical

behaviour of the I-V characteristics at forward and reverse bias. As can be seen, the leakage current increases gradually with the polishing and etching processes, and a sharp increase occur with the sample after the lapping step.

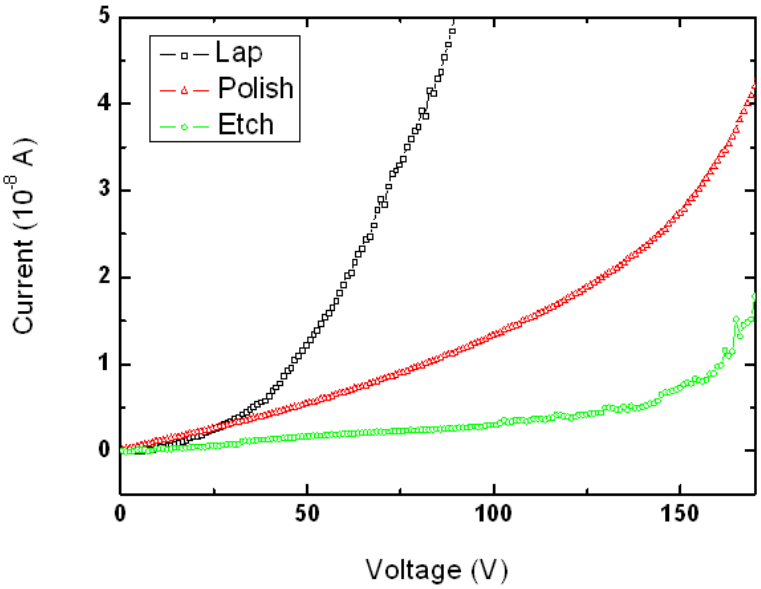

Figure 3.22. I-V characteristics of the CZT sample with different surface treatments.

Different surface roughness can determine the quantity of oxide formed, where rougher surface will enlarge the surface areas for the formation of oxides than the smoother surfaces. However, interface traps and oxide charges occur when the metal contact is deposited on CZT material. The current-voltage curves of the lapping and polishing processes show that the leakage current increases when the surface roughness increases, indicating that improve the surface quality can decrease the trapping centres, which are responsible of the fast increase of the current when the voltage increases.

Hossain et al. obtained a gradually rise of the leakage current when the surface roughness increases, they mentioned that when the roughness of the surface increase, fewer carriers may exchange into the signal, leading to an increase of leakage current and the degradation of the detector quality [2].

Cui et al. remarked that both mechanical polishing and chemical etching can affect the surface leakage current [1]. The centres resulting from mechanical polishing can enhance the trapping sites and influence the surface leakage current by supplying more conductive pathways and altered the distributions of the electric field.

Some other authors mentioned that the Br-Methanol etching can remove the surface layer introduced by cutting and mechanical polishing to obtain a clean surface before electrode deposition, which will in return produce Te enriched surface. The Te enriched surface is favourable for Schottky contact with low barrier height, but also lead to greater surface leakage [5].

While the leakage current of the surface after chemical etching is significantly reduced, which could be explained by the improvement of the crystalline quality of the surface, as discussed by the HRXRD and PL studies, shown in Figure 3.19 and Figure 3.21.

3.3.5. Gamma-ray Response

To understand the influence of surface treatment and roughness on the detector performance, a comparative investigation using 1 μ Ci radioactive ^{133}Ba gamma source were carried out by using detector of 5×5×3 mm^3 havested from n-type crystal.

Figure 3.23 exhibits the gamma response of the sample with different surface treatment at the same applied voltage of 100 V. This voltage has been selected for giving low noise detectors. It is necessary to mention that, the noise increases severely as the applied voltage increases due to the quality of the surface of the material.

In this figure, we can observe the 31 keV photopeak with high noise which decreases when the surface roughness decreases and the surface quality increases. The peak/valley ratio (P/V) can be calculated by the counts of 31 keV peak (e.g. 631) divide by the counts of the valley before this peak (e.g. 390). Therefore, the P/V ratio of the 31 keV photopeak after etching is 1.62, which is higher than after lapping (1.22) and polishing treatments (1.42).

This is in agreement with *Hossain et al.*, lapping process has a much higher surface roughness than the other treatments, which may exchange fewer carriers into the signal leading to the degradation of the detector quality [2]. In consequence, we could conclude that the quality of the sample surface is significantly influence the detector performance.

As previously discussed, when the surface quality impoved, the leakage current decreases, and therefore the performance of the detector improves.

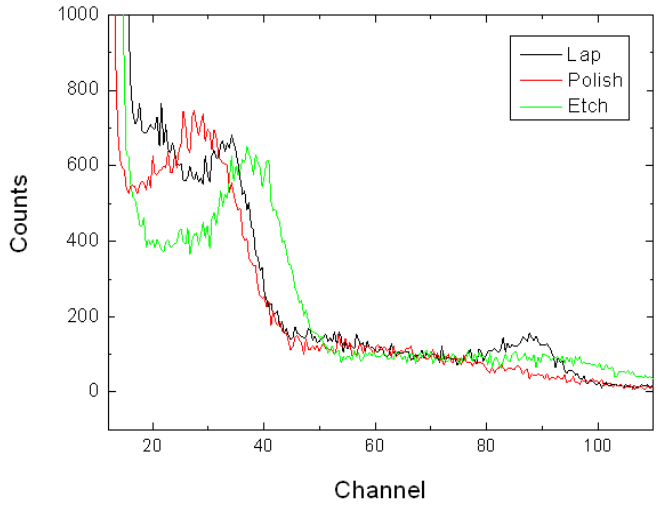

Figure 3.23. ^{133}Ba gamma response of the CZT sample with different surface treatments.

3.4. Methods of Contact Deposition

In this section, different methods for contacts deposition used in our work will be described. The ability to form suitable contacts is critical to the fabrication of high quality CdTe/CZT devices. Contacts can determine to a large degree the performance of the detectors. Even though the detector is fabricated from high quality material, nonoptimized contacts will result in an inferior performance. Therefore, a proper contact design, as well as the choice of the electrical contact material, deposition methods, interface control, surface treatment, and passivation is critical in the fabrication of CdTe/CZT nuclear detectors [21-23].

In fact, the type of contacts, the type of the bulk material and electrical properties (doping, trapping centres), the deposition methods for the contact layer, as well the surface state determine the barrier height between the contact and the bulk material, whether is Ohmic or Schottky contact [29]. Generally, the contact must be chemically and mechanically stable to allow bonding and prolonged operation and should not create charge trapping or recombination in the near-surface region. For this reason, the surface leakage current should also be minimized to reduce the noise in the detector [21][24][25]. The comparison of these three deposition methods will be further discussed in chapter 4.

3.4.1. Sputtering Deposition

Sputtering is a Physical Vapour Deposition (PVD) method which removes the material from the target by energy transfer in collisions in energetic atomic projectiles. Sputtering deposition offers a better control of the process such as film thickness and film properties (grain size and step coverage, etc) than evaporation.

A schematic diagram of a typical sputtering system is shown in Figure 3.24. The wafer is placed at the bottom of the vacuum chamber, while target material (Au in our work) is set at the top of the chamber. The inert gas plasma (such as argon) is incorporated into the chamber, causing, and the gas is ionized. The ions are accelerated towards the surface of the target, resulting in the atoms of the source material to break off from the target in vapour form and condense on all surfaces of the chamber including the substrate [26]. Sputtered atoms ejected from the target have a wide energy distribution, typically up to tens of eV. The sputtered ions can fly from the target in straight lines and impact energetically on the substrates or vacuum chamber, causing resputtering.

The deposition of gold by sputtering method was carried out by using a sputtering Quorum Q150TS, which is a high resolution sputter coater, suitable for oxidising and non-oxidising metals. Figure 3.25 displays photographies of the sputtering machine and the deposition chamber used in our work. The vacuum chamber pressure is generally set to 10^{-5} mbar. The density of Au deposition was 19.32 g / cm^3 for a coating current of 20 mA, being the coating rate of 9 nm / min.

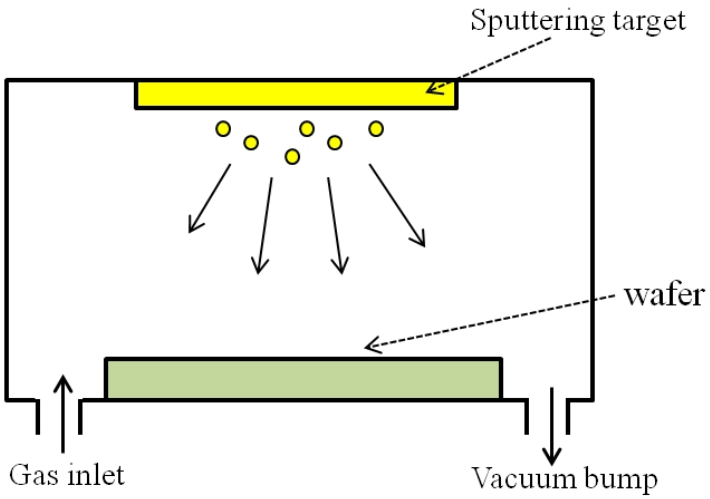

Figure 3.24. The principle of sputtering.

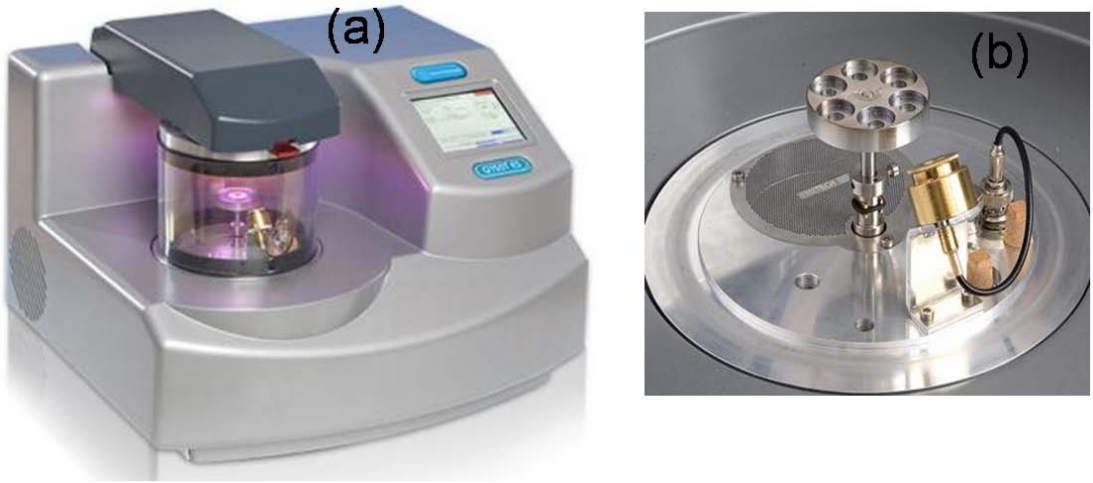

Figure 3.25. Quorum Q150TS sputtering machine (a), sputtering deposition chamber (b).

3.4.2. Evaporation Deposition

Evaporation deposition is also a PVD common method of thin film deposition. In this process, the substrate, which needs to be deposited, is placed inside a chamber. When the chamber is under vacuum, a source material is then heated to the point where it starts to boil and

evaporate. The vacuum is required to allow the vapour particles to travel freely in the chamber, and subsequently condense on the surface of the substrate.

Generally, if the substrate has a rough surface, the evaporated materials deposit mostly from a single direction leading to a nonuniform layer. This behaviour is observed in our case where the roughness after deposition is closed to the value obtained after the chemical etching done on the material.

Figure 3.26 presents the evaporation equipment used in our work (Edward 306). The deposition of thermally evaporated Au electrodes has been carried out by a joule effect evaporator with an initial pressure below 10^{-6} Torr. Gold is heated to melt by passing the electrical current through a filament shaped basket. The material in the form of vapor is condensed on the substrate. With a deposition time of 1 min, an optically thin Au layer of around 10 nm thick can be obtained.

Figure 3.26. High vacuum coating system: Edward 306 evaporator.

3.4.3. Electroless Deposition

Contacts deposited by the electroless method are frequently used for CdTe/CZT materials to create a stronger chemical bond between metal and semiconductor compared to the physical deposition methods like sputtering and evaporation, and at the same time to minimize the formation of oxides at the metal/semiconductor interface. It is also the easiest method to deposit fast and reproducible contacts [27]. In the electroless plating process, the deposition happens spontaneously on the surface which forms a sufficiently high electrochemical potential with the solution. This process is desirable because it does not require any use of external electrical power during processing [28].

The electroless deposition is a chemical reduction process which depends upon the reduction process of ions in an aqueous solution containing a chemical reducing agent and the subsequent deposition of the corresponding metal, which means that practically Au ions take the place of Cd, Zn, or Te, presented on the substrate of the CdTe/CZT crystal, and then transfer them into the solutions. The morphology of the surface of coatings depends of the nucleation and growth of Au spheroids at the CdTe/CZT sample, which will be the object of a further study in chapter 4.

The electroless solutions used in our work were prepared with 1 g of metal chloride salts of Au, Pt, Ru, Pd and Rh respectively, dissolved in 25 mL of de-ionized water. It should be noticed that the pH of the solutions were nearly 1-2, so the depositions were done in acidic environment without the necessity to adjust the pH. It is also important to comment that the deposition time with different deposition processes depends on the metals used.

Figure 3.27 presents the same sample after polishing and after Au deposition processes. We can observe a smooth Au contacts deposited on CdTe/CZT sample after the fine polishing step. We can comment that it is extremely important to require a fine polish surface prior to the deposition to minimize the roughness and damage layers, in order to achieve better performance detectors. For the detectors prepared in our work, the surface was always treated with lapping and polishing processes until 1 μm Diamond, then etch with 2 % Br-Methanol immediately followed by the contact deposition .

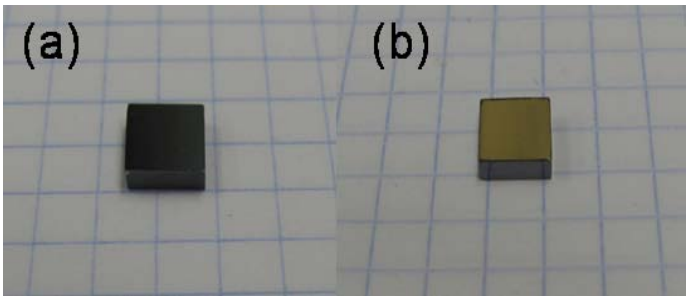

Figure 3.27. The CdTe/CZT sample after fine polishing step (a) and with Au contact (b).

3.5. Importance of the Lateral Edges Treatment

The surface treatment to the lateral sides is exceedingly important, improper treatment may influence the overall leakage current and deteriorate the device performance. There are several challenges to produce detector grade materials based on CdTe/CZT, one of which includes the mechanical engineering processes, such as ingot slicing, wafer lapping, mechanical polishing, and chemical etching have been discussed in the previous section.

In fact, in the CdTe/CZT device the total leakage current includes surface leakage current and bulk leakage current. The bulk current and surface leakage current are the two parameters which contribute to the total leakage current of the semiconductor device. It is important to mention that bulk leakage current depends strongly on the material resistivity, while the morphology and stoichiometry at the surface of the device also affects the surface leakage current [29].

Nemirovsky reported that the total leakage current for unpassivated CdTe/CZT detectors is dominated by surface leakage current rather than the leakage current of the bulk material [30]. This indicates that the surface passivation can potentially improve the detector performance. Indeed, the lateral edges of the device can act as a 'short circuit' under the correct circumstances [31]. For this reason, it is essential to study the treatment of the lateral edges of the detector, in order to optimum the practical methods to improve the detector performance.

3.5.1. Mechanical Polishing Edge Treatment

Lateral edges treated by mechanical polishing process have been investigated for the fabrication of CdTe/CZT detectors. After the planar detectors have been fabricated with Au contact, the edges of the detectors have been lapped with 3 μm Al_2O_3 abrasive, followed by polishing with 1 μm Al_2O_3 abrasive, and finally fine polished with 1 μm Diamond slurry.

The Current-Voltage characteristics have been carried out after each step with the applied bias from –200 V to +200 V. The I-V curves of the lateral edges of the CZT detectors after different lapping or polishing treatments are exhibited in Figure 3.28. As can be seen, the Schottky contact behaviours are visible in all the voltage ranges for three different treatments. It should be noted that the CZT material grown in our laboratory are mainly n-type due to

indium doping. Both sides of the samples are deposited with Au contacts, therefore blocking contacts may form on the surface of the detectors.

As can be observed in this figure, the leakage current of the detector decreases when the lateral edges were polished compared with the sample proceeded only with the lapping process, being the leakage current higher compare to the sample after the polishing treatment. This behaviour can be associated with the surface roughness of the lateral edges of the detectors. We suppose this phenomenon could be related with the surface damage layer produced by the lapping process which can create dislocations and effectively reduce the electrical resistivity of the surface layer [32]. As previously discussed in Figure 3.4 and Figure 3.6 (see section 3.1), the lapping treatment may bring more surface damages and much rougher surface compared with the polished one.

In the same way, some authors mentioned that rougher surface of the lateral edges may bring more defects and trapping centres to the detectors, which can increase the leakage current and deteriorate the detectors [2][3]. In consequence, the roughness of the surface also plays an important role on the edge quality of the detectors.

In the same figure, one can observe that the leakage current in the positive side is slightly higher after treat with diamond polish than only after 1 μm Al_2O_3 polish, but similar in the negative side. As previous discussed in section 3.1.2, fine polishing is an important step to improve the surface quality for better detector performance, however, it is not a necessary step for the lateral edges of the detectors. In fact, after polishing the edges with 1 μm Al_2O_3 abrasive, a considerable smoother surface can be obtained, a subsequent step by diamond polishing can introduce excess unexpected pressure to slightly damage the edges which can degrade the detectors performance.

We can conclude that the treatment of the lateral edges of the planar detectors with polishing step can help to reduce the leakage current and improve the detector performance. Although 1 μm Diamond polishing of the lateral edges can improve the surface morphology and reduce the surface roughness, it does not shows lower leakage current than after polished with alumina abrasive. Therefore, for mechanical polishing treatment of the lateral edges of the detectors, the necessary steps should be 3 μm Al_2O_3 lap and 1 μm Al_2O_3 polish.

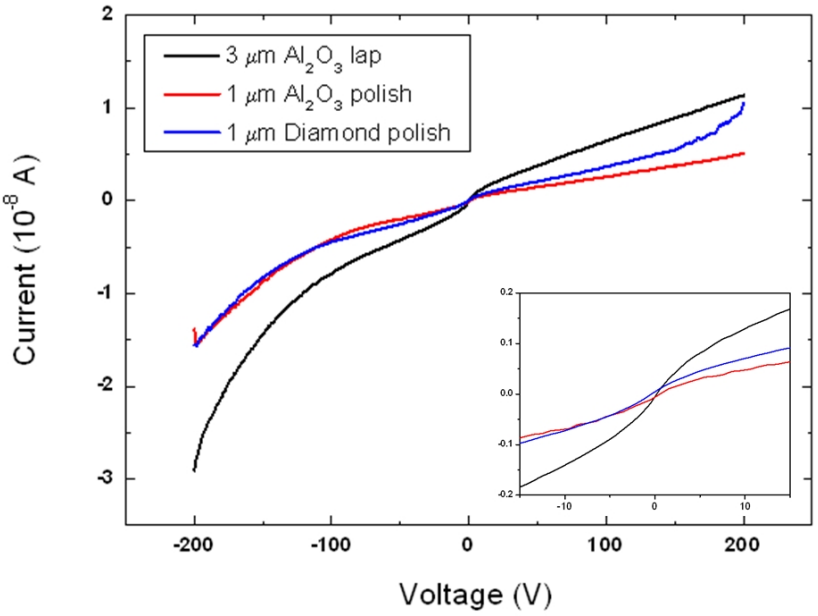

Figure 3.28. I-V curves of the lateral edges of the CZT detectors after different lapping or polishing treatment.

3.5.2. Passivation Edge Treatment

Passivation of the lateral edges plays an important role in reducing the leakage current and attendant noise, hence enhancing the spectral energy resolution particularly for X-ray and gamma-ray detectors [33-35].

It has been reported that bromine methanol etch leaves the CdTe/CZT surface depleted in cadmium and rich in tellurium [8]. This residual Te film on the surface is highly conductive compared to the high resistivity bulk CdTe/CZT and thus increase the leakage current. Passivation is generally carried out to eliminate this conductive Te layer via the creation of an insulator. Most of the passivation treatments convert the electrically conductive tellurium film into a higher resistive layer of $CdTeO_3$, which was served as probable stable phase formed during the oxidation of CdTe/CZT surfaces [36-38]. However, this process must be carefully controlled on the lateral edges of the detectors to avoid any damage to the contacts itself [39].

Generally, surface passivation can be carried out by using both wet and dry methods. Passivation using dry methods is done by oxidizing the Te-rich surface via oxygen plasma or

by depositing sputtered AlN or SiN_x, followed by etching using an argon ion beam [40]. Wet methods are more popular, which are commonly carried out by creating a passivating layer on CdTe/CZT to reduce the leakage current. Several etchants such as NH_4F/H_2O_2, KOH, H_2O_2 after KOH, KOH/H_2O_2, $(NH_4)_2S$ are widely used [41-45].

Passivation process is a total oxidation, implying that it can create oxide layer immediately after etching. After passivation in NH_4F or H_2O_2 solution, Te-rich surface can be fully oxidized to TeO_2. The preferential dissolution of Cd reduces the surface leakage current and prohibits the uncontrolled formation of native oxides [41][42]. NH_4F/H_2O_2 is an effective etchant which reports the most stoichiometric surface and the lowest leakage current [43]. Passivation using $(NH_4)_2S$ for 3 min can leave a CdS layer on the surface, which can prevent the formation of Te oxides and form a high resistivity CdS or $CdTeO_3$ layer, reducing the leakage current and the polarization effect [8][44][45].

Wright et al. demonstrated that the leakage current at the applied bias of 100 V after the passivation in NH_4F/H_2O_2 solution decreased to 142 nA from 3.2×10^4 nA of initial leakage current after chemical etching [42]. *Chattopadhyay et al.* found that the KOH passivant can produce a more stoichiometric and smoother CdZnTe surface [37]. *Chen et al.* reported that the leakage current was reduced to around 37 % by using the 15 % H_2O_2 for 5 min on $Cd_{0.9}Zn_{0.1}Te$ surface after Br-Methanol etching [35]. They also proved by XPS technique that most of Te on the surface was oxidized to TeO_2.

The passivation process in our investigation was carried out by using a 2% Br-Methanol etchant for 2 min, followed by an aqueous solution of 30% H_2O_2 for 2 min. Figure 3.29 exhibits the PL spectra before and after passivation steps, and Table 3.3 summarizes the PL results of the passivation process. In this figure can be observed that, the main neutral donor bound exciton (D^0, X) peak is located at 1.661 eV and neutral acceptor bound exciton (A^0, X) at 1.649 eV. The emission peak at 1.615 eV is the shallow donor–acceptor pair DAP, and its longitudinal optical photon replica at the shoulder of the lower energy side of the DAP peak. The A-center band is located at 1.509 eV, which is associated with a complex defect involving a Cd vacancy and a donor impurity.

After passivation process, we can observe that the intensity of all centers is significantly lower than before passivation, the reason may due to the fast formation of thick oxide on the surface, revealing that the passivation treatment can attenuate the intensity of the signal coming from A-centers. The FWHM value of (D^0, X) becomes slightly larger after

passivation treatment, indicating that the density of defects and impurities in the surface and near-surface region increases after passivation treatment. These behaviours allow us to conclude that the passivation process can introduce more defects into the crystal, and it will be necessary to modify the passivation process in the future work.

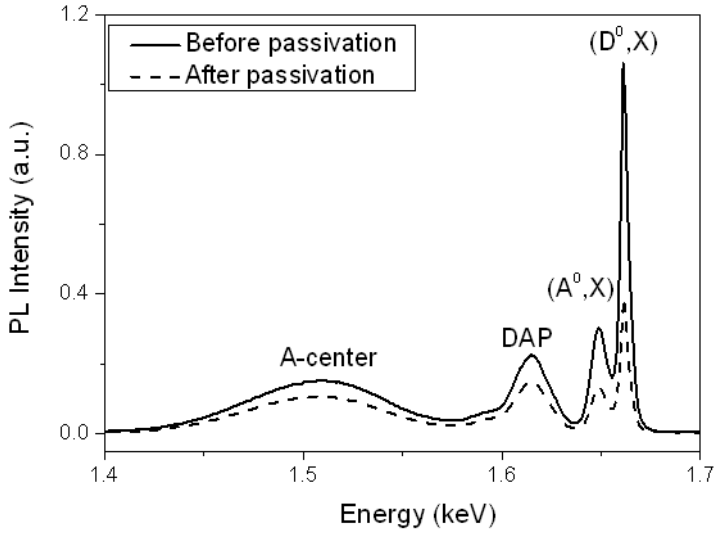

Figure 3.29. PL spectra of the sample before and after passivation.

Table 3.3. PL results of the CZT sample before and after passivation.

	$I_{(D^0,X)}/I_{(A^0,X)}$	$I_{(D^0,X)}/I_{DAP}$	$I_{(D^0,X)}/I_{A\text{-center}}$	FWHM (D^0, X) (meV)
Before passivation	3.50	4.71	6.95	4.6
After passivation	2.94	2.64	3.67	4.7

In order to identify the surface composition of the samples before and after passivation treatment which will give us the information for improving the passivation process, X-ray Photoelectron Spectroscopy (XPS) analysis has been carried out in our group [46].

Figure 3.30 presents the Te3d peaks of the surface of CZT after different passivation treatments. As can be seen, the sample with only etching treatment before passivation has two sharp peaks with the binding energy of 572.8 eV for $Te^0 3d_{5/2}$ and 583.2 eV for $Te^0 3d_{5/2}$. After the passivation treatment, two sharp $Te^{4+}3d$ peaks appear and become sharper, whereas two

$Te^0$3d peaks become weaker or even disappear, revealing that TeO_2 layer is successfully formed on the surface of CZT, which is in consistent with *Wang et al.* [41].

According to the XPS results, taking into account the calculation of the surface composition (Te, Cd, and Zn elements) and the peak area of each chemical state (Te^{+4}/Te^0), the quantitative analysis of the studied samples are exhibited in Table 3.4 [45]. In order to understand these results, the estimated equation for the thickness (*d*) of tellurium oxide layer on CZT can be expressed by [46]:

$$d = -\lambda \ln\left[1-(Te^{4+}d_{5/2} + Te^{0}d_{5/2})\right] \quad \text{Eq. 3-6}$$

where λ is the non-elastic mean free path, which in our XPS experiment has a value of 14 Å according to *Tanuma et al.* [47]. $Te^{4+}3d_{5/2}/Te^0 3d_{5/2}$ is the ratio of Te atom obtained from XPS spectra. The thickness of the tellurium oxide layer with different passivation treatment is calculated individually and summarized in Table 3.4.

As one can observe, the [Te]/([Cd]+[Zn]) ratio is tending to 1 for the sample passivated immediately after etching process (1.10), indicates that the surface region is closer to the ideal stoichiometry. It is evident that sample surface passivated immediately after etching step has higher Te^{4+}/Te^0 value (0.98) than passivated with the etched sample holding in air after 24 h (0.93), which means that the telluride oxide layer is thicker for the sample passivated immediately after the etching step. In addition, we can observe a high quantity of carbon with all the processes, which can be explained by the presence of residues which come from the mechanical polishing process or methanol evaporation.

Finally, we can see that the thickest oxide layer is obtained with the sample passivated immediately after etching step (53 Å), implying that this method can produce the thickest passivating layer compared with the others.

In conclusion, the passivation should be operated immediately after the etching process in order to produce a fast and thick oxide layer for the lateral edges of the detectors fabricated in our work.

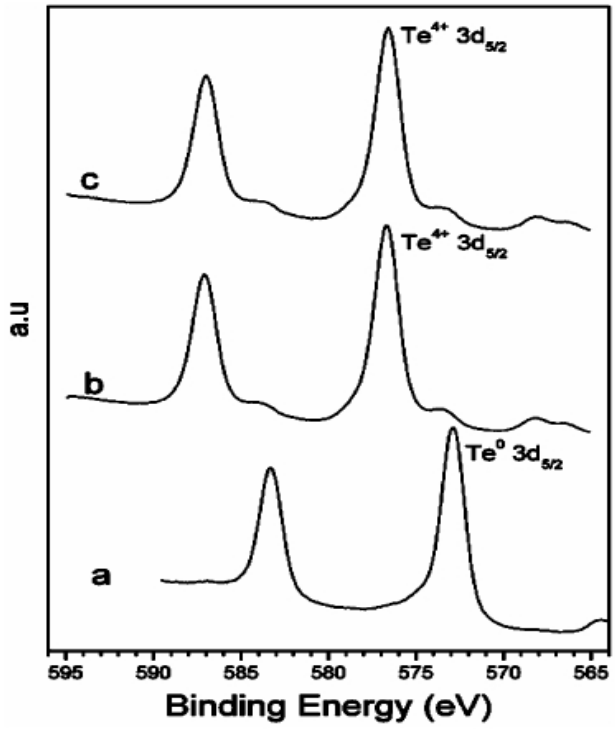

Figure 3.30. Te3d XPS spectra for CZT surface with different treatments. (a) Before passivation, (b) Passivate immediately after etching step, (c) Passivate after etching step holding in air for 24 h [46].

Table 3.4. Quantitative XPS analysis results of CdZnTe wafer surface after different surface treatment.

	%Te	%Cd	%Zn	%C	[Te]/([Cd]+[Zn])	Binding Energy	Chemical State	Te^{4+}/Te^{0}	$d_{oxide\ layer}$ (Å)
a	43.17	27.73	1.26	26.10	1.48	572.8	Te^{0}	0	0
b	18.22	15.25	1.20	10.34	1.10	576.7	Te^{4+}	0.98	53
c	18.56	13.64	0.78	9.86	1.28	576.7	Te^{4+}	0.93	37

In addition, the comparison of leakage current behaviours has been carried out with the Current-Voltage (I-V) characteristic. Figure 3.31 shows the I-V characteristics of the CZT detector for different surface treatment of its lateral edges. The treatments were operated followed consecutively by three steps: 1 μm Al_2O_3 Polish, 2 % Br-Methanol etching (2 min), and 30 % H_2O_2 passivation (2 min). The characterization was done after each step, named with the final process.

The I-V characteristics of the detectors show quasi-ohmic behaviours in all the ranges of applied voltages (-200 V ~ +200 V) for three different treatments. As can be seen, the leakage current reduces gradually when the etching and passivation processes are carried out. This figure shows clearly the influence of the surface conductivity on the leakage current. Indeed, considering that after passivation process the Te conductive layer is oxidized to create TeO_2, which allow a decrease of the surface leakage current, being an important contributor of the total leakage current.

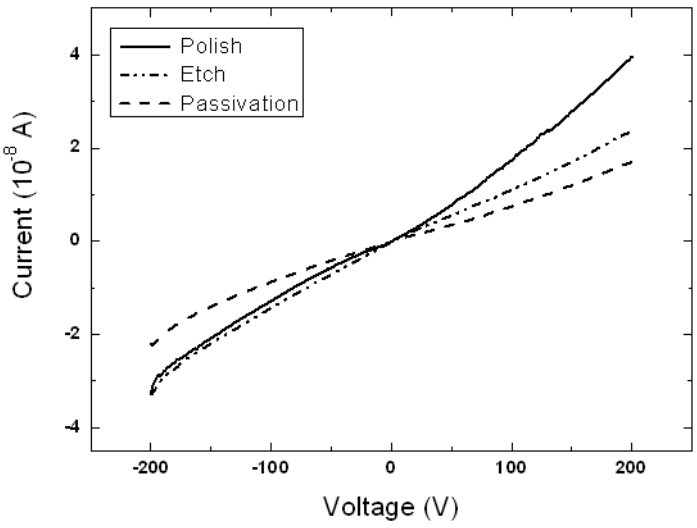

Figure 3.31. I-V curves of the lateral edges of the CZT detector after different surface treatment.

The aging behaviour after etching was investigated, in order to identify the oxidation kinetics of Te. Therefore, the lateral edges of the detector were etched with 2 % Br-Methanol for 2 min and then holded in air, allowing the partial oxidation of the lateral edges with time. After 1 month of exposure, the lateral edges of this detector were passivated with 30 % H_2O_2 agent for 2 min and then the I-V characteristic was achieved.

The Figure 3.32 displays the current-voltage characteristics of the same CZT detector after chemical etching of the lateral edges and holding in air with different aging time from a few minutes until 1 month. It has been accepted that the Te-rich surface will have a certain amount of TeO_2 and $CdTeO_3$ oxide after different aging time in air [5-8].

As can be seen, the leakage current slightly increases when the aging time increases from a few minutes to 1 week. We can observe that the leakage current significantly increases after

holding in air for two weeks, which may due to the defects produced by the oxide layers. We can also observe the highest leakage current achieved with the detector holding in air for 3 weeks, however, the leakage current sharply decreases after 3 weeks until 1month. It should be noted that etching is a partial oxidation process, thus the lateral edges of the detector can be gradually oxidized with the increasing aging time in air. After a certain period (e.g. 3 weeks), the oxide layers are enough thick which may result in the decrease of leakage current.

In Figure 3.32 (b), the leakage current of the detector passivated after 1 month of aging in air after etching step at the same applied voltage of 100 V is also presented. One can observe a lower leakage current of the detector after passivation treatment than aging for 1 month after etching step, implying that passivation is necessary after the etching step to create a thick oxide layer in a short time.

As previous mentioned in Figure 3.30 and Table 3.4, the laterals edges of the detector passivated immediately after chemical etching can obtain the thickest oxide layer. Therefore, we could suppose that the lateral edges of the detector immediately passivate after etching may achieve lower leakage current than aging in air for 24 h after etching.

In summary, the passivation process is essential to be operated after etching step on the lateral edges of the CdTe/CZT detectors.

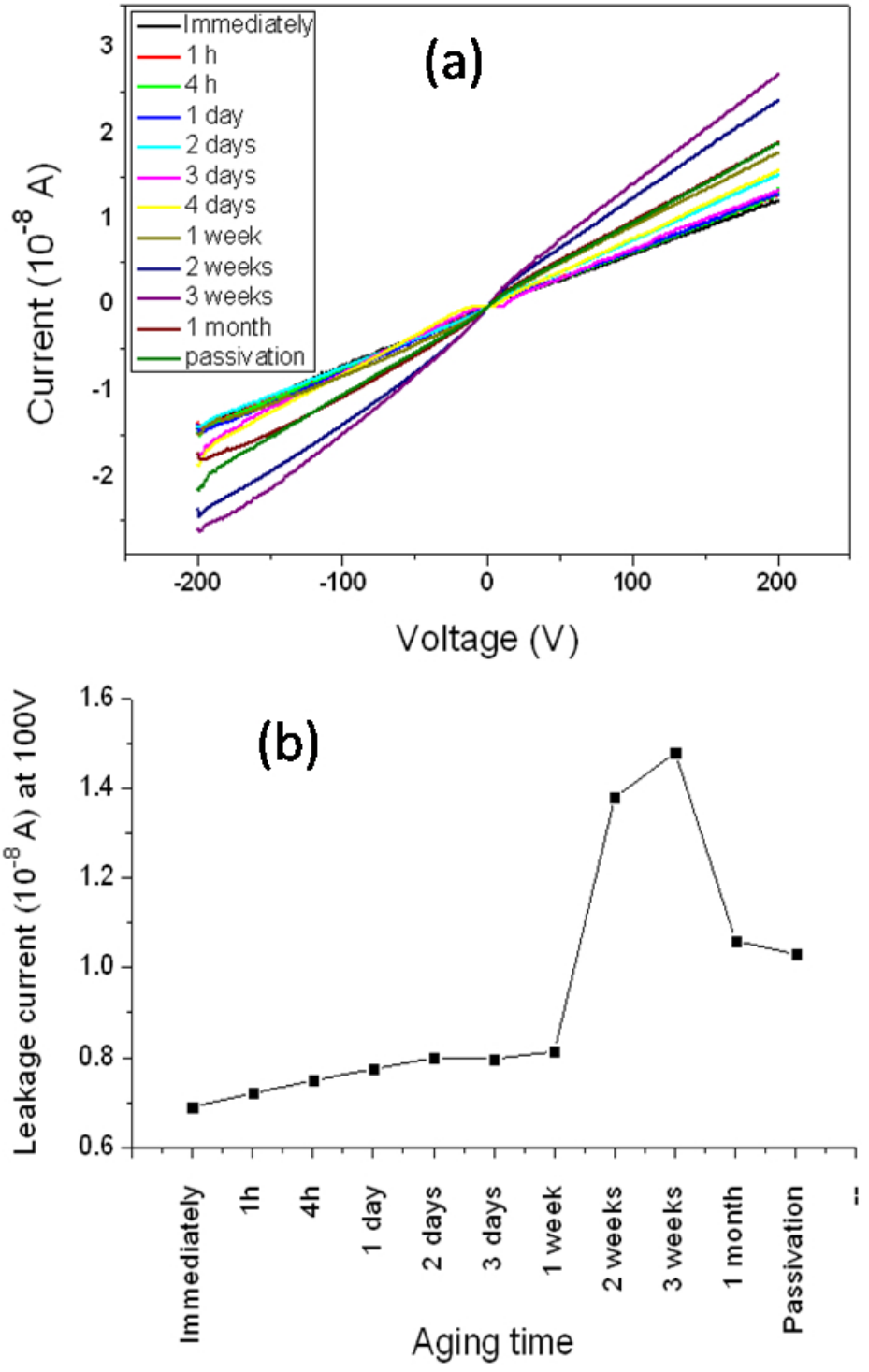

Figure 3.32. I-V curves of the edges of the CZT detector after surface treatment with different holding periods in air. (a) The whole leakage current at the applied bias from -200 V to +200V, (b) The leakage current at the applied bias at 100 V.

3.6. Conclusions

The process of the detector fabrication includes the surface preparation, electrode deposition, and lateral edges treatments have been described in this chapter. The importance of each step can be summarized as following:

- Cutting, lapping, and mechanical polishing processes can introduce surface damages, dislocation, and defects into the bulk material, which can increase the leakage current and deteriorate the detector performance. Polishing is a necessary step to decrease the surface roughness and increase the infrared transmission compared with lapping.

- The chemical etching step is extremely important before the electrode deposition, which obviously improves the crystallinity and gives a lowest FWHM value. Moreover, this step can remove the amorphous layer and defects on the sub-surface, decrease the leakage current, and enhance the detector performance compared with the other processes in our work.

- Br-Methanol has been selected as the best etchant for CZT material in our research, 2 % or 3 % is chosen as the optimal etching concentration, and Methanol is favourable to be used for cleaning the surface after Br-Methanol etching.

- The lateral edges of the detectors with passivation treatment immediately after etching step was demonstrated to produce a thick oxide layer in a short time, which could reduce the leakage current and improve the detector performance.

3.7. Bibliography

[1] Y. Cui, M. Groza, A. Burger, R.B. James, Effects of Surface Processing on the Performance of $Cd_{1-x}Zn_xTe$ Radiation Detectors, *IEEE. Trans. Nucl.*, Vol **51**, No. 3, 1172-1175 (2004).

[2] A. Hossain, A.E. Bolotnikov, G.S. Camarda, Y. Cui, S. Babalola, A. Burger, R.B. James, Effects of Surface Processing on the Response of CZT Gamma Detectors: Studies with a Collimated Synchrotron X-Ray Beam. *Journal of Electronic Materials*, Vol **37**, 1356 (2008).

[3] G. Tepper, R. Kessick, C. Szeles, An Investigation of the Electronic Properties of Cadmium Zinc Telluride Surfaces using Pulsed Laser Microwave Cavity Perturbation, *Proc. SPIE.* Vol **4507**, 79 (2001).

[4] Source Logitech Ltd: http://www.logitech.uk.com/chemicalpolishing.asp.

[5] A.A. Rouse, C. Szels, J.O. Ndap, S.A. Soldner, K.B. Parnham, D.J. Gaspar, M.H. Engelhard, A.S. Lea, S.V. Shutthanandan, T.S. Thevthasan, D.R. Baer, Interfacial Chemistry and the Perfomance of Bromine-Etched CdZnTe Radiation Detector Devices, *IEEE. Trans. Nucl*, Vol. 49, 2005 (2002).

[6] M.E.Özsan, P.J. Sellin, P. Veeramani, S.J. Hinder, M.L.T. Monnier, G. Prekas, A. Lohstroh, M.A. Baker, Chemical Etching and Surface Oxidation Studies of Cadimum Zinc Telluride Radiation Detector, *Surf.Interface Anal*, Vol. **42**, 795 (2010).

[7] Q. Zheng, D. Dierre, J. Crocco, V. Carcelen, H. Bensalah, J.L. Plaza, E. Dieguez, Influence of Surface Preparation on CdZnTe Nuclear Radiation Detectors, *Appl. Surf. Sci*, Vol **257**, 8742-8746 (2011).

[8] S.H. Cho, J.H. Suh, J.H. Won, K.H. Kim, J.K. Hong, S.U. Kim, Surface leakage current control with heterojunction-type passivation in semi-insulating CdZnTe material, *Nucl. Instru. Meth. A*, Vol **591**, 203 (2008).

[9] J. Ramiro, L. Galán, E. García Camarero, I. Montero, Y. Laaziz, X-ray Photoelectron Spectroscopy of Electrodeposited Cadimum Mercury Telluride Thin Films and Their Native Surface Oxides, *J. Mater. Res.*, Vol **16**, 7, 1942-1952 (2001).

[10] H. Yoon, J.M. Van Scyoc, M.S. Goorsky, H. Hermon, M. Schieber, J.C. Lund, R.B. James, Investigation of the Effects of Polishing and Etching on the Quality of Cd1-xZnxTe Using Spatial Mapping Techniques, *Journal of Electronic Materials*, Vol. **26**, 6, 529-533 (1997).

[11] Y. Li, Z. Gu, G. Li, W. Jie, Infrared Transmission Spectra of Cd1-xZnxTe (x=0.04) Crystals, *Journal of Electronic Materials*, Vol **33**, No. 8, 861-866 (2004).

[12] C. Szeles, Y.Y. Shan, K.G. Lynn, A.R. Moodenbaugh, Trapping Properties of Cadmium Vacancies in $Cd_{1-x}Zn_xTe$, *Phys. Rev. B.*, Vol **55**, 11, 6945 (1997).

[13] J.G. Werthen, J.P. Häring, A.L. Fahrenbruch, R.H. Bube, Effects of Surface Preparation on the Properties of Metal/CdTe Junction, *J. Appl. Phys.*, Vol **54**, 10, 5982 (1983).

[14] M.J. Mescher, J.F. Hoburg, T.E. Schlesinger, R.B. James, Analysis on the Measurement of Leakage Currents in CdZnTe Radiation Detectors, *IEEE. Trans. Nucl.*, Vol **46**, 6, 2289-2296 (1999).

[15] S. Sen, D.R. Rhiger, C.R. Curtis, M.H. Kalisher, H.L. Hettich, M.C. Currie, Infrared Absorption Behaviour in CdZnTe Substrates, *Journal of Electronic Materials*, Vol **30**, 6, 611-618 (2001).

[16] G. Yang, W. Jie, Q. Li, T. Wang, G. Li, H. Hua, Effects of In Doping on the Properties of CdZnTe Single Crystals, *J. Cryst. Growth.*, Vol **283**, 431-437 (2005).

[17] H. Chen, J. Tong, Z. Hu, T. Shi, G.H. Wu, K.T. Chen, M.A. George, W.E. Collins, A. Burger, R.B. James, C.M. Stahle, L.M. Barlett, Low-temperature Photoluminescence of Detector Grade $Cd_{1-x}Zn_xTe$ Crystal Treated by Different Chemical Etchants, *J. Appl. Phys.* Vol **80**, 6, 3509-3512 (1996).

[18] V.A. Gnatyuk,T. Aoki, M. Niraula, Y. Hatanaka, Influence of Laser Irradiation and Laser-induced In Doping on the Photoluminescence of CdTe Crystals, *Semicond. Sci. Technol.*, Vol **18**, 560-565 (2003).

[19] J. Franc, H. Elhadidy, V. Babentesov, A. Fauler, M. Fiederle, Comparative Study of Vertical Gradient Freeze Grown CdTe with Variable Sn Concentration, J. Mater. Res., Vol 21, No. 4, 1025 (2006).

[20] J. Franc, V. Babentsov, M. Fiederle, E. Belas, K.W. Benz, P. Höschl, Defect Structure of High Resistive CdTe:In Prepared by Vertcial Gradient Freeze Method, *IEEE. Trans. Nucl.*, Vol **51**, 3, 1176-1181 (2004).

[21] Y. Nemirovsky, A. Ruzin, G. Asa, Y. Gorelik, Study of Contacts to CdZnTe Radiation Detectors, *Journal of Electronic Materials*, Vol **26**, No. 6, 756-764 (1997).

[22] S.H. Lee, I.J. Kim, Y.J. Choi, J.K. Hong, H.K. Lee, Y.C. Chung, Y. Yi, S.U. Kim, M.J. Park, The Comparison on the Performance of a Gamma-ray Spectrometer with the Variation of Pt(Au)/CdZnTe/Pt(Au) interface, *J. Cryst, Growth.*, Vol **214/215**, 1111-1115 (2000).

[23] L. Wang, W. Sang, W. Shi, Y. Qian, J. Min, D. Liu, Y. Xia, Electrical Properties of Contacts on P-type Cd0.8Zn0.2Te Crystal Surfaces, *Nucl. Instru. Meth. A.*, Vol **448**, 581-585 (2000).

[24] G.F. Knoll, *Radiation Detection and Measurement*, 2nd edition, (New York: Woley) (1989).

[25] E.E. Haller, F.S. Goulding, *Handbook on Semiconductors*, Vol **4**, ed. by C. Hilsum, chap. 11, 937-963, (Elsevier Science Publishers B.V., 1993).

[26] MEMS: https://www.mems-exchange.org/MEMS/processes/deposition.html.

[27] Q. Zheng, F. Dierre, M. Ayoub, J. Crocco, H. Bensalah, V. Corregidor, E. Alves, R. Fernandez-Ruiz, J.M. Perez, E. Dieguez, Comparison of Radiation Detector Performance for Different Metal Contacts on CdZnTe Deposited by Electroless Deposition Method, *Cryst. Res. Technol.*, Vol **46**, No. 6, 1131-1136 (2001).

[28] Q. Zheng, F. Dierre, V. Corregidor, R. Fernández-Ruiz, J. Crocco, H. Bensalah, E. Alves, E. Diéguez, Deposition of Nanometric Double layers Ru/Au, Ru/Pd, and Pd/Au onto CdZnTe by the Electroless Method, In press, *J. Crystal Growth* (2011), doi:10.1016/j.jcrysgro.2011.04.014.

[29] Alireza Kargar et al., The Final Surface treatment Effect on Performance of CdZnTe Frisch Collar Gamma Ray Detectors, *Proc. of SPIE*, Vol **7079**, 70790B (2008).

[30] Y. Nemirovsky, Passivation with II-VI Compounds, *J. Vac. Sci. Technol. A*, Vol **8**, No. 2, 1185-1187 (1990).

[31] J. Crocco, H. Bensalah, Q. Zheng, F. Dierre, P. Hidalgo, J. Carrascal, O. Vela, J. Piqueras, E. Dieguez, Study of the Effects of Edge Morphology on Detector Performance by Leakage Current and Cathodoluminescence, *IEEE. Trans. Nucl.*, Vol **58**, No. 4, 1935-1941 (2011).

[32] F. Wang, A.L. Fahrenbruch, R.H. Bube, Properties of Metal-Semiconductor and Metal-insulator-semiconductor Junctions on CdTe Single Crystal, *J. Appl. Phys.*, Vol **65**, 3552-3559 (1983).

[33] P.N. Luke, Single-polarity Charge Sensing in Ionization Detectors Using Coplanar Electrodes, *Appl. Phys. Lett.*, Vol **65**, 2884 (1994).

[34] A.J. Nelson, A.M. Conway, C.E. Reinhardt, J.L. Ferreira, R.J. Nikolic, S.A. Payne, X-ray Photoemission Analysis of Passivated $Cd_{(1-x)}Zn_xTe$ Surfaces for Improved Radiation Detectors, *Materials Letters*, Vol **63**, 180 (2009).

[35] K.T. Chen, D.T. Shi, H. Chen, B. Granderson, M.A. George, W.E. Collins, A. Burger, R.B. James, Study of Oxideized Cadimum Zinc Telluride Surfaces, *J. Vac. Sci. Technol. A*, Vol **15**, 1 (1997).

[36] D.R. Rhiger, R.E. Kvaas, *J. Vac. Sci. Technol. A*, Vol **21**, 168 (1982).

[37] K. Chattopadhyay, M. Hayes, J. Ndap, A. Burger, W.J. Lu, H.G. Mcwhinney, T. Grady, R.B. James, Surface Passivation of Cadimum Zinc Telluride Radiation Detectors by Potassium Hydroxide Solution, *Journal of Electronic Materials*, Vol **29**, No. 6, 708 (2000).

[38] C. Szeles, Advances in the Crystal Growth and Device Fabrication Technology of CdZnTe Room Temperature Radiation Detectors, *IEEE. Trans. Nucl. Sci.*, Vol **51**, 1242-1249 (2004).

[39] G.S. Camarda, A.E. Bolotnikov, G.A. Carini, R.B. James, L. Li, Effects of Tellurium Precipitates on Charge Collection in CZT Nuclear Radiation Detectors, Chapter 4, Countering Nuclear and Radiological Terrorium, *Springer Netherlands*, 978-1-4020-4897-5 (2006).

[40] L. Marchini, A. Zappettini, E. Gombia, R. Mosca, M. Pavesi, Study of Surface Treatment Effects on the Metal-CdZnTe Interface, *IEEE. Trans. Nucl. Sci Symp. Conf. Rec.*, R-12-68 (2008).

[41] X. Wang, W. Jie, Q. Li, Z. Gu, Surface Passivation of CdZnTe Wafers, *J. Mater. Sci. in Semcond. Proc.*, Vol **8**, 615-621 (2005).

[42] G.W. Wright et al., Evaluation of NH_4F/H_2O_2 Effectiveness as a Surface Passivation Agent for $Cd_{1-x}Zn_xTe$ Crystals, *Proc. SPIE*, Vol **4141**, 324-335 (2000).

[43] K. Chattopadhyay, Surface Passivation of Cadimum Zinc Telluride Radiation Detectors by Potassium Hydroxide Solution, *J. Elect. Mater.*, Vol **29**, 6, 708-712 (2000).

[44] K.C. Kang et al., Surface Passivation by Surfur Treatment of Undoped p-CdTe (100), *J. Appl. Phys.*, Vol **88**, 2013-2015 (2000).

[45] X. Cheng, S. Zhu, B. Zhao, Z. He, D. Gao, J. Fang, Effect of Surface preparation on the Properties of Au/p-$Cd_{1-x}Zn_xTe$, *Appl. Surf. Sci.*, Vol **253**, 8408-8407 (2007).

[46] H.Bensalah, J.Crocco, V.Carcélen, J.L.Plaza, Q.Zheng, A.Zappettini, G.Domínguez, L.Soriano, E.Diéguez, Study of Ammonium Fluoride Passivation Time on CdZnTe Bulk Crystal Wafers, *Cryst. Res. Technol.*, Vol **46**, 659-663 (2011).

[47] S. Tanuma, C.J. Powell, D.R. Penn, *Surf. Analysis*, Vol **1**, chap. 5, Eds.: D. Briggs and M.P. Seah (Wiley, New York, 1990).

CHAPTER 4. ELECTRODE DEPOSITION ON CDTE/CZT

The bulk material type (p or n) and detailed electrical properties (doping, trapping centres), surface treatment, choice of contact material and deposition technology could determine if the contact is injecting or non-injecting, and also its behaviour (Ohmic or Schottky contact). The ideal contact should have: a low specific resistance, good adhesion, good uniformity, and stability properties. In general, for metallization, common methods are used: sputtering, thermal evaporation, and electroless deposition method.

The capability to form suitable contacts is greatly important to the fabrication of high quality CdTe/CZT devices. Although the detector is fabricated in high quality material, non optimized contacts will also lead to an inferior performance. Therefore, proper contact design, the choice of electrical material, methods of deposition, interface control, surface preparation, and passivation are significantly important for the fabrication of CdTe/CZT detectors.

In this chapter, the properties of the contacts on high resistivity CdTe/CZT crystals in terms of deposition methods, electrical materials, and other influence factors have been investigated. In the first section, different deposition methods using sputtering, evaporation, and electroless techniques were investigated. The shallow and deep level defects in CdTe/CZT based detectors fabricated by different deposition methods have been considered. Current-Voltage characteristics as well as the Gamma-ray spectroscopy of the CdTe/CZT planar detectors have been studied. Meanwhile, the thickness of the contact layer, the composition and concentration profile of the surface layers, and the quality of the interface has been investigated by the RBS technique.

In the second section, different parameters which are associated with the quality of the contacts have been studied. In particular, the effect of deposition time of three metallisation processes using electroless deposition method has been investigated. The structural properties, surface roughness, the thickness of the contact layer, and the orientation of the contacts were studied by SEM, AFM, EDX, XRD and RBS techniques. Furthermore, the effect of the annealing step after the deposition step was explored via I-V characteristics.

In the third section, single layer deposited on CdTe/CZT materials with the best deposition method concluded by the first section have been investigated by means of TXRF, RBS, I-V, and gamma-ray spectroscopy measurements.

Finally, the feasibility of the deposition of multi-layers on CdTe/CZT material was researched. The mechanisms which are associated with the chemical reactions occur during

different depositions of multi-layers structures were considered. The thickness and the stoichiometry of the multi-layers on CdTe/CZT materials were studied by RBS measurement. TXRF technique was the first time to be used for evaluating the presence of Cd and Te in the electroless chemical solutions. I-V measurement and gamma-ray spectroscopy have been implemented in our work to study the quality of the single-layer and double-layer detectors.

4.1. Selection of the Best Deposition Method

To obtain a detector structure, thin-film metal electrodes (Au, Pt...) are typically deposited on the surface of CdTe/CdZnTe materials, by using various deposition techniques such as electroless, evaporation or sputtering [1-5]. These deposition techniques can create a certain amount of defects, both extrinsic and intrinsic at the interface region leading to recombination/trapping effects that can deteriorate the detector performance [6-8]. In this section, our objective is to study the influence of the deposition methods and type of metal contacts on the defects generated at the metal/semiconductor interface.

Experimental Details

The CZT samples used in this investigation were grown by the Vertical Gradient Freeze method. Single elements have been diced closed to each other from the same wafer to limit the axial irreproducibility of the composition in the ingot. After that, the samples were lapped by abrasive alumina powder of 3 µm and polished with 1 µm diamond abrasive. The dimension of the samples was $5 \times 5 \times 2$ mm^3. The samples were etched using 2 % Br-Methanol solution for 2 minutes prior to the fabrication of contacts.

Metal contacts were deposited immediately after chemical treatment (typically within 1-2 minutes) to minimize the effects of surface re-oxidation. Three distinct procedures were used for studying different deposition methods on the CZT: (1) Sputtered Au deposition, (2) Au thermal evaporation, (3) Electroless Au deposition. For characterization by PL measurement, the requirement of thin optically transparent layers is mandatory.

The deposition of Au by sputtering was carried out using a high resolution sputtered coater Quorum Q150TS, which is suitable for oxidizing and non-oxidizing metals. The vacuum chamber pressure was set to 10^{-3} mbar during the deposition process. The deposition density of Au layer was 19.32 g/cm^3, and a 10 nm thick layer of Au was deposited on the surface of the samples.

The deposition of thermally evaporated Au electrodes was carried out by a joule effect evaporator with an initial pressure below 10^{-6} Torr. Gold is heated to melting by injecting electrical current though a filament shaped basket (Gold is in the basket). The material in the form of vapour is then condensed on the substrate. With a deposition time of 1 min, an optically thin Au layer of around 10 nm thick was obtained.

The electroless solutions were prepared with 1 g of metal chloride salts of Au, Pt, Ru respectively, dissolved in 25 mL of de-ionized water. The deposition time was 10 seconds to obtain a thin optically transparent Au layer on the samples.

More details of the process can be found in Chapter 3. In fact, a deeper study of the optimum time for this best deposition method will be described in the next section.

4.1.1. Composition of the Layer Produced by Electrode Deposition

Rutherford Backscattering Spectrometry (RBS) was used to determine the composition and the depth distribution of the main elements on the samples. In fact, other techniques could be used for surface composition analysis, such as SEM, SIMS. Nevertheless, we have selected the RBS technique, which can provide a complete picture about the surface and subsurface elements composition.

Figure 4.1 illustrates the RBS fitting spectra and the depth profile of the CZT samples with three different Au deposition methods. For the fitting curves, the following assumptions were considered: (1) the substrate has a 6 at% of Zn concentration; (2) the tellurium oxide was considered as a compound of TeO_2; (3) to overcome the poor mass resolution of the technique when the elements with close atomic numbers are present, different spectra at different incidence angles were recorded.

Figure 4.1 (a) shows the spectra collected and the best fit obtained for Au contacts, different channels of different elements (Au, Cd, Zn, Te) are observed for all the Au deposition methods. We can observe that these three deposition methods have similar behaviours for Au, Cd, and Zn, except Te, for which the electroless Au deposition method present a small extra channel between 300 and 350, which is inside the range of Au, suggesting that more diffusion of Au is done and intermixed with Te oxide layer.

Figure 4.1 (b) displays the depth profile distribution of the bulk CZT, TeO_2 layer and Au layer used for these simulations. In this figure we can observe that the thickness of Au layer is similar for all the three deposition methods, and at the same time we can also see clearly the presence of TeO_2 layer between Au layer and bulk material with all the deposition methods.

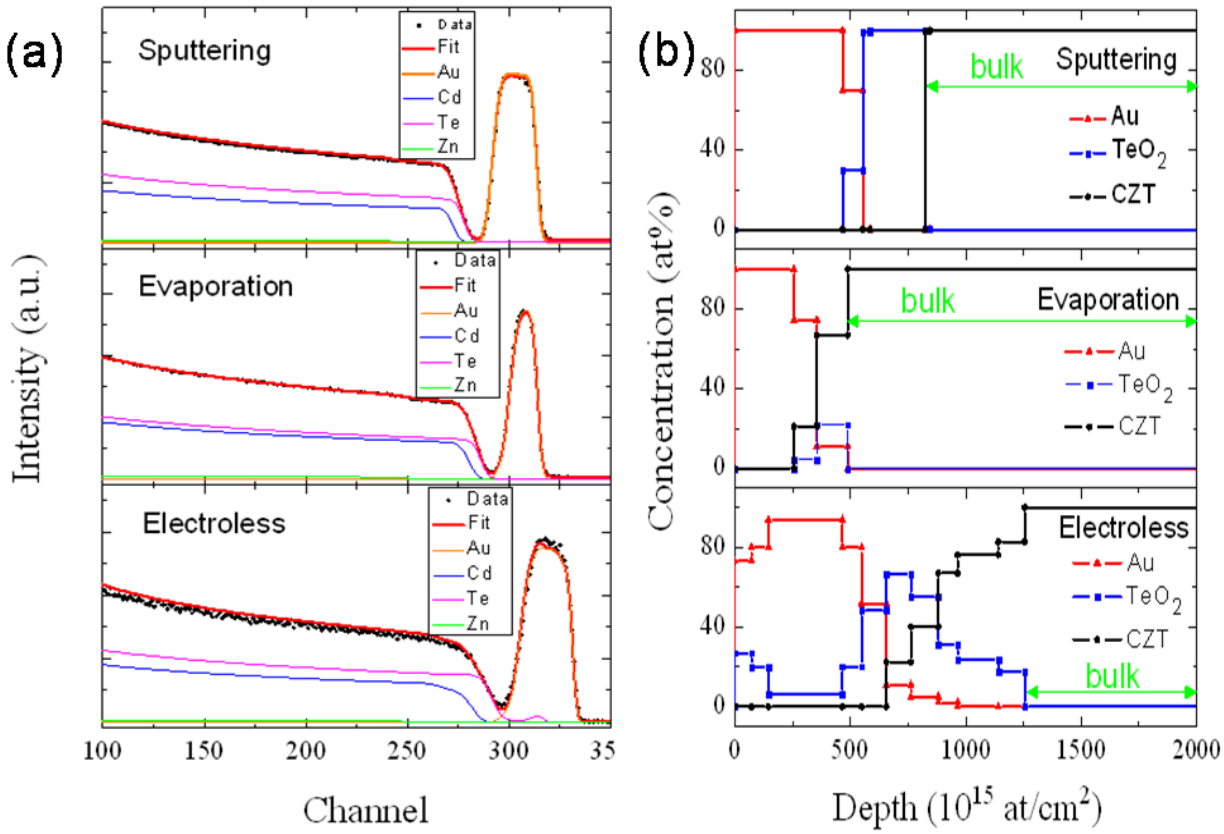

Figure 4.1. RBS spectra and fits (a), depth profiles (b) of CZT detectors fabricated by different methods of Au deposition.

In comparison, the presence of TeO_2 layer with sputtering method is at higher concentration of 100 at% and less intermixing between Au layer and CZT bulk material, revealing that sputtering deposition method introduce a thicker TeO_2 layer between the contact and material which may create defects and degrade the detector performance. With the evaporation deposition method, one can observe that a small appearance of TeO_2 layer (20 at%) and less interdiffusion between Au layer and CZT.

The electroless deposition method shows a more complex behaviour that one can see a strong intermixing between layers of TeO_2 and CZT and Au. Particularly, the depth of TeO_2 layer between Au layer and CZT is much higher than the other deposition methods. This intermixing layer gives a smoother interface between the contact and the bulk material, which seems to be beneficial for the detector performance.

This strong intermixing layer by the electroless deposition method can be explained by the preferential reaction of deposition between the ions of gold chloride of the solution and the creation of cadmium vacancies at the interface. Indeed, it is supposed that Au atoms

preferentially dispersed on Cd-vacancies owing to the proximity of the covalent radius of Au and Cd, and Au atoms replace Cd-vacancies (Au_{Cd}).

4.1.2. Study of the Defects Present in the Detector by PL Measurements

Photoluminescence (PL) spectroscopy is a sensitive, noncontact, and non-destructive method, suitable to characterize the point defects, such as substitutional impurities (donors and acceptors) and native or intrinsic defects in CZT materials. The low temperature PL spectrum can provide excellent overall picture of the material quality which could be valuable as a predictor of the detector performance.

Figure 4.2 exhibits the low temperature (4.2 K) PL spectra obtained from near-surface region of three CZT samples with different Au deposition methods. The intensities of the PL spectra were normalized to the (D^0, X) peak considering that the FWHM of the (D^0, X) peak is an indicator of crystalline quality of the crystals. It is important to note that the penetration depth into the material was < 20 nm owing to the excitation wavelength chosen. Therefore, optically thin Au layer was deposited on the samples.

Schlesinger et al. reported that the clearest indicator of the difference in quality is that the spectrum of the sample is dominated by the excitonic luminescence, while that of the poor-quality sample is dominated by the defect-related luminescence. The other indicators which determine the high quality material are the sharpness of the spectrum and the predominance of the donor-bound exciton (D^0, X) peak [5]. One can observe that the spectra of all the samples presented were dominated by the excitonic luminescence, indicating that good quality materials were chosen for this study.

In the exciton region (1.64-1.70 eV), the sharp neutral donor-bound exciton (D^0, X) peak at 1.659 eV and neutral acceptor bound exciton (A^0, X) at 1.650 eV are observed in all samples. In the donor-acceptor region (1.57-1.64 eV), the shallow donor–acceptor pair (D, A) emission at 1.625 eV and its longitudinal optical photon (1LO) replica located at the shoulder on the lower energy side of the (D, A) peak are shown in all the spectra of the three samples before or after Au deposition where no significant difference can be seen. Nevertheless, in the defect region (1.42-1.57 eV), the A-center band at 1.47 eV is clearly visible in all spectra. A band which is related to a complex defect involves a Cd vacancy and a donor impurity [9].

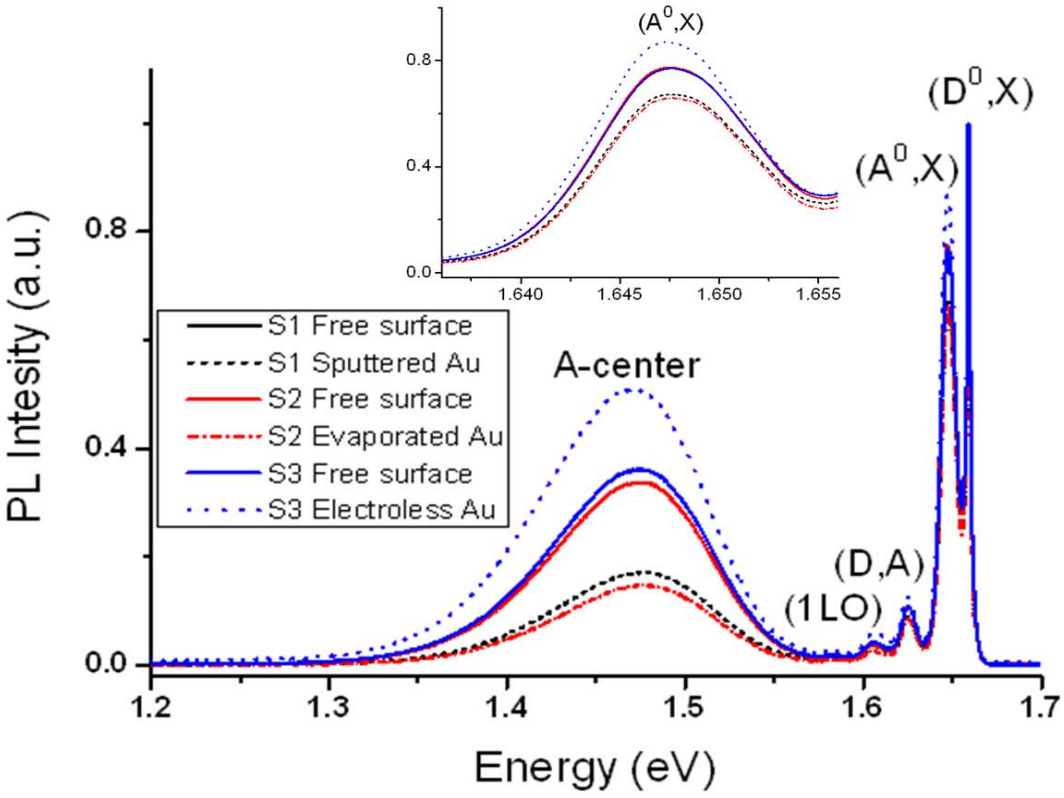

Figure 4.2. Low temperature (4.2 K) PL spectra of CZT detectors fabricated by different Au deposition methods.

The summary of the intensity of the peaks, the FWHM of the (D^0, X) peak, and the intensity ration between the (D^0, X) peak and the other major peaks is illustrated in Table 4.1. The intensity of (A^0, X) and (D, A) peaks before and after electrode deposition of the three methods, nearly remain constant with slightly variation.

As presented in Figure 4.2 and Table 4.1, we observe the intensity of A-center decrease greatly after the deposition with the sputtering and evaporation methods, a significant difference between the free surface and contacted surface. The introduction of electrical contacts into CZT materials can reduce the effects of the Cd vacancies [1][10].

Generally, the intensity of the A-center band for CZT crystals with contacts is lower than the intensity measured for the contact-less crystal, indicating that the concentration of defects responsible for this band have decreased. The possible mechanism is the donors $[Au]^{3+}$ recombine with the cadmium vacancies acting as acceptors $[V_{Cd}]^{2-}$ following the reaction [10]:

$$[Au]^{3+} + [V_{Cd}]^{2-} \rightarrow [Au^{3+} \cdot V_{Cd}^{2-}]^{+} \qquad \text{Eq. 4-1}$$

$$[Au]^{3+} + [V_{Cd}]^{2-} \rightarrow [2Au^{3+} \cdot 3V_{Cd}^{2-}]^{0} \quad \text{Eq. 4-2}$$

$$2[Au^{3+} \cdot V_{Cd}^{2-}]^{+} + [V_{Cd}]^{2-} \rightarrow [2(Au^{3+} \cdot V_{Cd}^{2-})^{+} \cdot V_{Cd}{}^{2-}]^{0} \quad \text{Eq. 4-3}$$

In Figure 4.2, one can observe the intensity of the A-center with Au contacts by sputtering and evaporation methods decrease sharply in comparison with the electroless method, revealing that the Au donors further compensate with Cd vacancies (Eq. 4-2 and Eq. 4-3) according to the self-compensation effects and also the electro-neutrality condition principle [11].

Table 4.1. Comparison of PL (4.2 K) results of CZT detectors: before and after metallization process with different methods. (σ = ± 0.01).

		I(D^0,X)	I(A^0,X)	I(D,A)	I(A-center)	I(D^0,X)/ I(A^0,X)	I(D^0,X) /I(D,A)	I(D^0,X) /I(A-center)	FWHM (D^0,X) meV
S1	Free surface	1.00	0.77	0.11	0.36	1.30	9.2	2.8	2.2
	Sputtered Au	1.00	0.67	0.09	0.17	1.49	11.1	5.8	2.1
S2	Free surface	1.00	0.77	0.11	0.34	1.30	9.3	3.0	2.0
	Evaporated Au	1.00	0.66	0.09	0.15	1.52	11.6	6.8	2.0
S3	Free surface	1.00	0.77	0.11	0.36	1.30	9.2	2.8	2.4
	Electroless Au	1.00	0.87	0.13	0.51	1.15	7.8	2.0	2.4

The decrease of the (A^0, X) peak after metal contact deposition process indicates that the Cd vacancies (V_{Cd}) are dominantly compensated by the metal donors, i.e., by the formation of the metal-complexes and reducing the concentration of the defect complex (A-center). Particularly, the distinct decrease of the intensity of the (A^0, X) peak with Au contact using evaporation method, implying that more V_{Cd} are compensated by Au donors. However, one can observe the slightly increase of the intensity of (A^0, X) peak with the electroless deposition method (0.87), suggesting that the inconspicuous recombination between Au and Cd vacancies are probably due to the interface relationship between the Au layer and CZT. Another reason could be the creation of Cd vacancies during the electroless deposition. Indeed, the $AuCl_4^-$ ions preferentially react with Cd and form Cd vacancies at the surface, and

transfer Cd^{2+} ions into the electroless solution. This excess of Cd vacancies require more Au donors for compensation, thereby less recombination process occur. The further investigation with RBS technique of the interface composition and depth distribution will be carried out in 4.1.2.

As shown in the table 4.1, the intensity of donor-acceptor pair (D, A) peak of the electroless Au contact surface is much higher than the free surface, indicating that the density of shallow donor level related to Au donors increases significantly. One possible explanation is that there are still a large number of Au donors left after the V_{Cd}^{2-} are dominantly compensated and after the recombination of excess Au donors and other shallow levels, such as Na and Li.

The $I_{(D^0, X)}/I_{A\text{-center}}$ ratio indicates a density of A-center, which act as hole traps. As shown in Table 4.1, the electroless Au deposition shows the lowest $I_{(D^0, X)}/I_{A\text{-center}}$ ratio (2.0), which indicates the high concentration of A-center in the crystals. We assume that in the samples where Cd vacancies are bound into A-center, that are relatively shallow hole traps, the concentration of deep Cd vacancy related defects is decreased.

As shown in Figure 4.2, the increase of A-center after Au deposition, implying that the electroless deposition methods introduce more defects into material, that is in agreement with the RBS results which displaying more interdiffusion of Au layer into bulk material. The influence of these three different deposition methods on the detector performance will be further studied as following in order to find the best deposition method.

4.1.3. Electrical Behaviours of the Detectors by Different Deposition Methods

(i) Current-Voltage Characteristics

The current-voltage (I-V) measurement was performed at room temperature with the planar devices measured using a Keithley 2400 sourcemeter.

The current-voltage (I-V) characteristics of the planar devices with three deposition methods at the electric field of -500 V/cm ~ +500 V/cm are exhibited in Figure 4.3. The same detectors fabricated from n-type material were used for this investigation; different contacts were tested by reporocessing the samples (meaning the contacts are removed and the samples are repolished of a few microns). It is important to emphasise that oscillations in the I-V characteristics are observed which can be explained by the fact that the leakage current of the samples are very close to the limit of detection of the instrument Keithley or because of the noise from the electric power.

As shown in Figure 4.3, we observe the contacts of different deposition methods display Schottky contact behaviours at all the applied electric field. The lowest leakage current with the whole range of applied field can be obtained by using electroless method for contact deposition, while for the sputtered gold contacts, higher leakage current is observed. Particularly, the leakage current of sputtered Au contacts decreases significantly at the reverse bias of -20 V ~ - 200 V (-50 V/cm ~ -500 V/cm). Electroless Au deposition method and Au evaporation methods display much lower barrier height and similar behaviour in comparison with the sputtered Au contacts.

It is interesting to find out that the I-V characteristics are in agreement with the PL and RBS analys. In fact, the thicker TeO_x layer with the sputtering method may increase the leakage current, despite the fact that this method gives lower concentration of defects. Although the electroless method can introduce more defects into the material, the intermixing TeO_2 layer can enhance the cohesion of the Au layer with CZT, which may reduce the leakage current. We can conclude that the thickness of TeO_x layer may play a critical role in the detector performance.

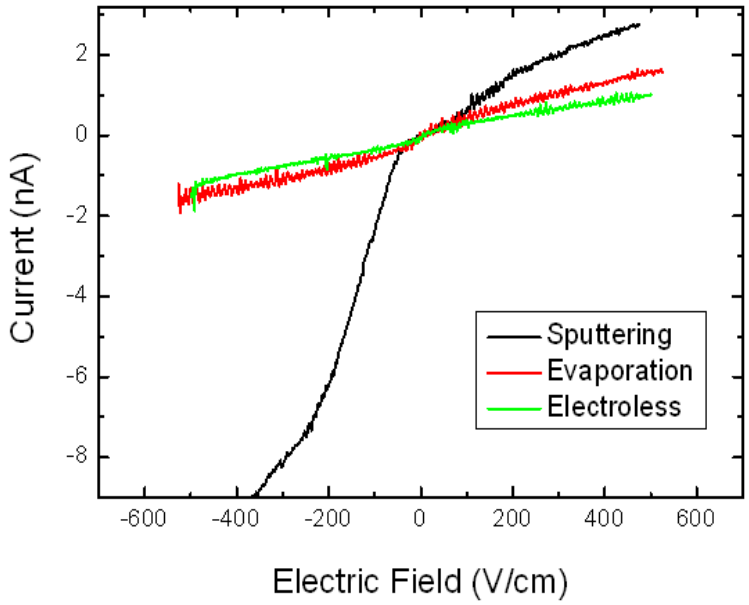

Figure 4.3. Comparison of I-V curves obtained from the same CZT detector using different Au deposition methods.

(ii) Gamma-ray Spectroscopy

The performance of these detectors has been characterized using the ^{133}Ba and ^{241}Am radioactive sources, which was mounted on a custom Teflon fixture with gold coated mounting plate (anode) and contacted using a gold cantilever (cathode). The planar detectors with Au contacts were irradiated from the cathode side.

Figure 4.4 shows the gamma-ray spectroscopy of the planar devices by using different deposition methods. To compare the spectra, the applied voltages had been changed from 600 V to 800 V. It is important to note that the same detectors were repolished and recontacted for comparison, the thickness of the detectors are quite similar after reprocessing, therefore, the same electric fields can be obtained with the same applied bias.

In Figure 4.4, the 31 keV and 81 keV photopeaks with ^{133}Ba source and 60 keV with ^{241}Am photopeak can be observed. One can also observe a slightly shift of all the photopeaks to the higher energies as the applied voltages increases, which is due to the charge collection (further discuss in section 5.2.5.3). By comparison with these three deposition methods, we observe a significant difference of the noise Peak/Valley (P/V) ratio of 31 keV with ^{133}Ba gamma spectra by three deposition methods.

The summary of the gamma spectra of the planar detectors fabricated by different Au deposition methods at the applied bias of 700V is presented in Table 4.2. We observe that the Peak/Valley ratio of the 31 keV photopeak of electroless Au deposition method (5.6) is much higher than sputtering (1.9) and evaporation (2.2) methods, indicating that less noise appears with this deposition method. The noise level is associated with the value of the applied voltage and increases with the increasing leakage current. The FWHM of the 31 keV photopeak is 15.3 % for the electroless deposition method, which is lower than the sputtering method (16.1 %), but higher than the evaporation method (12.9 %).

For gamma ray applications, the detector performance is usually quantified by the photopeak resolution and Peak/Valley ratio. These two parameters contribute to the quality factor which is defined by:

$$Quality\ factor = \sqrt{\frac{\frac{peak}{valley}ratio}{\%FWHM}} \qquad \text{Eq. 4-4}$$

With the %FWHM is the resolution and the Peak/Valley ratio for the photopeak concerned, the quality factor is considered as a good indicator of spectrometer performance.

As shown in Table 4.2, the quality factor of the 31 keV peak is 0.60 for Au contacts prepared by electroless deposition method, which is higher than the ones prepared by sputtering (0.34) or by evaporation (0.41), revealing that better detector performance was achieved with the electroless deposition method. This dependence is probably related with the composition of the intermixing layers, mainly with the presence of TeO_2 layer formed between the Au contact and the CZT bulk material and the interaction of the Au with Cd vacancies resulting in formation of A-center.

As compared with Figure 4.3, the I-V characteristics of the electroless Au deposition method display the lowest leakage current, which is consistent with the results of the gamma spectroscopy measurements. Indeed, the decrease of the noise level observed in the spectra with electroless method is coinciding with the decreased leakage current observed in the I-V characteristics. We observe the X-ray escape peak of the ^{241}Am gamma spectroscopy with the contacts prepared by electroless Au deposition method. These results show obviously that the electroless deposition method lead to devices with lower noise and also gave the best performance for CZT materials. We can conclude that the electroless deposition is the

optimum deposition method for the CZT detectors with the lowest leakage current and best resolution.

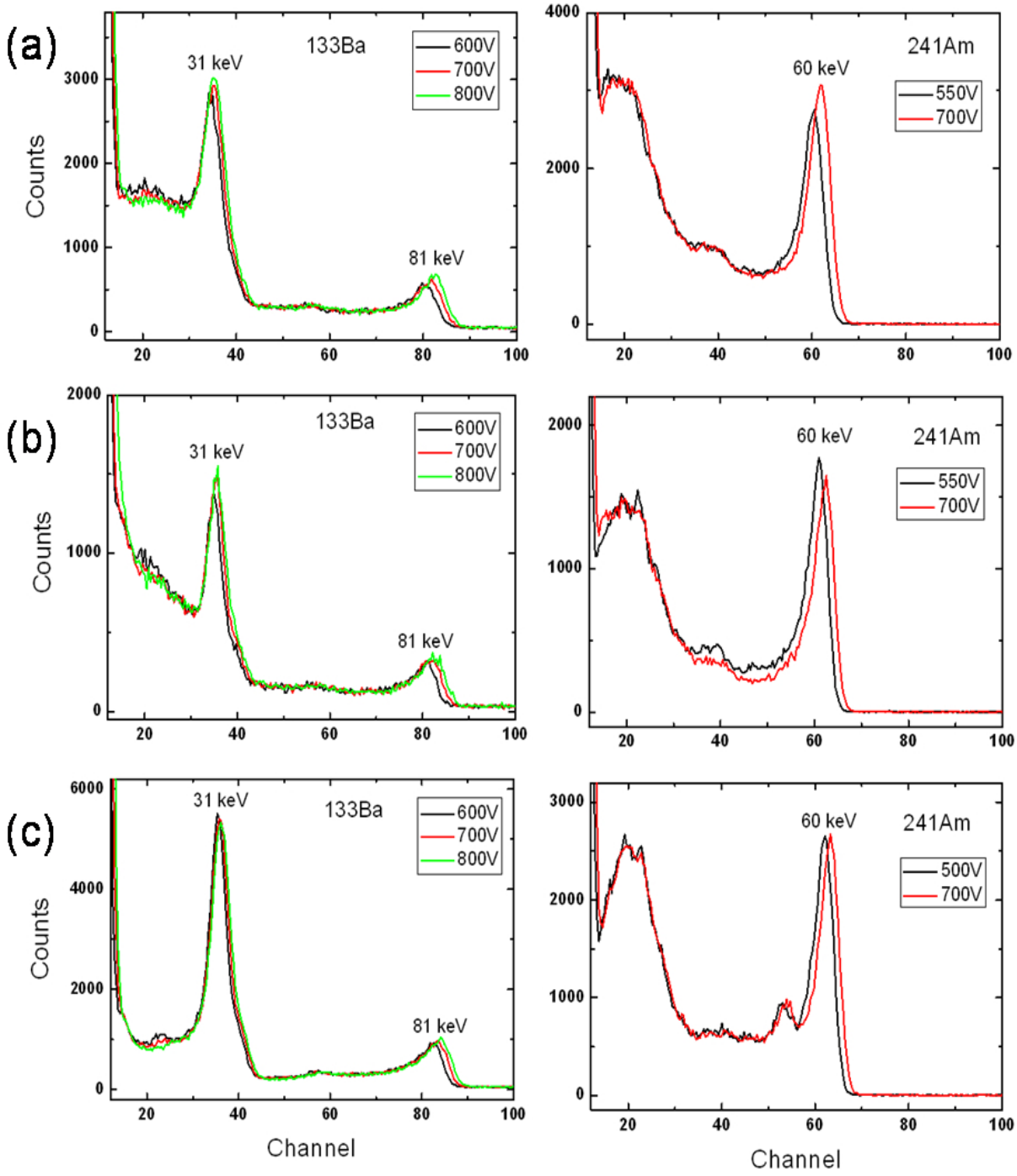

Figure 4.4. Room temperature gamma spectra (^{133}Ba and ^{241}Am) of CZT detectors fabricated by different Au deposition methods. (a) Sputtering, (b) Evaporation, (c) Electroless.

Table 4.2. Comparison of ^{133}Ba and ^{241}Am spectra of CZT detectors (700 V) fabricated by different Au deposition methods.

	Sputtering	Evaporation	Electroless
^{133}Ba 31 keV FWHM %	16.1	12.9	15.3
P/V of the 31 keV peak	1.9	2.2	5.6
Quality factor of the 31keV peak	0.34	0.41	0.60
^{133}Ba 81 keV FWHM %	8.0	7.9	8.4
P/V of the 81 keV peak	2.5	2.6	3.2
Quality factor of the 81 keV peak	0.56	0.57	0.62
^{241}Am 60 keV FWHM %	8.0	8.8	6.8
P/V of the 60 keV peak	4.8	7.4	4.7
Quality factor of the 60 keV peak	0.77	0.92	0.84

4.1.4. Conclusions

Three different deposition methods (Sputtering, Evaporation, and Electroless) have been investigated by PL, RBS, I-V, and gamma ray techniques in order to the find the best deposition method.

- The deposition of Au electrodes onto CZT material can reduce the effect of Cd vacancies by acting as Au donors, A-center decrease significantly after the Au deposition with the sputtering and evaporation methods but not with the electroless method.

- With electroless deposition method, the strong intermixing appear among Au, TeO_2 and CZT, the depth of TeO_2 layer between Au layer and CZT is much higher than the other two deposition methods. The sputtering method shows the thickest Te oxide layer, while the evaporation method displays the thinnest oxide layer at the interface.

- The Au contacts deposited by three different deposition methods have shown Schottky contact behaviours with different barrier height. The contacts deposited by electroless method exhibit better detector performance compared with the sputtering and evaporation deposition methods.

4.2. Optimisation of the Parameters for Preparation of Single Layer

4.2.1. Influence of the Deposition Time on the Quality of the Detectors

The quality of the contacts on CdTe/CZT material can be affected by several factors, including the contact material, the thickness and composition of the layers, the quality of the interfaces between the metal and semiconductor, the formation of an oxide layer, the mechanical induced stress and the corresponding electrical interactions, etc.

In this section, our objective is to study the effect of deposition times by the electroless method on CZT material. In order to understand the deposition process, Atomic Force Microscopy (AFM), Scanning Electron Microscope (SEM), Energy Dispersion X-ray (EDX), X-ray diffraction (XRD), and Rutherford Backscattering Spectroscopy (RBS) measurements have been carried out to give information about the surface and subsurface composition and structure of the deposited layers.

The CZT material used for this study was grown by VGF method and doped with indium of 3-5 ppm, the conductivity of the crystal is n-type. The dimension of the samples were 5×5×2 mm^3. The samples were lapped with 3 μm and 1 μm alumina powder, followed by a fine polishing using 1 μm diamond abrasive. Finally, they were chemically etched with 2 % Bromine/Methanol for 2 minutes and rinsed with methanol.

The contacts were deposited on the samples immediately after chemical etching in order to minimize the surface re-oxidation. The electroless solutions were prepared with 1 g of metal chloride salt of Au, Pt, or Ru, respectively, dissolved in 25 mL of de-ionized water. The deposition time was varied from 10 seconds to 5 hours.

4.2.1.1. Influence of the Deposition Time on the Surface Roughness

In this part, the work will be focused on the surface structure and roughness of the metallic film layers deposited on CZT with different the deposition time by using AFM.

Figure 4.5 presents the AFM 3D images of the surface of Au layers after different deposition times. The scanned areas of the surface are 10 μm × 10 μm. As we can observe, Au layers begin to grow as small clusters (after 10 seconds) and then, when time increases these

clusters coalesce and form an Au layer. When time increases (after 30 minutes), the clusters group together until the surface was entirely covered by the Au layer. When the deposition time increases even more to 1 hour, the Au layer is formed of larger clusters, and after 3 hours, we can observe a change in the morphology of the layer: Au begins to grow into islands. A possible reason for these modifications of morphology is the release of surface stress by relaxation. In fact, when the deposition time increases, the surface stress increases, leading to the release of elastic energy by the formation of bigger islands at a critical thickness.

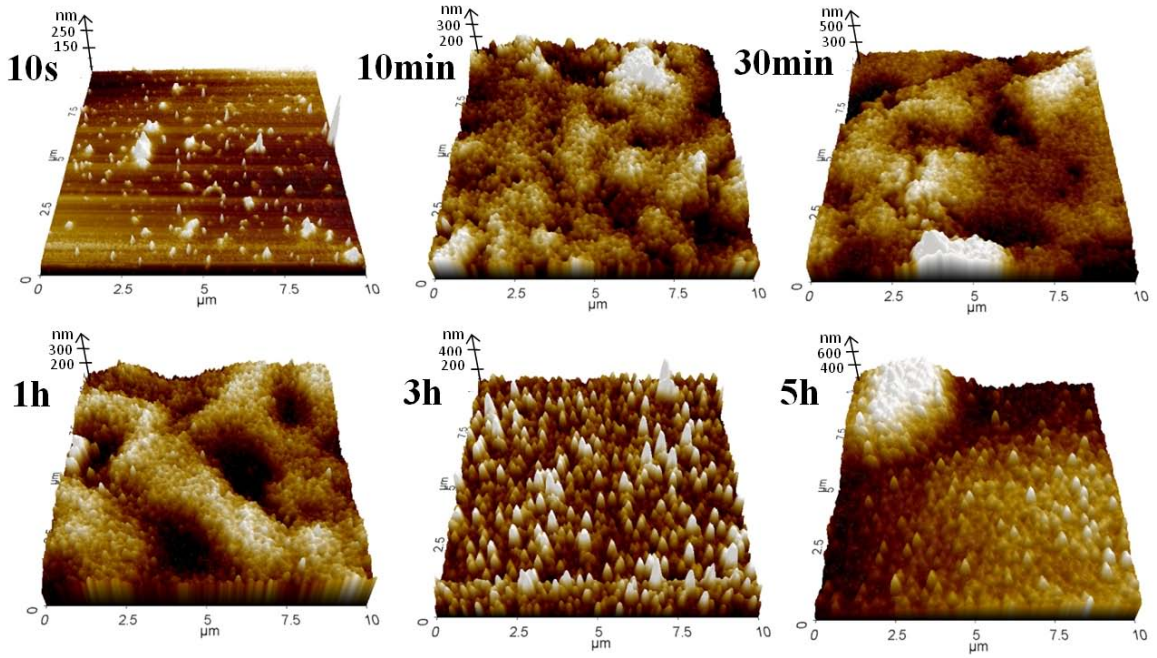

Figure 4.5. AFM 3D images of the surface of Au layers at different deposition time.

The growth behaviours of Pt layers on CZT are presented in Figure 4.6. One can observe that, after 10 s, the Pt layers grow as small clusters. These clusters coalesce when the deposition time increases, and then after a certain time the surface was fully covered by the Pt layer. Similarly, Figure 4.7 illustrates the AFM 3D images of the surface of Ru layers on CZT with different deposition time. As can be seen, the surface was not entirely covered by Ru layer even after 5 hours, indicating that the deposition rate of Ru layers is much slower than that of Au layers or Pt layers.

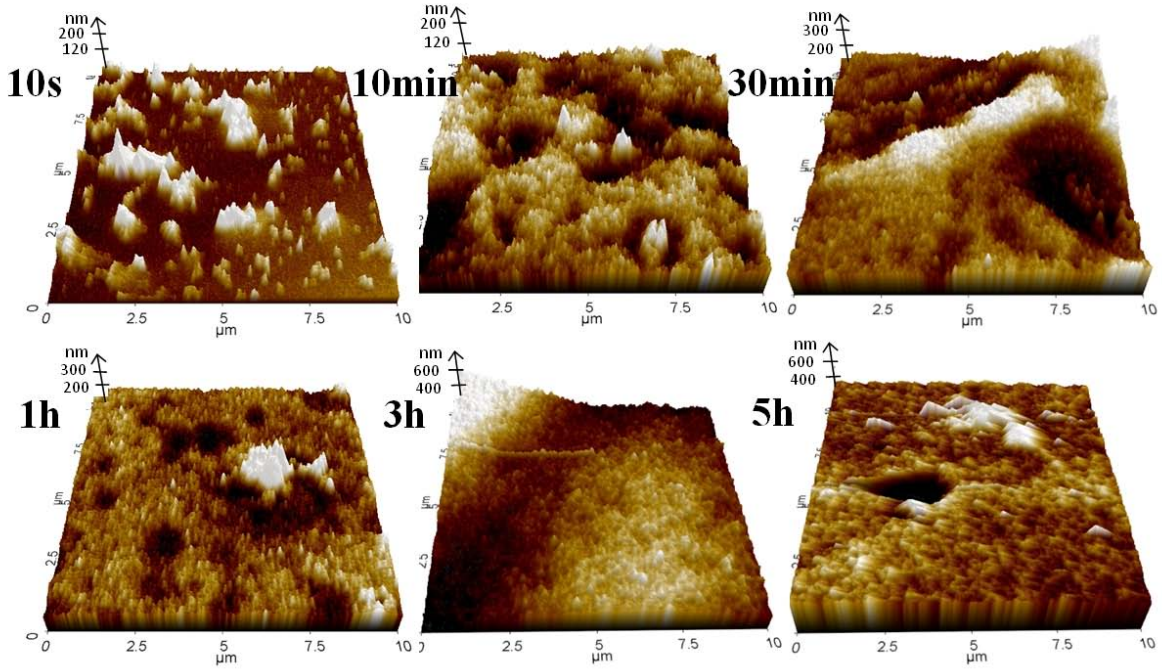

Figure 4.6. AFM 3D images of the surface of Pt layers at different deposition time.

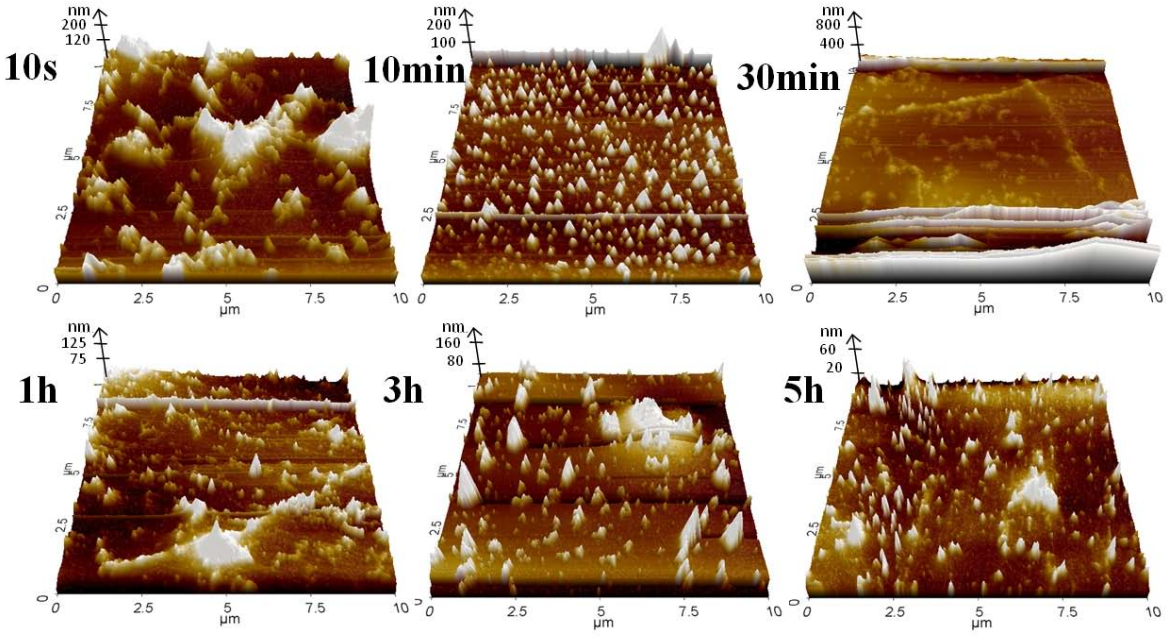

Figure 4.7. AFM 3D images of the surface of Ru layers at different deposition time.

In order to study the surface roughness of the metallic film layers on CZT with different deposition time, the average roughness values have been determined from an imaged area of 10 μm^2 which was representative of the topography of the samples.

Figure 4.8 shows the surface roughness (Ra) versus deposition time for different metallic film layers present on the surface determined by AFM. As can be seen, the roughness varies with deposition times, which is also consistent with the AFM 3D images exhibited in Figure 4.5, Figure 4.6, and Figure 4.7.

From the results, we observe the roughness of the growth layers is very time dependent, where maximum and minimum values are present. For Au layers, one can see that Ra reaches the maximum value of 20-30 nm for the deposition time at 10 min and 4 h, where the Au layers were deposited on CZT by small clusters.

Moreover, we can observe the roughness of Pt layer gradually increases with the deposition time, which is in agreement with the AFM 3D images shown in Figure 4.6, where a flat 2D surface can be obtained at 5 h, implying that the growth of Pt layers on CZT was followed by the clusters coalesced until entirely covered the surface.

Furthermore, we can observe the average roughness of Ru layers on CZT decreases with deposition time, which could be explained by the fact that the deposition rate of Ru layers was much lower than the Au layers or Ru layers. The results can be related with the AFM 3D images displayed in Figure 4.7, where the surface was still covered by small clusters even after 5 h of deposition.

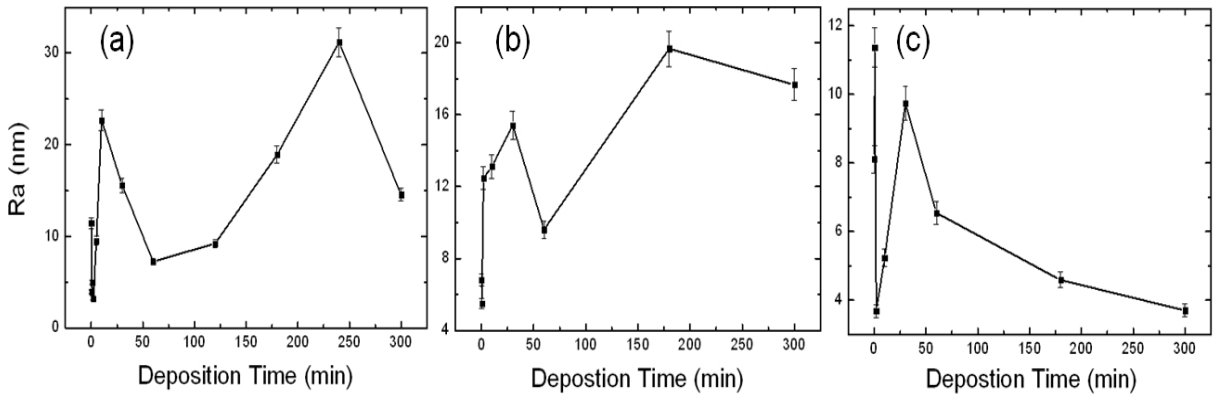

Figure 4.8. Surface roughness versus deposition time of different film layers on CZT measured by AFM. (a) Au layer, (b) Pt layer, (c) Ru layer.

4.2.2.2. Influence of the Deposition Time on Surface Morphology

The surface morphology of the deposited layers on CZT materials has been investigated in order to further understand the growth behaviours of the metallic films. Low magnification

images were studied by the Hitachi S-3000N SEM to provide the topography and morphology information of contacts surface, while high magnification images were studied by using Philips XL 30S-FEG high resolution SEM equipment in order to compare the morphology of contacts, meanwhile, the thickness of the metallic thin film layers was evaluated by the cross section of the samples.

Figure 4.9 and Figure 4.10 exhibit the SEM images of the Au layers with different deposition time at low magnification and high magnification, respectively. As can be seen in Figure 4.9, at low magnification, no micro-cracks can be observed with the surface of Au layer, however, the morphology of the surface of Au layers altered to larger cluster size, which is supposed to be related with the surface stress.

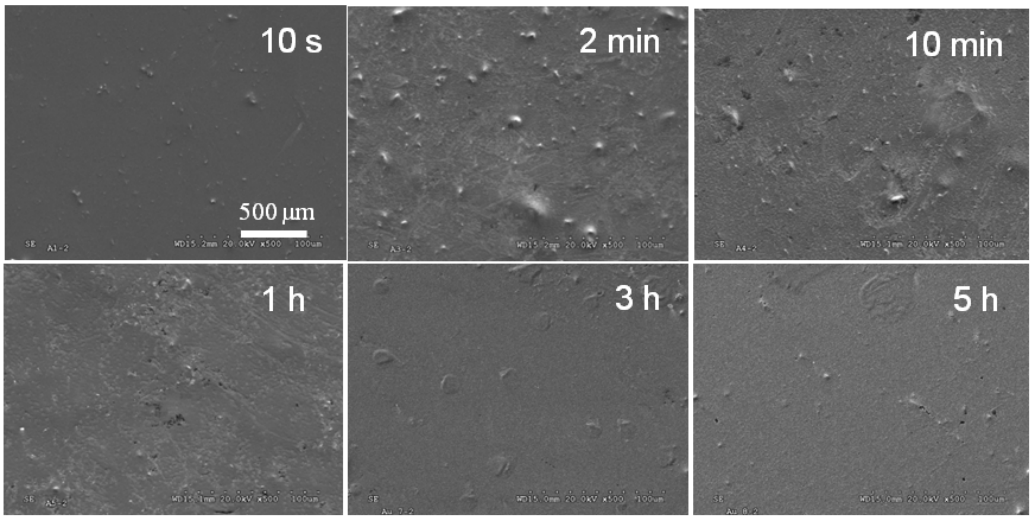

Figure 4.9. SEM images at lower magnification of different time of Au deposition on CZT by electroless method, the same scale of 500 µm was presented.

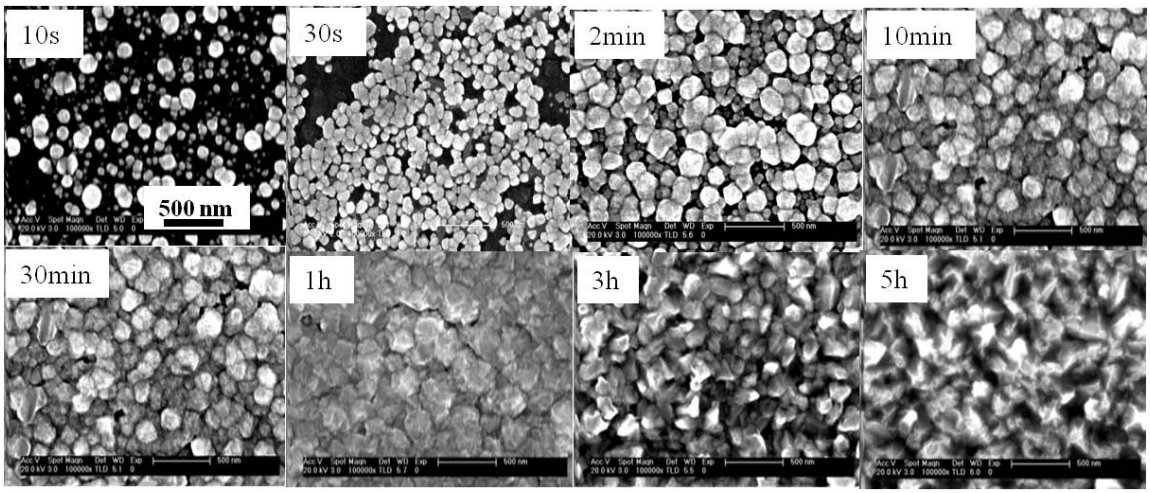

Figure 4.10. SEM images at higher magnification of different time of Au deposition on CZT by electroless method, the same scale of 500 nm was displayed.

At high magnification presented in Figure 4.10, one can observe that the morphology of Au layers varies with time, especially at short deposition time (10 s - 10 min), the size of Au clusters increase with time. Moreover, one can see that, at long deposition time (3 h - 5 h), the morphology of Au clusters seems to be larger and stable.

For the deposition of Pt layers, the morphology of the layers is presented in Figure 4.11 and Figure 4.12 at different magnifications. In Figure 4.11, at lower magnification, the SEM images show a flat surface with a gradual covering by the Pt layers at short deposition time (10 s - 2 min). At 10 min, micro-cracks can be seen on the CZT surface which is different from the deposition of Au layers. As shown in Figure 4.12, we can observe the changes of the morphology of Pt layers with different deposition time at high magnification of 10k ×. It is remarkable that the morphology changes from round-shape to elongated shape after 30 min of growth of the metallic film layers.

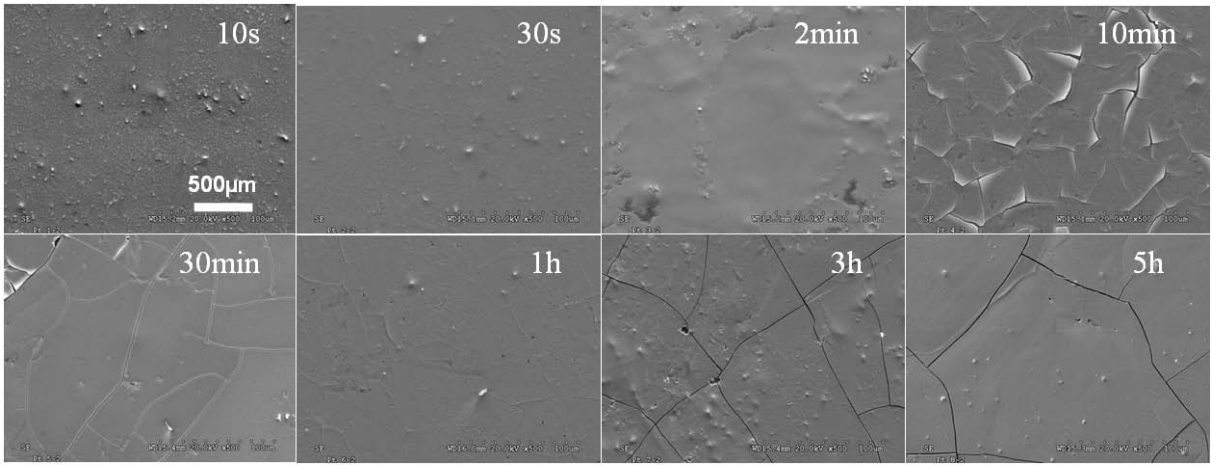

Figure 4.11. SEM images at lower magnification of the surface of Pt layer on CZT at different deposition time, the same scale of 500 µm was presnted.

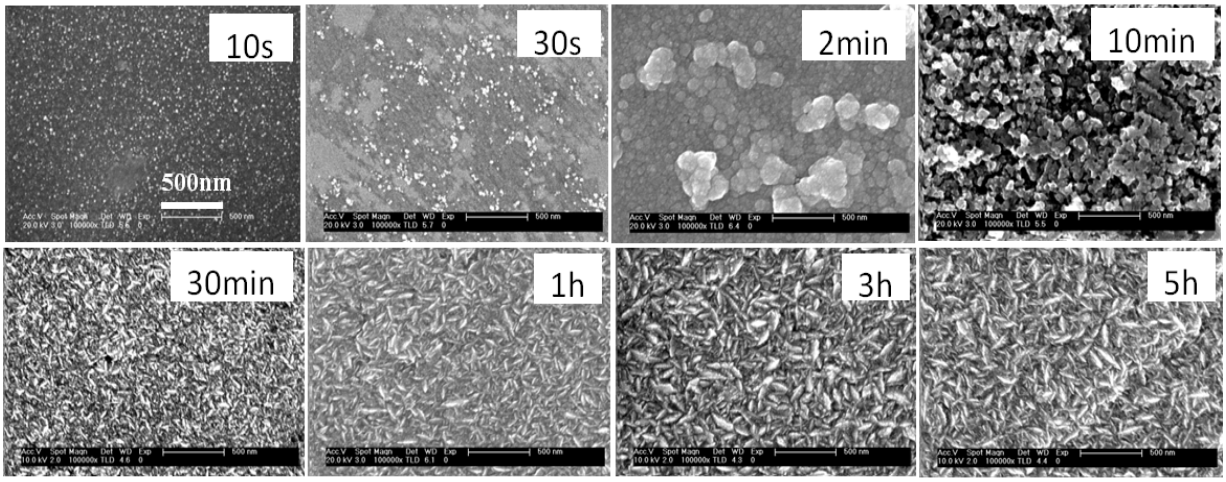

Figure 4.12. SEM images at higher magnification of the surface of Pt layer on CZT at different deposition time, the same scale of 500 nm was displayed.

For Ru layers, the SEM images of the surface of Ru layers at low and high magnifications are presented in Figure 4.13 and Figure 4.14. As can be seen in Figure 4.13, the surface of Ru layers shows similarity to the surface of Pt layers, where the appearance of micro-cracks on the surface of the deposited layer. At a certain time close to 30 min, micro-cracks appear and seem to be oriented in one direction on the surface of CZT material. When the deposition time increases, the micro-cracks seems to grow and merge together, at 3 hours of deposition, the Ru layers have the tendency to be peeling off from the substrate.

In Figure 4.14, at higher magnification, one can observe a much slower growth of Ru layers on CZT compared with Au layers or Pt layers, the surface is not entirely covered by Ru layers even after 5 h, implying that the deposition kinetics of Ru layers on CZT is lower than that of Au layers or Pt layers.

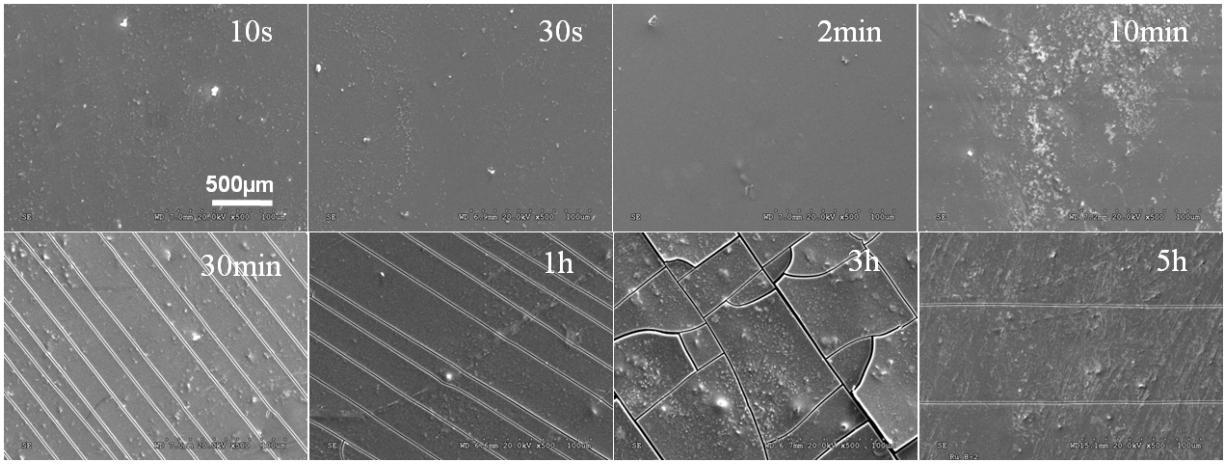

Figure 4.13. SEM images at lower magnification of the surface of Ru layer on CZT at different deposition time, the same scale of 500 µm was presented.

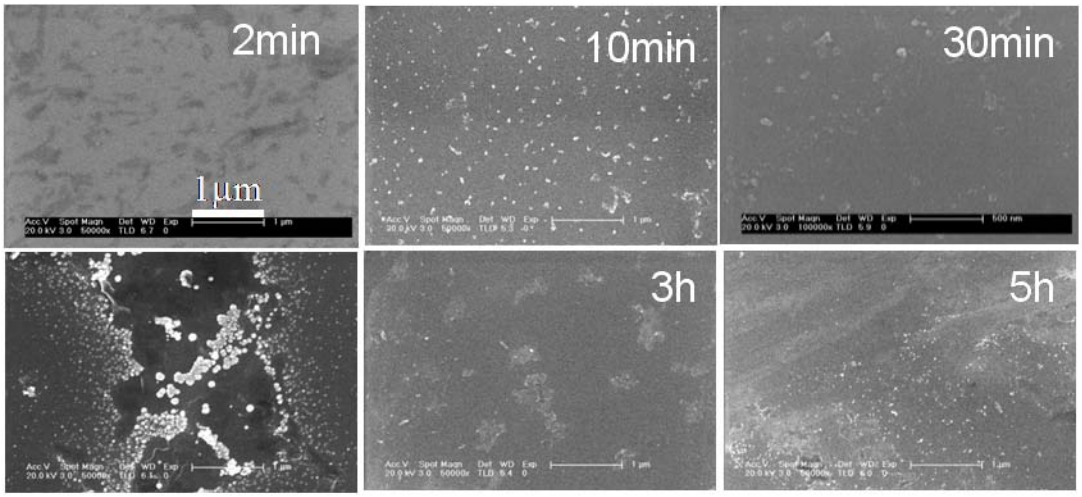

Figure 4.14. SEM images at higher magnification of the surface of Ru layer on CZT at different deposition time, the same scale of 1 µm was displayed.

In fact, when the deposition time of metallic film layers increases, surface stress is developing into the thin films and the morphology of the surface is altered. Due to the difference of lattice constants between the film and the substrate, misfit stress arises when the deposition time increases, the information is shown in Table 4.3.

Table 4.3. Parameter of the contact materials.

	Young's Modulus (GPa)	Hardness (GPa)	Lattice Constant (Å)	Lattice Mismatch with CZT
Au	79	2.5-3	4.1	37 %
Pt	168	4.3	3.9	39 %
Ru	286	6.5	2.7	58 %

Bottiger et al. demonstrated that the stress of the films can be released by the formation of misfit dislocations at a critical film thickness, which is depending on the metal contacts and methods of deposition [12]. Several impurities, such as Cl^-, can be incorporated into the films during the deposition process and affect the stress.

As we can see from Figure 4.9, surface stress is released and the morphology of the Au layers is modified when the thickness of Au layers reaches a certain value, and thus bigger clusters can be observed after 3 hours of deposition. For the deposition Pt or Ru layers on CZT (see Figure 4.11 and Figure 4.13), when a critical thickness is reached, one can deduce that a non equilibrium phase of metastable growth follows and misfit dislocations can be relieved, which lead to the creation of macroscopic cracks at the surface of the contacts.

To explain the micro-cracks behaviours discussed above, Young's modulus of the metallic films is considered, which is a measure of the stiffness of an elastic material and is a quantity used to characterize materials. It is defined as the ratio of the uniaxial stress over the uniaxial strain in the range of stress in which Hooke's Law holds. Young's modulus may have different values depending on the direction of the applied force with respect to the material's structure.

Young's modulus (E) can be calculated by dividing the tensile stress by the tensile strain in the elastic (linear) portion of the stress-strain curve:

$$E = \frac{\sigma}{\varepsilon} \qquad \text{Eq. 4-5}$$

where σ is the tensile stress, ε is the tensile strain. This relationship only applies in the elastic range and indicates that the slope of the stress versus strain curve can be used to find Young's modulus.

As shown in Table 4.3, the Young's modulus value of Au, Pt, and Ru are 79 GPa, 168 GPa, and 286 GPa, respectively. In fact, the hardness also displays similar tendency for three metals. Au has a smaller Young's modulus and harness, implying that Au films have higher elasticity and can support more tensile strain than Pt and Ru when the same stress is applied. Ru has a larger lattice mismatch with CZT, a larger Young's modulus and a larger hardness value, which leads to the appearance of micro-cracks at a thinner metallic layer thickness than in the case of Pt layers.

In order to understand the orientation of the deposited films which presented micro-cracks behaviours (Pt or Ru layers), the structural properties of the layers have been studied by the XRD technique. Figure 4.15 exhibits the XRD patterns of the Pt or Ru layers deposited on CZT material. It is important to mention that the CZT materials used for investigation are polycrystalline.

We can observe that Pt layers do not present any preferential directions (shown in Figure 4.15), thereby different orientations can be observed (such as (111) and (200)), revealing that Pt film is polycrystalline. However, Ru films show the same orientation (such as (100) and (200)), meaning that the Ru layers are monocrystalline, suggesting that the Ru layers are epitaxial grown on CZT.

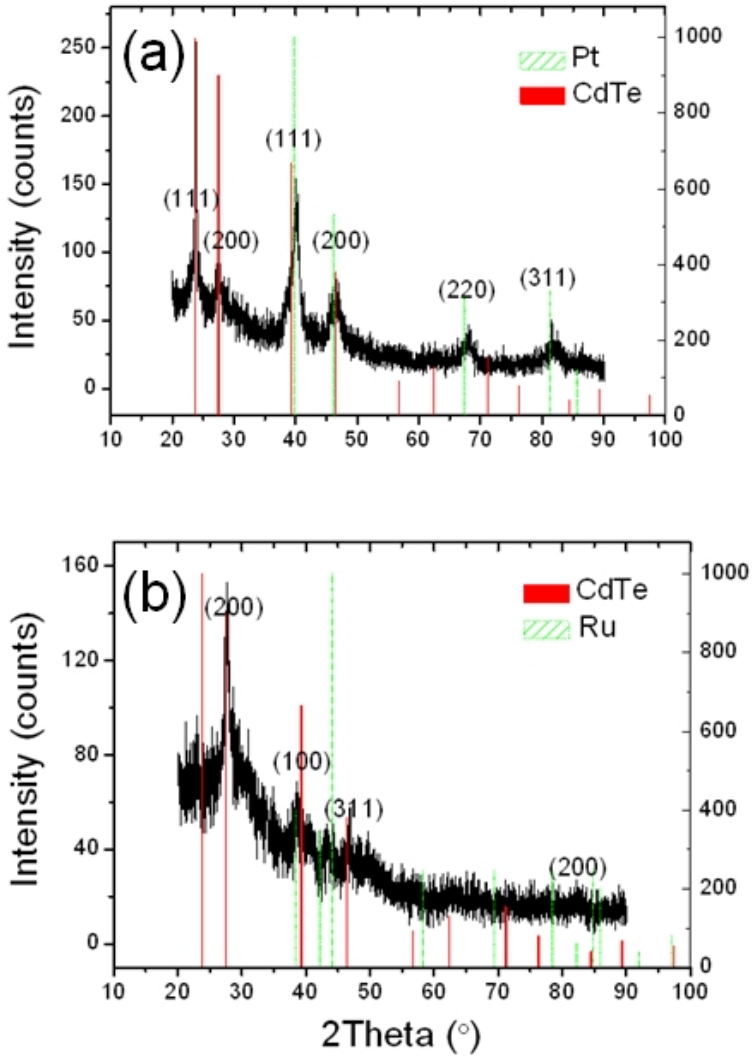

Figure 4.15. XRD Patterns of the metallic film on CZT after 30 min of deposition. (a) Pt layer, (b) Ru layer.

4.2.2.3. Influence of the Deposition Time on the Relative Atomic Concentration

The EDX results can give useful information about the composition of the layers. The relative atomic concentrations of the main elements with different deposition time on the surface and subsurface of CZT are exhibited in Figure 4.16. It is necessary to note that the relative atomic concentrations of Cd, Zn, Te, and the metal contacts (Au, Pt, or Ru) sum to 100 %.

As can be observed, the relative atomic concentration of the metallic elements increases as the deposition time increases, therefore, the relative atomic concentration of others elements

(Cd, Zn, Te) decreases. Indeed, as we can see in Figure 4.16 (a) and (b), when the deposition time increases, the concentration of Cd and Te decreases, whereas the concentration of Au or Pt increases rapidly with time.

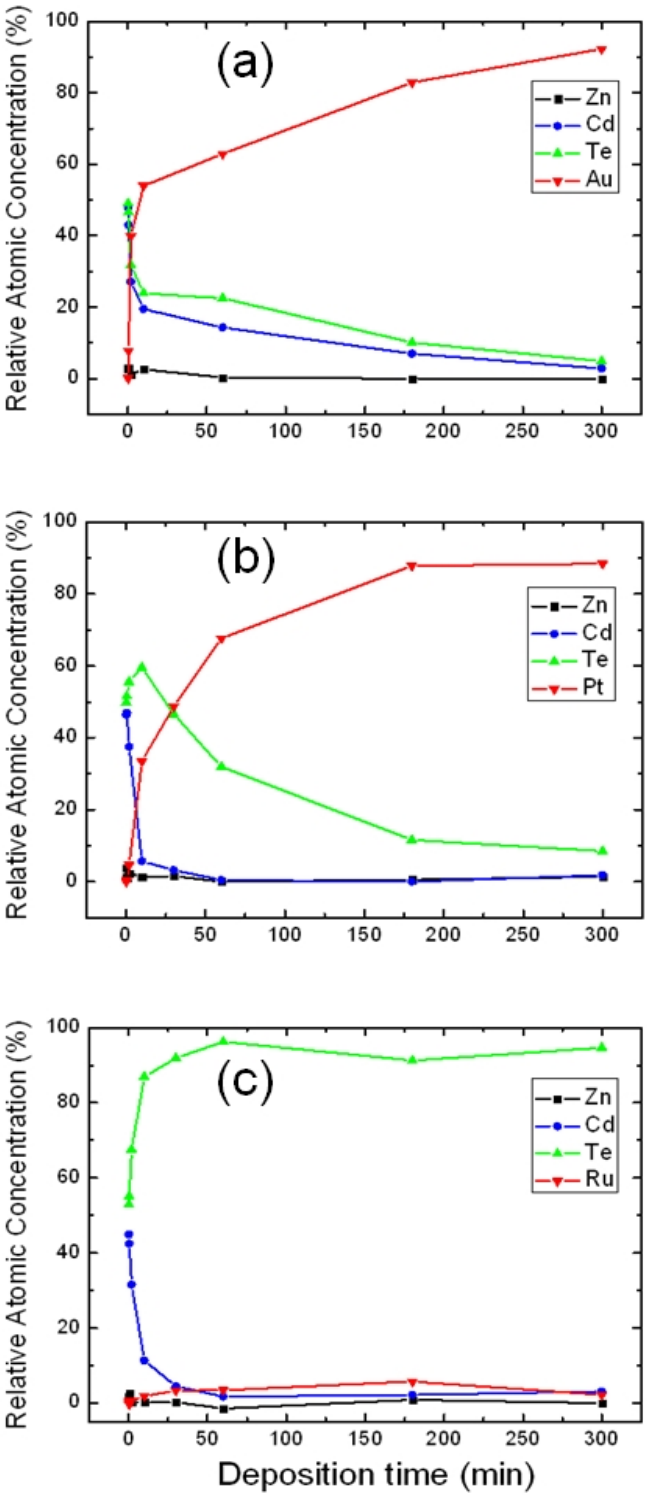

Figure 4.16. EDX figures of the main elements on the surface of CZT. (a) Au layer, (b) Pt layer, (c) Ru layer.

These behaviours can be understood if we consider the chemical reactions happening in the electroless solutions. For the deposition of Au layers, when the samples are dipped into $AuCl_3$ aqueous solution, the $AuCl_4^-$ ions are supposed to react with Cd, Zn, and Te. Due to the fact that the composition of Zn in the $Cd_{1-x}Zn_xTe$ crystal is in minority (~ 10 % in our case), the reaction of Au ions with Zn is negligible in comparison of Cd (Eq. 4-7).

Meanwhile, the difference of standard potentials of the reaction between $AuCl_4^-$ and Cd is higher than the one between $AuCl_4^-$ and Te, which means that Au reacts preferentially with Cd. Therefore, the aqueous solution of $AuCl_3$ with CZT involves a majority transfer of Cd^{2+} ions into the solution, leaving a Te rich layer on the surface, and a precipitation of Au layer to compensate the electrochemical equilibrium, as displayed in Eq. 4-6 — Eq. 4-9 [13][14]. As a result, one can observe in Figure 4.16 (a) that the relative atomic concentration of Cd decreases faster than Te.

Indeed, when Cd react with $AuCl_4^-$ ions (Eq. 4-6), an oxide-reduction reaction takes place, where the oxidation reaction was chosen as $AuCl_4^-+3e\leftrightarrow Au(s)+4Cl^-$, with a standard potential of +1.00 V, and the reduction reaction occurring with Cd is $Cd^{2+}+2e\leftrightarrow Cd(s)$, with a standard potential of –0.4 V. Therefore, the redox reaction between $AuCl_4^-$ ions and Cd can be obtained in Eq. 4-6, where the potential difference is calculated as +1.40 V.

It is important to comment that only when the potential difference is positive, the reaction is supposed to happen. The potential difference of redox reaction means that the reaction is total and consequently strongly shifted to one direction. In addition, the reaction of Au deposition is a direct reaction. For the redox reactions between $AuCl_4^-$ ions and Te, two possible reactions are presumed (Eq. 4-8 and Eq. 4-9). It should be noted that the Au contact solutions were prepared in acid environment, where the presence of hydroxide ions OH^- can be considered negligible and its concentration is much smaller than the concentration of H^+ [15]. In consequence, the reaction of $AuCl_4^-$ ions with Te shown in Eq. 4-9 is preferable.

These behaviours can be expressed by these thermodynamics equations for the standard hydrogen electrode (SHE) [15][16]:

$$2AuCl_4^- + 3Cd(s) \rightarrow 2Au(s) + 8Cl^- + 3Cd^{2+} \qquad \Delta E^0 = +1.40\ V \qquad \text{Eq. 4-6}$$

$$2AuCl_4^- + 3Zn(s) \rightarrow 2Au(s) + 8Cl^- + 3Zn^{2+} \qquad \Delta E^0 = +1.76\ V \qquad \text{Eq. 4-7}$$

$$4AuCl_4^- + 3Te(s) \rightarrow 4Au(s) + 16Cl^- + 3Te^{4+} \qquad \Delta E^0 = +0.43\ V \qquad \text{Eq. 4-8}$$

$4AuCl_4^- + 3Te + 6H_2O \rightarrow 4Au(s) + 16Cl^- + 3TeO_2 + 12H^+$ ΔE^0 = + 0.41 V Eq. 4-9

The relative atomic concentration of Cd decreases faster in the case of Pt deposition than Au deposition (see Figure 4.16), which is probably due to the double consumption in the chemical reaction of Pt deposition (Eq. 4-10 — Eq. 4-15) in opposition of the chemical reaction of deposition of the Au contacts (Eq.4-6 — Eq. 4-9).

One can observe in Figure 4.16 (c) that, the relative atomic concentration of Ru increases very slowly for the deposition time from 10 s to 5 h, means that the deposition rate of Ru layer on CZT is much lower than that of Au layer or Pt layer. We can assume the reason could be that the kinetics of transfer from Ru^{3+} ions into Ru^{2+} ions is much faster than the kinetics of transfer from Ru^{2+} ions into Ru (Eq. 4-16 - Eq. 4-21) [15][17].

The deposition reactions of Pt and Ru are described as following as a succession of reactions by using intermediate ions which are $PtCl_4^{2-}$ for Pt and Ru^{2+} for Ru:

$PtCl_6^{2-} + Cd(s) \rightarrow PtCl_4^{2-} + 2Cl^- + Cd^{2+}$ ΔE^0= + 1.08 V Eq. 4-10

$PtCl_4^{2-} + Cd(s) \rightarrow Pt(s) + 4Cl^- + Cd^{2+}$ ΔE^0= + 1.16 V Eq. 4-11

$2PtCl_6^{2-} + Te(s) \rightarrow 2PtCl_4^{2-} + 4Cl^- + Te^{4+}$ ΔE^0= + 0.11 V Eq. 4-12

$2PtCl_4^{2-} + Te(s) \rightarrow 2Pt(s) + 8Cl^- + Te^{4+}$ ΔE^0= + 0.19 V Eq. 4-13

$2PtCl_6^{2-} + Te(s) + 2H_2O \rightarrow 2PtCl_4^{2-} + 4Cl^- + TeO_2 + 4H^+$ ΔE^0= + 0.09 V Eq. 4-14

$2PtCl_4^{2-} + Te(s) + 2H_2O \rightarrow 2Pt(s) + 8Cl^- + TeO_2 + 4H^+$ ΔE^0= + 0.16 V Eq. 4-15

$2Ru^{3+} + Cd(s) \rightarrow 2Ru^{2+} + Cd^{2+}$ ΔE^0= + 0.65 V Eq. 4-16

$Ru^{2+} + Cd(s) \rightarrow Ru(s) + Cd^{2+}$ ΔE^0= + 0.85 V Eq. 4-17

$4Ru^{3+} + Te(s) \rightarrow 4Ru^{2+} + Te^{4+}$ ΔE^0= - 0.32 V Eq. 4-18

$2Ru^{2+} + Te(s) \rightarrow 2Ru(s) + Te^{4+}$ ΔE^0= + 0.23V Eq. 4-19

$4Ru^{3+} + Te(s) + 2H_2O \rightarrow 4Ru^{2+} + TeO_2 + 4H^+$ ΔE^0= - 0.34 V Eq. 4-20

$2Ru^{2+} + Te(s) + 2H_2O \rightarrow 2Ru(s) + TeO_2 + 4H^+$ ΔE^0= + 0.21 V Eq. 4-21

As can be seen, the potential difference of the redox reaction presented in Eq. 4-18 and Eq. 4-20 are negative value, implying that these two spontaneous reactions are impossible to happen.

Similarly, the Pt solutions or Ru solutions used for investigation were prepared in acid environment (see section 3.4.3), thereby the reactions with Te is preferentially occur with H^+ (Eq. 4-14, Eq. 4-15, Eq. 4-20, Eq. 4-21).

Furthermore, one also observe that the potential difference of the reaction of Pt (Eq. 4-11) or Ru (Eq. 4-17) solutions with Cd is higher than react with Te, which means that the majority of the reactions between CZT and the Pt or Ru solutions are between Cd and the contact metals. We can conclude that the reactions between the electroless solutions and CZT are preferentially occur with Cd, which is in consistence with the other references [13][15]. In these thermodynamics equations, we can also conclude that the surface will become richer in tellurium due to the Cd vacancies created during the different depositions.

4.2.2.4. Influence of the Deposition Time on the Thickness of the Layer

RBS technique was used to have a better understanding about the diffusion profiles and the interface composition. The thickness of Au layers was studied by RBS technique in order to understand the deposition kinetics and determine the optimum deposition time. It should be noted that even though the thickness of Pt or Ru layers was not determined by RBS technique, the SEM technique was carried out to estimate the thickness of these three metallic layers.

Figure 4.17 exhibits the best layer structures after the fitting process. In all cases an inter-diffusion region between the Au layer and CZT bulk material can be observed as well as a significant concentration of TeO_2. At a short deposition times (see Figure 4.17 (a), (b), (c)), the thickness of Au layers increases as the deposition time arises. For a longer deposition time (as shown in Figure 4.17 (d), (e)), the growth rate of Au layers slows down and seems to saturate, whereas the TeO_2 layer becomes thicker.

This tendency can be explained by the fact that the contact deposited on CZT has a porous structure, as shown in Figure 4.5. Indeed, Au preferentially reacts with Cd, leading to the formation of Te and the reject of Cd^{2+} into the solution, but after a longer deposition time, less Cd exists at the surface, less Au can be deposited on CZT, therefore the reaction of the

oxidation of Te with the oxidant ions is emphasized, mainly leading to a higher density of TeO_2 layer created with deposition time.

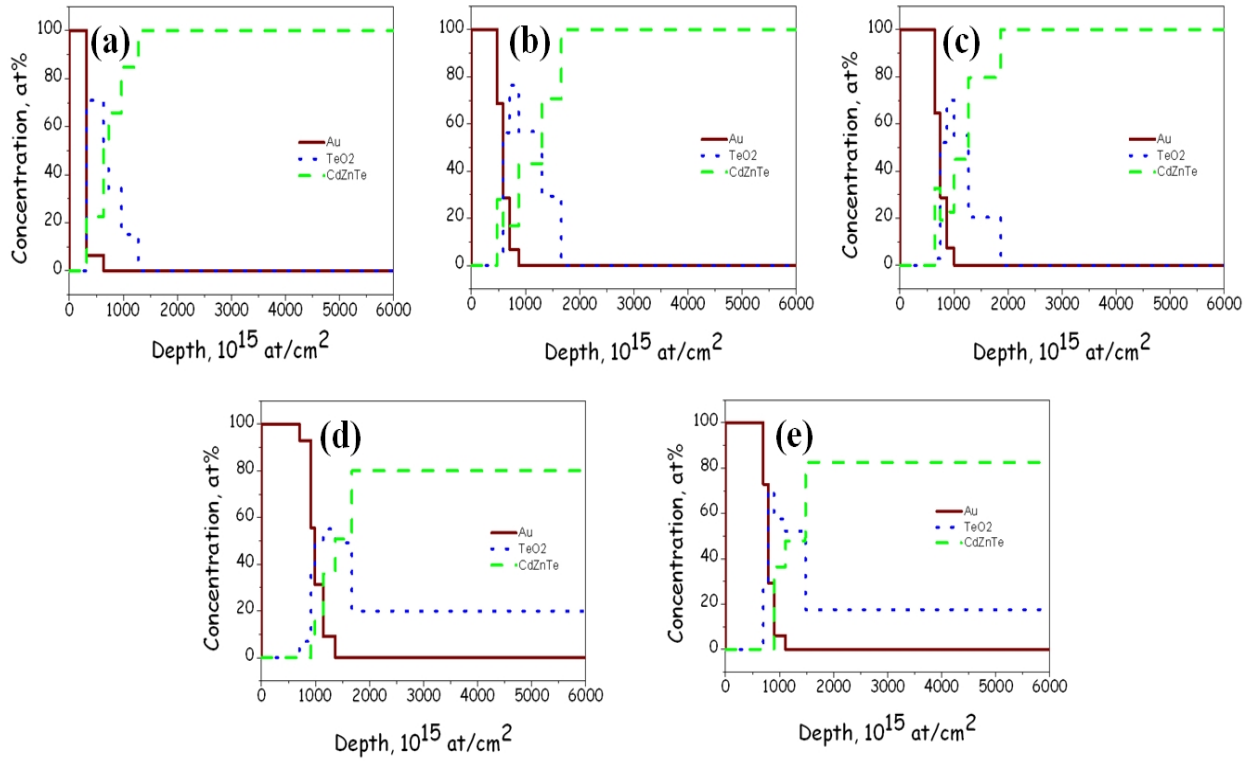

Figure 4.17. RBS depth profiles of elements on the substrate till reaching the stoichiometric compositions of CZT. (a) 2 min, (b) 10 min, (c) 30 min, (d) 3 h, (e) 5h.

Figure 4.18 displays the thickness of Au layer deposited on CZT as a function of time by the electroless method which has been evaluated by RBS. In fact, this figure displays a behaviour which is in agreement with the previous results shown in Figure 4.17. Before 1 hour, a fast growth of Au layer deposited on the CZT material, however, after a long time, the thickness of Au layer saturates asymptotically at a value of 120 nm, which was supposed by a fast reaction with Cd sites and reduction of the kinetics of deposition when less Cd sites are available.

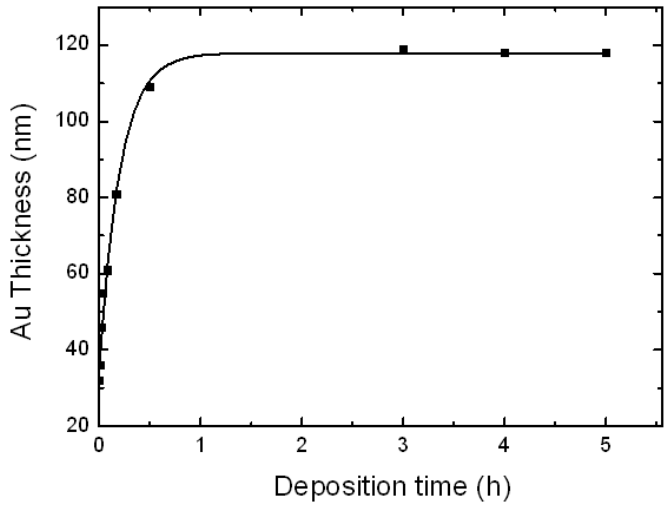

Figure 4.18. The thickness of Au layers deposited on CZT as a function of deposition time calculated by RBS.

The thickness of the metallic films layers has been estimated by the high resolution SEM technique, which was used to characterize the cross section of the samples where the layers thickness can be evaluated.

Figure 4.19 displays the images of the contacts layers deposited on the surface of CZT materials. In fact, different metallic films layers at 1 hour of deposition time were presented for one example for comparison, the thickness at different deposition times will be displayed in Table 4.4. As can be seen in Figure 4.19, after 1 hour of deposition, the thickness of the detached layer at the edge of the samples for deposition of Au layer, Pt layer and Ru layer can be estimated at approximately 110 nm, 220 nm, 30 nm, respectively. Indeed, the thickness of Au layer estimated by SEM is in consistent with the value estimated by RBS technique.

As shown in Table 4.4, the thickness of Au, Pt, or Ru layers increases with the deposition times. At short deposition time (e.g. 10 min), the thickness of Au layer is quite similar with that of Pt layer, indicate a similar deposition rate. However, at long deposition time from 1 h, one can observe the dramatically increase of the Pt thickness, which is much thicker than the Au layer, revealing that the double reactions of Pt deposition and the single reaction of Au deposition described above in Eq. 4-6 Eq. 4-15 could explained this behaviour. Moreover, one can see the much smaller Ru deposited layer on CZT, at about 40 nm even after 5 hours

of deposition, implies that the kinetics of the chemical reactions should be studied in the future work in order to understand these behaviours.

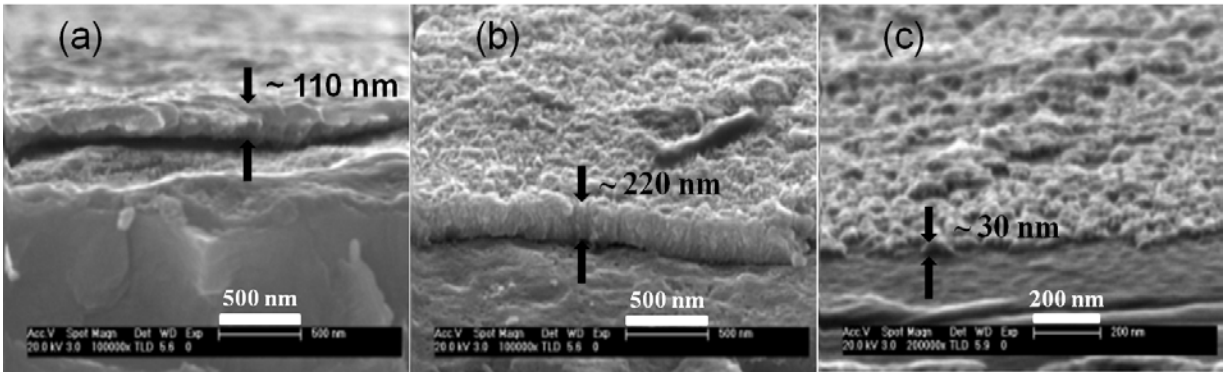

Figure 4.19. SEM images of the metallic layers at 1 hour of deposition on CZT. (a) Au layer, (b) Pt layer, (c) Ru layer.

Table 4.4. The thickness of Au, Pt, or Ru layers with different deposition time estimated by SEM technique.

	Au	Pt	Ru
2 min	~ 50 nm	~ 50 nm	N/A
10 min	~ 90 nm	80~90 nm	N/A
1 h	~ 110 nm	~ 220 nm	~30 nm
3 h	~ 130 nm	~ 380 nm	30~40 nm
5 h	~ 140 nm	660~700 nm	~ 40 nm

Due to the fact that the Pt or Ru layers on CZT could be broken (micro-cracks), the thickness of the layers could be overestimated, hence the SE and BSE images of the cross section of the samples were investigated.

Figure 4.20 illustrates the high resolution SE images and BSE images of the Pt layers deposited on CZT with 5 hours deposition time, while the images of Ru layers were not presented here because of the much smaller thickness hardly to be identified. It should be mentioned that only at longer deposition are exhibited in order to recognise the structure of Pt layer with micro-cracks and the peeling off behaviour.

As we can observe, the thickness of Pt layers after 5 hours of deposition reaches a value of around 660 nm. Meanwhile, one can see a few Pt layers present on the substrate, which is

probably due to the cracks of the Pt layer leading to the peeling off of the contact after 5 hours of deposition.

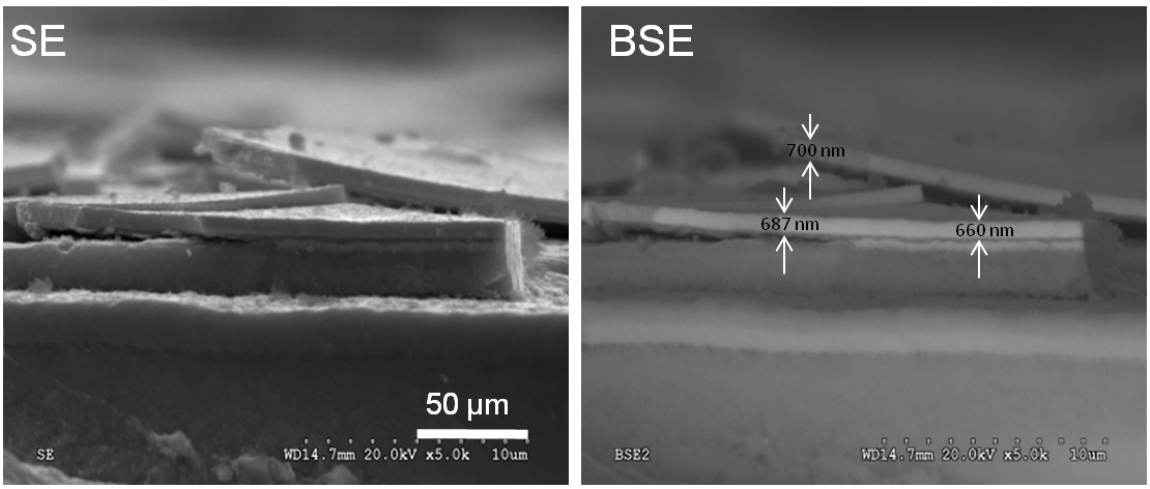

Figure 4.20. SEM image and backscatted SEM image of the Pt layer on CZT after 5 hours of deposition.

4.2.2. Effect of an Annealing Step on the Contact

It is accepted that the contacts between the metal and semiconductor have a critical affect on the performance of detectors [18]. The post annealing treatment of the fabricated detectors is reported to be an important process to increase the bulk resistivity of CdTe and CZT material and improve the detector performance [19].

Mergui et al. investigated the thermal annealing of the contacts of the CdZnTe detectors in air, vacuum, and hydrogen atmosphere. They reported that the detectors annealed in air achieved better detector performance, while the annealing under vacuum and hydrogen results in poor detector performance [20].

Chattopadhyay et al. reported the annealing effect Au conatcts on CdTe and CZT detectors under vacuum after heat treatments in the temperature range of 150 - 200 °C [21]. They demonstrated that Au diffuses into CdTe and CZT material and changes the electrical properties of the interfacial layer after the annealing treatment, leading to the reduction of barrier height, increase of noise in device, and degradation of the detector performance. When the annealing step is carried out for a long time or at high temperature, the deep level defects are introduced into the crystal and can deteriorate the detectors [21].

Shi et al. treated the Au contact of CZT strip detectors with annealing under vacuum, they proved that the leakage current was decreased below 150 °C but increased at 170 °C. This treatment was reported to improve the adhesion of the metal to CZT for wire bonding and also increased the interstrip resistance [22]. *Park et al.* researched the post thermal annealing effect on the Schottky detector with Au/CZT/In contact. They exhibited that the low temperature annealing at 130 °C especially under air can reduce the leakage current and enhance the detector performance [23].

In this section, the relationship between the annealing treatment and leakage current with different Au deposition methods which has been investigated in section 4.1 will be further studied, in order to understand the effect of the annealing step on the adhesion of the metal and semiconductor with different deposition methods.

The samples with the size of $5 \times 5 \times 2$ mm^3 from the same wafer of the crystal grown by VGF method was employed. The samples were fine polished and chemical etched with 2 % Br-Methanol for 2 min. Au electrode was deposited on the samples by using sputtering, evaporation, and electroless method, respectively.

The thermal annealing treatment of Au contacts on CZT was carried out under air at the same temperature (373 K) for different holding time. It is necessary to mention that different annealing temperature and annealing time were carried out to studied the annealing effect, here only present the same temperature with different time in order to understand the leakage current behaviour and find the optimum annealing time.

Figure 4.21 displays the I-V characteristics of different annealing time at 373 K in air. With the sputtered Au contact, we can observe that the leakage current continually reduces as the annealing time increases. Particularly, the leakage current is significantly reduced after the annealing step for 32 hours. We assume that the adhesion of the Au contact deposited by sputtering method is not strong enough due to the presence of thick Te oxide and the annealing step can enhance the adhesion between the contact and CZT by Au diffusion mechanism. For the evaporated Au, the leakage current of the detector increases with annealing time. For the detector with Au contact by electroless method, one can observe unobvious change of leakage current by annealing step for annealing time below 26 hours. In the case of n-type material, it is known that Au leads to a Schottky barrier. As can be seen, a small barrier height appears around 0 V.

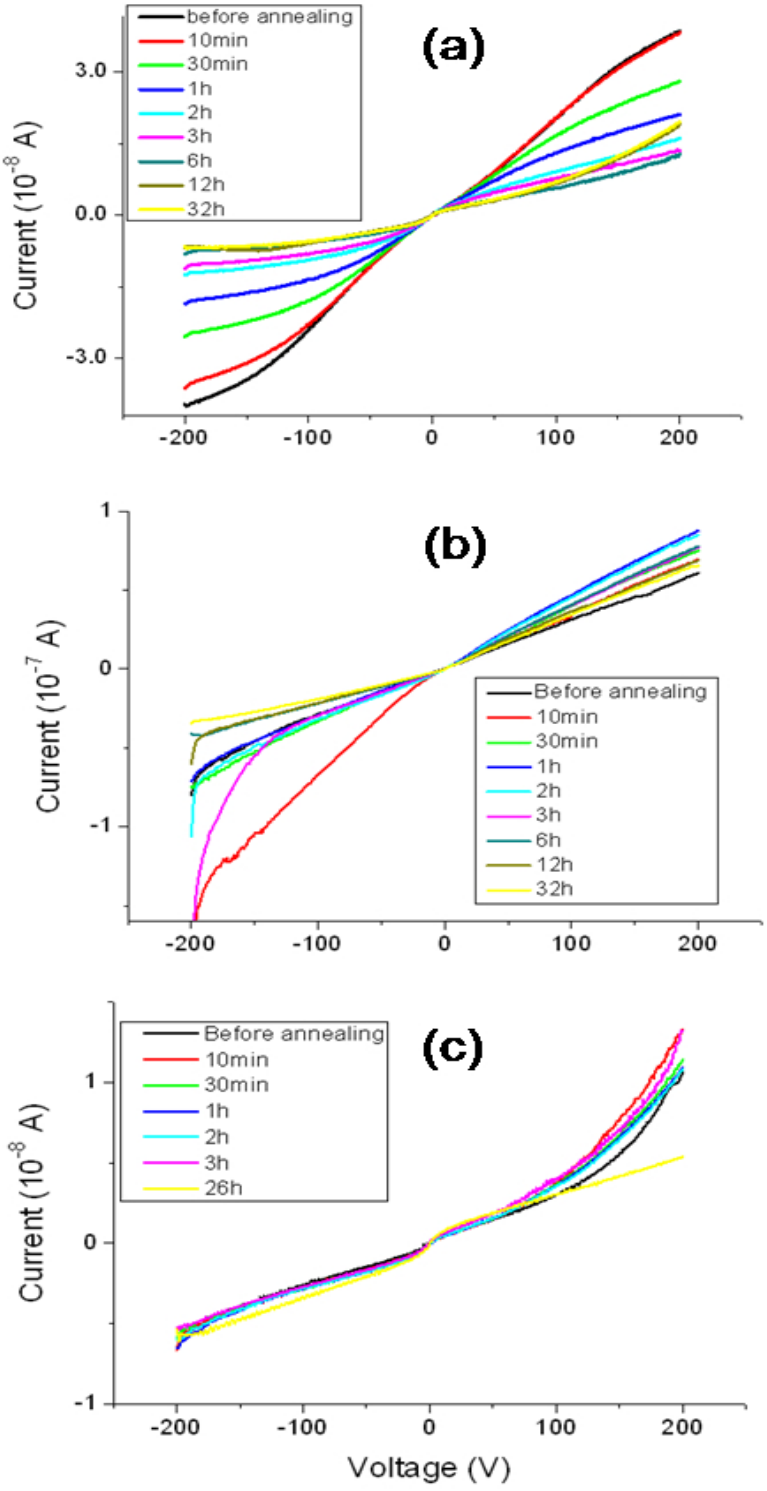

Figure 4.21. I-V characteristics of the detectors with different deposition processes after the annealing step at 373 K. (a) Sputtering Au, (b) Evaporation Au, (c) Electroless Au.

As previously presented in Figure 4.1 (b), a thick TeO_2 layer appear between Au layer by sputtering method and the CZT bulk material, indicating a weak adhesion between Au and CZT. The evaporation method used for electrode deposition produce a very thin TeO_2 layer at

the interface between Au and CZT. Meanwhile, for the electroless method, the thick intermixing layers between the Au contact and CZT bulk material is reported to give better detector performance.

It is supposed that after the annealing treatment, Au diffuse into CZT material, however, the oxidation of the interface of the deposited Au contact during annealing in air is accelerated. Therefore, the annealing process is necessary for sputtered Au on CZT to promote the interdiffusion of Au layer and its conjugated interface Au/CZT. For the evaporated Au, a further annealing step is not required, which is in agreement with *Chattopadhyay et al.*, they reported that the increase of deep level defects is observed when the annealing is performed for a longer time [21].

Several authors commented that the Au-CdTe contact depends on the specific atmosphere in which the detector is annealed and the evident of the formation of an intermediate Au-Te compound [21][24]. As previous discussed, the Au contact by electroless method introduce strong interdiffusion layer between Au layer and CZT bulk material, hence the annealing step is not necessary to strength the intermixing layer.

For these three methods, a long time of exposition to an annealing temperature, allow to reach a decrease of the leakage current. These behaviours can be explained by the fact that a layer of oxide can be formed to the interface between Au/CZT leading to a reduction of the leakage current but also can be detrimental to the detection performance.

Ideally, next step will be the characterization of the interface after annealing by using RBS technique. Indeed, annealing step allow the modification of the composition and quality of Te oxide at the interface and a diffusion of Au from the contact to the interface. Therefore, these two mechanisms play a role in the formation of defects at the interface and lead to a change in the leakage current and I-V characteristics.

4.2.3. Conclusions

Different parameters of the preparation of single layer on CZT have been investigated, in particular, the influence of the deposition time and the annealing step after contact deposition have been studied.

- The deposition by electroless plating of thin metal film of Au, Pt, or Ru layer on CZT shows a modification of morphology on the surface and a modification of roughness versus deposition time. At a critical thickness, micro-cracks appear at the surface of the Pt or Ru layer, whereas the Au layer does not present any micro-cracks or peeling off.

- At short deposition time, the thickness of Au layer is quite similar with that of Pt layer. At long deposition time, the thickness of Pt layer increase dramatically, while the thickness of Au layer saturates at a value of 120 nm.

- For Ru, the deposition rate is much slower than Au or Pt, which may be explained by the double consumption in the chemical reactions. The XRD studies reveal that Pt films deposited on CZT are polycrystalline, while Ru films are monocrystalline.

- The annealing step presents the decrease of leakage current with sputtering method but increases with the evaporation method as the annealing time holding in air increases. With the electroless Au contact, the annealing treatment under air displays insignificant variation of leakage current for a long annealing time.

4.3. Deposition of Single Layer on CdTe/CZT

To create a stronger chemical bond between the metal and the semiconductor, the electroless method is the most used compared with other physical deposition methods such as sputtering or thermal evaporation. From previous discussion, the contacts deposited by electroless method shows better gamma spectra, compared with sputtering or evaporation deposition methods.

The quality of the contacts deposited by electroless deposition depends strongly on parameters such as: the work function, the number of valence electrons of the elements, time of deposition, the chemical compounds at the surface of the samples, the surface defects created, the variation of morphology at the surface, the homogeneity of the deposition, the thickness of the layer of oxidation, etc [25][26]. All these parameters need to be optimized to obtain a detector with the best performance.

In this section, the investigation has been carried out with the performance of devices with different type of single contacts prepared by electroless deposition method in planar configuration by analyzing the elements and their compositions at the surface of the semiconductor and at the interface metal/semiconductor.

The samples were prepared by electroless deposition of standard metal contacts such as gold (Au) and platinum (Pt), and new metal contacts from the platinum group ruthenium (Ru) or rhodium (Rh) onto the CZT materials, respectively [27]. These platinum group metals have a high work function and a large number of valence electrons, moreover, they are chemically inert to the atmosphere making them stable as electrical contacts. These elements have also a lower price than Pt or Au, making them interesting in the reduction of the costs of detectors.

The samples in the work were lapped by abrasive alumina powder of 3 μm and polished with 1 μm diamond powders. The size of the samples was $10 \times 10 \times 2$ mm^3. Prior to do the deposition, the samples were etched with 2 % Br-Methanol solution for 2 minutes and rinsed with methanol. Metal contacts were deposited onto the sample surface immediately after etching to minimize surface re-oxidation.

The deposition time of Au, Pt, Ru, and Rh contacts are 2 min, 2 min, 4 min, and 2 h, respectively. As previously discussed of the influence of deposition time on the preparation

of single layer on CZT in section 4.2.1, the optimum deposition time was chosen here for further study.

4.3.1. Composition of the Single Layer Produced on CdTe/CZT

4.3.1.1. Total Reflection X-ray Fluorescence

Total reflection X-ray Fluorescence (TXRF) has been previously carried out for a fast identification of the element presents at the surface of the sample to estimate if the deposition has been successfully done. TXRF takes advantage of the grazing incidence angle at which the X-ray primary beam impinges the surface of the sample such that total reflection occurs. The X-rays excite atoms in the top layers of the sample and the fluorescence is detected by a Si (Li) detector. Therefore, the film deposited on the top of the sample can be analyzed.

Figure 4.22 displays the spectra recorded for the samples with different metallisation processes as a function of X-ray energy. We can observe the existence of Zn, Cd-K_α, Cd-K_β, Te-K_α, and Te-K_β of all the spectra, clearly in identify the CdTe/CZT material. Meanwhile, we can see the appearance of metal contacts on the surface of on the samples. Especially, we clearly see the Au-L-lines present on the sample, as shown in Figure 4.22 (a).

Moreover, the presence of Pt, Ru and Rh contacts on the surface of CdTe/CZT samples by Pt-L-lines at the energy of 9.4 and 11.0 keV, Ru-Kα at the energy of 19.2 keV, Rh-Kα at the energy of 20.2 keV were shown in Figure 4.22 (b), (c), (d), respectively. However, the intensity of Rh contact on CdTe/CZT material is quite low even after 2 hours deposition, implying that the deposition kinetics of Rh is considerably slow. In conclusion, the contacts were successfully deposited on the surface of the CdTe/CZT crystal.

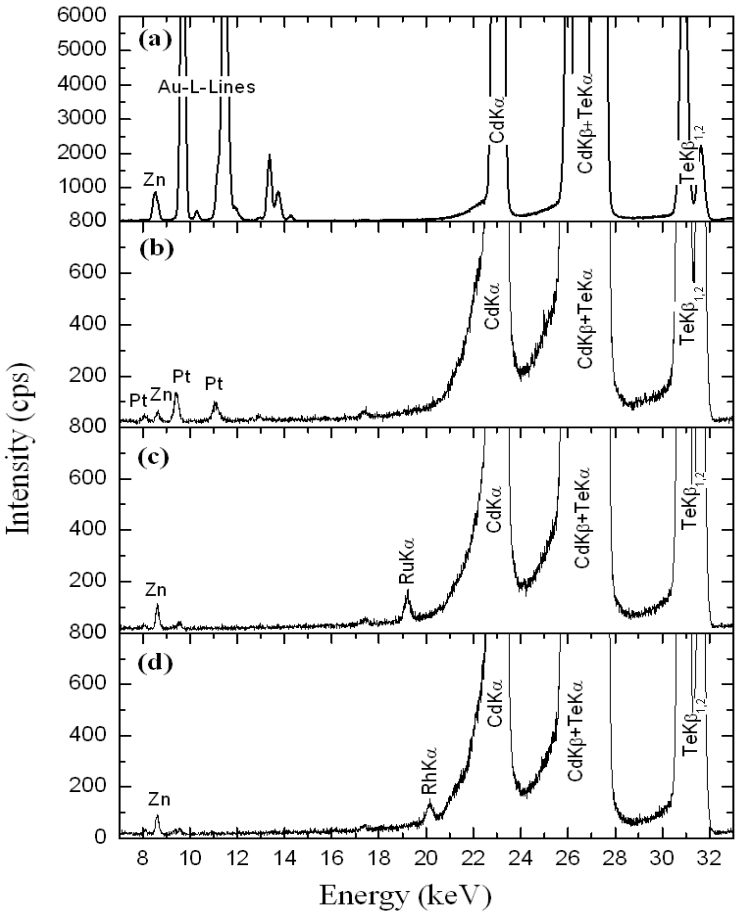

Figure 4.22. TXRF spectra on the surface of CdTe/CZT samples after deposition. (a) Au, (b) Pt, (c) Ru, (d) Rh.

For a better understanding of the diffusion profiles and the interface composition, the deposited layers were studied by RBS technique [28][29]. The experimental procedure is carried out into two steps: first of all, an acquisition of the experimental spectra; secondly, a model is build considering different layers and the resulting theoretical spectra is compared with the experimental data.

Figure 4.23 (a) presents the experimental and fitted spectra for different single metallic layer on CdTe/CZT. We observe that both Au and Pt contact on CdTe/CZT exhibit the extra channel of Te between 300 and 350 inside the channel of the contacts, which is not the same case for Ru or Rh conttact, revealing that more Au or Pt diffuse inside the CdTe/CZT material by electroless deposition method. Moreover, the appearance of Ru and Rh at the channel around 300 can be seen, the low intensity indicates the slow deposition of Ru or Rh contact, which is consistent with the TXRF spectra (see Figure 4.21).

Figure 4.23 (b) exhibits the best layer structures as a function of depth for different metallisation. RBS depth profiles exhibited some complexity in the layers formed between the contacts and the substrates due to different inter-diffusion processes. As can be seen, a significant concentration of TeO_2 was found in the interfacial layers for these four metallisation processes. We can observe a thicker TeO_2 layer formed between Ru or Rh layer and the CdTe/CZT material.

One can observe the interdiffusion between the contacts and bulk material, whereas the appearance of diffusion depth of Pt layer and Au layer are quite similar, which is much higher than the Ru or Rh contact. We assume this behaviour is due to the reaction kinetics between the metals and CdTe/CZT.

Roumié et al. demonstrated that, during deposition, Cd left the material surface as ions Cd^{2+} and Te precipitated on the surface creating a p-type film and forming some hetero-junction TeO_x layers between the metal contact and the substrate with some concentration of Cd [16]. These behaviours can be explained by the preferential reaction of ions inside the electroless solution with Cd leading to the formation of Te rich layer at the surface of the sample. Moreover, in presence of a strong oxidant, like the ions used for deposition, as water, this layer and Te precipitates at the surface of the semiconductor can oxidize and create TeO_2.

Indeed, different hetero-junctions are formed between the metallic contact (M) and the CZT: M-TeO_x and TeO_x- CZT [14]. Other elements like Cl, or Zn, H exist with a smaller amount. In fact, the interface thickness as well as the TeO_x form explains the electrical behaviour of such metal contacts and therefore, the final performance of the devices [30].

Comparing these four metal depth profiles, Au exhibits the lowest depth of TeO_2 and CZT on the surface of the sample, suggesting a fast deposition of Au which limits the out-diffusion of TeO_2 and CZT in the Au contact. However, Pt present more inter-diffusion of TeO_2 with CZT material. For Au or Pt contact deposited on CdTe/CZT, the deposition rate is significantly fast, a thickness of around 50 nm can be achieved after 2 min deposition (see section 4.2.1). As previous discussed in section 4.2.1, the deposition rate of Ru layer on CZT is extremely slow, a very thin layer of around 40 nm can be obtained even after 5 hours of deposition (see Table 4.4). For the deposition time of Rh layer is sufficiently long (2 h), the deposition rate is also slow, resulting in a shallow depth of Rh layer.

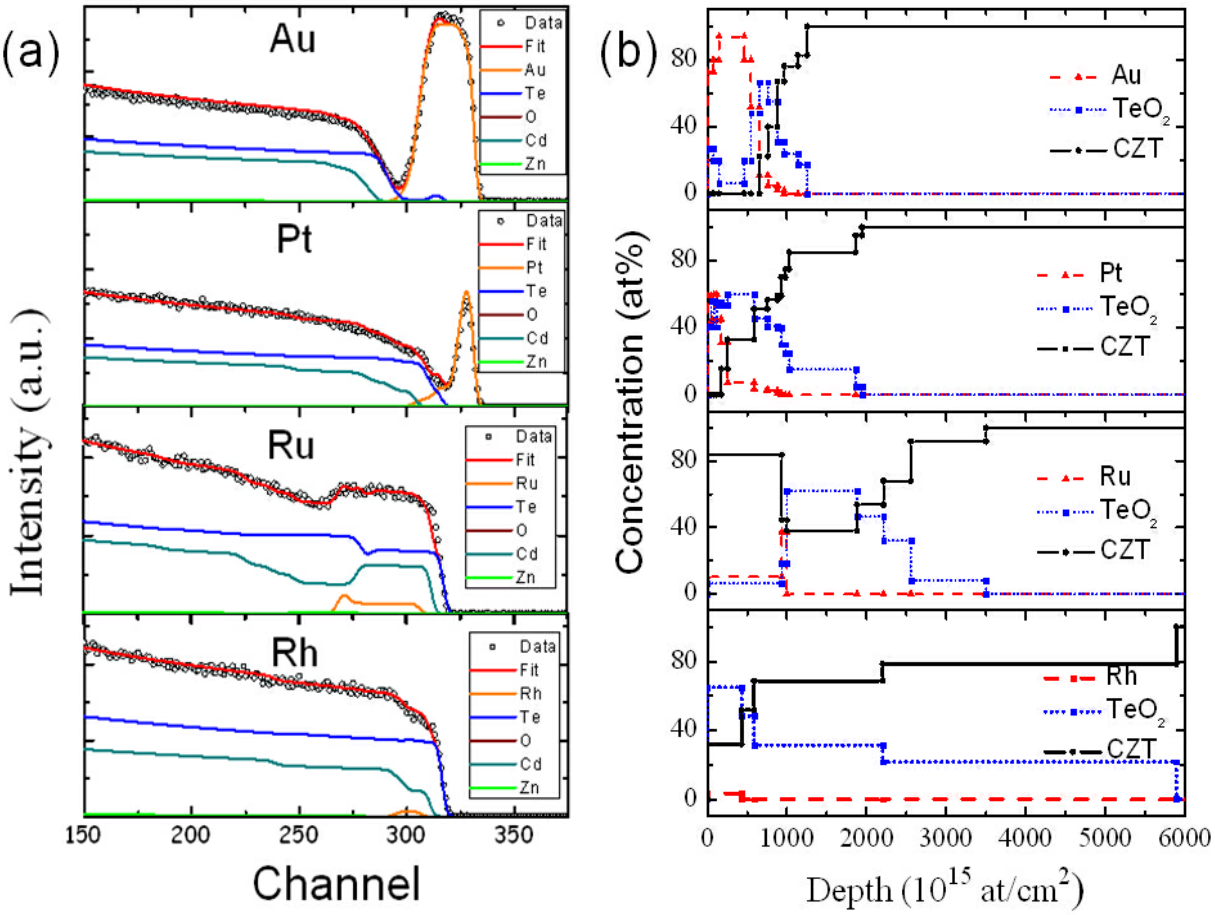

Figure 4.23. Experimental, fitted RBS spectra of the samples (a) and depth profile (b) with different metallisation process.

Using the RBS depth profiles, the thicknesses of the metal layers including diffusion region were estimated assuming Bragg´s rule, as shown in Table 4.5. We observe the thickness of Au contact and interlayer is approximately 160 nm, which is slightly higher than Pt (130 nm) and Ru (140 nm). As can be observed, the thicknesses of the different single layer included diffusion layers depend on the kinetics of reactions which occurred at each deposition. It is important to mention that the thickness presented in Table 4.5 is estimated with the pure contact layer and the diffusion of the contact layer in the bulk material, which is different from the results shown in Table 4.4 (thickness of pure layer).

Table 4.5. Thickness of the contact + diffusion layers for different metals on CZT samples.

Layer	Au	Pt	Ru	Rh
Thickness(nm)	~160	~130	~140	~60
Deposition time	2 min	2 min	4 min	2 h

The above TXRF and RBS results can be understood if we consider the chemical reactions which occur during the electroless deposition stage. The chemical reactions of Au, Pt, or Ru with CZT were presented from Eq. 4-6 to Eq. 4-21. In addition, the reactions of Rh with CZT can be written as [16]:

$$2Rh^{3+} + 3Cd(s) \rightarrow 2Rh(s) + 3Cd^{2+} \qquad \Delta E^0 = +1.16V \qquad \text{Eq. 4-22}$$

$$4Rh^{3+} + 3Te(s) \rightarrow 4Rh(s) + 3Te^{4+} \qquad \Delta E^0 = +0.19\ V \qquad \text{Eq. 4-23}$$

$$4Rh^{3+} + 3Te + 6H_2O \rightarrow 4Rh(s) + 3TeO_2 + 12H^+ \qquad \Delta E^0 = +0.17\ V \qquad \text{Eq. 4-24}$$

It should be noted that the Au contact solutions were prepared in acid environment, where the presence of hydroxide ions OH^- can be considered negligible and its concentration is much smaller than the concentration of H^+ [15]. In consequence, the reaction of $AuCl_4^-$ ions with Te shown in Eq. 4-9 is preferable.

As can be seen in Eq. 4-22, the potential difference of the Rh^{3+} ions reaction reacting with Cd is higher (+1.16 V) than with Te in Eq. 4-23 (+0.19 V) and Eq. 4-24 (+0.17 V), indicating that Rh preferentially react with Cd, transferring Cd^{2+} into $RuCl_3$ solution, leaving a Te layer on CZT and precipitating the Rh layer on this layer. The preferential reaction with Cd leads to the appearance of Te rich surface, where long deposition time results in a strong oxidation of Te.

4.3.2. Study of the Defects Present in the Detector by PL Measurements

PL spectra at low temperature were used to evaluate the material quality which could be valuable as a predictor of the detector performance. Figure 4.24 exhibits low temperature PL spectra at 4.2 K of the CZT samples with different metallisation processes. It is necessary to note that the study of Rh is similar to Ru, which is not presented here. The intensities of the

PL spectra were normalized to the (D^0, X) peak for better comparison. Similarly with Figure 4.2, the (D^0, X) peak and (A^0, X) peak of the near band-edge region are presented at 1.659 eV and 1.650 eV, respectively. The shallow donor–acceptor pair (D, A) emission and A-center can also be seen.

In Figure 4.24, we can observe the decrease of the intensity of A-center and (A^0, X) peaks with the Pt and Ru contacts, indicating that a high concentration Pt or Ru donors compensate with Cd vacancies, which is in opposition with the Au contact. As previously discussed in section 4.1.2, the deposition of Au layer on CdTe/CZT by electroless method can introduce more defects that is in agreement with RBS results, which also presents more interdiffusion of Au into the bulk material.

Table 4.6 summarized the information of the intensities of all the peaks and the relationship between these peaks presented in Figure 4.24. As can be seen, the intensity of (A^0, X), (D, A), and A-center decrease significantly with Pt and Ru contacts after the deposition, indicating more compensation and recombination between the donors and Cd acceptors.

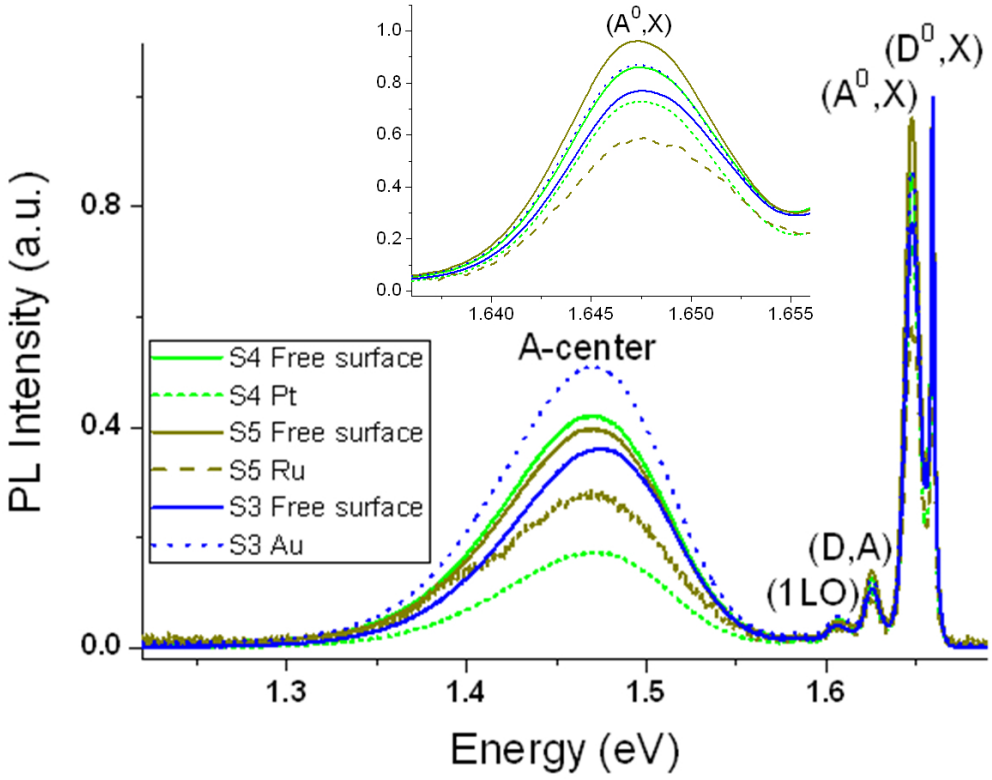

Figure 4.24. Low temperature (4.2 K) PL spectra of CZT detectors fabricated by different metallisation methods.

Table 4.6. Comparison of PL (4.2 K) results of CZT detectors: before and after metallization process with different methods. (σ = ± 0.01)

		$I(D^0,X)$	$I(A^0,X)$	I(D,A)	I(A-center)	$I(D^0,X)/I(A^0,X)$	$I(D^0,X)/I(D,A)$	$I(D^0,X)/I(A\text{-center})$	FWHM (D^0,X) meV
S4	**Free surface**	1.00	0.86	0.12	0.42	1.16	8.1	2.4	2.1
	Pt	1.00	0.73	0.10	0.17	1.37	10.1	5.8	2.1
S5	**Free surface**	1.00	0.94	0.14	0.40	1.06	7.2	2.5	1.9
	Ru	1.00	0.58	0.08	0.28	1.72	11.9	3.6	1.9
S3	**Free surface**	1.00	0.77	0.11	0.36	1.30	9.2	2.8	2.4
	Au	1.00	0.87	0.13	0.51	1.15	7.8	2.0	2.4

4.3.2. Electrical Behaviours of the Deposition of Single Layer on CdTe or CZT

4.3.2.1. Deposition of Single Layer on CdTe

Current-voltage (I-V) characteristics of three different metal contacts were studied on p-type materials based on CdTe:Cl (from Acrorad), as presented in Figure 4.25. The same detectors were reproduced by different metallisation processes for comparison.

As can be seen, Pt displays a linear ohmic behaviour in all the range of voltages, while the other contacts show quasi-ohmic behaviours with a tendency in double injection of carriers (V^2) below -20 V and an ohmic contact from -20 V to +100 V. These different behaviours for forward and reverse bias can be explained by the difference of polarity between the two sides of the detectors (Te or Cd side) and particularly to the interface composition [31].

As displayed in Table 4.7, at low voltages between -10 V and +10 V, the ohmicity coefficient of different metallisation process was calculated, where Au is 0.9969, which is the most close to an ideal ohmic contact. Although the ohmicity coefficient of Pt contact (0.9969) is lower than the other three contacts, the leakage current of the detector fabricated with Pt contact is much lower than the others, which also influences the detector performance.

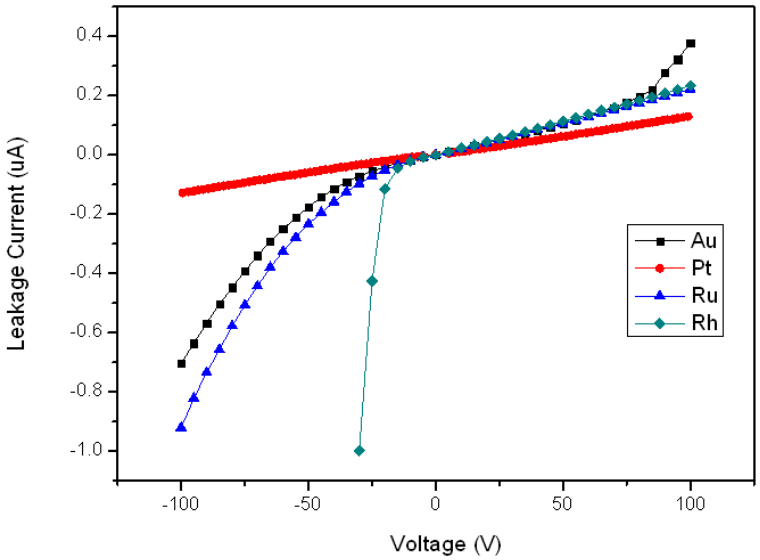

Figure 4.25. Comparison of I-V curves of CdTe detector fabricated by different electroless deposition contacts.

Table 4.7. Fitted parameters according to $I=aV^b$ for the curves in Figure. 4.10 at low voltages.

Contact	Au	Pt	Ru	Rh
a	1.8×10^{-9}	1.0×10^{-9}	2.0×10^{-9}	2.2×10^{-9}
b	0.9969	0.9887	0.9962	0.9974

The electron affinity of CdTe is about 4.7 eV, which requires the metals with a higher work function to form an ohmic contact on p-type materials. Au has the work function of 5.1 eV, Pt of 5.65 eV, Ru of 4.71 eV, and Rh of 4.98 eV [32]. A barrier free contact to CdTe is obtained when the work function of the contacting material is greater than that of the semiconductor, that is to say $W_M > W_S$. As a consequence, Pt displays more linear ohmic properties due to its higher work function, where high barrier height decreases the probability that electrons will pass through the barrier, which is reflected in a lower leakage current.

For CdTe material, the detector performance of different metallisation processes was carried out, the gamma-ray spectroscopy with ^{57}Co source have been exhibited in Figure 4.26. As can be seen, the 122 keV photopeak was clearly in evident with four different metallisation

processes. The comparison of the ^{57}Co gamma spectra of the CdTe detectors fabricated with different metal contacts are shown in Table 4.8.

The gamma-ray spectra for the detectors with Pt contact presented a much better performance than the other three contacts, with the FWHM of the 122 keV of 11.0 keV as opposed to 16.3 keV for Au and 20.0 for Ru. The Peak/Valley ratios (P/V) are 1.78 and 2.55 for Ru and Rh, and 1.39 and 2.89 for Au and Pt, respectively. Moreover, the leakage currents at 100 V for Au, Pt, Ru and Rh are 450, 94,145 and 149 nA, respectively.

This behaviour can be explained by the interfacial layer composition, especially the presence of TeO_x, formed between the metallic contact and the CdTe as well as the defects created during the contact deposition process. These different hetero-junctions can affect also the spatial distribution of the electrical field and thus lead to the various qualities of the three detectors.

These two new developed contacts on CdTe/CZT materials by our laboratory exhibited good detector performance which is close to the other two classical contacts (Au and Pt). It is important to comment that sometimes some irreproducibility can occur on the same detector due to the mechanical polish treatment or deposition process. We can conclude that the optimization of these new contacts in terms of concentration, time and pH could enhance this performance.

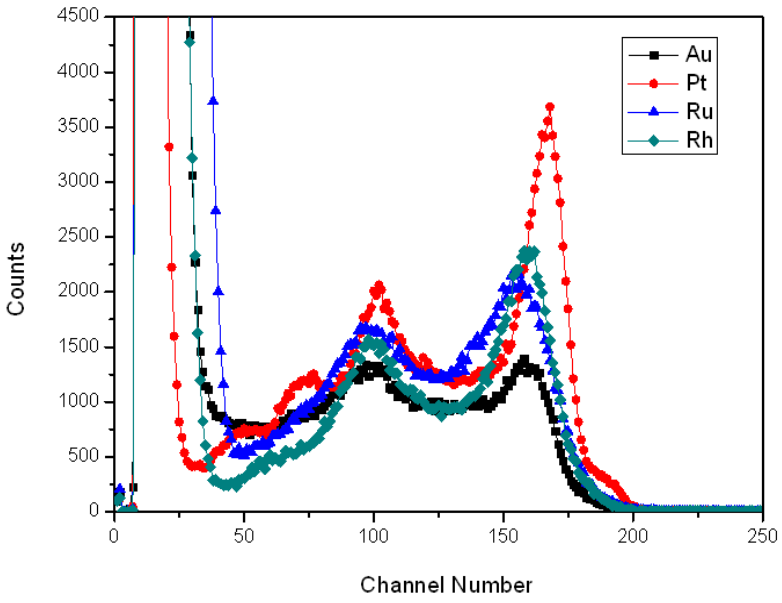

Figure 4.26. ^{57}Co gamma spectrum of CdTe detectors fabricated by different Au deposition contacts.

Table 4.8. Comparison of ^{57}Co gamma spectrum of Cd(Zn)Te detectors fabricated by different metal contacts.

	Au	Pt	Ru	Rh
V	100	100	100	100
FWHM (keV)	16.3	11.0	20.0	14.4
I (nA)	450	94	145	149
Channel number of the 122 keV peak	162	167	162	160
P/V	1.39	2.89	1.78	2.55

4.3.2.2. Deposition of Single Layer on CZT

Room temperature I-V system was carried out on planar devices in order to study the ohmicity and the quality of the deposited contacts. The same detectors were prepared by polishing to study different metallisation processes.

Figure 4.27 displays the Current-Voltage (I-V) characteristics of three different metal contacts on $Cd_{0.9}Zn_{0.1}Te$:In (from CGL) at the electric field of -500 V/cm ~ +500 V/cm. Due to the n-type CZT material, the I-V curves display blocking (Schottky) contact behaviours for different metal contacts in planar configurations at all the range of applied electric fileds. I-V characteristics of different metallisation process present similar behaviour to each other. Ru contact shows slight higher leakage current at positive bias, while Au contact displays the lowest leakage current in the negative bias.

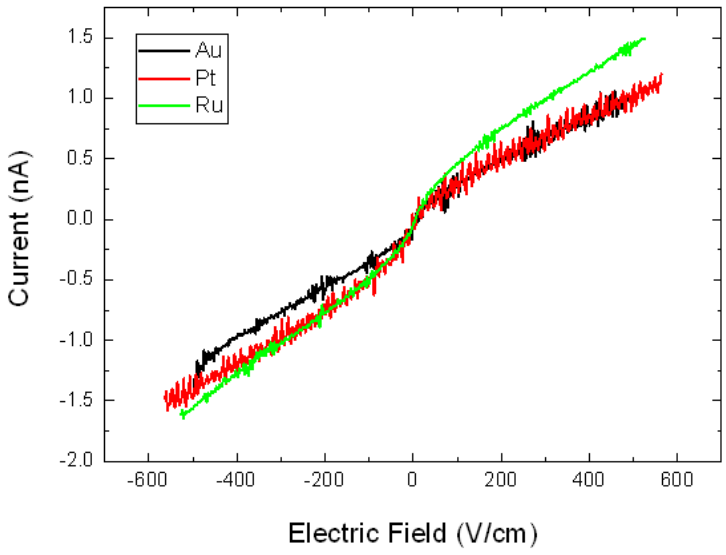

Figure 4.27 Comparison of I-V curves of CZT detector fabricated by different metallisation process.

The spatial performance of the same detector with different deposited contacts has been evaluated by using the ^{133}Ba and ^{241}Am radioactive gamma sources. The samples have been irradiated from the cathode side to take advantage of the transport properties of the electrons (higher $\mu\tau$ product).

Figure 4.28 illustrates the gamma-ray spectroscopy of the planar detectors with different metallization processes. Different applied voltages were operated on the planar detectors in order to find the optimum voltage. It is important to note that the best side was chosen to irradiate at cathode side. We observe that the 31 keV and 81 keV photopeaks with ^{133}Ba source and 60 keV with ^{241}Am photopeak evidence with all the detectors deposited with Pt, Ru, or Au contact.

With the ^{133}Ba radioactive source, one can observe the significant difference of the gamma spectroscopy for applied voltages above and below 700 V with Ru contact detectors. Indeed, the charge collection efficiency changes with different applied voltages and electric fields, the pulse height of irradiations will be stopped within the depletion layer at low applied voltages. We can observe the much lower pulse height at the applied voltages of 500 V and 600 V than that of 700 V, indicating that incomplete charge collection due to trapping and recombination occur with low applied voltages and electric fields. The same behaviours

happen with Au contact detectors, the charge collection complete at the applied voltages from 600 V. For the detector fabricated by Pt contact, the pulse height shows only a slightly change from 500 V to 800 V, implying that the charge collection almost complete within this range.

The information of the gamma spectra with these two radioactive sources was summarized in Table 4.9. For better comparison, the gamma response at the applied voltage of 700 V was exhibited. By comparing the different metallisation processes, we can see that the FWHM of the 31 keV and 81 keV photopeaks with ^{133}Ba radioactive source of the detectors fabricated with Pt contact are 15.2 % and 7.0 %, respectively, which are slightly lower than that of Au contact (15.3 % and 8.4 %).

However, the FWHM values of these two photopeaks with ^{133}Ba source are much higher with Ru contact (21.0 % and 9.5 %), indicates lower resolution. The Peak/Valley ratio (P/V) of 31 keV photopeak with ^{133}Ba radioactive source is 5.6 for Au contact, which is higher than the ones prepared by Pt contact (3.9) or Ru contact (2.8). As previous mentioned, the detector performance quantified by the photopeak resolution and Peak/Valley ratio. Therefore, we obtain higher quality factor of 31 keV photopeak ^{133}Ba radioactive source of the detector prepared by Au contact (0.60) than fabricated by Pt (0.51) or Ru (0.37) contact, revealing that the detector performance can be achieved with Au deposition method.

In addition, one can observe higher FWHM value of the 60 keV photopeak with ^{241}Am source of the detectors deposited by Ru contact (11.2 %) than that of Pt (6.8 %) and Au (9.3 %) contact. Nevertheless, the Peak/Valley ratio of this photopeak is higher (9.2) than the other two metallization process (5.2 for Pt and 3.7 for Au), which indicates that low noise level obtained with detector with Ru contact. Finally, the quality factor of 60 keV peak is slightly higher with Ru contact (0.91) than with Pt contact (0.75) or Au contact (0.74).

Moreover, we observe one X-ray escape peak on the detector prepared by Au contact, which can be attributed to the lower leakage current and therefore to a better sensitivity of the detector. It shows the lowest FWHM value of 60 keV peak compared to the other metallisation methods, indicates the best detector performance obtained with Au, which is also in agreement with the lowest leakage current in all the applied voltages (see Figure 4.27). These consequences are probably associated with the composition of the intermixing layers, mainly with the presence of TeO_2 layer formed between the metallic contact and the CZT

bulk material and the interaction of the metal with Cd vacancies resulting in formation of A-centers.

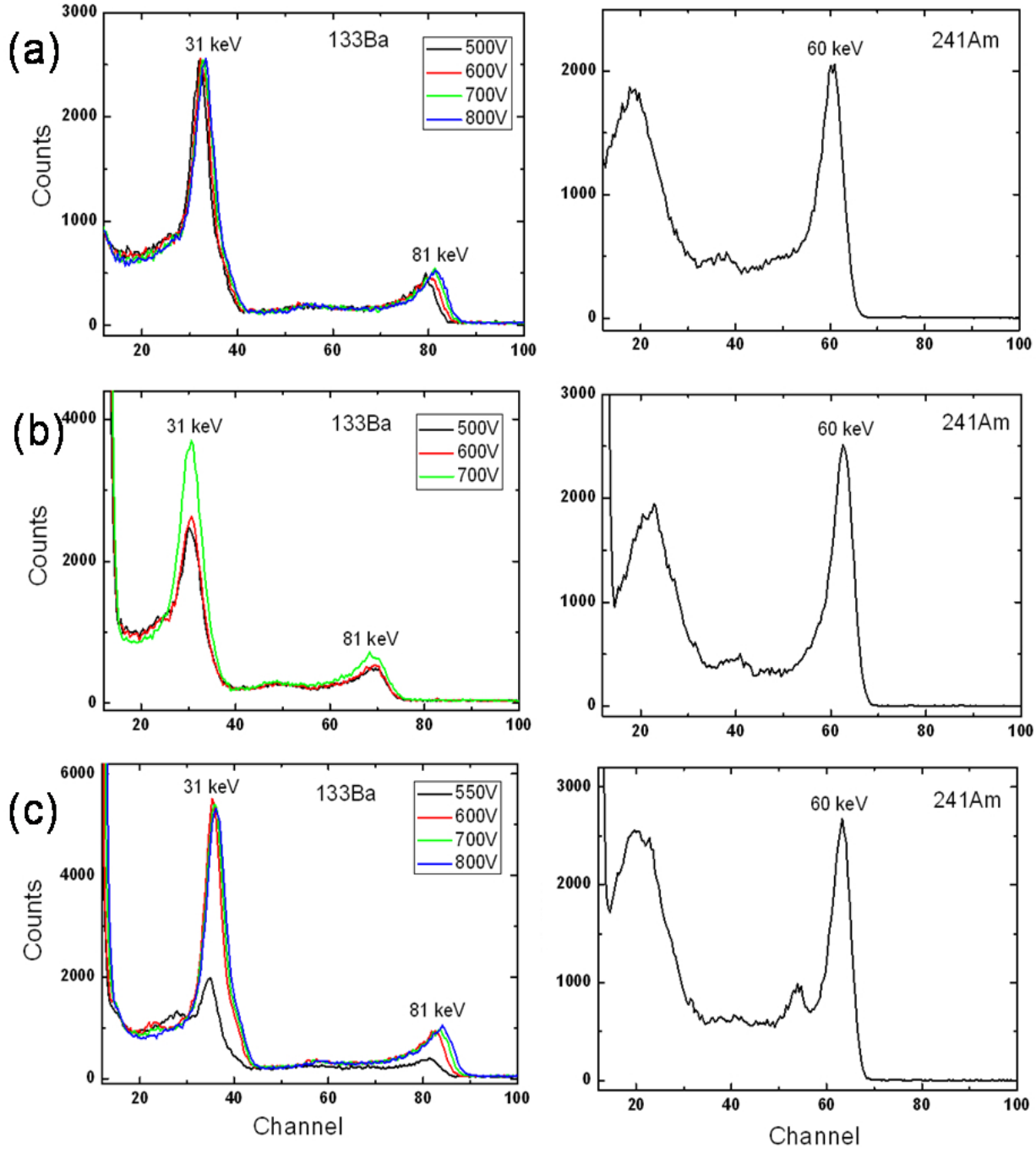

Figure 4.28. Room temperature gamma spectra (^{133}Ba and ^{241}Am) of CZT detectors fabricated by different metallisation methods. (a) Pt, (b) Ru, (c) Au.

Table 4.9. Comparison of ^{133}Ba and ^{241}Am spectra of CZT detectors fabricated by different metallisation methods.

	Pt	Ru	Au
^{133}Ba 31 keV FWHM %	15.2	21.0	15.3
P/V of the 31 keV peak	3.9	2.8	5.6
Quality factor of the 31keV peak	0.51	0.37	0.60
^{133}Ba 81 keV FWHM %	7.0	9.5	8.4
P/V of the 81 keV peak	4.2	2.7	3.2
Quality factor of the 81keV peak	0.77	0.53	0.62
^{241}Am 60 keV FWHM %	9.3	11.2	6.8
P/V of the 60 keV peak	5.2	9.2	3.7
Quality factor of the 60 keV peak	0.75	0.91	0.74

4.3.4. Conclusions

Different types of contacts have been deposited on the CdTe/CZT samples by using electroless deposition method, including classical contacts (Au and Pt) and the new metal contacts from the platinum group (Ru and Rh).

- The elements and their compositions at the surface of the semiconductor and at the interface of metal/semiconductor have been analyzed by TXRF and RBS techniques. The metal elements have been successfully identified on the samples by TXRF technique. By RBS depth profiles, a significant concentration of TeO_2 appears in the interfacial layers for four metallisation processes.

- The defects introduced by the metal contacts indentified by PL technique indicating more compensation and recombination between the donors and Cd acceptors with Pt or Ru contact than with Au contact.

- The performance of planar detectors prepared with different type of single layers has been studied. For different metallisation processes on CdTe material, the contacts show quasi ohmic behaviours in all the voltage ranges. For deposition on CZT

material, the I-V characteristics exhibited Schottky contact behaviours for different metal contacts at all the range of applied voltages.

- For the detectors deposited on CdTe material, Pt contact gives better performance. For the detectors fabricated on CZT material, Au contact has shown the best performance.

4.4. Deposition of Multi-layers on CZT

The objective of this work is to use a system of multi-layers deposited by electroless to modify the work function of the contact and the inter-diffusion layer at the interface of metal/semiconductor. This system has the properties to have a work function different with the semiconductor than the single elements, leading to a different nature of the contacts, and potentially to an improvement in the performance of the radiation detectors.

In this work, we have studied the feasibility of the deposition of nanometric multi-layers (e.g. Ru/Au, Ru/Pd, Pd/Au, and Ru/Pd/Au) on CZT materials by using electroless method. In fact, the deposition of multi-layers on CdTe is similar with CZT, while only the study with CZT is presented in this section.

The mechanisms underlying the chemical reactions occurring during the different depositions in the multi-layers structures can be anticipated by determining the standard electromotive force (emf) of the standard hydrogen electrode (ΔE^0) of the chemical reactions [16]. The thickness and the stoichiometry of the layers on the surface, as well as the depth profiles of the elements present are studied by RBS measurement. Meanwhile, TXRF is used to identify the presence of elements into the solutions and on the samples.

The samples with the size of $5\times5\times2$ mm^2 were cut from the ingot grown in CGL. The preparation processes of the samples used for study follow the information provided in chapter 3. Indeed, for the electroless solutions used for investigation were prepared with 1g of $HAuCl_4$ in 25 mL of DI water for Au solution, 1 g of $RuCl_3$ in 25 mL of DI water for Ru solution, and with 1g of $PdCl_2$ in 25 mL of DI water for Pd solution.

The studied samples were prepared by a first metal layer of Pd or Ru onto the semiconductor substrates (CZT), a second metal layer of Au or Pd on the top of the first layer, and the third layer of Au on top of the second layer.

The sample preparation is shown in Figure 4.29. The Ru contact as a first layer was deposited for 4 min or 60 min (named Ru4 or Ru60), the Pd layer as the first layer was prepared for 2 min or 60 min (Pd2 or Pd60). The second deposited layer with Au contact was prepared for 2 min (Au2), or Pd as a second layer for 2 min (Pd2). The third layer was with Au contact for 2 min. Therefore, the double or triple layers deposited on CZT can be named with contact and

number. For example, Pd2Au2 means double layers with the deposition of Pd contact as a first layer for 2 min and the deposition of the second layer (Au) for 2 min.

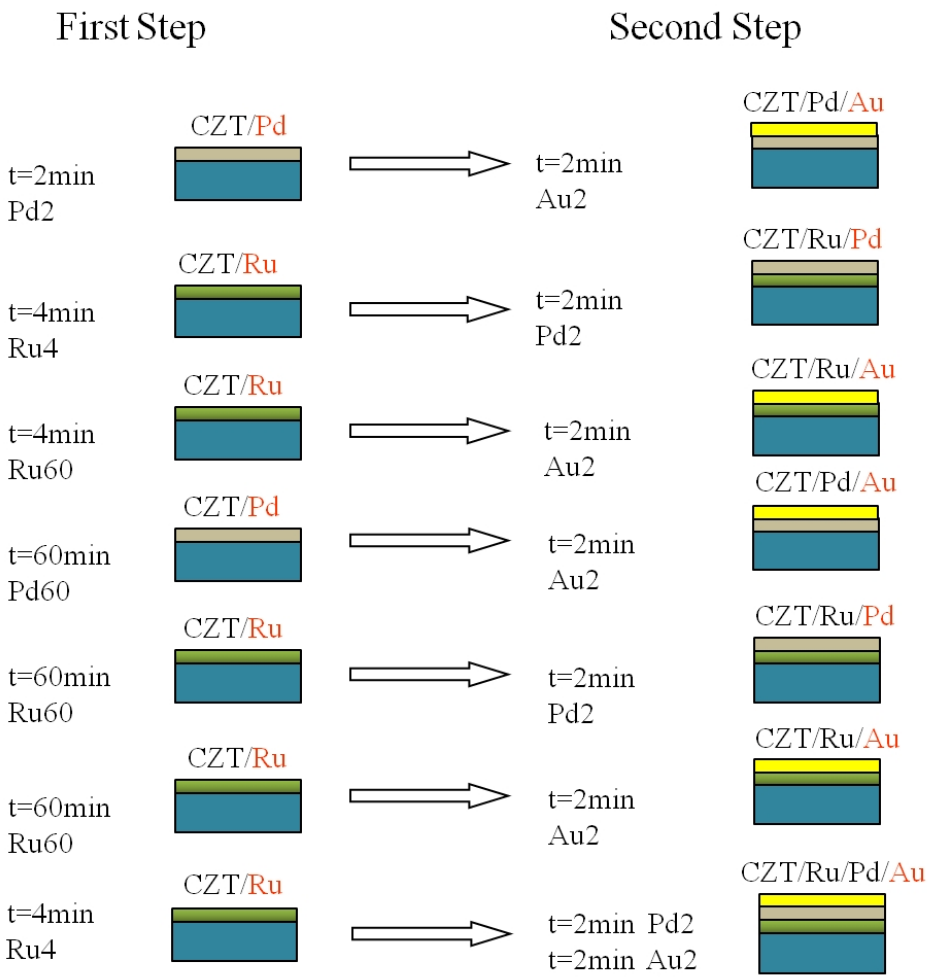

Figure 4.29. The process of the experimental setup.

4.4.1. Theory of Single and Multi-layers Deposition

A. Simple layer

The reactions of metal deposition on CZT can be explained as follow, considering Ru as an example: In a first step, the reaction of Ru^{3+} with CZT involves a transfer of charges between Ru^{3+} and Cd (Te and Zn) leading to the formation of Ru^{2+} and Cd^{2+} (TeO_3^{2-} and Zn^{2+}) ions which are rejected in the solution [13][33]. This behaviour is described by the thermodynamics equations for the standard hydrogen electrode (SHE), as discussed in Eq. 4-16 — Eq. 4-21 [16].

In an acidic environment, the presence of hydroxide ions OH^- can be considered negligible and its concentration is smaller than the concentration of H^+. In consequence, the dominant reaction (Eq. 4-16, Eq. 4-17) occurring between Ru^{3+} (or Ru^{2+}) and Te, a significant concentration of TeO_2 layer can be formed in the interface between Ru layer and CZT bulk material.

For depositing Pd as a first layer, the reaction is similar to the case of Ru except the reactions are in one step, the mainly reaction with Cd is presented as following:

$$Pd^{2+} + Cd(s) \rightarrow Pd(s) + Cd^{2+} \qquad \Delta E^0 = +\ 1.35\ V \qquad \text{Eq. 4-25}$$

B. Double layers

When a sample covered with Ru is introduced in an Au (or Pd) electroless solution, the $AuCl_4^-$ (or Pd^{2+}) ions react with Ru, leading to the deposition of Au (or Pd) on the surface and the dissolution of Ru under the form of Ru^{2+} into the solution.

$$2AuCl_4^- + 3Ru(s) \rightarrow 2Au(s) + 3Ru^{2+} + 8Cl^- \qquad \Delta E^0 = +\ 0.55\ V \qquad \text{Eq. 4-26}$$

$$Pd^{2+} + Ru(s) \rightarrow Pd(s) + Ru^{2+} \qquad \Delta E^0 = +\ 0.50\ V \qquad \text{Eq. 4-27}$$

In fact, the opposite chemical reaction of Au (or Pd) deposition, as first layer, and Ru, as second layer, is forbidden due to the emf difference, which is negative.

Similarly, when Pd is deposited as first layer and Au deposited as second layer, the $AuCl_4^-$ ions react with Pd leading to the deposition of Au and the dissolution of Pd under the form of $PdCl_4^{2-}$ into the solution.

$$2AuCl_4^- + 3Pd(s) + 4Cl^- \rightarrow 2Au(s) + 3PdCl_4^{2-} \qquad \Delta E^0 = +0.41\ V \qquad \text{Eq. 4-28}$$

C. Triple layers

Similarly to the deposition of double layers on CZT, in the case of a triple layer of Ru/Pd/Au, the CZT sample is in first dipped in the Ru electroless solution which allows the deposition of a first layer of Ru (Eq. 4-17). After this step, the sample is dipped in another electroless solution composed of Pd^{2+} ions, at this moment the Pd^{2+} ions are going to react with the Ru solid at the surface of the CZT sample leading to the deposition of Pd layer on CZT and the reject of Ru^{2+} into the solution (Eq. 4-27).

The third and last step consists of a dipping of this sample covered with double layers in another electroless solution composed of $AuCl_4^-$ ions. These ions having higher redox potentials than the Pd(s) layer are going to react with Pd(s) leading to the deposition of Au layer and reject of $PdCl_4^{2-}$ into the solution (Eq. 4-28).

4.4.2. Study of the Deposition of Double Layers on CZT

4.4.2.1. Composition of the Double Layers Deposited on CZT

By taking advantage of the grazing incidence angle at which the X-ray primary beam incident on the samples, the films deposited on the surface and also the elemental content of electroless solutions deposited on a conventional quartz reflector were analyzed by TXRF. In this way, the different layers were characterized to identify the presence of multi-layers and to investigate the process of deposition. Moreover, by analyzing the elements present in the electroless solution after different depositions and also over the deposited layer, it is possible to compare and discuss the theoretical chemical reactions of deposition proposed.

Figure 4.30 exhibits the spectra recorded for the samples as a function of X-ray emission energy. For a better comparison the intensity was normalized to the Te-Kα line. It should be noted that the position of the peaks associated with Zn, Cd and Te are not modified. Figure 4.30 (a) displays the results for samples Ru4 and Ru4Au2. For the Ru4 sample, the Ru-K_α line at 19.2 keV is clearly visible and corresponds to the first deposition layer. For the Ru4Au2 sample, the Au-L lines show high peaks intensity, whereas the intensity of Ru peaks decrease due to the second layer (Au) deposition process described above.

It is worth noting that the Ru peak lines and Au peak lines similarly presented on the sample Ru60Au2, as shown in Figure 4.30 (d). One can suppose that depositing Ru contact on CZT as a first layer for 4 min is sufficient enough to create Ru as a buffer layer.

The same behaviour occurs with the sample Ru4Pd2, as can be seen in Figure 4.30 (b). When deposited Pd as a second layer, according to the diffuse speed of different metals, we can observe the higher density of Ru layer presented on the sample Ru4Pd2 than sample Ru4Au2 (Figure 4.30 (a)). We can assume that Au diffuse faster than Pd when deposited on the top of the first layer (Ru), leading to a faster transfer of the first layer (Ru) into the solutions. Therefore, we can conclude that when deposit Au layer as a second layer, the deposition of Au layer can replace the first layer very rapidly.

For Pd as buffer layer (Pd2) and Au as second layer (Pd2Au2), the TXRF results are illustrated in Figure 4.30 (c). Apparently, we can see the Pd (Pd2) peak lines (K_α, K_β) at 21.1 and 23.8 keV, respectively, and Au-L lines after the second deposition (Pd2Au2). It has shown the feasibility to create double layers on CZT material.

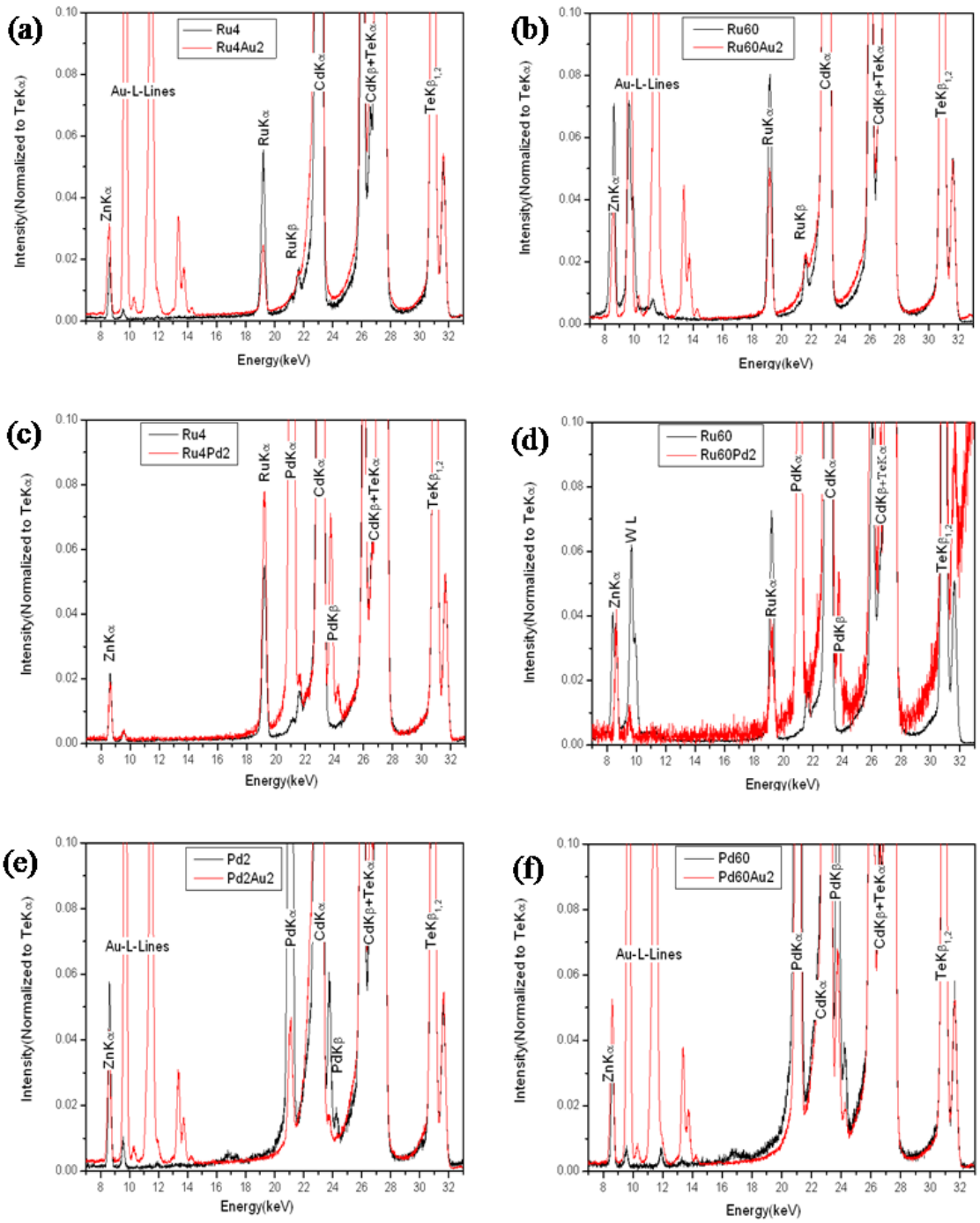

Figure 4.30. TXRF spectra on the surface of CdZnTe samples with single and double layers. (a) Ru4Au2; (b) Ru60Au2; (c) Ru4Pd2; (d) Ru60Pd2; (e) Pd2Au2; (f)Pd60Au2.

It should be noted that after deposited Pd as a first layer for 1h, it is also possible to identify the presence of double layers. When Pd is deposited as a first layer for a long time, follow by the deposition of a second layer of Au for 2min, one can still observe a high intensity of Pd appear on the sample (Pd60Au2). Meanwhile, we can observe Au-L-lines clearly put in evidence in Figure 4.30 (e) and (f). One can conclude that the double layers of Pd/Au can be clearly seen, even though the deposition of the first layer for a long time.

The elements present in the electroless solution were also analysed by TXRF technique for different deposition times. One millilitre of solution, for each deposition solution, was standardised with 100 ppm of Zr as an internal standard which allows for the normalisation of the different TXRF spectra for comparative purpose. The elements presence or absence from the solution was compared before and after each deposition process.

From the results that we cannot observe the difference of the Cd/Te peak lines in Au or Pd electroless solution which are not shown here, we can explained these behaviours by the fact that the quantities of Cd (and Te) rejected in Au (or Pd) solution are not important enough to be identified.

Figure 4.31 presents the TXRF spectra obtained for different times of deposition in a $RuCl_3$ solution after 0 min (Ru0), 4 min (Ru4) and 60 min (Ru60). It is interesting to note that the quantities of Cd (and Te) rejected in Ru solution can be identified. Certainly this is due to the fact that the reaction with Ru is a succession of two reactions and not single like Au or Pd.

In Figure 4.31, the Cd (K_α, K_β) and Te-K_α peak lines can be observed in Ru solution after different deposition times (Ru4 and Ru60). This result is consistent with the double reactions of Ru with CZT yielding more Cd^{2+} in the solution (Eq. 4-16, Eq. 4-17). It can be seen that after 4 min of deposition, the transition line Cd-K_α was weakly observed. However, after 60 min of deposition, the transition lines Cd (K_α, K_β) were clearly recognizable. It can be seen that the intensity of Te-K_α line is much lower than the Cd (K_α, K_β) lines for Ru4, suggesting that the reactions of deposition rejected mainly Cd in the solution, corroborating the proposed theoretical equations.

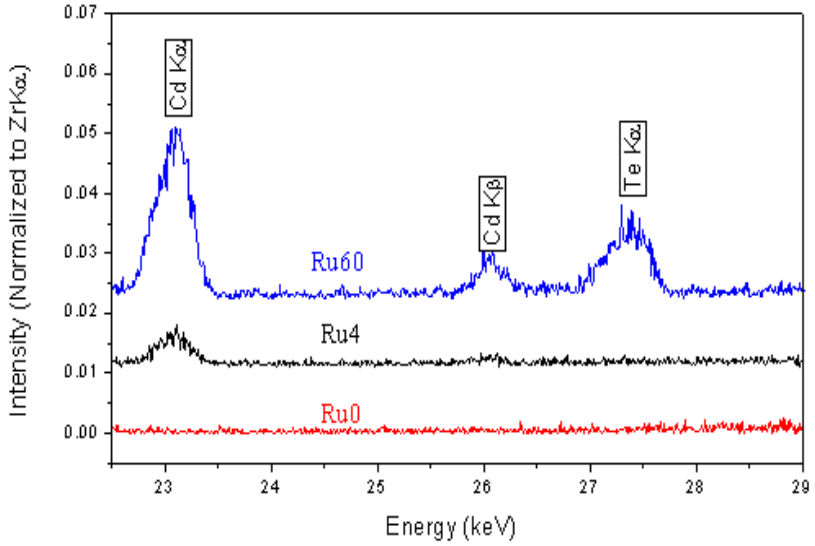

Figure 4.31. TXRF comparative spectra obtained for different times of deposition in a $RuCl_3$ solution: after 0 min, 4 min and 60 min.

RBS technique is one method to determine the thicknesses of the different layers and elemental depth distribution, which has been used in studies of interfaces and diffusion profiles on the deposition of double layers in this section.

Figure 4.32 displays the RBS spectra and the best fitted curves obtained for six representative samples with double layers, the fitted partial spectra of the different elements are also shown. For the fitting process, the substrate was assumed to have a constant composition ($Cd_{1-x}Zn_xTe$, x=0.06 %). The mass resolution for heavy elements is poor, making it difficult to separate Ru from Pd (Z_{Ru} = 44; Z_{Pd} = 46), the error in the determination of the Ru and Pd concentrations is large. However the thickness can be determined quite accurately.

From the study of the obtained spectra, one can observe a different behaviour for the different layers deposited on the CZT substrate. By comparison of Figure 4.32 (a) and (b), the first layer (Ru) were deposited at different time (4 min and 60 min), we can observe that Cd and Te appear in higher channel, and the integrated intensity of Au are larger when the deposition time of the first layer (Ru) is longer. Moreover, we can see that more Au diffuse inside the CZT material when the buffer layer (Ru) is deposited for a long time (Ru60Au2).

Similarly, when the same first layer is deposited at a longer time (Ru60), but a different second layer at a short time (Pd2), we can also observe a high intensity of the Pd layer appearing on the surface of CZT (Ru60Pd2), as presented in Figure 4.32 (c) and (d). We can

conclude that the deposition of the second layer is depending on the deposition time of the buffer layer.

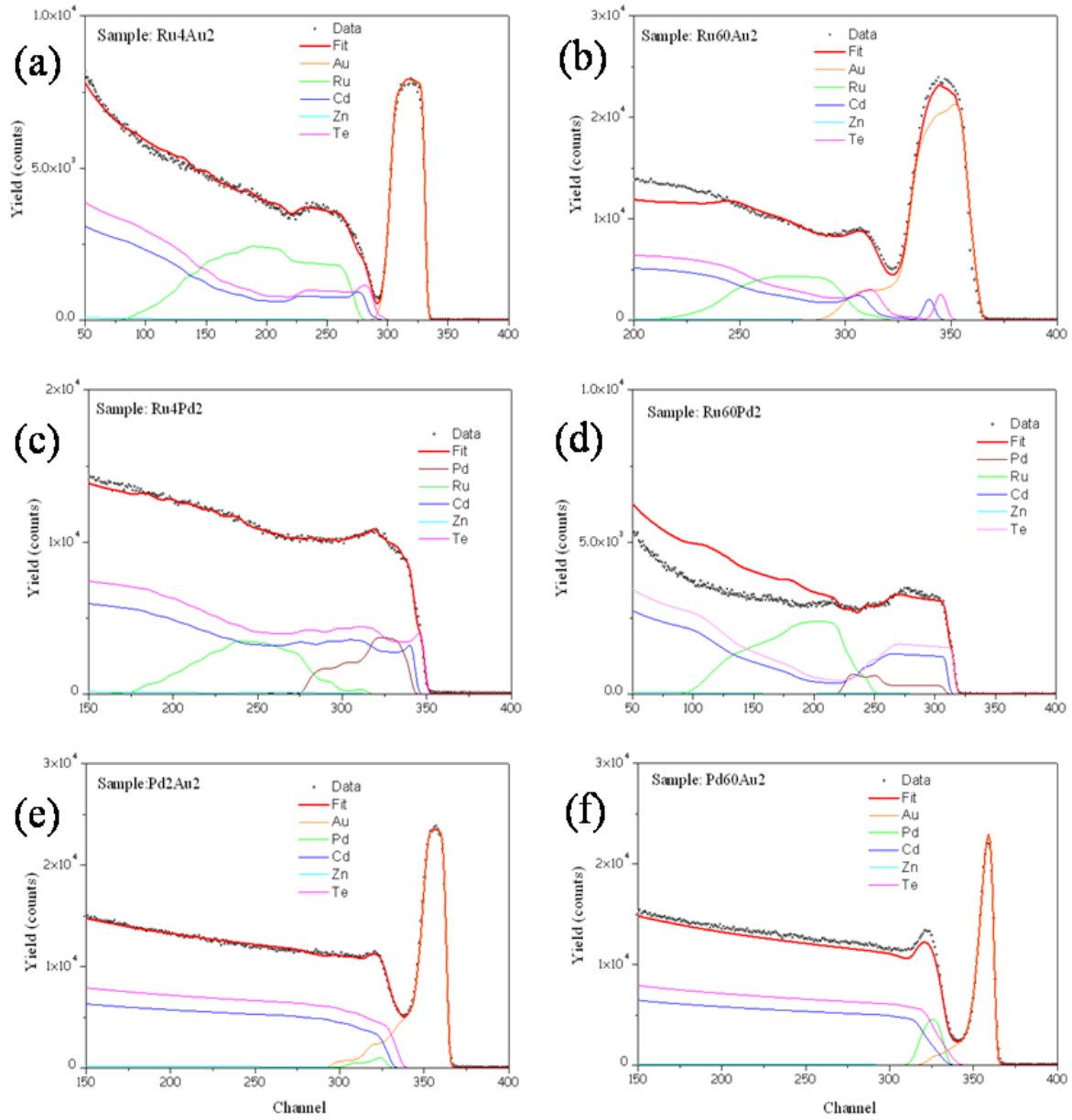

Figure 4.32. Experimental and fitted RBS spectra of the samples.
(a) Ru4Au2; (b) Ru60Au2; (c) Ru4Pd2; (d) Ru60Pd2; (e) Pd2Au2; (f)Pd60Au2.

Figure 4.33 exhibits the best layer structures as a depth function for the analysed samples. RBS depth profiles exhibited some complexity in the layers formed between the contacts and the substrates due to different inter-diffusion processes. The hetero-junctions observed for the different contacts will define the final performance of devices.

By using the RBS depth profiles, the thicknesses were estimated assuming the Bragg´s rule for the density of each layer, calculated from the elemental densities. The thickness of the different layers depends on the kinetics of reactions, occurring at each deposition. The redox potentials being not usable to determine the kinetics of reaction, an empirical study by measuring the thickness deposited or the concentrations present into the solution are generally more suitable to their determinations.

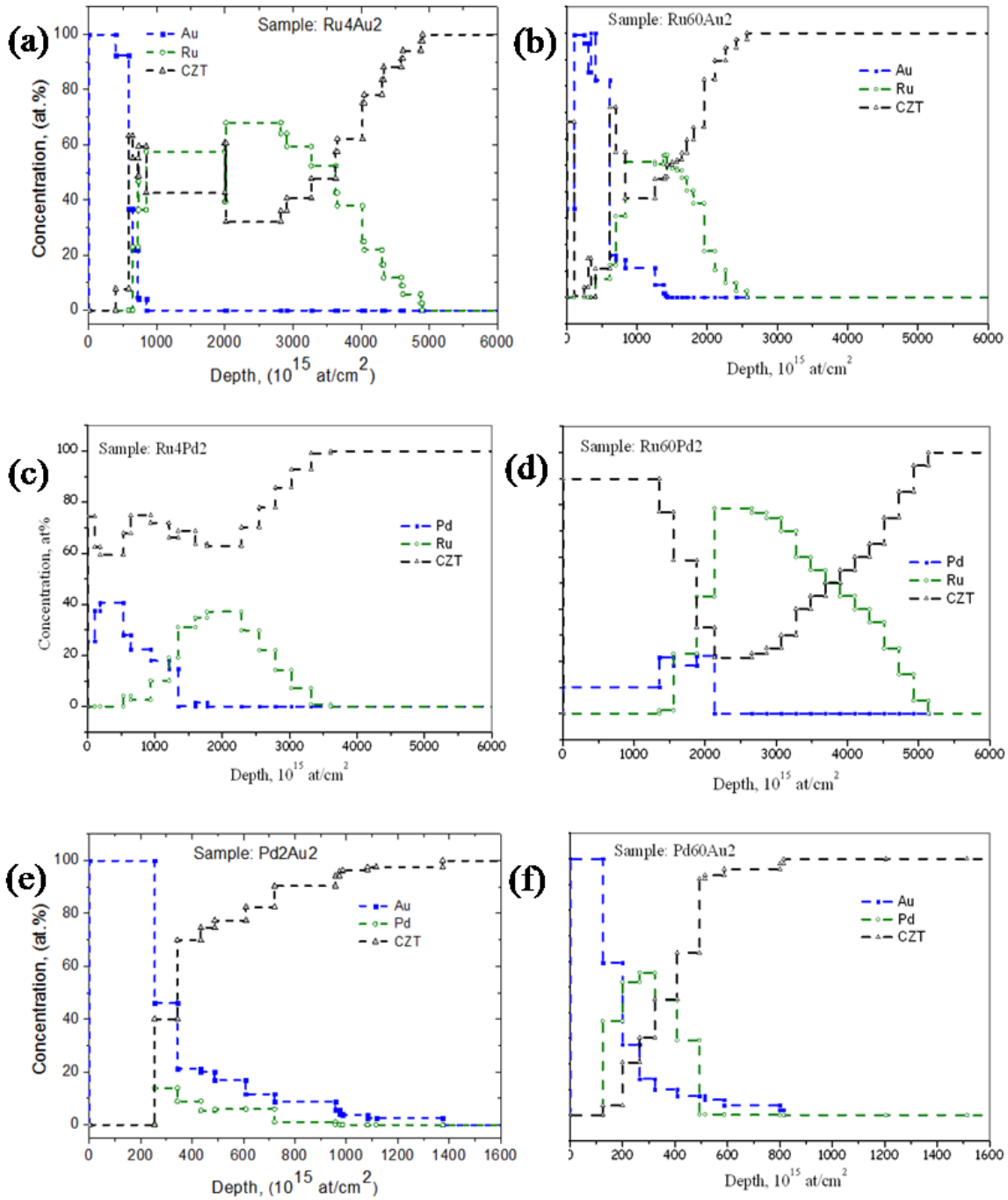

Figure 4.33. Best layer structures as a depth function for:
(a) Ru4Au2; (b) Ru60Au2; (c) Ru4Pd2; (d) Ru60Pd2; (e) Pd2Au2; (f)Pd60Au2.

From the RBS data, we can conclude that under identical growth conditions, the Au layer is thicker when it is grown on a Ru layer (~ 93 nm) than on a Pd layer (~ 42 nm). It is important to mention that the thickness estimated here is followed by the pure contact layer and the diffusion of the contact layer in the CZT bulk material.

Furthermore, the Au atoms can diffuse deeper into the Pd layer than into the Ru layer. When Ru or Pd is constituents of the layers, a fraction of CZT is always present as a component of the layer, therefore, a pure layer is never reach. Even in the sample with double layers of Ru/Pd (Ru4Pd2), CZT is also presented on the subsurface. In addition, it should be noted that the kinetics of inter-diffusion is different between different metals, as previous discussed in section 4.3.

4.4.2.2. Electrical Behaviours of the Double Layers Deposited on CZT

The electrical behaviours of double layers deposited on CZT have been investigated. Figure 4.34 displays the Current-voltage (I-V) characteristics of two different structures of double layers: RuAu on the both sides (RuAu-RuAu), or RuAu on one side and Ru on the other side (RuAu-Ru). The detectors deposited with double layers were prepared on $Cd_{0.9}Zn_{0.1}Te$:In material (from CGL), a n type material was determined by hot probe method.

As can be seen in Figure 4.34, the I-V characteristics for these two structures display a blocking (Schottky) contact behaviour in all the voltages ranges (from -200V to 200V). It is necessary to mention that the same detectors were investigated in order to first understand the performance of the detectors deposited with double layers. As can be oberved, at the same electric field, two different structures of contacts exhibit simular I-V behaviour at the forward bias, whereas the single-double layer display slightly higher leakage current than the double layers at the reverse bias.

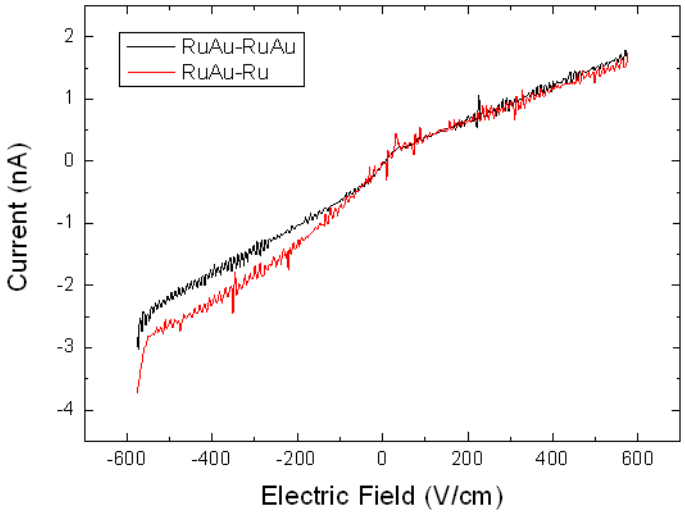

Figure 4.34. I-V characteristic for CZT planar detector with double layers RuAu-RuAu.

The gamma-ray responses with ^{133}Ba radioactive source for single-double-layer RuAu-Ru irradiated at different cathode side are presented in Figure 4.35. In Figure 4.35 (a), we can observe the 31 keV and 81 keV photopeaks of ^{133}Ba gamma source at the electric fields from1700 V/cm to 4600 V/cm when irradiate the planar detector from the double layers (RuAu) side, revealing that the planar device with single-double-layer contacts could be considered for gamma-ray applications. When the electric field increases from 1700 V/cm, one can observe the pulse height of 31 keV and 81 keV photopeaks increases and shifts to higher energies side, indicating the improvement of charge collection.

As we can see in Figure 4.35 (b), the resolution is very poor when irradiate the detector from the single layer (Ru) side compared with the irradiation at the double layers side. We can assume that one side of the detectors deposited with double layers may block the leakage current go through, which could be better for the device that block both sides. These results are in agreement with the I-V characteristics presented in Figure 4.34.

Table 4.10 shows the gamma-ray information with ^{133}Ba source of the results presented in Figure 4.35 (a), we can observe that the FWHM value of the 31 keV photopeak of the detector irradiated at RuAu side is around 20 – 25 % with the electric field from 1700 V/cm to 4600 V/cm, the Peak/Valley (P/V) ratio for the 31 keV photopeak is between 1.1 and 2.4, and the quality factor for this photopeak is at 0.22 - 0.24.

Figure 4.36 shows the gamma-ray response with the ^{133}Ba radioactive source of the planar detector with double layers (RuAu-RuAu) irradiated at cathode side. As can be seen, at the electric field of 1700 V/cm, the FWHM value of the 31 keV photopeak is 26.2 %, Peak/Valley ratio of the 31 keV photopeak is 1.5, and one can observe that the resolution of the double layers detector is lower than the single-double-layer detector.

In summary, we can conclude that the creation of hetero-structures of double layers on CZT by the electroless method can be considered for the future detector applications if we find out the proper configuration.

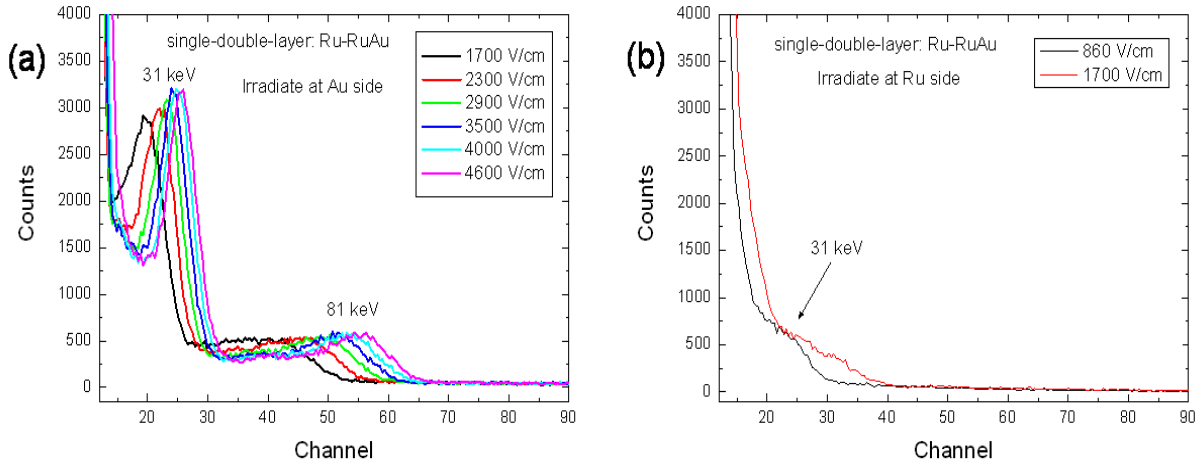

Figure 4.35. ^{133}Ba gamma-ray response of the CZT planar detector deposited with single-double-layer (RuAu-Ru).

Table 4.10. Information of the ^{133}Ba gamma spectra of single-double-layer (RuAu-Ru) planar CZT detector when irradiate at RuAu side shown in Figure 4.35 (a).

Electric field (V/cm)	^{133}Ba 31 keV FWHM %	P/V of the 31 keV peak	Quality factor of the 31 keV peak
1700	25.6	1.5	0.24
2300	23.6	1.1	0.22
2900	20.2	2.1	0.32
3500	19.8	2.3	0.34
4000	19.5	2.4	0.35
4600	19.5	2.4	0.35

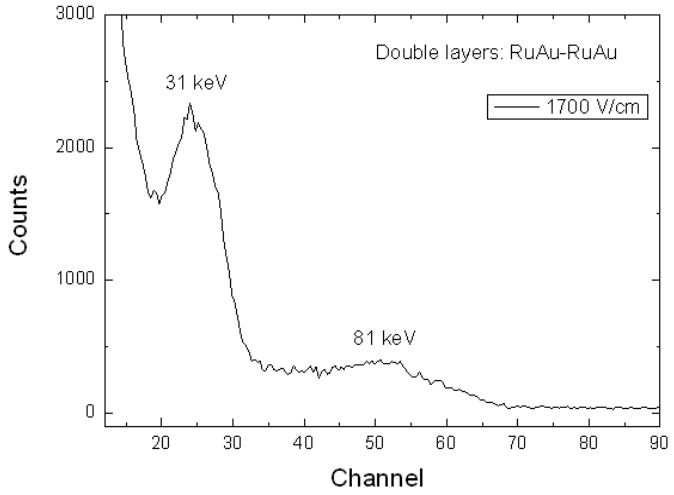

Figure 4.36. ^{133}Ba gamma-ray response of the CZT planar detector deposited with double layers (RuAu-RuAu).

4.4.3. Study of the Deposition of Triple Layers on CZT

The study of the deposition of triple layers on CZT has been carried out by the TXRF technique in order to identify the feasibility of the deposition.

Figure 4.37 exhibits the TXRF spectra recorded for the CZT samples deposited with triple layers as a function of X-ray emission energy. The triple layers were prepared by depositing Ru as a first layer, Pd as a second layer, and Au as the third layer on the top of the other two contacts. In Figure 4.37 (a) and (b), the TXRF figures exhibits the difference of the second layer (Pd), which was deposited for 2 min (Pd2) and 60 min (Pd60), respectively.

As presented by Figure 4.37, the Ru-K_α lines at 19.2 keV, Pd peak lines (K_α, K_β) at 21.1 and 23.8 keV, and Au-L lines are clearly visible in both samples which deposited the second layer with different times. However, the intensity of Au-L lines and Pd peak lines is much lower for the deposition of the second layer at a short time (Ru4Pd2Au2) than with a long time (Ru4Pd60Au2). We can assume that the deposition time of the second layer plays an important role for the process of contact deposition on CZT material.

As previous mentioned in Eq. 4-27 and Eq. 4-28, the mainly reactions of deposited a second layer may occur between Ru and Pd, or Pd and Au, transfer Ru^{2+} (or $PdCl_4^{2-}$) ions into the electroless solutions, and then deposit Pd or Au layer on CZT. However, due to the inter-

diffusion of the contact into the CZT material and the appearance of TeO_x layer, the position of a new deposited layer is greatly related with the presented layer. Therefore, the deposition of the third layer (Au) depends on the second deposited layer (Pd), as well as the first deposited layer (Ru).

When the second layer is deposited for a long time, the intensities of the peaks of the second and the third layer predominate. Therefore, a strong apparition of the three layers is obvserved by TXRF on CZT material.

In conclusion, this study has shown the capability to deposit triple layers on CZT, nevertheless, the studies of the detector applications with triple layers should be optimized for a future study.

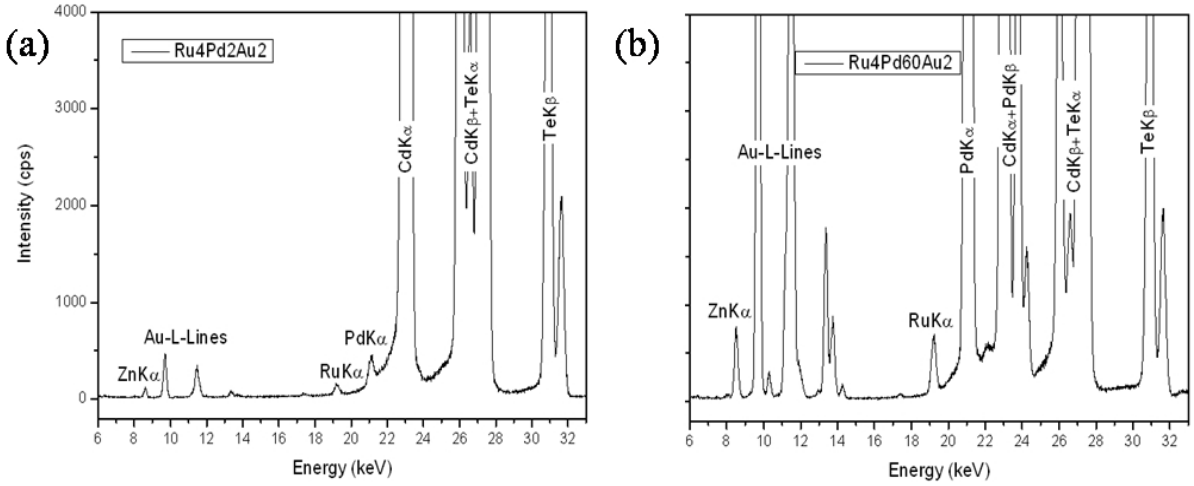

Figure 4.37. TXRF spectra on the surface of CZT samples with triple layers. (a) Ru4Pd2Au, (b) Ru4Pd60Au2.

4.4.4. Conclusions

The feasibility to deposit namometric multi-layers on CZT by electroless method has been investigated in terms of TXRF, RBS, PL, I-V, and Gamma ray techniques.

- TXRF technique allows the identification of hetero-structures of double and triple layers onto CZT material. The quantities of Cd (and Te) rejected in Ru solution can be identified by TXRF, but not with Au or Pd solutions. The inter-diffusion phenomena between layers are also clearly been demonstrated by RBS.

- By RBS technique, the diffusion of the contacts can be observed but the depth profiles exhibit that a pure layer cannot be reached. The kinetics of inter-diffusion between different contacts deposited on CZT are different.

- The I-V characteristics of two different structures of contacts exhibit similar I-V behaviours at the forward bias, whereas the single-double-layer display slightly higher leakage current than the double layers at the reverse bias.

- The detector performance of the single-double-layer contacts is better than the double layers contacts, suggesting that the CZT detectors prepared by the deposition of double layers could be considered for future detector applications.

4.5. Bibliography

[1] A. Burger, H. Chen, J. Tong, D. Shi, M. A. George, K. T. Chen, W. E. Collins, R. B. James, C. M. Stahle, and L. M. Bartlett, Investigation of electrical contacts for $Cd_{1-x}Zn_xTe$ nuclear radiation detectors, *IEEE Trans. Nucl. Sci.* Vol **NS-44**, 934 (1997).

[2] Q.Zheng, F.Dierre, J. Crocco, V. Carcelen, H. Bensalah, J.L. Plaza, E. Dieguez, Influence of surface preparation on CdZnTe nuclear radiation detectors, *Appl. Surf. Sci.*, Vol **257**, 8742-8746 (2011).

[3] E.Y. Lee, R.B. James, R.W. Olsen, H. Hermon, *J. Electron. Mater*, Vol **28**, 766 (1999).

[4] M.C. Duff, D.B. Hunter, A. Burger, M. Groza, V. Buliga, D.R. Black, *Appl. Surf. Sci.* **254**, 2889 (2008).

[5] T.E. Schlesinger, J.E. Toney, H. Yoon, E.Y. Lee, B.A. Brunett, L. Franks, R.B. James, Cadmium Zinc Telluride and Its Use as A Nuclear Radiation Detector Material, *Mat. Sci. Eng. R.*, Vol **32**, 103 (2001).

[6] M. Hage Ali, M. Ayoub, M. Roumie, F. Lmai, K. Zahraman, B. Nsouli, A. Zaiour, M. Sowinska, CdTe Nuclear Detector Electroless Contact Studies—New Results on Contact Structures, Interfaces, and Stress, *IEEE Trans. Nucl. Sci.*, Vol **51**, No. 4, 1875 (2004).

[7] M. Roumié, F. Lmai, A. Awada, K. Zahraman, B. Nsouli, A. Zaiour, M. Hage-Ali, M. Ayoub, J. Faerber, Depth Profiling and Stoichiometry of Constituents in Platinum Electroless Contacts on CdTe (111) under Different pH Values, *Thin Solid Films*, Vol **515**, 7843-7846 (2007).

[8] M.A. Lambert, P. Park, Current Injection in Solids, Academic Press, New York, 1970.

[9] A. Zappettini, V. Corregidor, E. Diéguez, M. Zha, F. Bissoli, L. Zanotti, luminescence properties of semi-insulating nominally-undoped CdTe crystals, *Semiconducting and Insulating Materials*, 2002. doi: 10.1109/SIM.2002.1242736.

[10] Q. Li, W. Jie, G. Yang, G. Zha, T. Wang, D. Zeng, Photoluminescence analysis on the indium doped Cd0.9Zn0.1Te crystal, *J. Appl. Phys.* Vol **100**, 013518 (2006).

[11] K.G. Lynn, M. Weber, H.L. Glass, J.P. Flint, C. Szeles, Improvement CdZnTe Detectors Grown by Bridgeman Process, *Mater. Res. Soc. Symp.*, Vol **487**, 229 (1998).

[12] J. Bottiger, J. Chevallier, P. Kringhoj, K.O. Schweitz, Stress in Thin Films, *Adhesion aspects of thin films*, **1**, 2001, 1-16.

[13] A. Musa, J. P. Ponpon, J. J. Grob, M. Hage-Ali, R. Stuck, and P. Siffert, Properties of Electroless Gold Contacts on p-type Cadimum Telluride, *J. Appl. Phys.* Vol **54** (60), 3260 (1983).

[14] A.M. Mancini, A. Quirini, L. Vasanelli, E. Perillo, E. Rosato, G. Spadaccini, E. Barbarino, Rutherford Backscattering Analysis of Electroless Gold Contacts on Cadimum Telluride, *J. Appl. Phys.*, Vol **53**, 5785 (1982).

[15] Q. Zheng, F. Dierre, V. Corregidor, R. Fernández-Ruiz, J. Crocco, H.Bensalah, E. Alves, E. Diéguez, *J. Crys. Growth*, (2011) doi:10.1016/j.jcrysgro.2011.04.014.

[16] CRC Handbook of Chemistry and Physics, Version 2005, David R. Lide, ed., CRC Press, Boca Raton, FL, 2005.

[17] Q. Zheng, F. Dierre, M. Ayoub, J. Crocco, H. Bensalah, V. Corregidor, E. Alves, R. Fernandez-Ruiz, J. M. Perez, E. Dieguez, *Cryst. Res. Technol.*, Vol **46**, 11, 2011, 1131-1136.

[18] Q. Li, W. Jie, L. Fu, X. Wang, X. Zhang, Metal-CdZnTe Contact and Its Annealing Behaviours, *Appl. Surf. sci.*, Vol **253**, 1190-1193 (2006).

[19] D. Alexiev, K.S. A.Butter, A.A. Williams, Gamma-ray Detectors from Thermally Annealed Bridgman-grown CdTe, *J. Cryst. Growth.*, Vol **142**, 303 (1994).

[20] S. Mergui, M. Hage-Ali, J.M. Koebel, P. Siffert, Thermal Annealing of Gold Deposited Contacts on High Resistivity p-type CdTe Nuclear Detectors, *Nucl. Instr. Meth. A.*, Vol **322**, 375-380 (1992).

[21] K. Chattopadhyay, X. Ma, J.O. Ndap, A. Burger, T.E. Schlesinger, M. Greaves, H.L. Glass, J.P. Flint, R.B. James, Thermal Treatments of CdTe and CdZnTe Detectors, *Proc. SPIE*, Vol **4141**, 303 (2002).

[22] Z.Q. Shi, C.M. Stahle, P. Chu, Chemical Etching and Post-annealing for High Performance CdZnTe Strip Detectors, *Mat. Res. Soc. Symp. Proc.* Vol **487**, 159-164 (1998).

[23] S.H. Park, J.H. Ha, J.H. Lee, H.S. Kim, Y.K. Kim, Thermal Annealing of Metal-Semiconductor Contact for CZT Detectors, IEEE Nuclear Science Symposium Conference Record, N24-296 (2007).

[24] I.M. Dharmadasa, J.M. Thornton, R.H. Williams, Effects of Surface Treatments on Schottky Barrier Formation at Metal/n-type CdTe Contacts, *Appl. Phys. Let.*, Vol **54**, 137-139 (1989).

[25] M. Roumié, K. Zahraman, B. Nsouli, F. Lmai, A. Zaiour, M. Hage-Ali, M. Ayoub, M. Sowinska, Ion Beam Analysis of CdTe Nuclear Detector Contact Grown by Electroless Methods, *Nucl. Inst. Meth. Phys. Res. B.*, Vol **240** (2005) 386.

[26] M. Roumié, F. Lmai, A. Awada, K. Zahraman, B. Nsouli, A. Zaiour, M. Hage-Ali, M. Ayoub, J. Faerber, Depth Profiling and Stoichiometry of Constituents in Platinum Electroless Contacts on CdTe (111) under Different pH Values, *Thin Solid Films*, Vol **515**, 7843-7846 (2007).

[27] M. Hage Ali, M. Ayoub, M. Roumie, F. Lmai, K. Zahraman, B. Nsouli and M. Sowinksa, CdTe nuclear detector electroless contact studies, new results on contact structures, interfaces and stress, *IEEE Trans. Nucl. Sci*, Vol **51**, 3300 (2004).

[28] V. Corregidor, P.C. Chaves, M.A. Reis, C. Pascual-Izarra, E. Alves, N.P. Barradas, Combination of IBA Techniques for Composition Analysis of GaInAsSb Films, *Materials Science Forum*, Vol **5614-516**, 1603-1607(2006).

[29] V. Corregidor, N.P. Barradas. E. Alves, N. Franco, L.C. Alves, P.C. Chaves, M.A. Reis, *Nucl. Instrum. Meth. B*, Vol **241**, 326 (2005).

[30] K. Zahraman, M. Roumié, A. Raulo, N. Auricchio, M. Ayoub, A. Donati, W. Dusi, M. Hage-Ali, F. Lmai, E. Perillo, P. Siffert, M. Sowinska, G. Ventura, *IEEE Trans. Nucl. Sci.*, Vol **53**, 1875 (2006).

[31] T. Asahi, O. Oda, Y. Taniguchi, A. Koyama, *J. Cryst. Growth.* **149** (1995) 23-29.

[32] H.B. Michaelson, *J. Appl. Phys*, 48, (1977).

[33] L. Wang, W. Sang, W. Shi, Y. Qian, J. Min, D. Liu, Y. Xia, Electroless Properties of Contacts on P-type $Cd_{0.8}Zn_{0.2}Te$ Crystal Surfaces, *Nucl. Inst. Meth. Phys. Res. A* **448** (2000) 581.

CHAPTER 5. INFLUENCE OF CRYSTAL GROWTH PROCESS ON CZT DETECTORS

This chapter will present a whole characterization of the detectors prepared with different crystal growth processes. The investigation is mainly focused on the influence of the presence of Te inclusions, the homogeneity of the alloy and doping, the luminescence behaviour, the surface states of the samples, and then the electrical properties of the detectors.

In the first section, the commercial CZT detectors from eV products were studied. The commercial detectors were characterized with regard to the structural, optical, and electrical properties. These detectors were considered as a reference to be compared with the detectors fabricated from the crystals grown in our laboratory.

In the second section, the characterization have been carried out in terms of structural, optical, and electrical properties of the samples harvested from two different ingots grown by CZT uncompounded and compounded starting materials, respectively. Several detectors were produced from different axial positions of these two ingots. I-V characteristics and gamma-ray response were studied separately with the detectors fabricated from these two ingots. Different applied voltages and electric fields were operated with different detectors in order to ascertain the optimum voltage (electric field) and saturation region for the completion of charge collection. Moreover, the detector properties achieved from these two different ingots were compared.

Finally, in the last section, the effects of twining structure on the surface and bulk properties of one ingot were investigated. The Te inclusions within the twin region and twin-free region were compared. In addition, the defects at the near-surface region of the material were examined by luminescence spectroscopy. At last, how these structures affect the electrical properties have been investigated.

5.1. Detector Prepared with Commercial CZT Samples

Commercial samples (eV Products) were characterized in our investigation as a reference in order to compare with the detectors produced in our laboratory. Therefore, the structural, electrical, and optical properties of the commercial detectors were investigated. Nevertheless, other characterization techniques where the material is destroyed will not be used considering the high value of the sample and the interest for future work.

5.1.1. Detector Surface Properties

The eV products samples were prepared by high pressure Bridgman (HPB) growth method. Figure 5.1 illustrates the photographies of the eV product commercial detectors. The dimensions of the samples are approximately $5 \times 5 \times 4$ mm^3. We can observe that each detector shows a clean surface with one dark black spot on the back side allowing the identification of the both sides if there is any mishandling. Moreover, a red laquer is present on the edges of the samples, which has the purpose to protect the samples from the exterior environment and passivate the detector. This red laquer is an industrial know-how and the composition has not been determined.

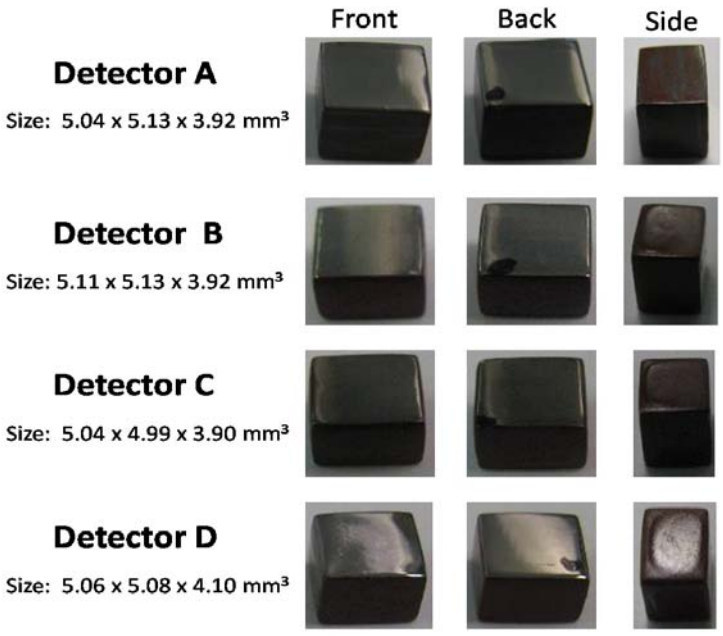

Figure 5.1. Photographies of the commercial detectors from the front, back, and lateral edge sides.

As can be seen in Figure 5.2, the surfaces of the commercial detectors (A and B) are quite smooth with minimal scratches, especially detector B with only a few surface contamination points. One must indicate that the other detectors follow the same behaviours.

Meanwhile, the relative atomic concentration of the surface of the commerical detectors has been characterized by Energy Dispersive X-ray Spectroscopy (EDX), and just as one example of the electrical composition of the detectors A and B is presented in Figure 5.3.

We can observe the high atomic concentration of Pt with detector A and B at around 30 % and 45 %, respectively, indicating that these two detectors were prepared with classical Pt electrodes. In addition, the relative atomic concentration of Cd, Zn, and Te are approximately 30 %, 5 %, and 30 % for these two detectors, respectively. In fact, the atomic concentration of the main elements on the surface region of these two detectors could provide the information about the relationship between the deposited contact and the bulk material.

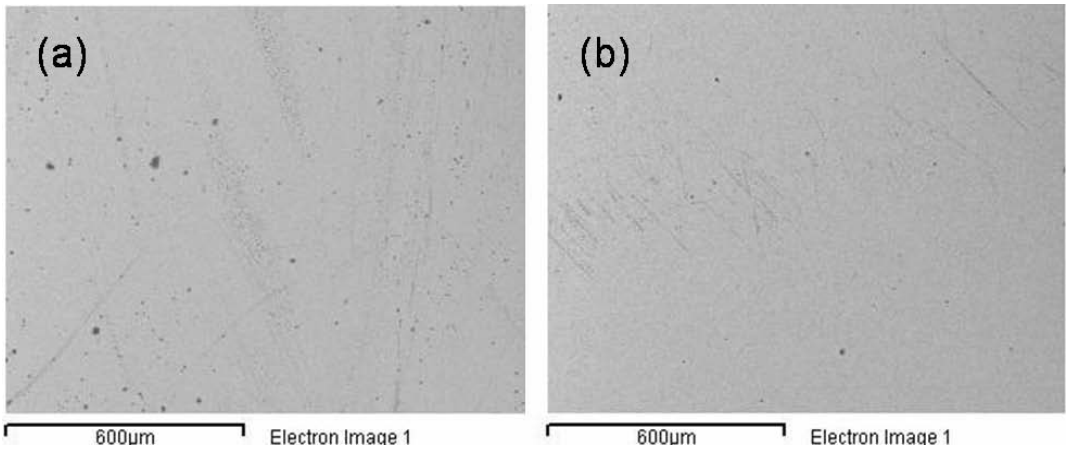

Figure 5.2. SEM images of the commercial detectors. (a) Detector A, (b) Detector B.

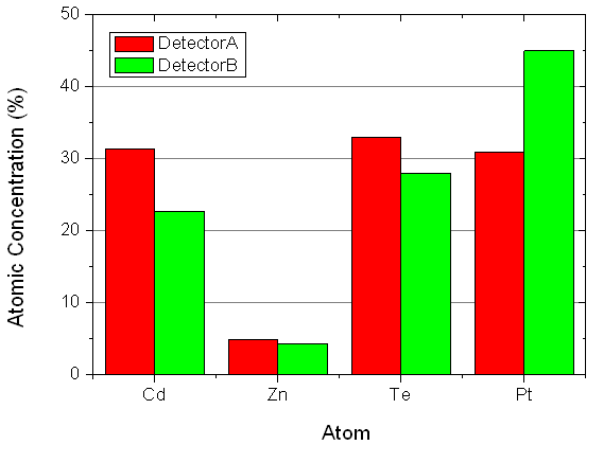

Figure 5.3. Relative atomic concentration of the main elements on the surface of CZT calculated by EDX technique.

It is necessary to mention that EDX technique cannot determine precisely the estimation of *x* in $Cd_{1-x}Zn_xTe$ material, which is due to the dependable characterization of the surface among all the elements present. The presence of the big difference in the Pt concentration among the detector A and B may come from the different deposition time, being the relative atomic concentration relationship between the contact and the bulk material a significant variation, -more details described in Chapter 4-. One must note that the composition of the other detectors C and D follow similar behaviours.

5.1.2. Te Inclusions by IR Microscope

The information of Te inclusions of the commercial detectors was given by using an 90i Nikon IR microscopy. Figure 5.4 exhibits the images of the Te inclusions on the subsurface of the detectors (A and B) at around 10 μm of the surface with the same magnification of 10× (780×480 μm^2).

As can be seen, higher density of Te inclusions with a diameter of approximately 7 μm is present in the sub-surface region of detector B. We can also observe that the size of Te inclusions in detector A is similar with detector B. Moreover, we can observe that the Te inclusions of detector B seems to align and follow a preferential orientation, which is a typical behaviour for the tellurium inclusions decorated in the grain boundaries or twins in this case, while this behaviour is not observed in detector A. The other two detectors C and D have similar behaviours as detector A, which are not presented here.

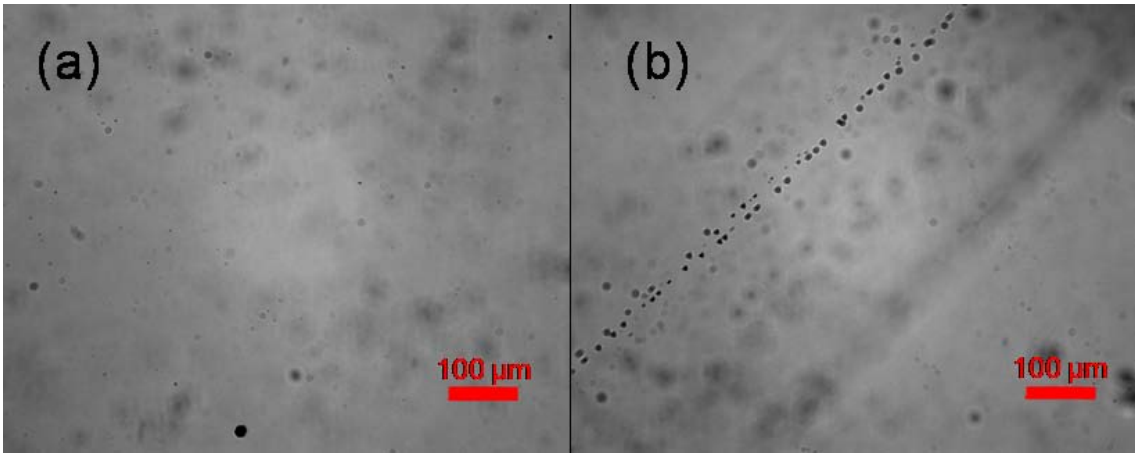

Figure 5.4. IR microscopy images of the Te inclusions presented in the commercial detectors. (a) Detector A, (b) Detector B.

5.1.3. Electrical Properties on Commercial CZT Detectors

The electrical properties of these four commercial detectors were studied in terms of resistivity, I-V characteristics, and Gamma-ray response. Contactless Resistivity Mapping (COREMA) system has been carried out to evaluate the uniformity and magnitude of the commercial samples' bulk resistivity.

Presented in Figure 5.5 are the COREMA mappings which have been completed for each detector. As can be seen, all the detectors exhibited high resistivity of $1 \sim 4 \times 10^9$ Ω.cm, and the resistivity seems to be higher for detector A.

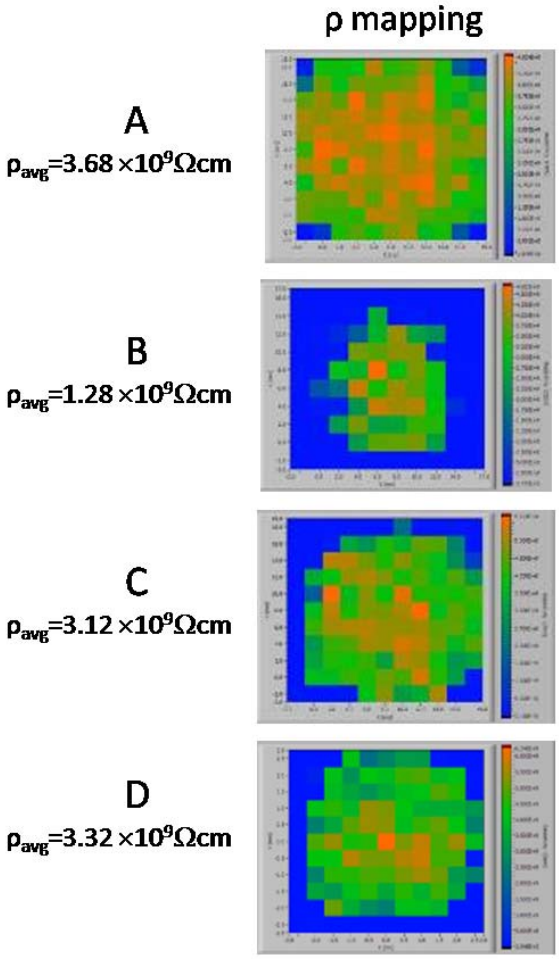

Figure 5.5. Resistivity mappings of the commercial detectors.

Figure 5.6 illustrates the I-V characteristics of all the commercial detectors with the electric field from -500 V/cm to +500 V/cm. As can be seen, the I-V characteristics display nearly ohmic contact behaviours for all the detectors. Detector A shows quasi-ohmic behaviour and

higher leakage current than the other detectors. Detectors B, C, D display more linear-ohmic behaviours, especially detectors C and D exhibit the lowest leakage current.

The Ohmicity coefficient of the detectors, *b*, can be calculated by $I = aV^b$, where *a* is a constant. The estimation has been carried out by using a small voltage range of -15 V ~ +15 V, as displayed in Table 5.1. We can observe that detector B displays the highest ohmicity coefficient value (0.992), which is more close to the ideal ohmicity.

In fact, we must take into account this coefficient, nevertheless, the ohmicity is one factor related with the detector performance, but there are several other parameters which can influence the detector quality.

The resistivity of the detectors measured by COREMA and calculated by I-V curves are exhibited in Table 5.1 for comparison. One can observe that all of the detectors presents high resistivity above 1 $\times 10^9$ Ω.cm by using COREMA technique, nevertheless, the resistivity calculated by I-V characteristics is one order of magnitude higher.

These differences can be explained by the fact that the contacts deposited on the commercial samples are partially blocking, leading to a slight high barrier height and a calculated resistivity which is higher than the bulk resistivity done by COREMA. As can be seen, detectors C and D show higher resistivity than the others by calculated from I-V characteristics.

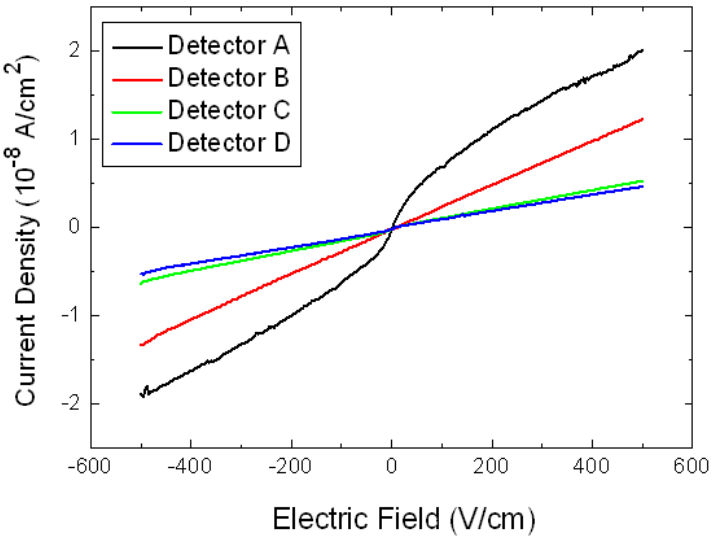

Figure 5.6. I-V characteristics of the commercial detectors.

Table 5.1. The resistivity measured by COREMA and calculated by I-V characteristics.

	Resistivity (measured by COREMA) Ω. cm	Resistivity (calculated by I-V) Ω. cm	Ohimicity (Ideal=1)
Detector A	3.7×10^9	1.4×10^{10}	0.989
Detector B	1.3×10^9	3.9×10^{10}	0.992
Detector C	3.1×10^9	7.4×10^{10}	0.987
Detector D	3.3×10^9	8.6×10^{10}	0.984

In order to calculate the barrier height we display the following ideas. The I-V technique is one of the most widely used methods for measuring the Schottky bairrer height. The I-V relationship under the thermo-ionic emission theory can be given by [1]:

$$I = I_0 \exp\left(\frac{qV}{nkT} - 1\right) \quad \text{Eq. 5-1}$$

where I_0 is the saturation current, V is the applied voltage, n is the ideality factor, T is the absolute temperature in Kelvin, k is Boltzmann constant, q is the electron charge. It is also well established that the barrier height is considered to be bias dependent, which result in the high ideality factor in Schottky diodes [4].

If the applied voltage V is much higher than kT/q, then the equation can be modified as [2]:

$$I = I_0 \exp\left(\frac{qV}{nkT}\right) \quad \text{Eq. 5-2}$$

The saturation current, I_0, can be expressed by:

$$I_0 = AA^*T^2 \exp\left(\frac{-q\Phi_{b0}}{kT}\right) \quad \text{Eq. 5-3}$$

where Φ_{b0} is the zero-bias barrier height, A is the contact area, A^* is the effective Richardson constant for thermionic emission which is 120 $Acm^{-2}K^2$ for CZT [3]. The zero-bias barrier height can be calculated by suing the theoretical value of the Richardson constant in Eq. 5-3, thereby can be written as [4]:

$$\Phi_{b0} = \frac{kT}{q} \ln\left(\frac{AA^{*}T^{2}}{I_0}\right) \quad \text{Eq. 5-4}$$

Therefore, barrier height at different temperature can be given, which is strongly related to the saturation current. Indeed, the saturation current (I_0) can be derived from the straight line intercept of *lnI* at *V=0* following Eq. 5-2.

Figure 5.7 (a) displays the dependence between ln I and the forward bias at different temperature for detector D as one example. In fact, for the ln I - V curve with the temperature of 298 K, ln I_0 can be obtained at -23.7, and the saturation current can be determined at 5.29× 10^{-11} A. Meanwhile, the contact area of detector (*A*) is around 0.226 cm^2, and then the barrier height can be calculated by using Eq. 5-4. As can be seen, the saturation current increases as the temperature rise [2].

Figure 5.7 (b) shows the barrier height as a function of temperature. One can also observe that the barrier height increases with the increasing temperature. The theoretical line is simulated following the experimental data.

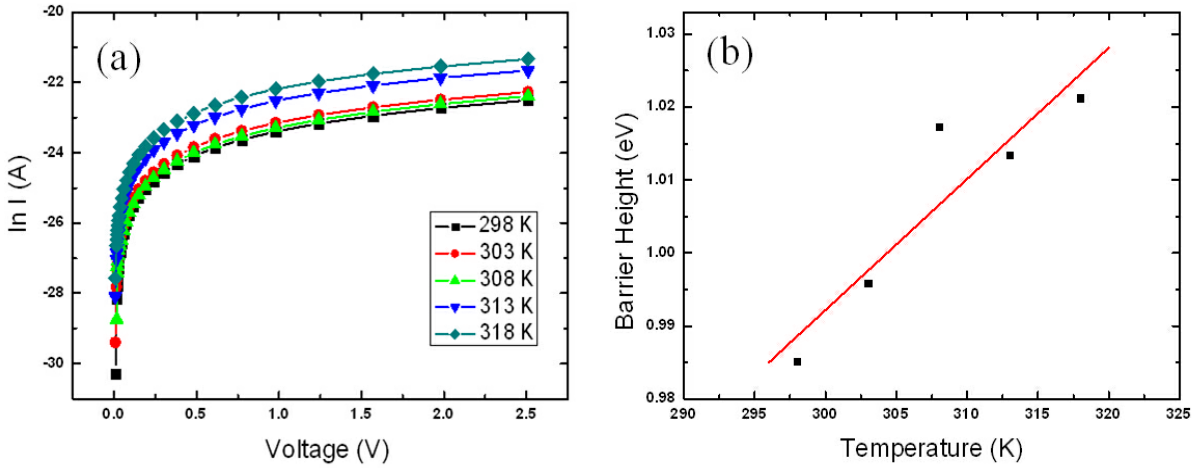

Figure 5.7. Current various forward voltage of detector D (a), Barrier height with temperature derived from the I-V curves.

Table 5.2 presents the zero-bias barrier height of the detector D at the temperature of 0 K (the slope in Figure 5.7 (b) at forward bias). At the reverse bias, the calculation will be done in the same way, although the results are not presented here, the calculated zero-bias barrier height is shown in Table 5.2.

One can observe that the zero-bias barrier height (Φ_{b0}) shows the same value of 0.46 eV for both the anode side and cathode side of the commercial detector D. This result means that this commercial detector has symmetric behaviour, which is a very important topic investigated in our group [5]. In fact, this value of barrier height could explain the ohmic contact results exhibited in Figure 5.6. Later in section 5.2.5.2, we will see the Schottky contact behaviour with higher barrier height.

Table 5.2. Information of barrier height at 0 K and 0 V.

Temperature (K)	Forward Φ_{b0} (eV)	Reverse Φ_{b0} (eV)
0	0.46	0.46

Figure 5.8 shows the gamma-ray response of the commercial detectors at the electric fields of 1000 V/cm and 1500 V/cm by using the ^{133}Ba radioactive source. The value of the electric filed has been chosen due to the fact that at higher value of the noise increases and the resolution is very poor.

We can observe the peaks at 31 keV and 81 keV photopeaks clearly present with detectors A, B and D at two different electric fields. It should be noted that the same behaviours can be observed with detector C, which is not present here. The detector performance of the commercial detectors is summarized in Table 5.3.

Detector D exhibits more noise at the valley before the 31 keV photopeak, which shows the lowest higher P/V ratio (1.8 and 1.7) than the other two detectors. The Full Width at Half Maximum (FWHM) of the 31 keV and 81 keV photopeaks for detector B at two electric fileds are 8.9 % and 4.3 %, 9.5 % and 3.6 %, respectively, which displays the lowest value than the other two detectors.

As can be seen in Figure 5.8, detectors A and B shows similar gamma response behaviour, whereas different leakage current observed in Figure 5.6. Although detector D achieves the lowest leakage current, the poorest detector performance is still obtained due to the highest noise of 31 keV photopeak shown in Figure 5.8. It means that the behaviour of leakage current is not the main factor to determine the detector performance. Some other parameters, such as Te inclusions, surface state, and lateral edges treatment could also affect the detector performance. Therefore, the different performance of the commercial detectors is determined by all the parameters exhibited in this section.

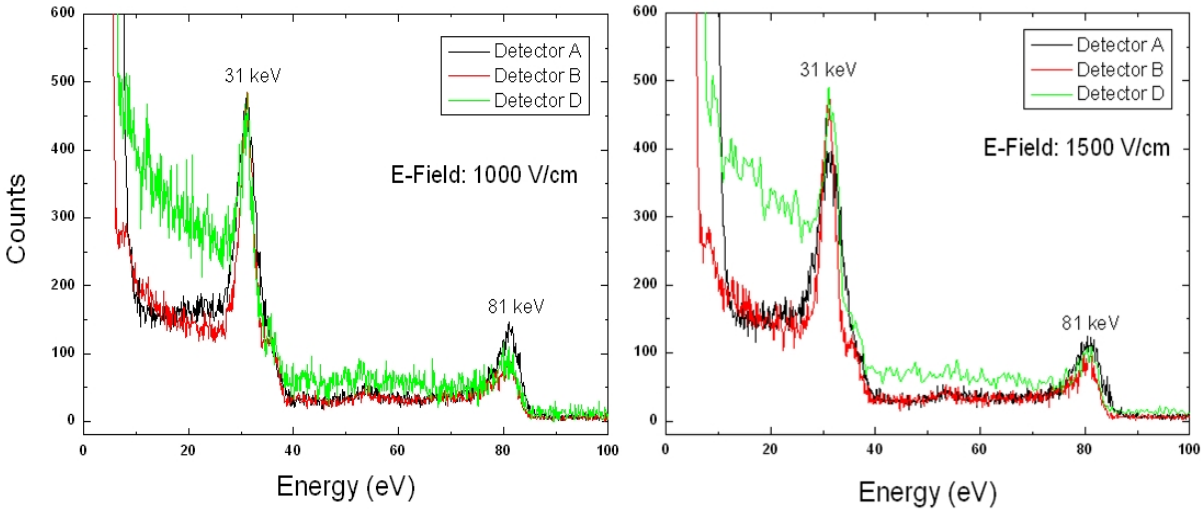

Figure 5.8. Gamma response of the commercial detectors using the ^{133}Ba radioactive source with two electric fields.

Table 5.3. Comparison of the detector performance of the commercial detectors.

	E-Field (V/cm)	FWHM 31 keV ^{133}Ba (%)	Peak/Valley (P/V)	Quality factor of 31 keV pek	FWHM 81 keV ^{133}Ba (%)
Detector A	1000	12.8	3.1	0.49	4.9
	1500	13.3	2.6	0.44	5.0
Detector B	1000	8.9	3.5	0.63	4.3
	1500	9.5	3.0	0.56	3.6
Detector D	1000	4.7	1.8	0.62	0.2
	1500	11.3	1.7	0.39	4.2

In this section, we also fabricate the home contacts on the commercial detectors with the objective to study the electrode deposition process. For that reason, the commercial detector D was selected, after removing the original Pt contact by polishing, a new Pt home-made contact was deposited. In fact, the detector was polished with 3 μm alumina abrasive and 1 μm Diamond slurries, the new contact was deposited with the Pt electroless solution produced in our laboratory (see chapter 3). Finally the lateral edges of the detectors were treated followed by the process presented in section 3.5.

Figure 5.9 presents the I-V characteristic of the detector D with as-received Pt contact and home-made Pt contact. We can observe that the leakage current of detector D slightly increases after home-made, which could be explained by the mechanical damages or some other uncontrolled factors during the reproduced stage. Nevertheless, linear ohmic contact can still be observed.

Figure 5.10 shows the gamma response of the new home-made planar detector D with the Pt contacts using ^{133}Ba gamma-ray radioactive source. As can be seen, at different electric fields, the 31 keV and 81 keV phototpeaks can be observed with home-made detector D.

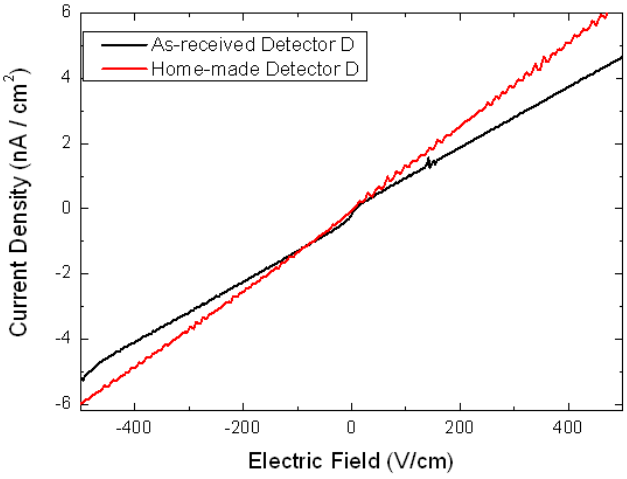

Figure 5.9. I-V characteristics of the commercial detector D.

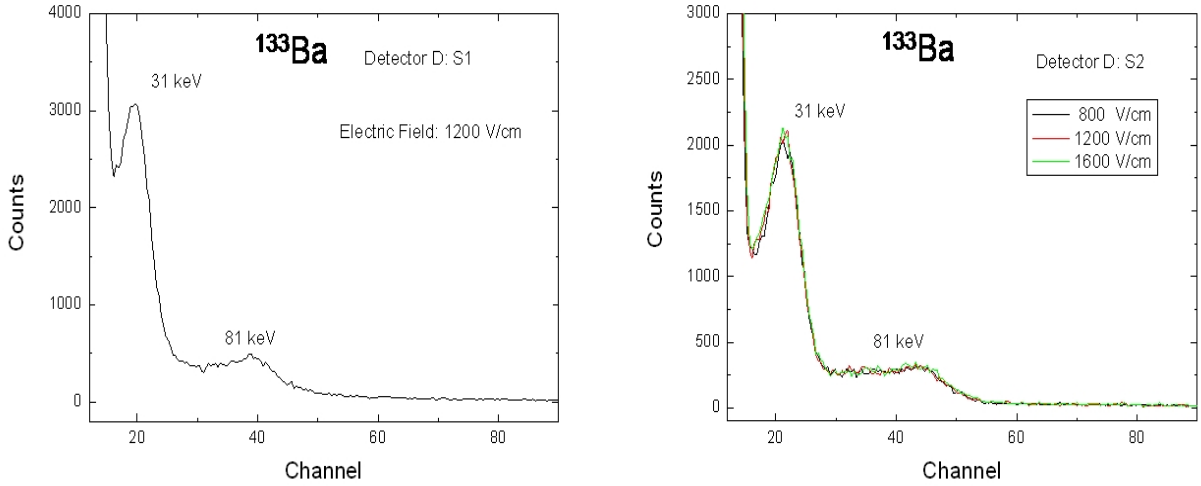

Figure 5.10. Gamma response of the reproduced detector D by using the ^{133}Ba radioactive source irradiated on both sides.

Table 5.4 summarizes the information of the detector performance of the commercial detector D before and after home-made contact process done in our laboratory. One can observe that the FWHM of the 31 keV and 81 keV photopeaks of the new reproduced detector D is higher than the as-received detector D, and the quality factor of the 31 keV photopeak of the reproduced detector D (0.3) is slightly lower than the as-received one (0.4).

We can conclude that the commercial detectors can be reproduced in our laboratory but with slightly lower performance, which may due to the surface preparation process and lateral edges treatment, such as the polishing process done in the commercial samples and the unknown passivating layer.

Table 5.4.The information of the ^{133}Ba spectra of the commercial detector D.

	FWHM 31 keV ^{133}Ba (%)	Peak/Valley (P/V)	Quality factor of 31 keV pek	FWHM 81 keV ^{133}Ba (%)
As-received Detector D	11.3	1.7	0.4	4.2
Home-made contact Detector D	23.2	1.8	0.3	12.0

5.1.4. Conclusions

The surface properties, Te inclusions, and electrical properties of the commercial detectors were investigated. Particularly, detector D was home-made to compare with the as-received one in order to enhance the detector preparation process in our laboratory.

- All the commercial detectors exhibit clean and smooth surface with minimal scratches, classical Pt electrodes were found on the detectors by EDX technique. The diameter of Te inclusions presented with detector B are 2~3 times larger than detector A.
- Nearly linear Ohmic behaviours can be observed with the commercial detectors except detector A.
- Slightly different detector performance exhibited with the commercial detectors.
- The leakage current of the home-made contact detector D shows linear-ohmic behaviour but slightly increases compared with the as-received detector D. The detector performance of the home-made detector D is slightly lower than the as-received one.

5.2. Detector Prepared with Crystals Grown with CZT Uncompounded or Compounded Starting Materials

The process of the crystal growth preparation has a very strong impact on the detector performance. It influences the presence of inclusions/precipitates, the homogeneity of the alloy and doping, and therefore the electrical properties of the detectors.

In this section, several home-made detectors will be characterized. These detectors have been prepared from two ingots grown in crystal growth laboratory (CGL). This section has high interest due to the fact that there are two important ways of CZT crystal growth preparation: using Cd, Zn, Te elemental uncompounded starting material, or CZT compounded material which has been purchased. Considering the high importance of the two ways of crystal growth preparation, this section mainly described the characterization of the detectors prepared using both ways with the same Vertical Gradient Freeze (VGF) growth method.

In fact, the most important differences between the detectors will be the starting materials and in consequence the heating process, because the other parameters of crystal growth are the same, such as growth rate (~ 3 mm/h), the cooling rate (~ 20 °C/h), and the temperature gradient at the solid-liquid interface (~ 10 °C/cm).

5.2.1. Sample Preparation

Two CZT ingots prepared with a diameter of 25 mm and length of 60 mm were grown by the Vertical Gradient Freeze method using a 5 independent heater zones furnace, which is capable to dynamically control the thermal gradients applied throughout the crystals during the growth. The same temperature ramp was applied to the crystals grown using Pyrolytic Boron Nitride (pBN) crucible. One ingot was grown using 7 N Cd, Zn, and Te starting materials with a 4.5 ppm dopant In named with "uncompounded", while the other ingot was grown using pre-synthesized 7 N CZT material doped with 1-3 ppm In named "compounded".

Figure 5.11 and Figure 5.12 exhibits the images of the two ingots and the samples obtained for the investigation. As can be seen, both ingots at the last-to-freeze region are highly polycrystalline and show a conical shape, regardless of the starting material composition. This polycrystalline region displays high void contents and is clearly a detrimental part.

Particularly, the ingot grown with CZT compounded materials did not exhibit secondary phases of unreacted Te on the surface of the crystal.

Both ingots were sliced perpendicular to the growth direction into single wafers, and a series of samples were obtained as a function of axial positions.

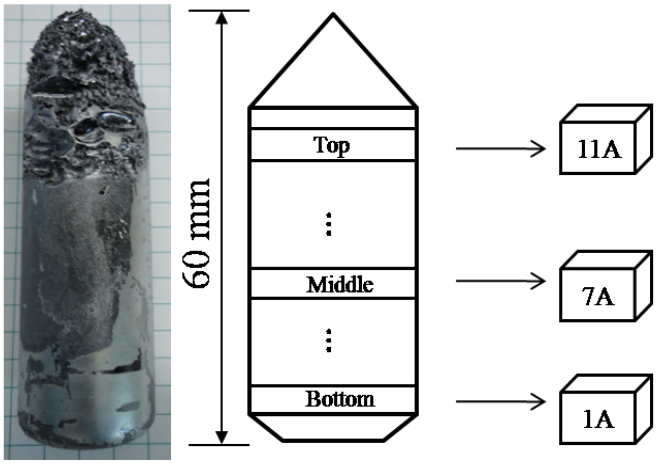

Figure 5.11. Information of the ingot grown with CZT uncompounded material and the samples obtained from this ingot (60 mm in length and 25 mm in diameter).

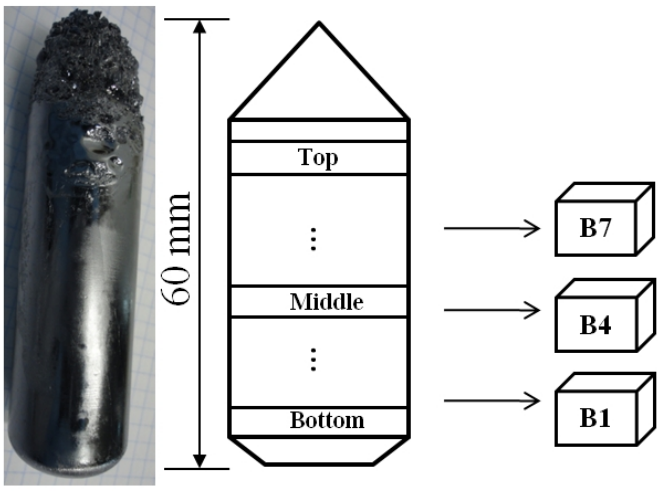

Figure 5.12. Information of the ingot grown with CZT compounded material and the samples obtained from this ingot (60 mm in length and 25 mm in diameter).

The samples were prepared following the process described in chapter 3: mechanical lapping, polishing, chemical etching with 2 % a Br-Methanol solution, in the case of detectors were prepared by deposit Au contact with the electroless method.

Presented in Figure 5.13 and Figure 5.14 are the photographs of several detectors with different axial positions obtained from the ingots grown with different starting materials. The thickness of the detectors fabricated from the ingots grown with CZT uncompounded material and compounded material was between 3 and 4 mm, considering the importance of thickness in the detector performance.

In fact, the detectors presented here are only examples of several detectors prepared in our work, in order to show the information of produced detectors. It is necessary to note that in our case some detectors (e.g. B1) are not mentioned in this chapter is due to the mishandling preparation process.

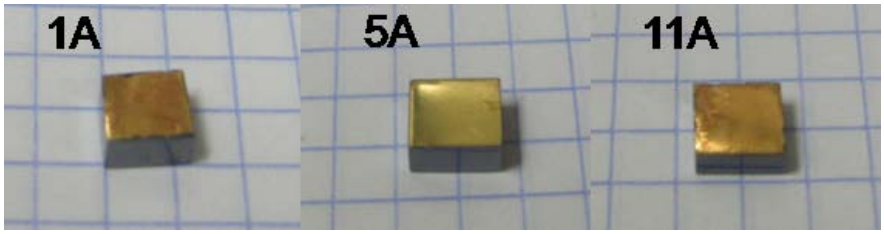

Figure 5.13. Images of the detectors fabricated from the ingot grown with uncompounded material with different axial positions.

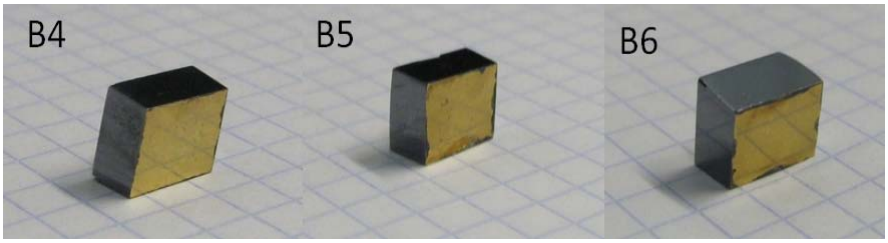

Figure 5.14. Photographies of the planar detectors harvested from the ingot grown with compounded material.

5.2.2. Chemical Composition of Samples from Different Crystals

Due to the segregation of the species, the variation of Zn concentration leads to a modification of the bandgap of the material, which has much more significant effect on the detector performance. At the same time, the distribution of dopants (such as In) is also of great importance to the quality of the crystals [6].

Toney et al. reported the theoretical basis about the optimum Zn concentration for CZT detectors [7]. They concluded that for optical performance, a bandgap of around 2.0 eV

would be the best for planar detectors, which is depending on the photon energy and corresponding to a Zn concentration of nearly 0.7-0.8. In fact, the impurities in CZT segregate into the top or bottom part of the ingot, depending on the value of the segregation coefficient for each element. The fluctuation of the dopant concentration of indium can result in the variation of resistivity, which can affect the stability and energy resolution of the detectors. Therefore, it is important to have homogeneous Zn and In distributions for fabricating high performance detectors and high yield [8][9].

The samples in our investigation from different ingots have been characterized with the ICP-MS technique in order to evaluate the concentration of Zn and In with different axial directions along the ingots. Figure 5.15 and Figure 5.16 illustrate the composition of Zn and In along the axial direction the ingot in this investigation.

In Figure 5.15 for the ingot grown with CZT uncompounded material, one can observe that the Zn concentration decreases with the axial direction along the whole ingot. At the solidified fraction of 0.6-0.8, the Zn concentration significantly decreases and reaches the value of 6-8 %. Meanwhile, the quantity of In along the ingot has a small variation at the bottom and middle parts of the ingot, but a large exponential increase when the solidified fraction is between 0.6 and 0.8, indicating that a certain amount of excess In is rejected into the melt during crystal growth is solidified at the end of the growth ingot. This sudden increase in the axial direction could be explained by the segregation phenomenon of indium along the ingot.

As can be seen in Figure 5.16 for the ingot grown with CZT compounded material, the concentration of Zn also changes with different axial direction along the whole ingot. In the first half (first-to-freeze) part of the ingot, the Zn concentration steady at around 10~12 %, whereas a gradually decrease of the Zn concentration present from the middle part to the top part of the ingot (last-to-freeze). The quantity of In along the ingot slightly increase from first-to-freeze part to the last-to-freeze part of the ingot (0 ~ 0.6). However, the In quantity increases exponentially as the solidified fraction from 0.6 to 0.8, which is similar to the ingot grown by uncompounded material, indicates the exceedingly poor quality from the very last freeze part that will not be investigated.

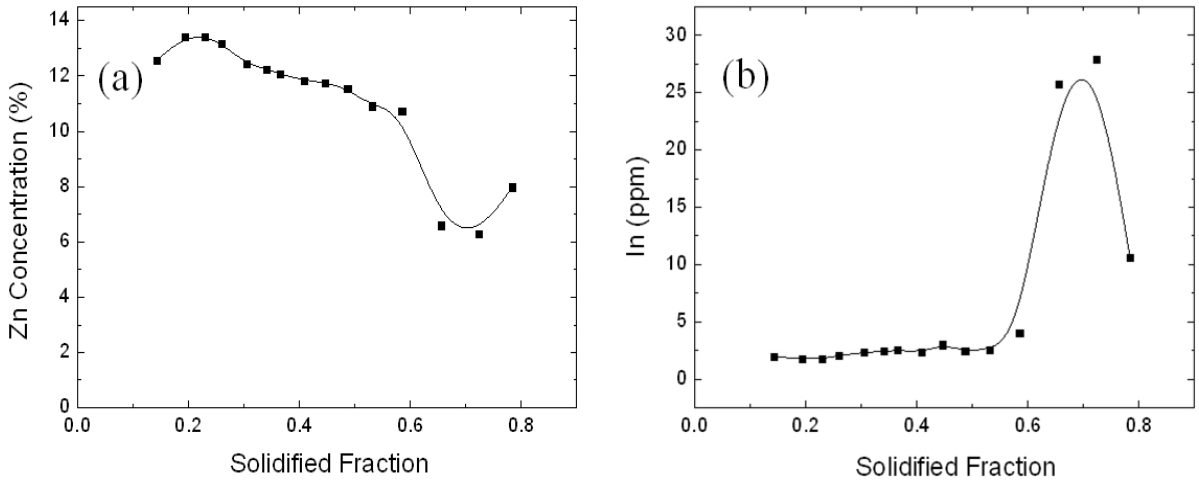

Figure 5.15. Distribution of the composition of Zn along the axial direction of the ingot grown with CZT uncompounded material (a), In distribution along the axial direction of the ingot (b).

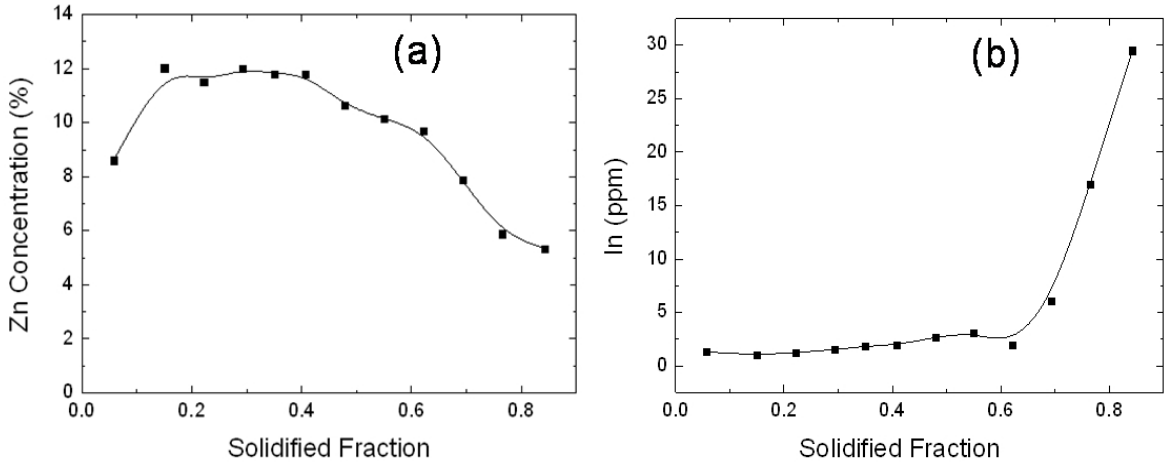

Figure 5.16. Distribution of the composition of Zn along the axial direction of the ingot grown with CZT compounded material (left), In distribution along the axial direction of the ingot.

The previous experimental results follow the distribution of Zn and In can be calculated by the Scheil equation [10]:

$$C_S / C_0 = k(1-g)^{k-1} \quad \text{Eq. 5-5}$$

where C_0 is the initial concentration of Zn (or In) which is given by the quantity added into the stariting materials, C_S is the concentration of Zn (or In) in the solid/liquid interface during

growth, which is approximately equivalent to the Zn concentration in the as grown ingot, *k* is the segregation coefficient in CZT, and *g* is the solidified fraction [11].

This equation is known as the normal freeze equation and describes the steady decrease in the Zn content as one moves along the grow axis of the boule. It is important to comment that the average zinc concentration decreases as one approach the last to freeze part of the ingot, leading to inherent composition non-uniformity [6].

After different fittings from Eq. 5-5, the segregation coefficient of Zn is calculated to be 1.4, while the segregation coefficient of In is equal to 0.39. It can be found that this segregation coefficient obtained in this investigation is much higher than the value of 0.13 for indium in CdTe demonstrated by *Rudolph* and *Zanio*, the value of 1.3 deduced for indium doped in $Cd_{0.9}Zn_{0.1}Te$ by *Li et al*, and 0.43 reported for indium doped in $Cd_{0.96}Zn_{0.04}Te$ by *Issihiki et al*. [8][11-14]. The reason for the difference among the segregation coefficients with different crystals could be explained by the value of Zn content namely *x*, which may greatly affect the In redistribution in $Cd_{1-x}Zn_xTe$, being in our case as In concentration of 2-3 ppm [10].

5.2.3. Te Inclusions by IR Microscope

The concentration and distribution of Te inclusions and precipitates within the material is one of the major reasons to the degradation of CZT detectors. Te inclusions can degrade the detector performance by distorting the internal electric field and the trapping free carriers generated by the incident radiation [15]. Moreover, the presence of Te inclusions can reduce the active volume of the detectors leading to a voltage breakdown and increasing the leakage current. It is important to note that even randomly distributed inclusions can also influence the performance of detectors [16][17].

Infrared microscopy has been used to identify the size and density of Te inclusions and Te precipitates. The information of Te inclusions in different samples harvested from two ingots grown by using uncompounded and compounded starting materials are exhibited in Figure 5.17 and Figure 5.18.

As can be seen in Figure 5.17, only a few round shape Te inclusions with the diameter of approximately 30 μm presented at the sub-surface region of the bottom sample of the ingot grown by uncompounded starting material (1A). In the middle part of the ingot (5A, 10A), we observe the Te inclusions appear with smaller size round shape about 10 μm but

connected by lines, called pipes. In the top part of the ingot (12A), a higher density of Te inclusions with a diameter of around 6 μm can be observed, indicating that more defects exist in the last-to-freeze region of the ingot.

One can observe that the last-to-freeze (top) region is highly polycrystalline. This polycrystalline region of the ingot represents high void content and is extremely detrimental to the yield of high quality material. In summary, lower concentration of Te inclusions exist in the first-to-freeze (bottom) region than the last-to-freeze (top) region which may harvest better quality materials. The detector performance will be investigated in section 5.2.5.

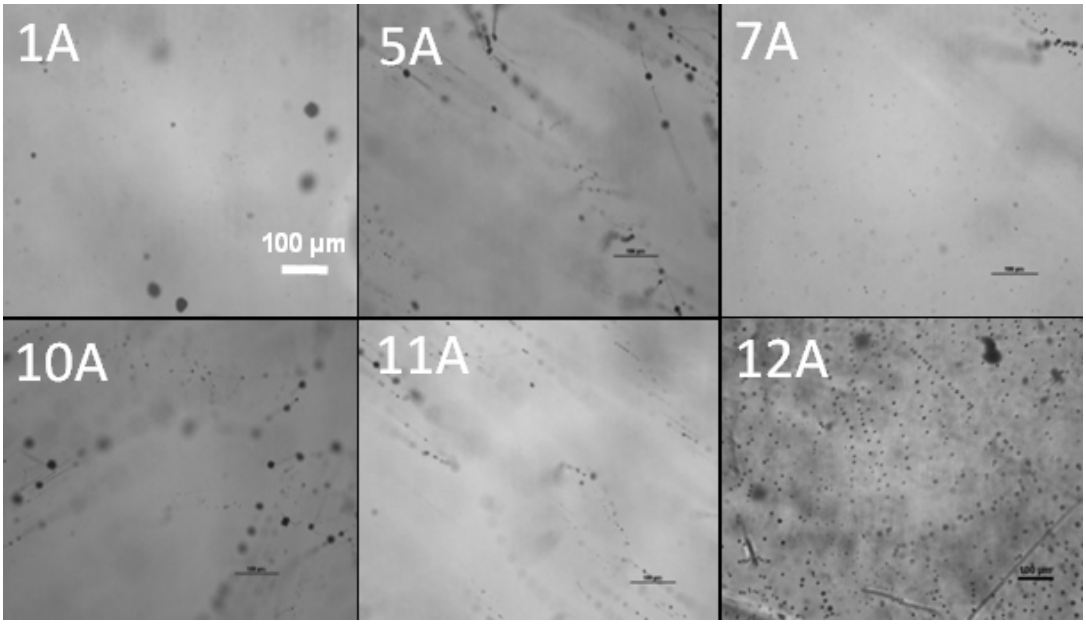

Figure 5.17. The IR microscope images of the samples from the ingot grown with uncompounded material, the same scale for all the images.

As presented in Figure 5.18, one can see a high density of small size Te inclusions with the diameter of about 1 ~ 2 μm in all the samples from the ingot grown with CZT compounded starting material. In comparison with the Te inclusions shown in Figure 5.17, one can observe that the density of Te inclusions in the crystal grown by CZT compounded material is slightly higher, but the dimension is much smaller. Therefore, the detectors fabricated from these two kinds of crystals are necessary to be determined.

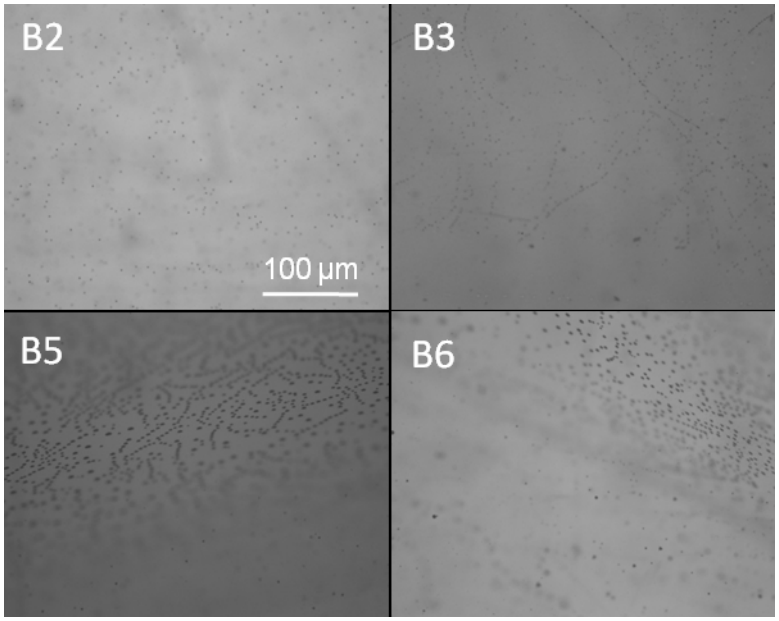

Figure 5.18. The IR microscope images of the samples from the ingot grown with compounded material, the same scale at 100 µm presented for all the images.

5.2.4. Luminescence Behaviours

5.2.4.1. Cathodoluminescence Spectroscopy

Cathodoluminescence (CL) technique has been operated at room temperature to provide the preliminary information of the luminescence properties of the CZT materials prepared in our work. First of all, the influence of the operate parameters (voltage and current) have been studied in order to find out the optimum selection.

Figure 5.19 displays the CL emission spectra of CZT samples at various accelerated voltages with the beam current of 15 nA. It can be seen that, the emission band at 1.56 eV increases at a faster rate when the applied voltages increases. The integrated intensity of the CL emission for the CZT samples at different applied voltages is plotted in Figure 5.21 (a). As we can observe, the integrated intensity of the emission peak at 1.56 eV has a slightly rise from 5 kV to 30 kV, and a rapid increase of integrated intensity occur at higher voltage (> 30 kV).

Figure 5.20 presents the CL emission spectra of CZT samples at various beam current. The electron acceleration voltage was set to 15 kV, while the current was changed from 5 nA to 70 nA. We can observe that the intensity of emission peak at 1.56 eV increases steadily as the beam current increases. Figure 5.21(b) shows the integrated intensity of the various CL

emissions as a function of beam current. As can be seen, the integrated intensity increases gradually as the beam current increases.

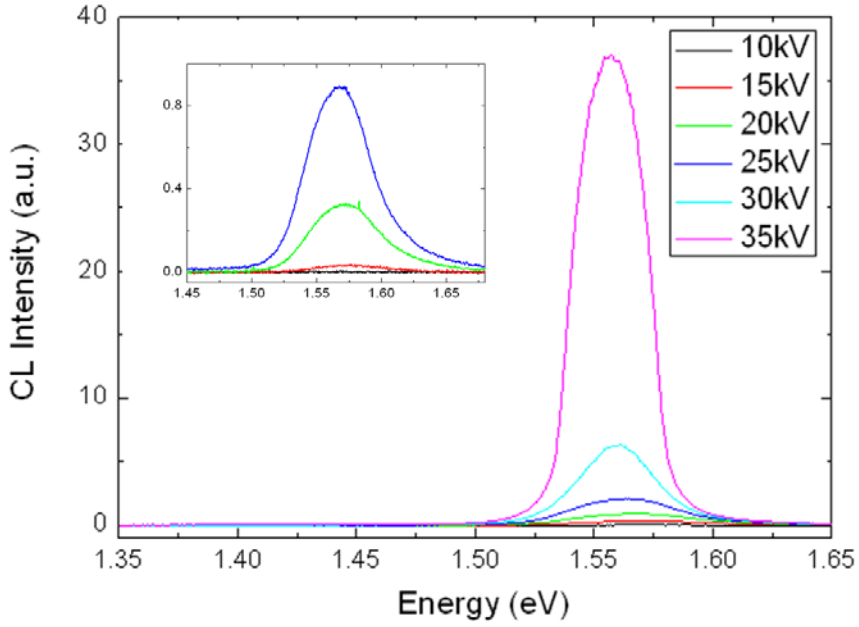

Figure 5.19. CL emission spectra from the same CZT samples at various increasing accelerated voltages carried out at room temperature with a beam current of 15 nA.

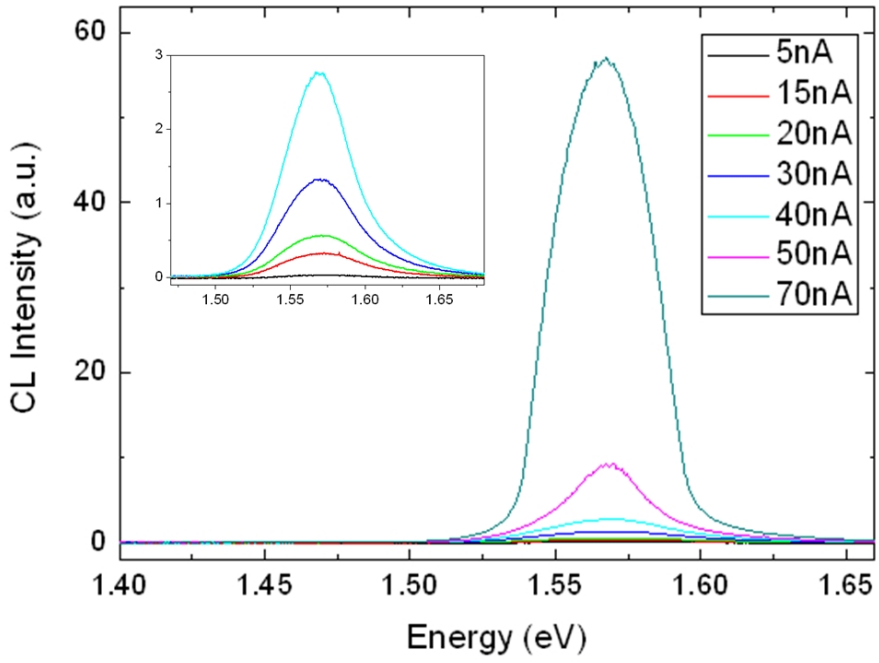

Figure 5.20. CL emission spectra from the same CZT samples at various increasing beam currents.

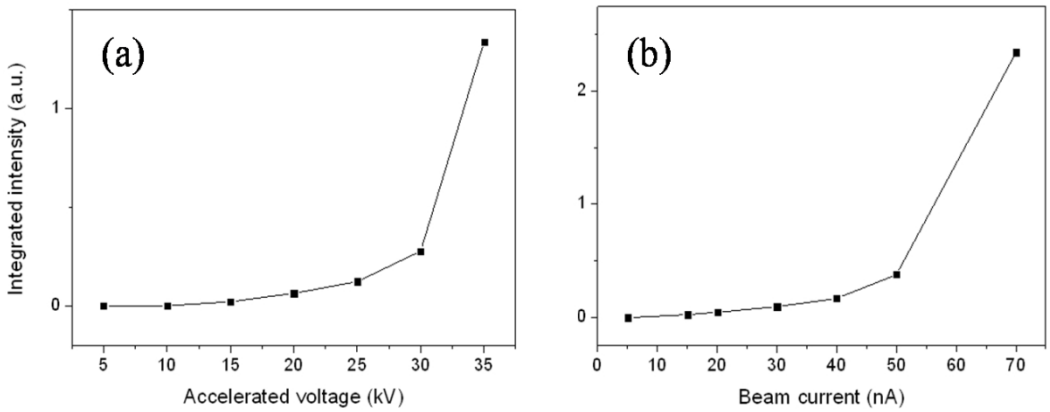

Figure 5.21. The integrated intensity of the CL emissions from the same CZT samples at various accelerated voltages (a) and various increasing beam currents (b).

Figure 5.19 and Figure 5.20 exhibit clearly the influence of the operate factors on the CL results, indeed, when the voltage or current increases, the electron beam can penetrate deeper in the bulk material and therefore the intensity of the peaks are increased.

The average penetration depth, *Re*, can be calculated by [18]:

$$\mathrm{Re} = (\frac{0.0398}{\rho}) * U_B^{1.75} \qquad \text{Eq. 5-6}$$

where ρ is the material density (g/cm^3), and U_B is the electron beam acceleration voltage (kV). For CZT, the material density is 5.78 g/cm^3. The average penetration depth as a function of accelerated voltage is summarised in Table 5.5. One can observe that the penetration depth is 2.65 μm at an accelerated voltage of 30 kV, which was chosen for the investigation as following.

Table 5.5. The penetration depth versus accelerated voltage calculated by Eq. 5-6.

Accelerated Voltage (kV)	Re (μm)
10	0.39
15	0.79
20	1.30
25	1.92
30	2.65
35	3.47

The CL emission spectra of the samples at different position of the ingot grown by CZT uncompounded material have been studied, as shown in Figure 5.22. It should be mentioned that only the information of one ingot is presented for overall view. For comparison, the spectra were normalized to the same peak intensity.

We can observe that the CL spectra of CZT samples at room temperature are composed of a single broad band peaking at energy close to the band-gap energy. One can see that the CL signal is bright at room temperature and exhibits an asymmetric line shape. By comparison of the curves, we can observe the emission peak located at 1.56 eV shift to higher energies as the zinc concentration increases. The strong relationship between the composition and the emission band can be observed, which allows us a further investigation by Photoluminescence technique.

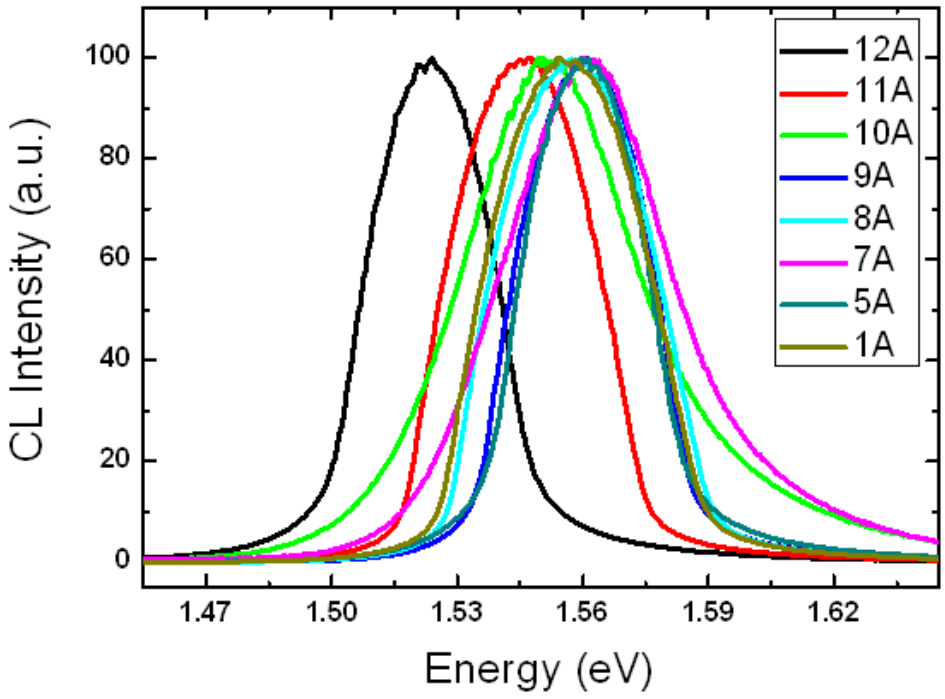

Figure 5.22. The CL emission spectra of CZT samples at different position of one ingot.

The energy peak position of the CL emission peak of the CZT samples as a function of the solidified fraction are plotted in Figure 5.23. The peak energy at 1.56 eV presents a gradually decrease when the Zn concentration decreases. One can see that at the top of the ingot (last-

to-freeze region), where there is the lowest concentration of Zn (but with more impurities and defects), the emission peak shift to the lowest energy side (1.52 eV).

This result could be interpreted if one takes into account that the peak position of emission line can be expressed by [19]

$$h\gamma = E_g - E_D + kT/2 \quad \text{Eq. 5-7}$$

where *Eg* is the band gap energy, E_D is the ionization energy of the donors, *k* is the Boltzmann constant, T is the temperature, and $h\gamma$ is the incident photon energy.

The approximate bandgap of CZT (with 10% Zn) is 1.6 eV, which allows specific operation at room temperature without significant dark current and prevents the excessive thermal generation of charge carriers. For the emission at 1.56 eV, the donor ionization energy should be 51.8 meV (a donor level located below the conduction band).

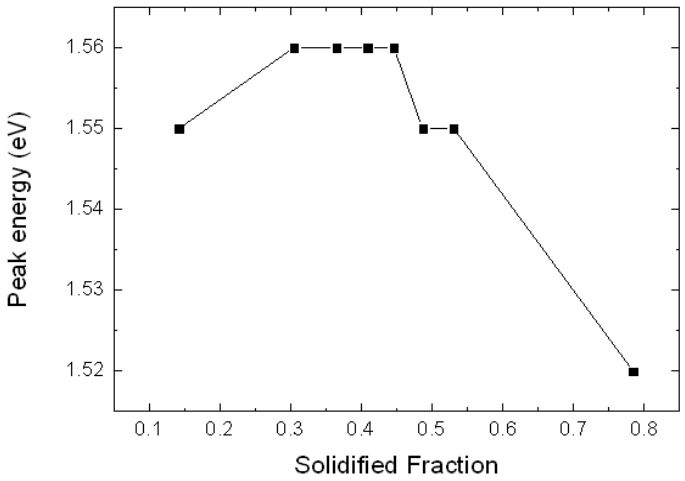

Figure 5.23. The peak energy of the CL emissions of the CZT samples with different position along the ingot.

5.2.4.2. Photoluminescence Spectroscopy

Photoluminescence technique has been used to evaluate the band structure of the crystal. Low-temperature PL spectrum represents the material quality, and also predicts the detector performance. The PL spectra for a high-quality crystal are dominated by the excitonic luminescence, whereas for a poor quality detector defect-related luminescence is dominant. In addition, another factor is the sharpness of the spectrum that is extent to which adjacent peaks can be resolved.

Moreover, the third indicator which applies to CZT is that the donor-bound exciton (D^0, X) peak tends to be dominant in high-quality crystals, while the acceptor-bound exciton (A^0, X) luminescence is stronger in low-quality samples. The reason can be explained by the relatively large number of donors compared to acceptors in the higher-quality material, and the donors is critical to enhance the electrical resistivity and vary the trapping centres refer to the formation of complexes [20].

A comparison of the low temperature PL spectra of the samples with different positions of the ingot grown by using CZT compounded material is shown in Figure 5.24. Polished samples were prepared for the measurement. Generally, the near-band-edge region contains some of the most useful information in the low temperature PL spectra. In Figure 5.24, in the near-band-edge region, we can observe that the dominant peak is the donor-bound exciton (D^0, X) for the CZT sample in our work ($\approx$x0.1), which is in contrast to CdTe and $Cd_{0.96}Zn_{0.04}Te$, where the typical dominant peak is (A^0, X) [6][20][21].

Meanwhile, one can comment that the concentration of cadmium vacancies in this crystal is rather low or greatly compensated by the donors [22]. The (A^0, X) peak is supposed the exciton bound to the shallow neutral acceptor, which is associated with the recombination between Cd vacancy acceptor and indium donor [23]. As shown in Figure 5.24, a decrease of the intensity of (A^0, X) peak from tip region (1A-5A) to the tail region (11A-12A), implying that less recombination occur between Cd vacancy and In donor. One can also observe that the energy of (A^0, X) peak shift to the lower energy part from the first freeze to the last freeze part of this ingot, which is suggested to relate with the concentration of zinc.

Indeed, Cd vacancies (V_{Cd}) exist in CZT material is due to the high Cd partial pressure in the growth process [12]. The compensation between the shallow acceptor Cd vacancies and the deep donor Te antisites is considered to be responsible for the high resistivity of CZT [24][25].

We observe that the emission intensities of (A^0, X), (D^0, X) and DAP decrease dramatically when the concentration of Zn decreases and disappear at the top of the ingot (8 %). From the bottom to the top of the ingot, as the concentration of Zn decreases, the (A^0, X) peak decrease gradually, revealing that more shallow acceptors are compensated. A distinct decrease of neutral donor bound exciton (D^0, X) peak can be seen, indicates that less indium atoms act as shallow donors by substituting at Cd sites, which could lead to the formation of the In-substituting defect $[In_{Cd}]^+$ [26].

The donor-acceptor pair (DAP) peak decreases until its disappearance at the tail of the ingot, indicating that the density of the shallow donor level related to In donors decreases greatly. It means that, at the bottom of the ingot, there are still a large quantity of In donors left after the compensation with Cd vacancies, as well as after the recombination of excess In donors with other shallow levels, such as Na and Li. The surplus of shallow donors (In) may lead to the n-type conductivity of the CZT crystal [22][27].

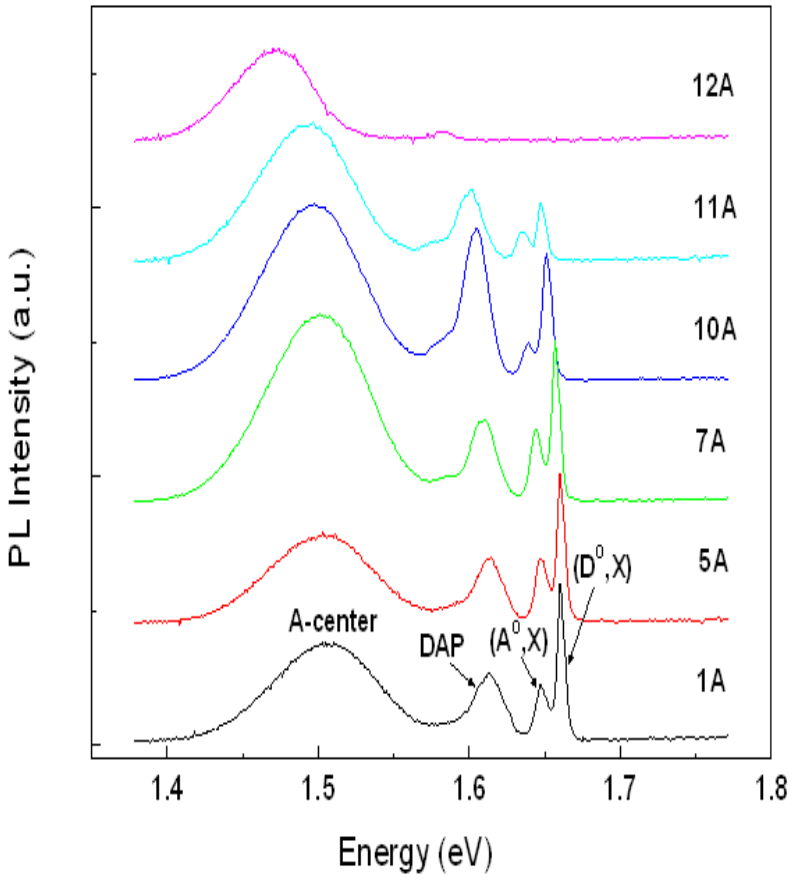

Figure 5.24. Low temperature (22 K) PL spectra of the CZT samples along the axial position of the ingot grown by uncompounded material.

When In is introduced into CZT crystals, the doped In atoms act as shallow donors, $[In_{Cd}]^{+}$, by substituting for Cd sites, forming the single negative donor-vacancy complex (A-centre), $[In_{Cd}^{+} - V_{Cd}^{2-}]^{-}$, to compensate with Cd vacancies [26]. One can observe a slightly decrease of the intensity of the A-centre from the bottom to the top of the ingot, indicating that A-centre

further recombined with extra accumulated In donor at the bottom region, $[In_{Cd}]^{+}$, forming the neutral complex described by the following equation [26]:

$$[In_{Cd}^{+} - V_{Cd}^{2-}]^{-} + [In_{Cd}]^{+} \rightarrow [2In_{Cd}^{+} - V_{Cd}^{2-}]^{0} \quad \text{Eq. 5-8}$$

According to this equation, most ionized indium donors are neutralized by A-centre. It should be noted that most Cd vacancies are compensated by In donors, the residual Cd vacancies can also be further compensated by another donors like $[Te_{Cd}]^{4+}$. The simple form of this neutral complex $[Te_{Cd}^{4+}\text{-}2V_{Cd}^{2-}]$ can be obtained by one Te antisite and two Cd vacancies [23].

Table 5.6 summarizes the PL results of CZT samples along the axial directions of the ingot grown with CZT uncompounded materials. Indeed, the $(D^0, X)/(A^0, X)$ ratio relates to the prevalence of the concentration of shallow donors over that of shallow acceptors throughout the cross-section [28]. By comparison, one can observe that, there is a decrease of the $(D^0, X)/(A^0, X)$ ratio in the CZT crystal from the tip to the tail of the ingot (except 10A), where is also the decrease of the Zn concentration in the crystal, indicating a relative increases of the concentration of Cd vacancies (V_{Cd}) and shallow acceptors such as Na_{Cd}.

Table 5.6. Summary of the PL results (22 K) of the samples from different axial positions of the ingot grown with CZT uncompounded material.

	Zn (%)	Na (%)	(D^0, X) (eV)	(A^0, X) (eV)	DAP (eV)	A-center (eV)	$I_{(D^0, X)}/I_{(A^0, X)}$	$I_{(D^0, X)}/I_{DAP}$	$I_{(D^0, X)}/I_{A\text{-center}}$	FWHM (D^0, X) (meV)
1A	12.5	0	1.6600	1.6467	1.6135	1.5067	2.67	1.25	1.60	6.1
5A	12.5	0.03	1.6600	1.6467	1.6146	1.5067	2.30	2.23	1.69	6.4
7A	12	0.07	1.6566	1.6435	1.6093	1.5012	2.16	1.95	0.86	6.6
10A	11.5	—	1.6511	1.6391	1.6052	1.4976	3.19	0.83	0.72	7.8
11A	11	0.14	1.6478	1.6359	1.6021	1.4931	1.84	0.81	0.43	7.7
12A	8	—	——	——	——	1.4735	——	——	——	——

One can conclude that the concentration of V_{Cd} and shallow acceptors (Na_{Cd}) is lower in the first-to-freeze region of the ingot than the last-to-freeze region. This conclusion is also in agreement with the ICP-MS technique which is not presented here, where Na is the main residual impurity present in the crystal (see table 5.6). As shown in Table 5.6, we can see that

the concentration of Na (obtained with ICP-MS) decreases gradually from the tip region to the tail region of the ingot. It is important to note that other impurity interstitials such as Ca and Fe also exists in the crystal acting as shallow acceptors (identified by ICP-MS), however, these shallow acceptors can be negligible due to its significant lower concentration than that of Na.

The assumption of the hydrogen-like energy levels displays that (D^0, X) peak lies approximately 13 meV lower than the bandgap energy, which can be considered as a reliable indicator of the bandgap [6][26]. As can be seen in Figure 5.24, the peak position of (D^0, X) steadily shift as one move away from the bottom part of the ingot, which is associated with the alloy composition, *x*.

The positions of donor-bound exciton (D^0, X) peak from the PL spectra shown in Figure 5.24 are displayed in Figure 5.25. As one can observe, the energy of (D^0, X) peak presents a red shift (to lower energy side) from the first freeze part to the last freeze part of the ingot. The relationship between the bandgap, *Eg*, and the zinc concentration, *x*, can be expressed by [6]:

$$E_g(x) = E_0 + (\Delta E - a)x + ax^2 \quad \text{Eq. 5-9}$$

where *a* is the bowing parameter, E_0 is the ground state energy. The values of the bowing parameter can vary from 0.17 eV to 0.43 eV, which may depend on the other parameters such as residual strain, and must be determined experimentally from different crystal [6][24][25]. The values of these parameters will be further determined as following.

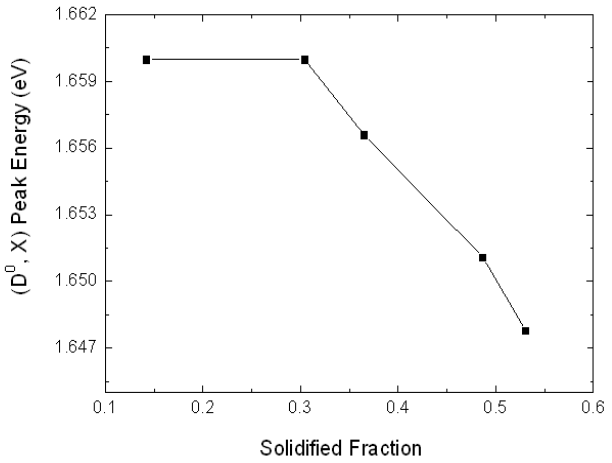

Figure 5.25. Peak energy of (D^0, X) at low temperature (22 K) PL spectra as a function of distance along the growth axis of the CZT crystal (x ≈ 0.1).

Siegle et al. demonstrated that the strain in the crystal can lead to a blue-shift (to higher energy side) of the near-band-gap exciton emission peak in GaN material, which is probably also occur in the case of CZT [25].

To corroborate the parameters E_0, a, and ΔE shown in Eq. 5-9, the temperature dependence of the PL spectra was investigated with two samples from different part of the same ingot. The temperature dependence of the PL spectra of the bulk CZT crystals from 22 K to 150 K were investigated, the PL results of the bottom sample (1A) is shown in Figure 5.26, and the PL results of the middle sample (7A) is displayed in Figure 5.27, being the samples representation of the ingot.

It is evident from these two figures that, as the temperature increases from 22 K to 150 K, the DAP peak located at 1.613 eV of this sample (1A) reduces, which completely disappears above 35 K. In fact, when the temperature increases, the electrons trapped at the shallow donor levels will be excited to the conduction band, therefore, the DAP recombination is mitigated, leading to its diminishing intensity. Similar behaviour can be observed with the DAP peak for the sample from the middle region of the ingot (7A), as shown in Figure 5.27.

One can see from these two figures, the (D^0, X) peak and (A^0, X) peak are quenched rather rapidly when the temperature rises, which disappear above 100 K. The (A^0, X) peak quenches significantly rapid when the temperature increases and merges with the other transitions. Furthermore, Above 50 K, we can observe a rapid decrease of the intensity of A-center peak, and this peak vanishes above 150K. Therefore, when the temperature increases, the luminescence is quenched due to thermally excited nonradiative transitions.

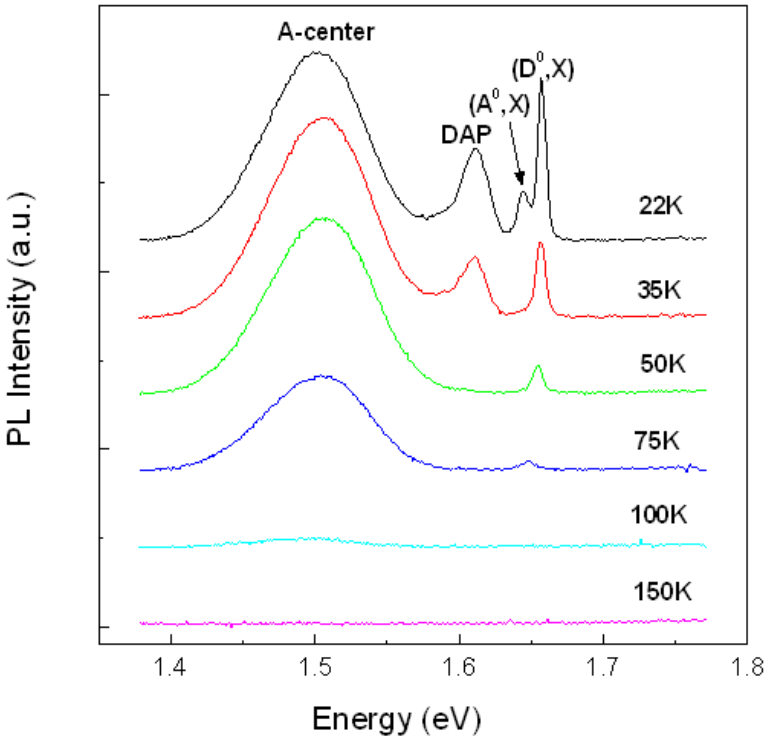

Figure 5.26. Temperature dependence of the PL spectra of the as-grown CZT sample (1A).

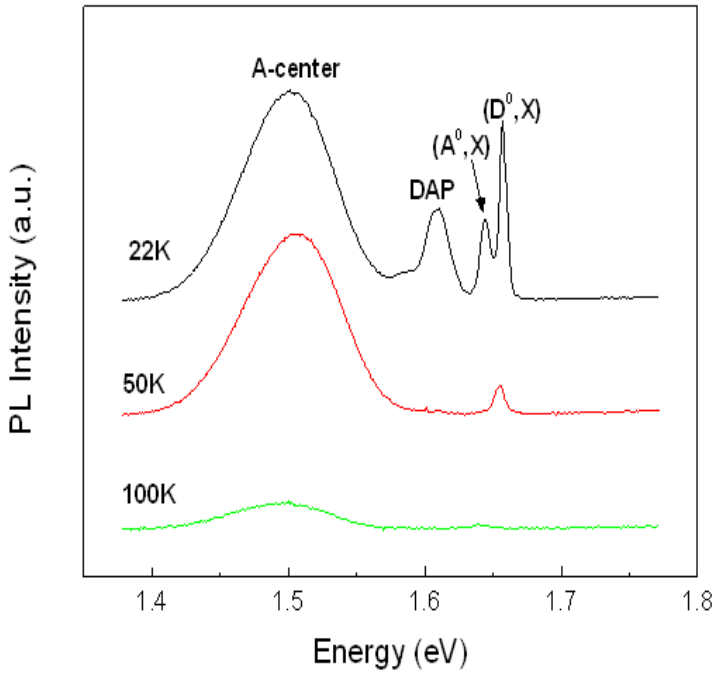

Figure 5.27. Temperature dependence of the PL spectra of the as-grown CZT sample (7A).

The experimental dependence of the PL intensity as a function of the temperature for each band can be fitted to the theoretical expression [29]:

$$I(T) = \frac{I_0}{1 + a_1 \exp(-E_1 / kT) + a_2 \exp(-E_2 / kT)} \quad \text{Eq. 5-10}$$

where *I(T)* is the integral intensity of the bound excitons (D^0, X) at various temperatures, I_0 is the integral intensity at 0 K, a_1 and a_2 are constants related to the relative energy density of states, *k* is Boltzmann constant, E_1 and E_2 are the thermal activation energies of the low temperature and high temperature quenching processes, respectively. This corresponds to the presence of two thermally activated nonradiative recombination mechanisms, and is often considered to reproduce the luminescence intensity at wide temperature range [30][31].

Figure 5.28 presents the logarithm of the integrated intensity for the (D^0, X) peak versus inverse temperature. The solid line exhibits the best fit for the *1/T* values as obtained from the results shown in Figure 5.26. The fitted parameters according to Eq. 5-9, giving values of E_1 = 1.55 ± 0.2 meV, E_2 = 15 ± 0.3 meV, a_1 = 9.3, a_2 = 660.

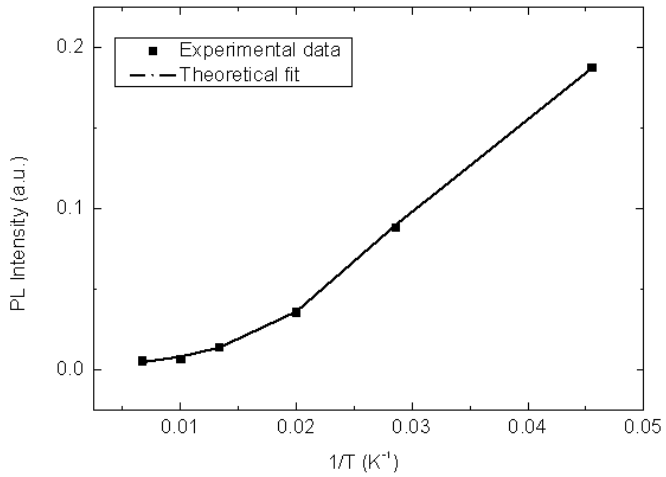

Figure 5.28. Temperature dependence of the integrated intensity for the (D^0, X) peak in CZT (1A). The solid lines are fitting results by Eq. 5-9.

Shin et al demonstrated that the high temperature quenching activation energy E_2 coincides closely with the result for the ionization energy of the acceptors, E_A. In addition, the fitted value for the low temperature quenching activation energy, E_1, is closed to the value of the exciton binding energy to the acceptor [29].

By assuming hydrogen-like energy levels, the previous results of sample 1A at the first-to-freeze region of the ingot grown by CZT uncompounded material allow us to calculate the energy gap as: $E_g = E(D^0, X) + (E_1 + 10.8) * 10^{-3} = 1.6721 eV$ [32].

In fact, $Cd_{1-x}Zn_xTe$ bulk crystals consist of donor and acceptor impurities, which can form pairs and act as stationary molecules imbedded in the crystal. The Coulomb interaction between donor and acceptor impurities will affect the binding energies of the isolated impurities. The recombination energy of a donor-acceptor pair (DAP) can be described by [29][32]:

$$E_{PL} = E_g - (E_A + E_D) + e^2 / \varepsilon R \quad \text{Eq. 5-11}$$

where E_{PL} is the peak energy of the DAP emission, E_g is the energy of the band gap, E_A is the acceptor ionization energy, e is the electron charge, ε is the dielectric constant, and R is the distance between the donor and acceptor in the pair. While R is much greater than the internal dimension or effective Bohr radii of the neutral donor or neutral acceptor, the emission lines will overlap and form a broad band in CZT.

Figure 5.29 exhibits the energy bandgap as a function of the Zn composition. The theoretical fitting of the experimental results allow us to determine the relationship between the energy bandgap, *Eg*, (± 1 meV), and the zinc concentration, *x*, (at 22K). By similitude with Eq. 5-9, we can determine the values of 1.590 eV for the ground state energy (E_0), 0.395 eV for the bowing parameter (α) and 0.996 eV for ΔE. Therefore, Eq. 5-9 can be written as:

$$E_g = 1.590 + 0.601x + 0.395x^2 \quad \text{Eq. 5-12}$$

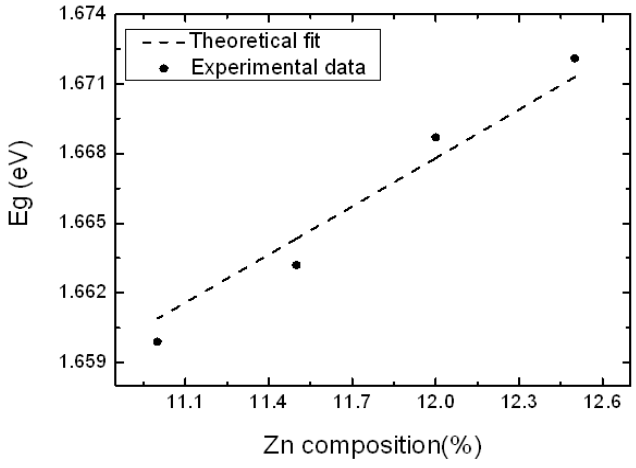

Figure 5.29. Zn composition as a function of Energy band gap.

For sample 1A operated at 22 K, the energy bandgap of 1.672 eV can be calculated by using Eq. 5-12. Therefore, the energy level diagram can be estimated, as exhibited in Figure 5.30. As can be observed, the level placed at 0.012 eV from the conduction band is referred to the shallow donors like In and Cl.

Moreover, the level situated at 0.060 eV below the conduction band can be considered as the Cd vacancy-donor complex containing two donors $[V_{Cd}^{2-}2D^{+}]^{0}$ [13]. This V_{Cd}-2D complex was first identified by *Bell* to maintain a lower ionization energy atabout 0.05 eV [33].

In addition, the energy level located at 0.164 eV above the valence band is related with the vacancy-donor complex $[V_{Cd}^{2-}D^{+}]$, which is also called A-centers [27]. *Ossau et al* reported that the ionization energies of the two complex acceptors $V_{Cd}^{-}2D$ and $V_{Cd}^{-}D$ are 49.5 and 135 meV, respectively [34].

Shin et al. mentioned that the electrons are trapped at the donor level (D) at low temperature, thus the recombination between the trapped electrons and the trapped holes at both acceptor levels of $V_{Cd}^{-}2D$ and of V_{Cd} occurs [29]. They reported that, for the p-type material, when the temperature increases, the trapped energy can be excited to the conduction band. It may explain why the intensity of DAP peak of the sample grown by the uncompounded material decreases when the sample is heated above 22K.

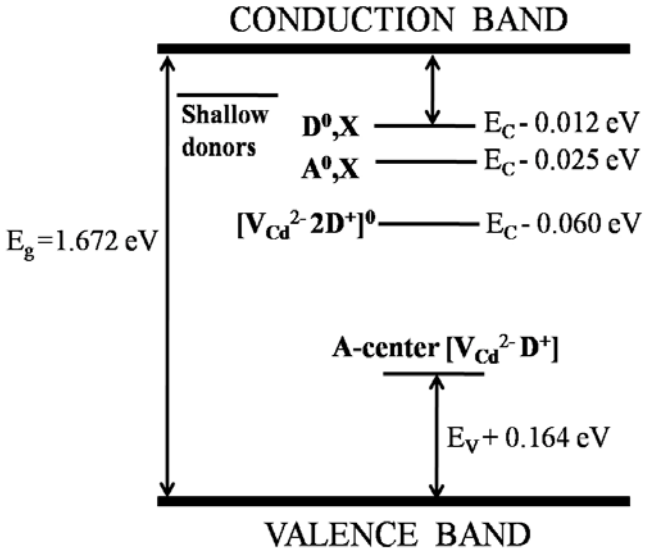

Figure 5.30. Energy levels for compensation in CZT.

5.2.5. Electrical Properties of the Detectors

5.2.5.1. Contactless Resistivity Mapping

The resistivity of the samples harvest from different axial region of the ingot has been first measured by using the COREMA instrument. Polished surface were prepared before to do the measurement, this technique can provide the information of resistivity values of the crystal before the detectors fabrication processes and also examine the samples without been influenced by the surface state.

The resistivity distribution of the samples along the axial positions of the ingot grown by CZT uncompounded material is displayed in Figure 5.31. High resistivity of 2×10^{8} ~ 1×10^{9} Ω.cm for all the samples can be observed, which seems similar but slightly randomly distributed among the samples from this ingot.

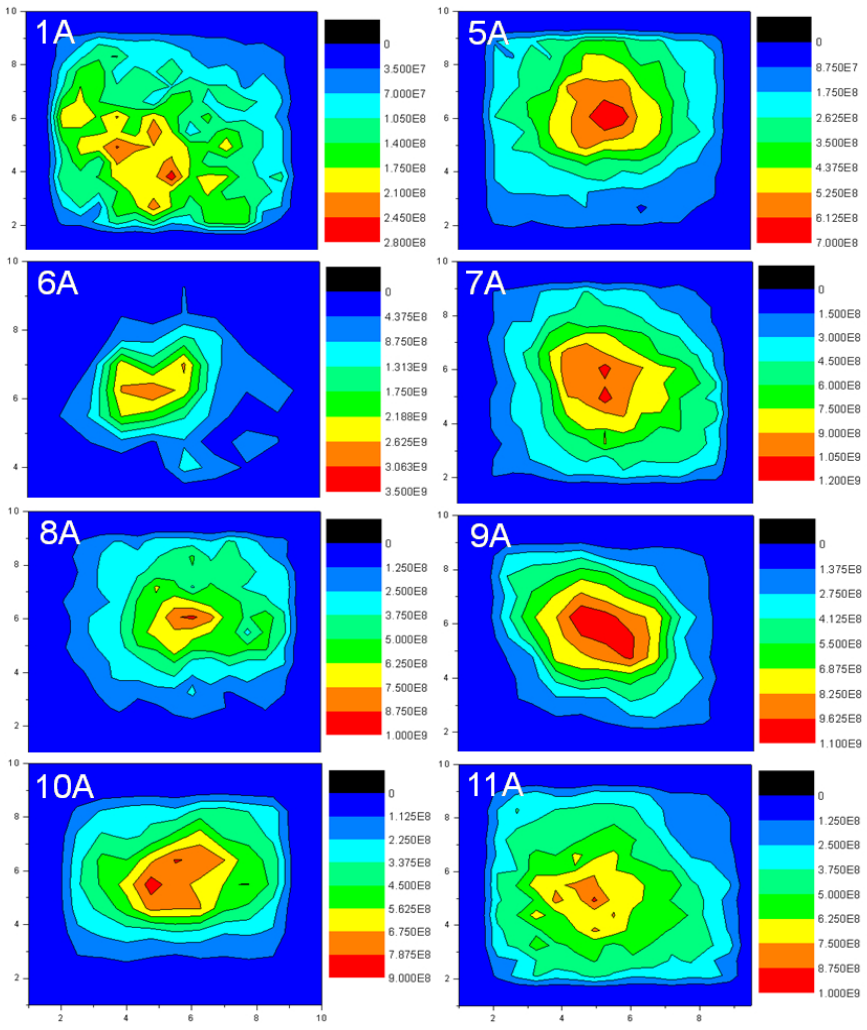

Figure 5.31. COREMA measurements of the samples harvest from the ingot grown by CZT uncompounded material.

Figure 5.32 illustrates the COREMA resistivity information of the samples from the ingot grown by CZT compounded material. All the samples presented high resistivity of 10^9 Ω.cm, which is one order of magnitude higher than the samples produced from the ingot grown by uncompounded material.

The resistivity distribution of all the samples is slightly different which can be associated with the distribution of Zn and In concentrations. We assume that the nonuniformity distribution of zinc and indium in both crystals can result in nonuniform detectors. For further investigation, I-V characteristics and gamma-ray response will be studied.

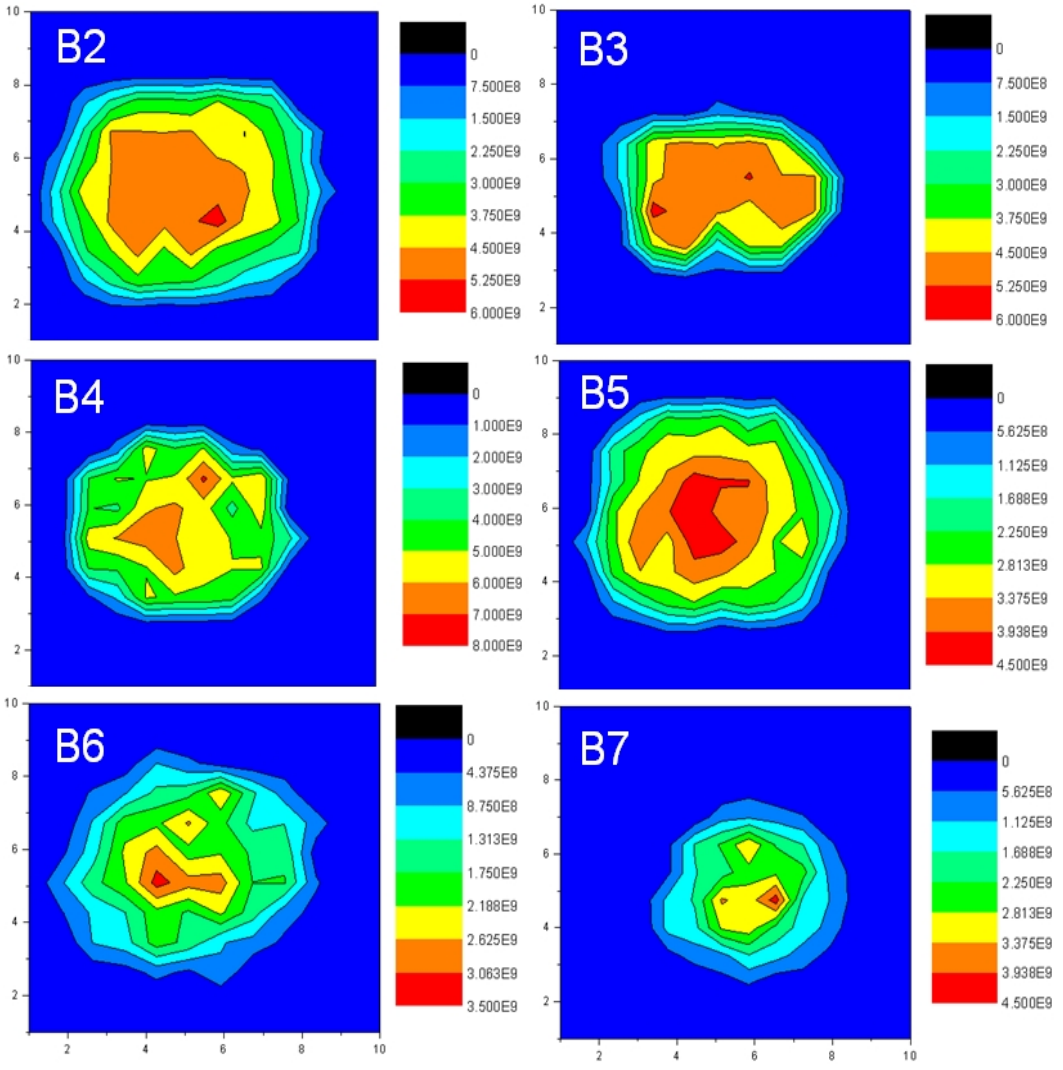

Figure 5.32. COREMA images of the samples obtained from the ingot grown by CZT compounded material.

5.2.5.2. Current-Voltage Characteristic (I-V)

a) Crystal grown with uncompounded material

I-V characteristics of different detectors fabricated from different axial position of the ingot grown with different starting materials have been investigated, as presented in Figure 5.33. All the detectors were fabricated with Au contacts on both sides using electroless deposition method followed the processes described in chapter 3. It is necessary to mention that the crystals obtained from our laboratory are n-type conductivity due to the concentration of indium dopant, therefore by using Au, the contacts will be blocking.

In Figure 5.33, we can observe that the I-V curves of all the detectors display Schottky contact behaviours at the applied bias between -200 V and +200 V. However, the barrier height of different detectors presents different behaviours according to the different positions in the ingot. Especially, the middle sample 5A and 8A displays a strong asymmetry between two faces of the detectors, one face presenting a higher leakage current than the other face, which can be explained by the activation of defects at higher voltage and therefore an increase of leakage current. The first-to-freeze sample (1A) exhibits lower leakage current, and its IV characteristic is more similar to a linear trend. As shown in this figure, the leakage current of the detectors from the tip region to the tail region of the ingot change significantly with random behaviours.

Table 5.7 presents the summary of the compositional and electrical properties of the samples obtained with various axial positions perpendicular to the growth direction from the ingot grown by CZT uncompounded material. In this table, one can observe that the bulk resistivity of the samples along this ingot is randomly distributed in the axial directions. The resistivity calculated by I-V and the bulk materials measured by COREMA are two orders of magnitude different, suggesting that the contacts deposited on the CZT material are blocking contacts.

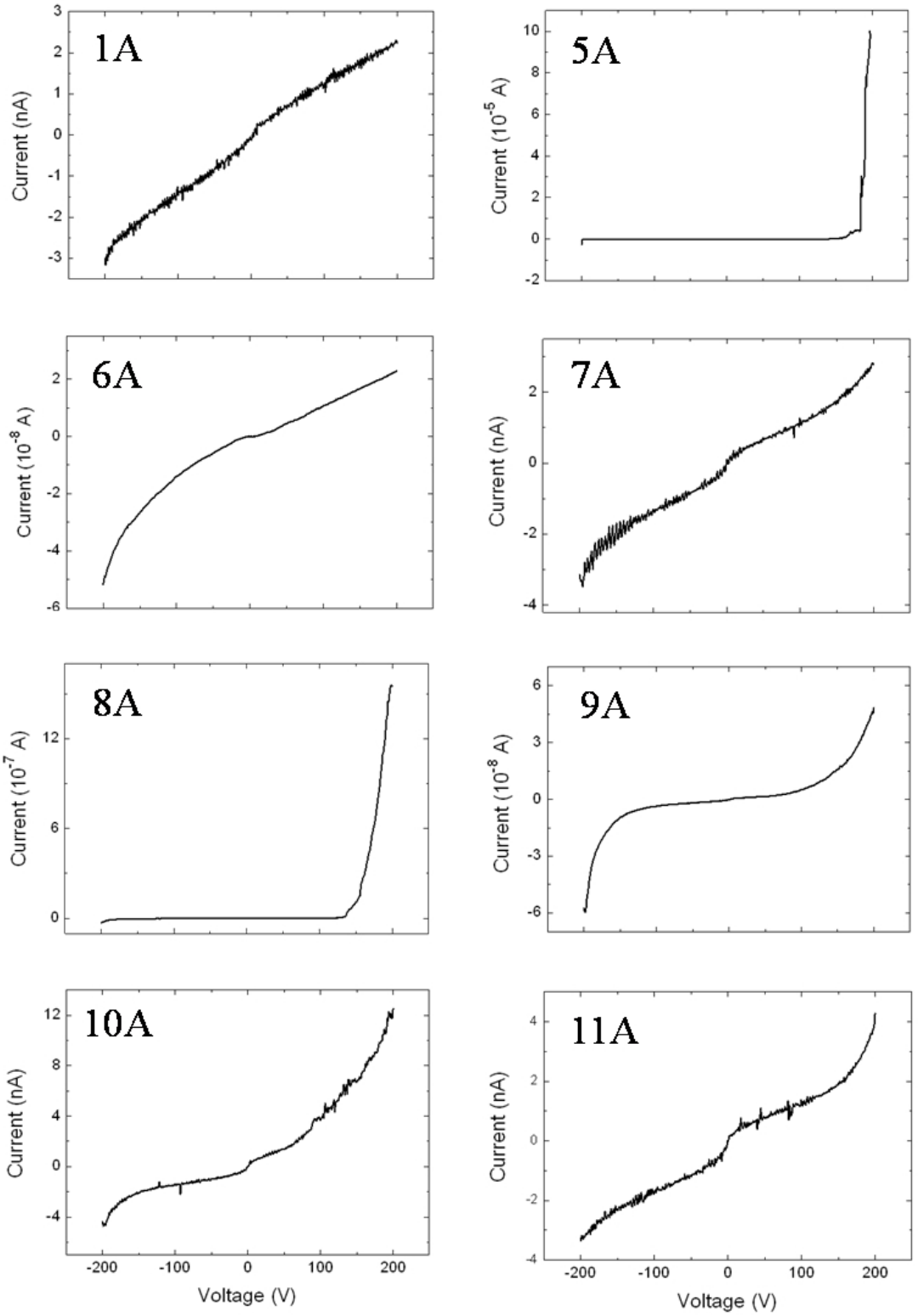

Figure 5.33. I-V characteristics of the detectors harvest from the ingot grown by uncompounded material.

Table 5.7. Compositional and electronic properties of CZT with different axial positions from the ingot grown by uncompounded material.

Sample Name	Solidified Fraction	Zinc Concentration (%)	Indium Dopant (ppm)	Resistivity (Ω.cm) Measured by COREMA	Resistivity (Ω.cm) (calculated by I-V)
1A	0.142	12.5	2	2.4 E+8	4.3 E+10
5A	0.304	12.5	2-2.5	7.0 E+8	9.6 E+10
6A	0.341	12-12.5	2-2.5	2.0 E+9	3.6 E+10
7A	0.365	12	2.5	1.0 E+9	4.2 E+10
8A	0.409	11.5-12	2-2.5	7.5 E+8	5.3 E+10
9A	0.446	11.5-12	2.5-3	1.1 E+9	3.8 E+10
10A	0.486	11.5	2.5	8.5 E+8	2.8 E+10
11A	0.530	11	2.5	8.0 E+8	5.8 E+10
12A	0.784	8	2.5	1.0 E+9	———

Figure 5.34 and Figure 5.35 illustrate the ln I – V characteristics at different temperature, and the barrier height as a function of temperature for detectors 1A and 5A, respectively. We can observe the increasing saturation current as a function of temperature for both detectors, which can be explained by the tunnelling current (see section 5.1.3). At the meantime, one can see that the barrier height increases with the increasing temperature. One can also observe that the theoretical fitted line is quite coinciding with the experimental data.

Table 5.8 shows the zero-bias barrier height of the detectors 1A and 5A at 0 K with forward bias and reverse bias operation. We observe that the zero-bias barrier height (Φ_{b0}) shows the same value of 0.70 eV for both sides of the detector 5A, but slightly difference appears with detector 1A.

As previous discussed in Figure 5.33, we can observe that the I-V curves display different Schottky behaviours for these two detectors. The I-V characteristic is more similar to a linear trend for detector 1A, but a strong asymmetry between the two faces of the detector 5A. However, the zero-bias barrier height of the detector 5A shows the same value for both faces, but an asymmetry occurs with detector 1A.

It is important to note that the barrier height is derived from the I-V data at low voltages from -2.5 V to +2.5 V. The asymmetry occurs with detector 5A at higher voltages may due to the activation of defects at higher voltage which can come from the bulk material. While the asymmetry appears with detector 1A at lower voltages, which is probably resulting from the small insulating behaviour which can be attributed to the oxide layer between contact/semiconductor.

By compared with the barrier height of commercial detectors (see section 5.1.3 where the ohmic contact we obtained a value of 0.46), we can observe in this section that the barrier height of the detectors harvested from our laboratory is slightly higher than the commercial detectors. One possible reason may related to the crystal growth methods, which are High Pressure Bridgman (HPB) method for commercial detectors and Vertical Gradient Freeze (VGF) method for home-made detectors presented in this section.

Another reason may be due to the fact that the commercial samples are ever p-type with unknown concentration of doping, while the sample used for CGL are ever n-type due to the fact that the difference of the CGL sample was to obtain n-type In doped high resistivity detector sample. In concequence, the levels of compensations and conductivity are different, leading to different barrier height values. Indeed, the process of metallization for both types of samples is very important. Depending of the process, the thickness of the contact and interlayer of the commercial detectors is different from the thickness of the contact produced in our laboratory, and therefore leading to a different harrier height between the contact and the semiconductor.

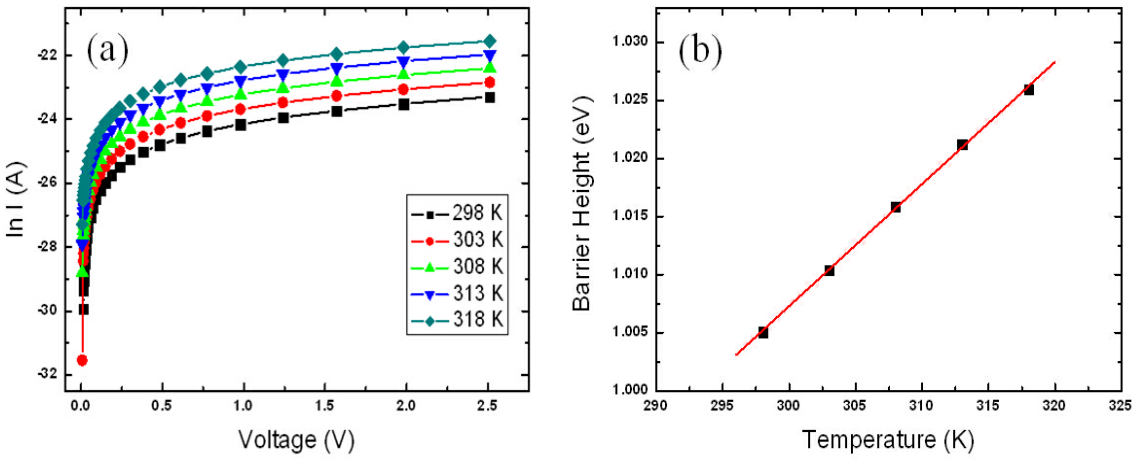

Figure 5.34. Current various forward voltage of detector 1A (a), Barrier height with temperature derived from the I-V curves.

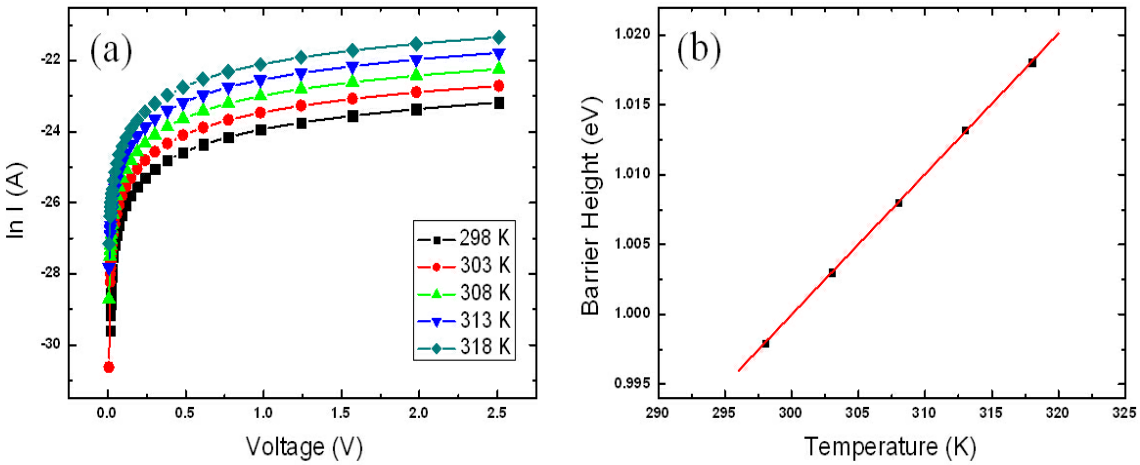

Figure 5.35. Current various forward voltage of detector 5A (a), Barrier height with temperature derived from the I-V curves.

Table 5.8. Information of barrier height at 0 K and 0 V.

	Forward Φ_{b0} (eV)	Reverse Φ_{b0} (eV)
Detector 1A	0.69	0.67
Detector 5A	0.70	0.70

b) Crystal grown with compounded material

The I-V characteristics of the detectors fabricated from of the ingot grown by CZT compounded materials are shown in Figure 5.36. Table 5.9 presents the compositional and electrical information of the detectors fabricated from the ingot grown with CZT compounded material.

As shown in this figure, the I-V curves of the detectors with different axial position obtained from this ingot display Schottky contact (blocking contact) behaviours with small barrier height at the applied bias of -200 V ~ +200 V. One can see that detector B3 and B7 display slightly higher leakage current than the other detectors.

As can be seen, all the detectors display almost symmetric I-V characteristics between the cathode side and anode side between -200 V and +200 V. We observe a quail-linear behaviour of the I-V characteristics of all the detectors at the voltages between -200 V and +200 V. This behaviour looks similar to quasi-ohmic contact behaviour. However, one can observe in the table that the resistivity calculated by IV at low voltage is two orders of

magnitude higher than the value measured by COREMA, indicating that Schottky contact behaviours exhibit with all the detectors.

By associating the Zn concentration with the I-V characteristics, it is interesting to find that lower leakage current occurs with the detectors at the Zn concentration of around 11 %. As can be seen, the leakage current of the detectors increases when the Zn concentration and therefore the band gap increases. One can suppose that the detector performance from the crystal grown by CZT compounded material is greatly depending on the Zn concentration. To confirm this statement, gamma-ray response of these detectors will be investigated.

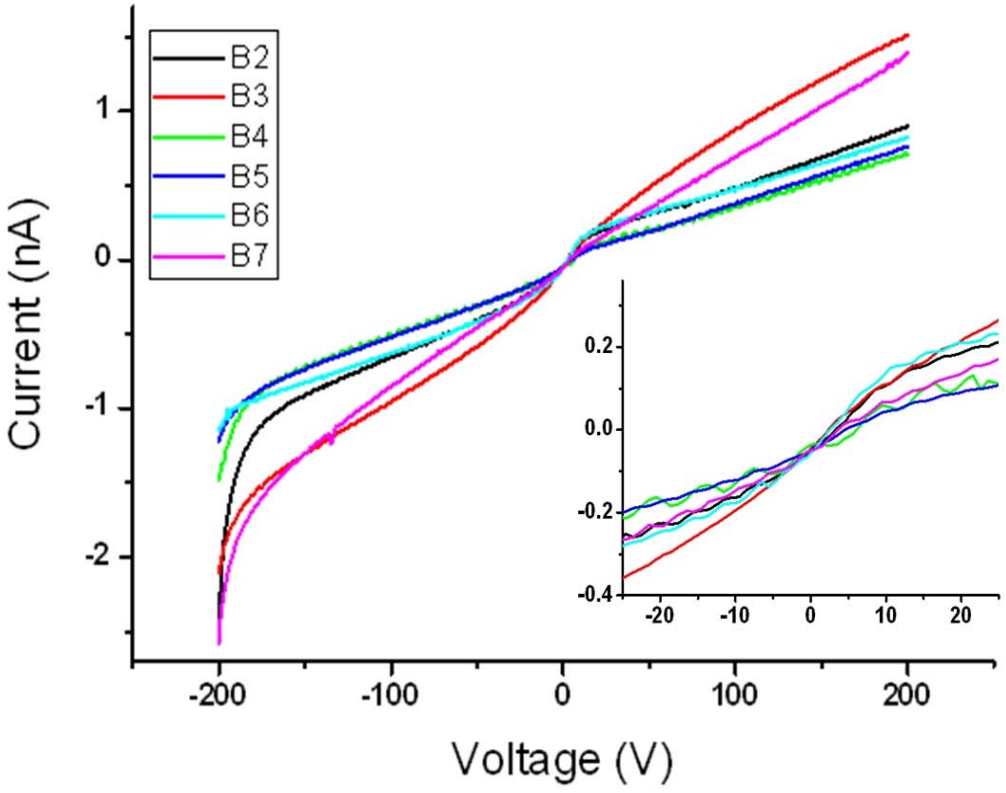

Figure 5.36. Comparison of the I-V curves of the detectors from the ingot grown by compounded material.

Table 5.9. Compositional and electronic properties of the samples with different axial positions from the ingot grown by compounded material.

Sample Name	Solidified Fraction	Zinc Concentration (%)	Indium Dopant (ppm)	Resistivity (Ω.cm) (Measured by COREMA)	Resistivity (Ω.cm) (Calculated by I-V)
B2	0.150	11.5	1.2	5.6E+9	7.4E+10
B3	0.293	12.0	1.5	5.5E+9	1.1E+11
B4	0.407	11.8	1.9	7.2E+9	1.2E+11
B5	0.479	10.6	2.7	4.3E+9	8.4E+10
B6	0.550	10.1	3.1	3.2E+9	8.6E+10
B7	0.693	7.9	6.1	4.2E+9	7.4E+10

5.2.5.3. Gamma-Ray Spectroscopy

In order to test the performance of the detectors fabricated from different axial position of these two ingots grown with different starting materials, the ^{133}Ba gamma radioactive source has been used for this investigation.

a) Crystal grown with uncompounded material

Figure 5.37 shows the 3D waterfall plots of the gamma response with ^{133}Ba radioactive source of the detectors with different axial directions from the ingot grown by CZT uncompounded material. As can be seen, the samples from 1A to 11A present the gamma response following the ingot growth direction, which is from first-to-freeze (bottom) region to last-to-freeze (top) region.

It should be mentioned that, the gamma response at only one electric filed was displayed in this figure for comparison is due to the materials quality. From the bottom part to the middle part of the ingot, one can observe the deterioration of the detector performance; nevertheless, 31 keV and 81 keV photopeaks can still clearly evident. We can see that the detector from the first-to-freeze (bottom) region of the ingot (1A) exhibits the best detector performance with the lowest noise.

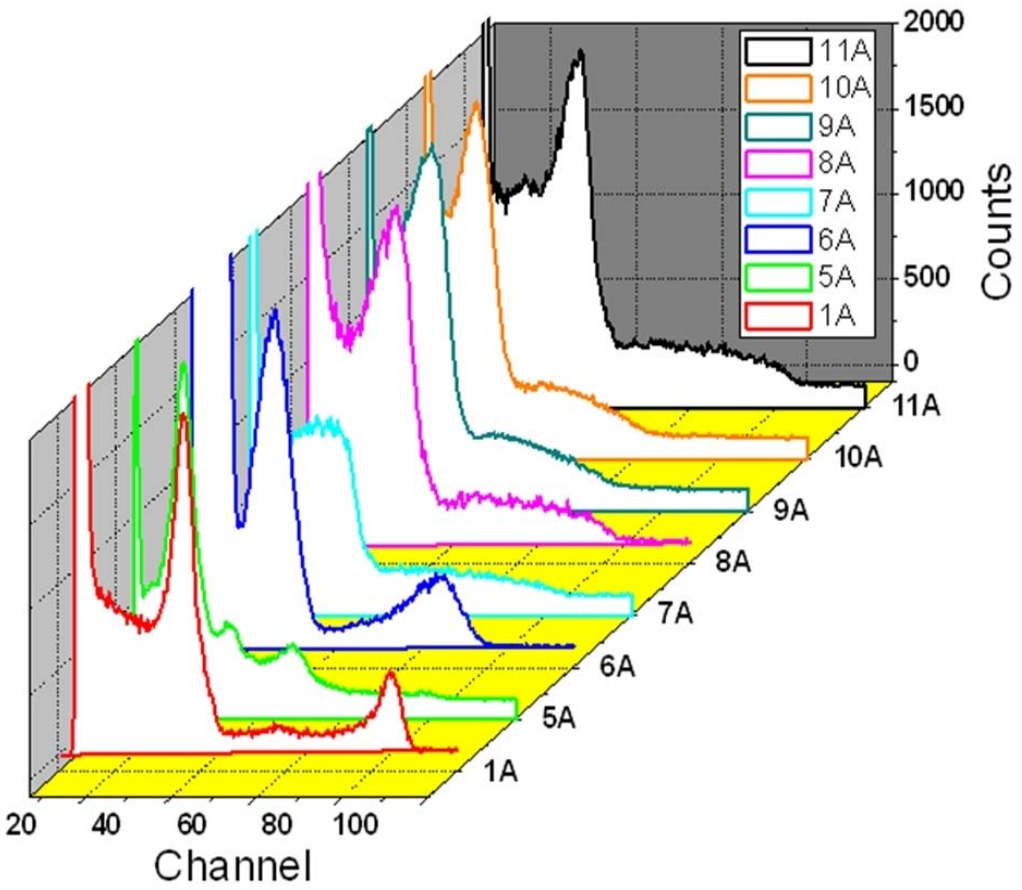

Figure 5.37. Room temperature gamma spectra response with ^{133}Ba source of the detectors harvest from the ingot grown by uncompounded material.

Table 5.10 displays the information of the detectors fabricated from this ingot with different axial positions. As can be observed, the Full-width-at-half-maximum (FWHM) values of the 31 keV and 81 keV photopeaks of detector 1A are 11.0 % and 5.2 %, respectively. In addition, the Peak/Valley ratio and quality factor of the 31 keV photopeak is 2.67 and 0.49, respectively. From the bottom part to the top part of the ingot, we observe the increase of FWHM values of 31 keV and 81 keV photopeaks with the ^{133}Ba source, and also the slowly decrease of the Peak/Valley ratio and the quality factor of the 31 keV photopeak. It is necessary to note that the performance of the detectors present slightly random behaviours, which may associated with the crystal growth conditions.

The gamma response behaviour of detector 1A is also in agreement with the I-V characteristics, which shows the lowest leakage current. Regarding the Te inclusions presented in Figure 5.17, we observe that detector 1A also presents the lowest density of Te inclusions in the material. We can conclude that the first-to-freeze (tip) region of the ingot

grown by CZT uncompounded material with the Vertical Gradient Freeze (VGF) method can achieve the best detectors among the whole ingot. It means that the detectors with better crystalline quality, less impurities or defects, and better detector performance can be obtained from the earlier freeze region of the ingot. While the later freeze region materials will give more impurities, Te inclusions, and defects and therefore a strong degradation of the radiation performance.

Moreover, the I-V curves of the other detectors fabricated from this ingot show different Schottky behaviours, which are also in agreement with varied behaviours of resistivity and the difference of detector performance. One can also conclude that the ingot grown by CZT uncompouned material may have a strong inhomogeneity in composition, as well as the electrical properties and detector performance. It is also important to remark that, even the samples harvested from the same wafer of the same ingot exhibit different detector properties.

Table 5.10. The information of the performance of the detectors fabricated from different axial positions from the ingot grown with uncompounded material.

Sample Name	Electric field of ^{133}Ba (V/cm)	FWHM 31 keV ^{133}Ba (%)	P/V of 31 keV peak	Quality factor of 31 keV peak	FWHM 81 keV ^{133}Ba (%)
1A	1780	11.0	2.67	0.49	5.2
5A	250	21.5	2.90	0.37	12.8
6A	1750	26.5	2.74	0.32	13.1
7A	700	—	—	—	—
8A	700	28.2	1.71	0.25	—
9A	300	39.6	1.83	0.22	—
10A	350	29.7	1.50	0.22	—
11A	700	20.2	1.71	0.29	—

The 3D waterfall plots and the related FWHM values of the photopeaks at different applied voltages of detector 1A with ^{133}Ba radioactive source are shown in Figure 5.38. It is necessary to mention that the thickness of detector 1A is approximately 2.8 mm, the voltages of this detector were applied from 200 V to 1000 V.

As can be observed in Figure 5.38 (a), detector 1A displays good performance at the electric field from 700 V/cm to 3500 V/cm. We can observe that the 31 keV and 81 keV photopeaks shift to higher channels when the applied voltages increase from 200 V, meaning that the charge collection efficient (CCE) increases. When the bias voltage and electric field are low (200 V), the pulse height from radiations that are fully stopped within the depletion layer continues to increase with the applied voltage. This variation is due to the incomplete collection of charge carriers resulting from trapping or recombination along the track of the incident particle. The fraction that escapes collection will decrease as the electric field increases.

One can also observe that the 31 keV and 81 keV photopeaks shift back to lower channels from 900 V to 1000 V, indicating that when the electric field is sufficiently high, the charge collection become complete and the pulse height no longer changes with further rises in the bias voltage and electric field [35].

As presented in Figure 5.38 (b), the FWHM values of the 31 keV and 81 keV photopeaks with the ^{133}Ba source varied with different applied voltages. At lower applied voltages from 200 V to 600 V, the FWHM values of these two photopeaks change slightly with applied bias, having a significant increase of FWHM when the applied voltages increase after 600 V, implying that the optimum applied voltages for this detector is around 600 V. Actually, the lowest FWHM with the 31 keV and 81 keV photopeaks are observed with the applied bias at 500 V.

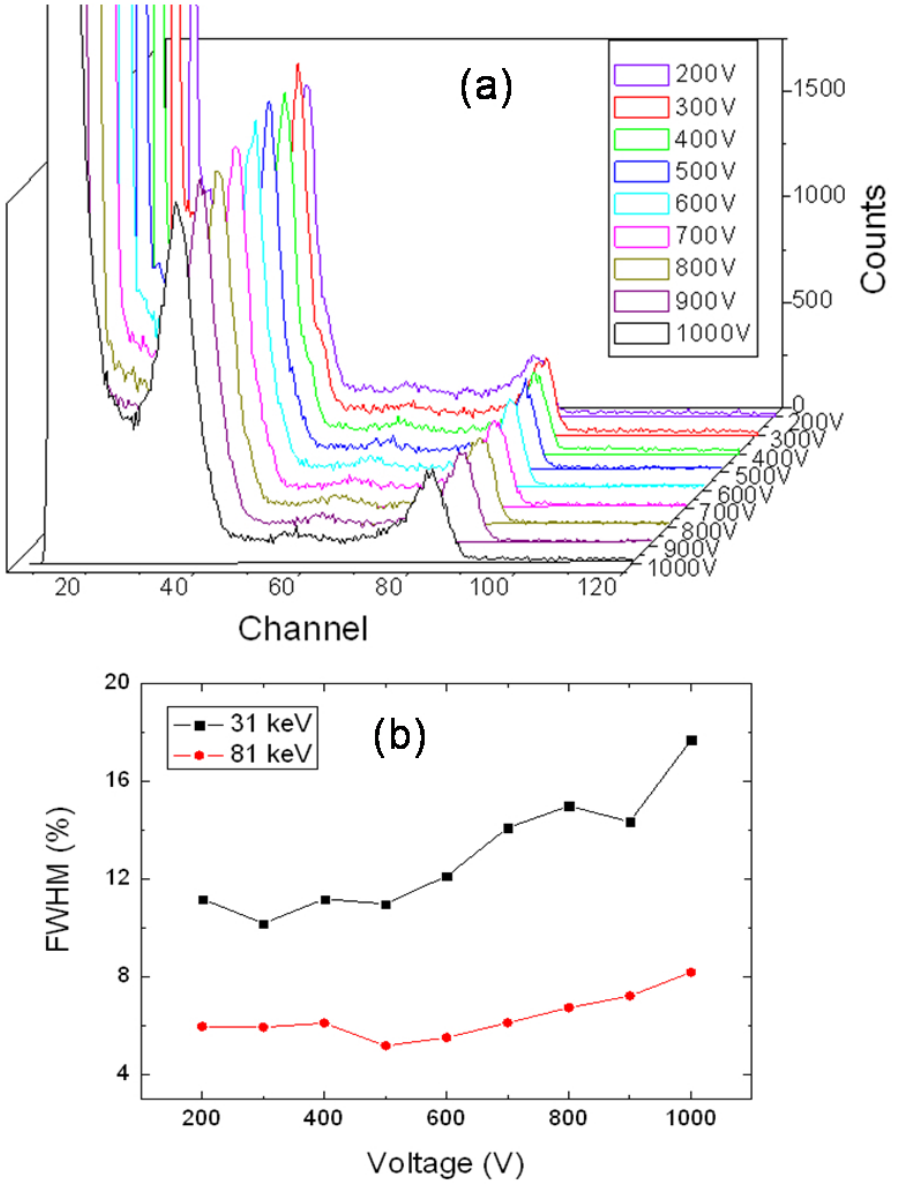

Figure 5.38. Gamma-ray response of detector 1A with the ^{133}Ba source at different applied voltages (a), FWHM of the 31 keV and 81 keV photopeaks of detector 1A at different applied voltages.

b) Crystal grown with compounded material

Figure 5.39 exhibits the gamma response with ^{133}Ba radioactive source of different detectors with different axial positions of the ingot grown by CZT compounded material. As can be seen, the detectors fabricated from this ingot display good performance with the 31 keV and 81 keV photopeaks clearly in evidence.

Different applied voltages have been operated in order to find the saturation region. As can be seen, a shift of the pulse height spectra toward lower energies appear at 2000 V for detector

B2, implying that the optimal applied voltage is at 1800 V (4285 V/cm). Therefore, good resolution remains in detector B2 when operated below 1800 V, whereas more radiation damage and deterioration of performance will appear above 1800 V. Similar behaviours can be observed with detector B6, the height spectra degrade and shift to lower energies at 900 V, indicating that the saturation region of this detector is at around 800 V (1900 V/cm).

In fact, the charge collection efficient will be modified as changing the applied bias and therefore the electric field. When reach one sufficient electric field, the charge collection becomes complete and the pulse height no longer changes with higher electric field and applied bias. The maximum region of this operation is called saturation region. Therefore, it is important to ensure that the operation is done at the region of true saturation to avoid significant deterioration in the energy resolution. To reach the saturation region, higher electric fields are generally required [36].

It is necessary to mention that the saturation region of some other detectors presented in Figure 5.39 may exist at higher applied bias and electric fields. Particularly, the saturation region of detector B3 is not found at 2000 V (5600 V/cm), suggesting that this detector can operate at even higher electric field than 5000 V/cm without the degradation of the device. We can conclude that good quality detectors achieved from the ingot grown by CZT compounded material can operate at high electric fields.

The best side of the planar devices was chosen to be irradiated at cathode side, as shown in Figure 5.39. It is important to mention that all the detectors presented in Figure 5.39 have the same thickness, therefore, the same electric field with same voltage can be obtained.

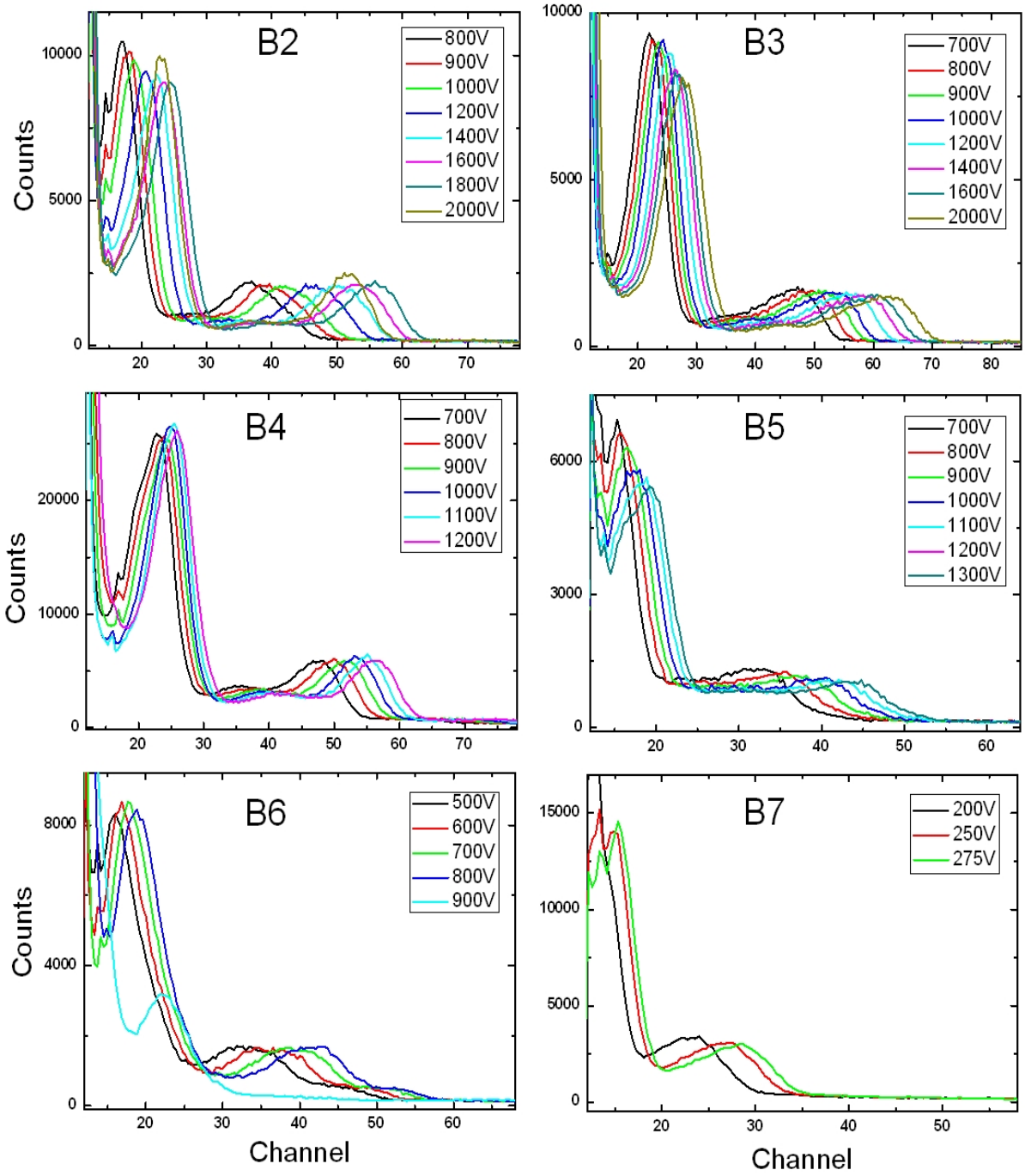

Figure 5.39. Room temperature spectra response with ^{133}Ba source of the detectors harvest from the ingot grown by compounded material.

Figure 5.40 exhibits the FWHM values of the 31 keV photopeak with the ^{133}Ba gamma source of all the detectors at various applied voltages presented in Figure 5.39. As one can observe, the average FWHM value of the detectors is around 25 %, which appear with the most detectors operated at different voltages achieved from the same ingot. Meanwhile, the

maximum value at about 36 % can be found with detector B7, which may related with the much lower Zn concentration (< 8 %) and higher In dopant (> 6 ppm). In summary, it is clearly shown a more homogeneous behaviour of the detectors harvested from the ingot grown by CZT compounded material than uncompounded material.

It is important to remark that the large differences of the FWHM values at different applied bias in the same detector are due to the charge collection efficiency (CCE). Indeed, a significant difference of FWHM values of the 31 keV photopeak with the detectors fabricated from the crystal grown by CZT compounded material indicates different performance and quality of detection.

Particularly, the detectors harvested from the same ingot can operate at different applied voltages, which means that the charge collection efficiency are different amongst detectors, the trapping effect within the detectors playing an important role resulting in these behaviours. Therefore, it is essential to study the charge collection efficiency within these detectors to understand the difference behaviours in a future work.

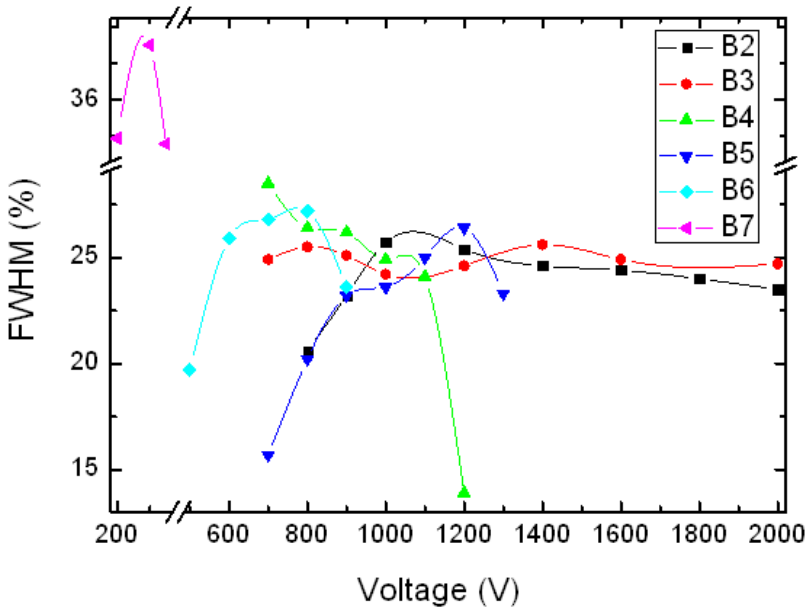

Figure 5.40. FWHM of the 31 keV photopeak with different applied bias of the detectors harvest from the ingot grown by CZT compounded material.

5.2.6. Comparison of the Detector Performance

5.2.6.1. Current-Voltage Characteristic (I-V)

I-V characteristics of two detectors fabricated from two different crystals with different growth conditions were shown in Figure 5.41. It is necessary to mention that the detectors presented were chosen from the best part (bottom) of each ingot which exhibited the best detector performance (1A and B4). As can be seen, the detector B4 from the ingot grown with CZT compound material display lower leakage current than the detector 1A from the ingot grown by uncompounded material.

As previous discussed, all of the detectors achieved from these two ingots display Schottky contact behaviours due to the n-type conductivity. However, higher barrier height can be observed with the detectors from the ingot grown by CZT uncompounded material than by compounded material.

Furthermore, the requirement of low net free-carrier density (10^5 – 10^6 cm^{-3}), low density of carrier traps, and recombination centres demand good control of the purity and the stoichiometry of the materials. The possibility to achieve large single crystals relies on the physical properties of the material in the liquid and solid phase, as well the thermal properties of the crystal growth equipment [31].

In fact, the melting point of Cd, Zn, and Te are 594.22 K, 692.68 K, and 722.66 K, respectively, which is much lower than the melting point of compounded CdZnTe (1373 K). The controlling of heat transport both in the melt and the solid are necessary in order to achieve better control over the defect formation and evolution during the crystal growth process. Therefore, more difficulties about heat transport control occur with the ingot grown by CZT uncompounded materials with three different melting points.

Meanwhile, the structural defects have an impact on the uniformity of CZT material, such as dislocation, sub-grain boundaries, Te precipitates/inclusions. These defects are related with charge trapping and recombination, severely affect the charge transport [36]. We suppose that higher concentration of dislocations was introduced into the crystal grown by CZT uncompounded material during the growth process, and also the solidification and cooling down stages. When the crystal was grown with CZT uncompounded materials, more stress brought into the crystal during the growth procedure, resulting from different melting point and thermal coefficient of species.

Zhang et al. reported that the stress induced in the CZT crystal by its contact with the ampoule significantly affect the crystal's homogeneity [32]. *Szeles et al.* mentioned that the charge trapping and recombination along the sub-grain boundaries is expected to produce non-uniform charge transport and poor performance of radiation detectors fabricated from the materials with high dislocation density [36].

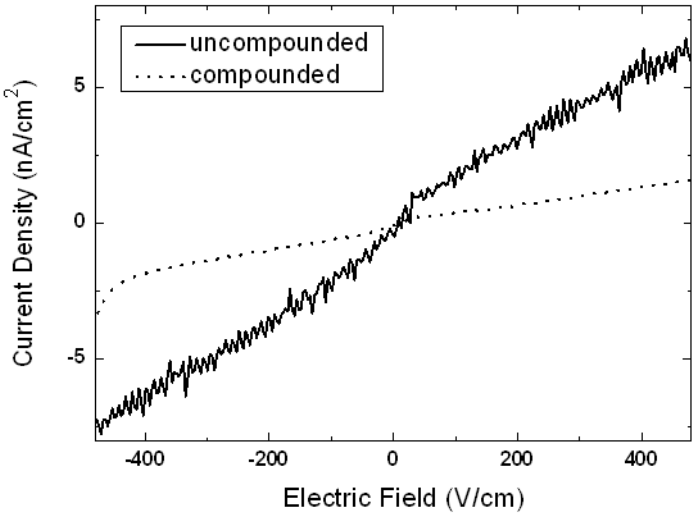

Figure 5.41. I-V characteristics of two detectors from two ingots grown with different starting materials.

5.2.6.2. Gamma-Ray Response

Three radioactive sources (^{133}Ba, ^{241}Am, ^{137}Cs) have been used in this work for comparing the performance of the detectors achieved from two ingots grown by different starting materials. Figure 5.42 exhibits the gamma spectroscopy of two detectors (1A and B4) from two ingots grown by CZT uncompounded and compounded materials, respectively. On the left, the gamma spectroscopy with the ^{133}Ba, ^{241}Am, and ^{137}Cs radioactive sources of detector 1A were illustrated separately, while the gamma response of detector B4 were exhibited on the right parts. The information of the gamma response with three radioactive sources of these two detectors are summarised in Table 5.11.

By comparison, we can observe that the performance of the detector obtained from the ingot grown with CZT uncompounded material is better than the one grown with CZT compounded material. With detector 1A from the crystal grown by CZT uncompounded material, the 276 keV, 303 keV, 356 keV, and 383 keV photopeaks at high energies with the

^{133}Ba source were clearly in evidence, the FWHM values are 2.5 %, 2.5 %, 2.5 %, 1.9 %, respectively. We can observe a good performance of this detector at high energies, while hole transport may have an impact on the shape of the photopeaks. However, for detector B4 from the crystal grown by CZT compounded material, only the 276 keV and 383 keV photopeaks with poor resolutions can be observed.

Moreover, the FWHM of 31 keV and 81 keV photopeaks at low energies with the ^{133}Ba gamma source are 11.0 % and 6.1 % for detector 1A, respectively, which is much lower than the detector B4 (17.4 % and 10.3 %). The Peak/Valley ratio of the 31 keV photoeak is 10.2 for detector 1A, which is higher than the detector B4 (5.0), implying better resolution and lower noise presented. The quality factor of this peak is 0.96 for detector 1A, but only 0.53 obtained with detector B4.

In the meantime, the 59.5 keV photopeak with the ^{241}Am source was clearly in evidence with both detectors, the FWHM values of this peak for detectors 1A and B4 are 7.3 % and 23.5 %, respectively. The Peak/Valley ratio of this photopeak of detector 1A is 9.3, which is nearly one times higher than that of detector B4 (5.4). The quality factor of the 59.5 keV photopeak of detector 1A is 1.13, which is much higher than that of detector B4 (0.48).

Furthermore, one can observe the high energy 662 keV photopeak with the ^{137}Cs radioactive source for both detectors. However, the resolution of this photopeak for detector 1A (2.6 %) is better than detector B4.

We can conclude that the performance of the detector (1A) chosen from the first-to-freeze (bottom) region of the ingot grown by CZT uncompounded material is better than the detector (B4) selected from the bottom region of the ingot grown by CZT compounded material.

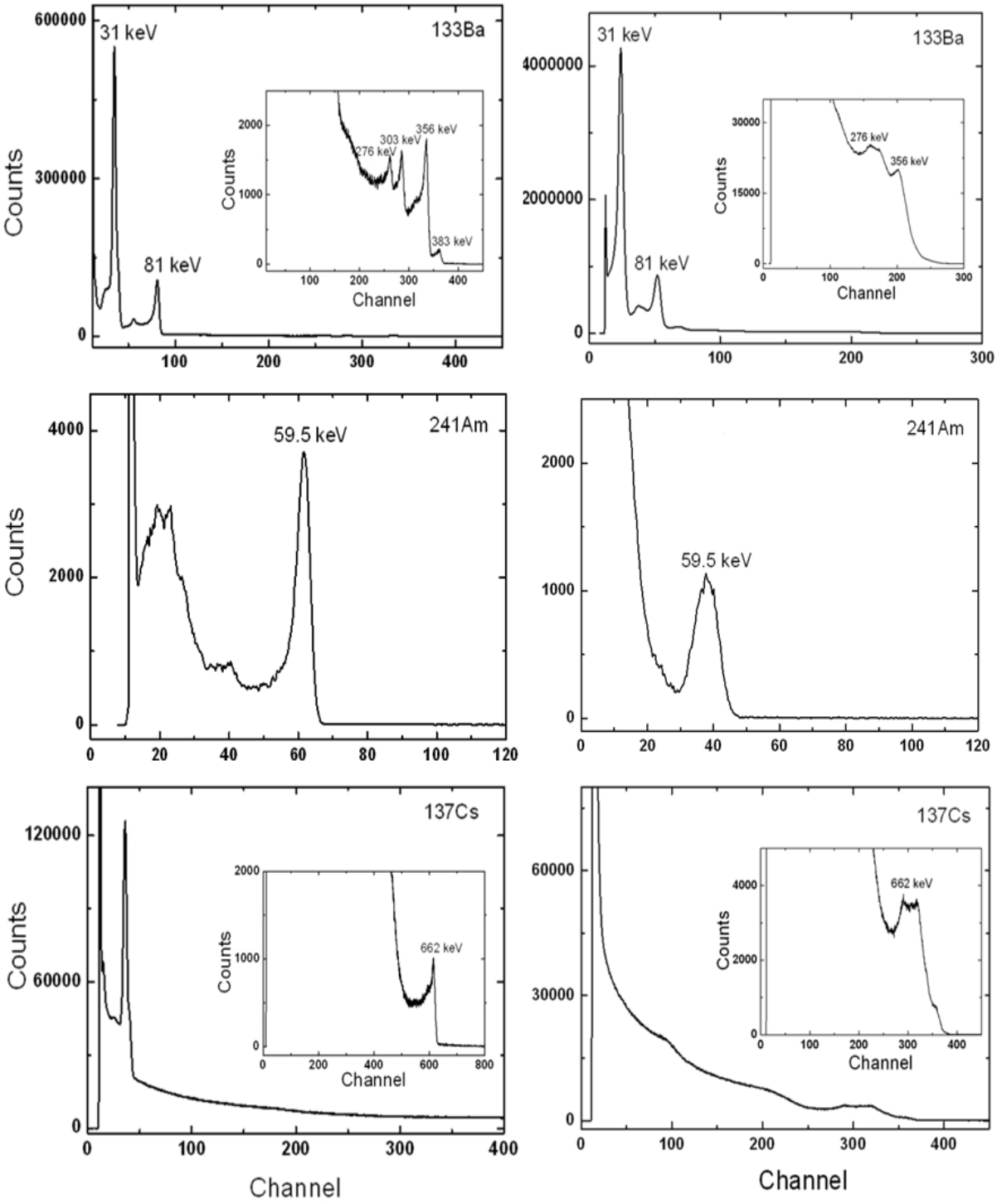

Figure 5.42. Gamma response with ^{133}Ba, ^{241}Am and ^{137}Cs sources of the detectors fabricated from the best part of two ingots grown by uncompounded (1A:left) and compounded (B4:right) material.

Table 5.11. Comparison of the ^{133}Ba, ^{241}Am, and ^{137}Cs spectra of the detectors from the best parts of two ingots with different growth starting materials.

	1A(uncompounded)	B4(compounded)
FWHM% of 31keV of ^{133}Ba	11.0	17.4
P/V of 31 keV of ^{133}Ba	10.2	5.0
Quality factor of 31 keV of ^{133}Ba	0.96	0.53
FWHM% of 81 keV of ^{133}Ba	6.1	10.3
FWHM% of 59.5 keV of ^{241}Am	7.3	23.5
P/V of 59.5 keV of ^{241}Am	9.3	5.4
Quality factor of 59.5 keV of ^{241}Am	1.13	0.48
FWHM% of 662 keV of ^{137}Cs	2.6	—

Indeed, as previous discussed, for the ingot grown with CZT uncompounded material, only the bottom part harvested the best detectors, which is significant different from the detectors obtained from the other regions. From the first-to-freeze (bottom) to the last-to-freeze (top) of the ingot, the performance of the detectors along the whole ingot deteriorate gradually, the speed of the degradation is faster than the crystal grown by CZT compounded material.

Nevertheless, different phenomenon can be seen with the detectors harvested from the ingot grown by CZT compounded material. In fact, similar behaviours with slightly difference of the detectors from the bottom-to-middle region of this ingot can be observed, several high quality detectors were achieved from this region with different axial positions. From middle-to-top region of this ingot, slightly degradation of the detector performance can be seen.

We can conclude that both ingots produce non-uniform samples, the first-to-freeze region harvest the best detectors, the performance of the detectors gradually deteriorate from tip to the heel of the ingot. By comparison, higher performance detectors can be harvested from the ingot grown by CZT compounded material. In addition, the ingot grown with CZT compounded material (with one melting point) can achieve more uniform materials.

It is important to mention that it is difficult to obtain uniform materials along the whole ingot by using Vertical Gradient Freeze (VGF) growth method. Indeed, the decreasing of Zn

concentration and large excess In remaining can be observed at the top part of both ingots even by using different starting materials.

Finally, the mainly comparison of different properties of the samples harvested from these two crystals grown with different starting materials (CZT uncompounded or CZT compounded) has been summarized in Table 5.12.

Table 5.12. Comparison of the properties of the samples harvested from these two ingots grown with different starting (uncompounded or compounded) materials.

	Uncompounded	Compounded
Zn concentration	Majority 10-12 %	Majority 10-12 %
Te inclusions	Low intensity, bigger size	High intensity, smaller size
Resistivity	$2\times10^{8} \sim 1\times10^{9}$ Ω.cm	$> 3\times10^{9}$ Ω.cm
Leakage current by I-V	Schottky, random with Zn %	Schottky, low leakage current, similar with Zn %
Gamma response (^{133}Ba)	Best detectors achieved at the bottom of the ingot, with higher resolution (11 % for 31 keV peak)	Good detectors achieved from the bottom-to-middle region of the ingot, but lower resolution (17 % for 31 keV peak)

5.2.7. Conclusions

Two different ways of crystal growth preparation by using CZT uncompounded material or compounded material have been investigated in terms of chemical composition, Te inclusions, luminescence behaviours, and electrical properties. Particularly, the performance of the detectors harvested from both ingots has been characterized by using three different radioactive sources for comparison.

- The concentration of Zn gradually decreases with the solidified fraction for both ingots. The quantity of In has a small variation at the solidified fraction of 0 - 0.6, but a large exponential increase occur between 0.6 and 0.8.
- Lower concentration of Te inclusions exist in the bottom than the top region for both ingots. Higher density with smaller size of Te inclusions presented in the ingot grown by CZT compounded material than by CZT uncompounded material.
- The detectors obtained from the ingot grown by CZT uncompounded material display higher leakage current than the detectors achieved from the ingot grown by CZT compounded material.
- The performance of the detectors harvested from the bottom part of the ingot grown with CZT uncompounded material is better than the detectors harvested from the bottom part of the ingot grown by CZT compounded material.
- Both ingots harvested non-uniform material, significant difference can be observed with the ingot grown by CZT uncompounded material, which only produces high quality materials at the very first freeze region of the ingot. For the ingot grown by CZT compounded material, high quality materials can be achieved at the half freeze region of the ingot with slightly differences.

5.3. Detector Prepared with Twinning Structure

The twin boundaries are one of the most common macroscopic material defects in CZT. Twinning in CZT is an important crystallographic structure, due to the crystallographic symmetry group of the Zinc Blende structure ($F\bar{4}3m$), which can be described by the rotation of the lattice by 180º about the <111> orientation or rotated 250.53° about the (011) plane [37-39].

The objective of this section is to investigate the effect of twinning structure on the surface and bulk properties of CZT, which may affect the detector performance. Meanwhile, the samples presented twinned and twin-free structures have been compared regarding their optical, structural, and electrical properties.

5.3.1. Effects on Orientation

The samples displayed twinning behaviour can be identified by the chemical etching. The etchant was prepared by HNO_3: HF: CH_3COOH to determine A-face and B-face of the (111) orientation.

Figure 5.43 presents the surfaces of the sample with twinned structure after chemical etching. As can be seen in Figure 5.43 (a), the top surface of the twin-free region is the (111)A surface, whereas the twinned region is rotated by 180º and exhibits (111)B termination. In Figure 5.43 (b), one can observe the top surface of the twin-free region is the (111)B surface, while the twinned region is rotated by 180º and exhibits (111)A termination.

In summary, for the region with twin structure, a mixture of (111)A and (111)B terminated surface is presented on both surfaces of the sample. For the twin-free region, the (111)A and (111)B terminations are uniform and either face of the sample is purely (111)A or (111)B.

This behaviour can be explained by the crystal structure illustrated in Figure 5.44. One can observe that each crystal shares the same lattice points at the twin boundary. Indeed, the twinning structure is resulting from the rotation of the crystal at 180° of the (111) orientation. Therefore, the twinned crystals have opposite surface terminations, one surface terminates as (111)A (Cd face), while the opposite surfaces exhibits the (111)B (Te face) termination, which is consistent with the surface structure presented in Figure 5.43.

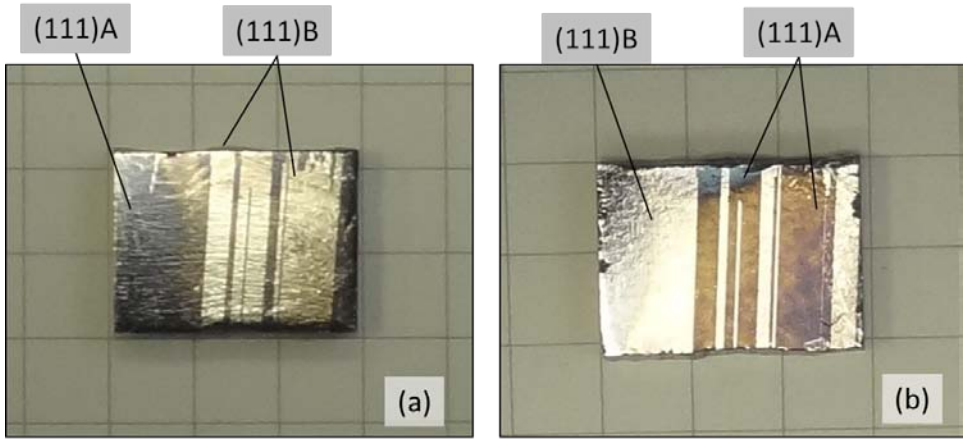

Figure 5.43. CZT sample with twin structure after chemical etching with the A-face and B-face of the (111) orientation.

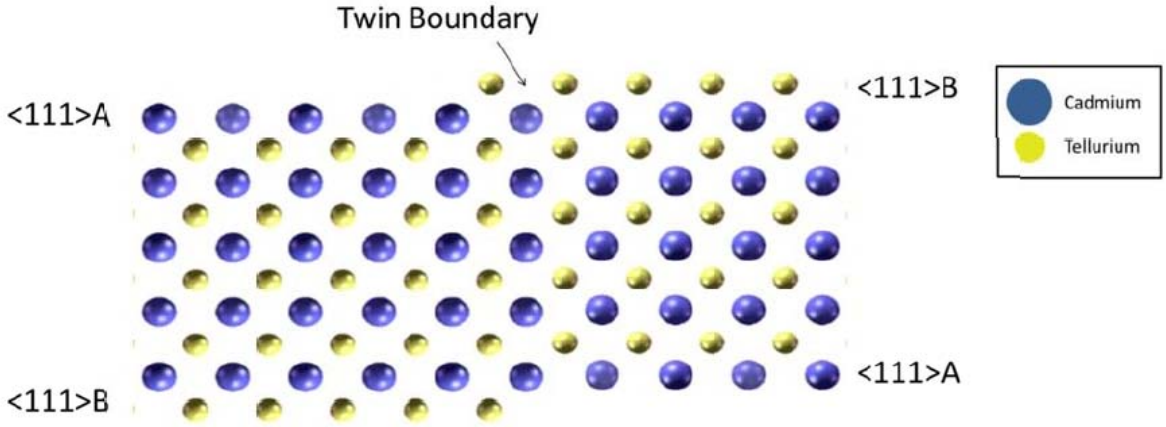

Figure 5.44. Crystal structure with twinning on different faces of CZT material.

5.3.2. Te Inclusions with or without Twinned Structure

Figure 5.45 shows the infrared microscopy of the whole wafer contains of the twinned region and twin-free region in this work. Apparently, the density of the Te inclusions in the twinned region is significantly higher than that of the twin-free region. The Te inclusions in the twinned region appear in strings shape which are confined to the plane of the boundary. The twin structures appear oriented vertically and extend through the entire wafer from one side to the other. It is probably that the close proximity of these metallic particles may permit charge to pass between the polarized electrodes. This type of behaviour has also been reported elsewhere, and is in agreement with the results presented here [40].

At the twin-free region, the Te inclusions are larger size, but more isolated. Therefore, the Te inclusions which are distributed throughout the CZT matrix generally have less effect on the bulk electrical properties.

The Te inclusions which are segregated along the twin boundaries are much closer in proximity, and thus can have a substantially larger affect on the bulk electrical properties. The density of Te inclusions present along the grain boundaries and twins can have a significant impact on the bulk electrical properties, leading to the increase of leakage current and high density of defects levels. One can observe that the twinned region displays high density of more closely spaced Te inclusions, while the twin-free region presents larger diameter but lower density of Te inclusions.

Parker et al. demonstrated that the electron trapping is the degradation mechanism created by the twin boundaries in CZT. They suggested that the electron trapping is probably induced by Te inclusions, which invariably decorate the twin planes. The high concentration of Te inclusions on the twin region can create area directly adjacent to the twins with lower concentration of dispersed Te inclusions [41].

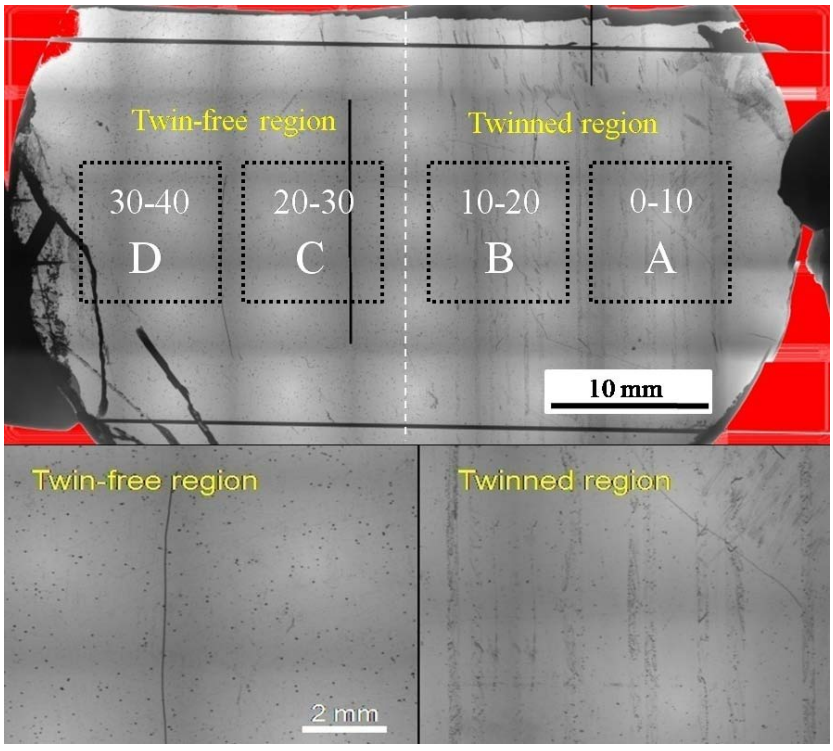

Figure 5.45. IR cartography images of a CZT wafer with the twinned region and twin-free region.

5.3.3. Luminescence Behaviours

5.3.3.1. Photoluminescence (PL) Spectroscopy

Photoluminescence (PL) spectroscopy is a widely used method to analyze the defect structure of semiconductors. It is obvious that in order to get a complete survey about the defects structure, a deep level PL study is inescapable. The deep levels seem to have an essential role on the electrical properties of CZT. There is a serious suspicion that deep levels in CZT have also an impact on the compensation mechanism.

PL spectroscopy at low temperature has been investigated in order to compare the defects in the near-surface region of the samples diced from the same wafer but with twin and twin-free structures. Figure 5.46 exhibits the low temperature (22 K) PL spectra of two samples at the same operation conditions. As previous shown in Figure 5.46, sample A is from the twinned region, whereas sample C is from the twin-free region.

As shown in Figure 5.46, the shallow donor–acceptor pair DAP and its longitudinal optical photon replica, which was located at the shoulder of the low energy side of DAP peak, are arranged at the detector-acceptor region of 1.560 ~ 1.630 eV. Meanwhile, the peak centered in 1.480 eV is called as A-center which is associated with the complex between the Cd vacancies and the donors. In the near-band-edge region, the neutral acceptor bound exciton (A^0, X) at around 1.640 eV are observed in all the samples. We observe that the intensity of all of the emission bands of the twin-free sample is higher than the sample which displays twinning behaviour.

However, the LO-photon replica (A^0X-1LO) at near 1.63 eV almost disappears for sample A, which contains twins and high concentration of Te-inclusions. These results are in agreement with the results of *Suzuki et al.*, they have demonstrated that there is a broadening of the binding energy of excitons at the acceptor and its replica due to compositional disorder in the bulk material [42].

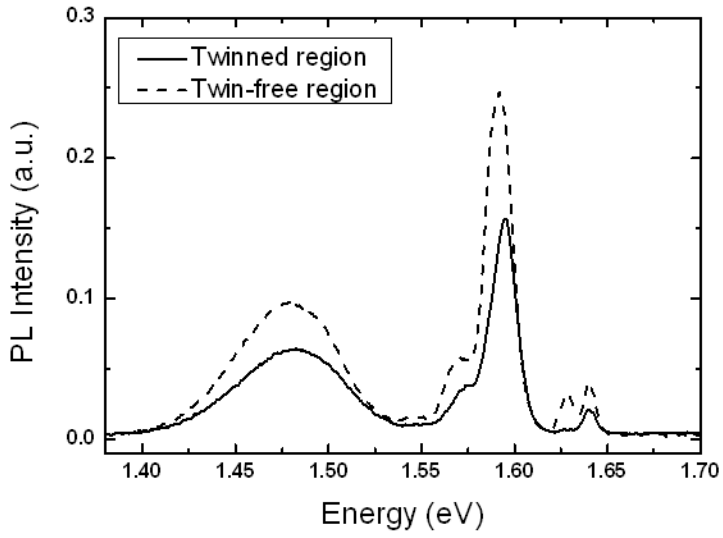

Figure 5.46. The PL spectrum of CZT samples with and without twins at 22 K.

5.3.3.2. Cathodoluminescence (CL) Spectroscopy

Room temperature CL spectra were also used to study the emission band of the surface states with the samples with and without twin regions, as shown in Figure 5.47. We can observe that the emission band at 1.55 eV remain the same position with all the samples from the same wafer. Indeed, samples A and B present twinned structure, while samples C and D are twin-free (see Figure 5.45). As can be seen in Figure 5.49, the FWHM values are different among the samples.

Figure 5.48 displays the FWHM and integrated intensity of the various CL emissions of the CZT samples with and without twin feature. Apparently, the sample A with twinned structure shows higher FWHM value and integrated intensity than the other samples, but this sample has higher density of Te inclusions.

One can conclude that structural defects such as twins in the sample may introduce defects into the bulk material which can getter impurities, which can deteriorate the crystal quality and also the optical properties of the material. Indeed, the levels of the impurity-bound excitons themselves are inhomogeneously broadened leading to a broadening of the peak in CL.

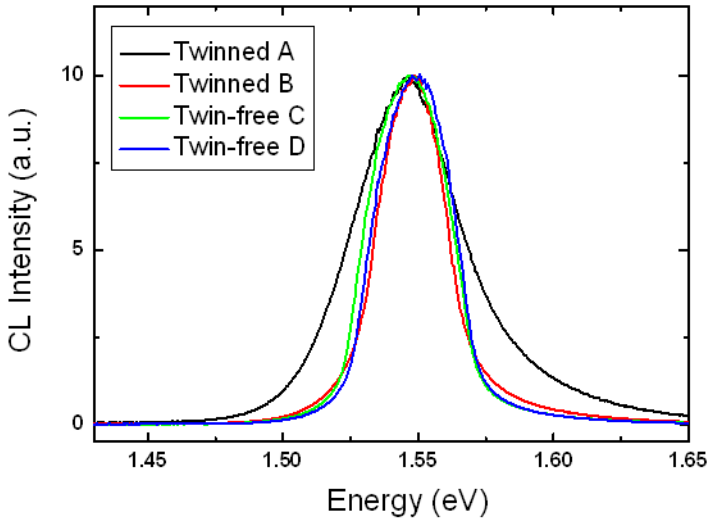

Figure 5.47. The CL emission spectra of CZT samples with and without twins.

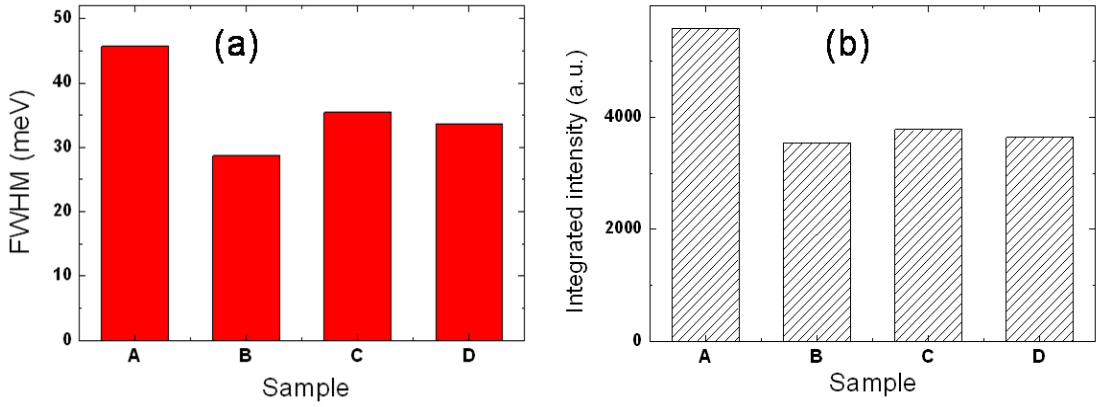

Figure 5.48. The FWHM (a) and integrated intensity (b) of the CL emissions from the CZT samples with and without twins.

5.3.4. Electrical Properties

Figure 5.49 illustrates the COREMA measurements and I-V characteristics of the wafer contains twinned structure (10-20) and twin-free (20-30) regions. As can be seen, the resistivity in the twinned region is at least 2 ~ 3 times lower than the resistivity in the twin-free region. The reason may be related with the higher density of Te inclusions presented within the twinned-region, acting like conduction line and therefore decrease the resistivity.

One can observe that the sample with twinned structure exhibits lower leakage current than the one without twin structure, which is in contrary with the resistivity measurement by COREMA. We suppose that this difference may be associated with the surface states of the crystal.

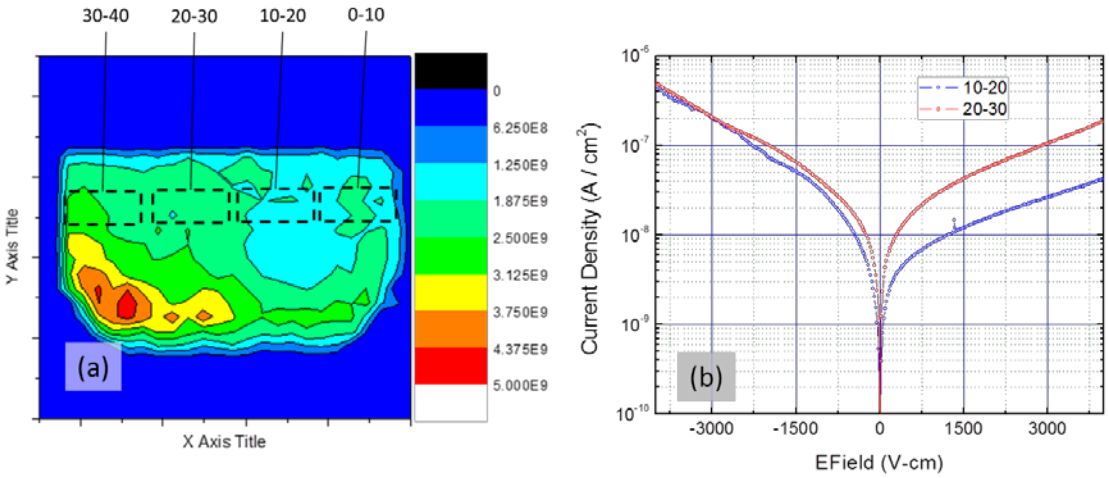

Figure 5.49. I-V measurements of the detectors with (10-20) and without (20-30) twin structure.

5.3.5. Conclusions

The twin structures in one crystal have been investigated with respect to the optical, structural, and electrical properties, in order to understand the effect of twin on the quality of the materials.

- For the region with twin structure, a mixture of (111)A and (111)B terminated surface is presented on both surfaces of the sample. For the twin-free region, the (111)A and (111)B terminations are uniform and either face is purely (111)A or (111)B.
- High density of more closely spaced Te inclusions presents in the twinned region, while the twin-free region displays larger diameter but lower density of Te inclusions.
- The PL intensity of all of the emission bands of the twin-free sample is higher than the sample which displays twinning behaviour.
- The sample with twinned structure has lower leakage current than the one without twin feature, which is in contrary with the COREMA measurement.

5.4. Bibliography

[1] J. Osvald, J. Kuzmik, G. Konstantinidis, P. Lobotka, A. Georgakilas, Temperature Dependence of GaN Schottky Diodes I-V Characteristics, *Microelectronic Engineering*, Vol **81**, 181-187 (2005).

[2] S.S. Al-Ameer, Thermal Study of Gallium Nitride Metal Contact, *JKAU: Sci.*, Vol **21**, 213-223 (2009).

[3] J. Zhang, W. Jie, Y. Hao, X. Wang, Investigation on Gold and Aluminum Contacts for $Cd_{0.8}Zn_{0.2}Te$ Crystals, *Semicond. Sci. Technol.*, Vol **23**, 075010 (2008).

[4] S.M. Sze, Physics of Semiconductor Divice, New York: John Wiley (1981).

[5] J. Crocco, Crystal Growth & Design, Device Fabrication, and Material Properties of Cd(Zn)Te for Radiation Detector Applications, Thesis, (2012).

[6] T.E. Schlesinger, J.E. Toney, H. Yoon, E.Y. Lee, B.A. Brunett, L. Franks, R.B. James, Cadimum Zinc Telluride and Its Use as A Nuclear Radiation Detector Material, *Materials Science and Engineering*, Vol **32**, 103-189 (2001).

[7] J.E. Toney, T.E. Schlesinger, R.B. James, Optimal Band Gap Variants of $_{Cd1-x}Zn_xTe$ for High-Resolution X-ray and Gamma-Ray Spectroscopy, *Nucl. Instrum. Methods. Phys. Res. A*, Vol **428**, 14 (1999).

[8] G. Li, W. Jie, Z. Gu, G. Yang, T. Wang, J. Zhang, Growth of In doped CdZnTe by Vertical Brideman Method and the Effect of In on the Crystal Properties, *J. Cryst. Growth.*, Vol **265**, 159-164 (2004).

[9] G. Li, W. Jie, T. Wang, Z. Gu, Characteristics of Doped Indium in Cd0.9Zn0.1Te Grown by the Bridgeman Method, *Semicond. Sci. Technol.*, Vol **19**, 457-460 (2004).

[10] T.S. Moss, Handbook on Semiconductors, Northern Holland Press Inc., Holland, **301** (1980).

[11] P. Fougeres, P. Siffert, M. Hageali, J.M. Koebel, R. Regal, CdTe and $Cd_{1-x}Zn_xTe$ for Nuclear Detectors: Facts and Fictions, *Nucl. Instrum. Meth. A.*, Vol **428**, 38-44 (1999).

[12] P. Rudolph, *Prog. Cryst. Growth. Charact.*, Vol **29**, 275 (1994).

[13] K. Zanio, Cadmium Telluride, in: R.K. Willardson, A.C. Beer (Eds.), *Semiconductor and Semimetals*, Vol **13**, Academic Press, New York, 246 (1978).

[14] M. Issihiki, M. Sato, K. Masumoto, *J. Cryst. Growth.*, Vol **78**, 58 (1986).

[15] A.E. Bolotnikov, Performance-limited Defects in CdZnTe detectors, *IEEE Trans. Nucl. Sci.*, Vol **54**, 821-827 (2007).

[16] G.S. Camarda, A.E. Bolotnikov, G.A. Carini, R.B. James, L. Li, Effects of Tellurium Precipitates on Charge Collection in CZT Nuclear Radiation Detectors, Chapter 4, Countering Nuclear and Radiological Terrorism, Springer Netherlands, 978-1-4020-4897-5.

[17] A.E. Bolotnikov, N. Abdul-Jabber, S. Babalola, G.S. Camarda, Y. Cui, A. Hossain, E. Jackson, J. James, K.T. Konman, A. Luryi, R.B. James, Effects of Te Inclusions on the Performance of CdZnTe Radiation Detectors, *IEEE Nuclear Science Symposium Conference Record*, 1788-1797 (2007).

[18] P. Wellmann, U. Karl, S. Kleber, H. Schmitt, Cathodoluminescence Characterization of Organic Semiconductor Materials for Light Emitting Device Applications, *J. Appl. Phys.*, Vol **101**, 113704 (2007).

[19] J.K. Radhakrishnan, G. Salviati, Cathodoluminescence Investigations on CdTe and Cd0.96Zn0.04Te Crystals, *Journal of Luminescene*, Vol **113**, 235-242 (2005).

[20] M. Schieber, T.E. Schlesinger, R.B. James, H. Hermon, H. Yoon, M. Goorsky, Study of Impurity Segregation, Crystallinity, and Detector Performance of Melt-Grown Cadimum Zinc Telluride Crystals, *J. Cryst. Growth.*, Vol **237-239**, 2082-2090 (2002).

[21] Q. Li, W. Jie, L. Fu, G. Zha, T. Wang, D. Zeng, Photoluminescence Analysis on the Indium Doped Cd0.9Zn0.1Te Crystal, *J. Appl. Phys.*, Vol **100**, 013518 (2008).

[22] M. Fiederle, V. Babentsov, J. Franc, A. Fauler, J.P. Konrath, Growth of High Resistivity CdTe and (Cd,Zn)Te Crystals, *Cryst. Res. Technol.*, Vol **38**, No. 7-8, 588-597 (2003).

[23] Q. Li, W. Jie, L. Fu, G. Yang, G. Zha, Photoluminescence Analysis on the Indium Doped Cd0.9Zn0.1Te Crystal, *J. Appl. Phys.*, Vol **100**, 01318 (2006).

[24] D.J. Olego, J.P. Faurie, S. Sivananthan, P.M. Raccah, Optoelectronic Properties of $Cd_{1-x}Zn_xTe$ Films Grown by Molecular Beam Epitaxy on GaAs Substrates, *Appl. Phys. Lett.*, Vol **47**, 1172 (1985).

[25] H. Siegle, A. Hoffmann, L. Eckey, C. Thomsen, Mater. Res. Soc. Symp. Proc. (Cambridge University Press, NY) Vol **449**, 677 (1997).

[26] G. Yang, A.E. bolotnikov, Y. Cui, G.S. Camarda, A. Hossain, K.H. Kim, R. Gul, R.B. James, Low-temperature Spatially Resolved Micro-photoluminescence Mapping in CdZnTe Single Crystals, *Appl. Phys. Lett.*, Vol **98**, 261901 (2011).

[27] M. Fiederle, A. Fauler, J. Konrath, V. Bebentsov, J. Franc, R.B. James, Comparison of Undoped and Doped High Resistivity CdTe and (Cd,Te)Te Detector Crystals, *IEEE Trans. Nucl. Sci.*, Vol **51**, 1864-1868 (2004).

[28] V. Babentsov, J. Franc, A. Fauler, M. Fiederle, R.B. James, Distribution of Zinc, Resistivity, and Photosensitivity in a Vertical Bridgman Grown $Cd_{1-x}Zn_xTe$ Ingot, *J. Cryst. Growth.*, Vol **310**, 3482-3487 (2008).

[29] H.Y. Shin, C.Y. Sun, The Exciton and Edge Emissions in CdTe Crystals, *Materials Science and Engineering B*, Vol **52**, 78-83 (1998).

[30] J. Krustok, V.Valdna, K. Hjelt, H. Collan, Deep Center Luminescence in p-type CdTe, *J. Appl. Phys.*, Vol **80**, 1757 (1996).

[31] D.P. Halliday, M.D.G. Potter, J.T. Mullins, A.W. Brinkman, Photoluminescene Study of A Bulk Vapour Grown CdTe Crystal, *J. Cryst. Growth.*, Vol **220**, 30-38 (2000).

[32] S. Jain, Photoluminescence Study of Cadimum Zinc Telluride, Thesis (2001).

[33] R.O. Bell, Binding energy of An Electron to A Three-defect-complex in CdTe, *Solid State Commun.* Vol **16**, 913 (1975).

[34] W. Ossau, T.A. Kuhn, R.N. Bicknell-Tassius, Linear and Quadratic Effects on PAMBE Grown CdTe, *J. Crystal Growth*, Vol 101, 135-140 (1990).

[35] G.F. Knoll, Radiation Detection and Measurement, Wiley, 3rd edition (2000).

[36] C. Szeles, S.E. Cameron, J.O. Ndap, W.C. Chalmers, Advances in the Crystal Growth of Semi-insulating CdZnTe for Radiation Detector Applications, *IEEE Trans. Nucl. Sci*, Vol **49**, 2535-2540 (2002).

[37] A. Castaldni, A. Cavallini, B. Fraboni, P. Fernandez, J. Piqueras, Deep Energy Levels in CdTe and CdZnTe, *J. Appl. Phys.*, Vol **83**, 4 (1998).

[38] A. Castaldni, A. Cavallini, B. Fraboni, L. Polenta, J. Piqueras, Cathodoluminescence and Photoinduced Current Transient Spectroscopy Studies of Defects in Cd0.8Zn0.2Te, *Phys. Rev. B.*, Vol **54**, 7622 (1996).

[39] K. Durose, G.J. Russell, *J. Crystal Growth*, Vol **101**, 246 (1990).

[40] M. Schieber, T.E. Schlesinger, R.B. James, H. Hermon, H. Yoon, M. Goorsky, Study of Impurity Segregation, Crystalline, and Detector Performance of Melt-grown Cadmium Zinc Telluride Crystals, *J. Crystal Growth*, Vol **237-239**, 2082-2090 (2002).

[41] B.H. Parker, C.M. Stahle, D. Roth, S. Babu, Jack Tueller, The effect of twin boundaries on the spectroscopic performance of CdZnTe detectors, *Proc. SPIE.*, **4507**, 68 (2001).

[42] K. Suzuki, S. Seto, K. Imai, T. Sawada, U. Neukirch, J. Gutowski, Effect of Compositional Disorder on the Optical Properties of $Cd_{1-x}Zn_xTe$, *Journal of Electronic Materials*, Vol **28**, No. 6, 785 (1999).

GENERAL CONCLUSIONS

The preparation and development of CdTe/CZT detectors for gamma ray radiation applications have been investigated in this thesis. The following conclusions summarize the results which have been obtained through this investigation.

For the detector preparation, a complete cutting, lapping, and mechanical polishing processes have been discussed, being the chemical etching process of extremely important before the electrode deposition which improves the crystallinity and decreases the leakage current. The lateral edges of the detectors with passivation treatment were demonstrated to produce an oxide layer in a short time and improve the performance of the detectors.

Three different electrode deposition methods (Sputtering, Evaporation, and Electroless) have been investigated in order to find the optimal deposition method.

- The deposition of Au electrodes into CZT material can reduce the effect of Cd vacancies by acting as Au donors.
- With electroless deposition method, a strong intermixing appears among Au, TeO_2 and CZT. The sputtering method shows the thickest Te oxide layer, while the evaporation method displays the thinnest Te oxide layer at the interface.
- The contacts deposited by electroless method exhibit better detector performance compared with sputtering and evaporation deposition methods.

Different critical parameters of the deposition of single layer on CZT by electroless method including the influence of the deposition time and the addition of an annealing step after contact deposition have been investigated.

- The deposition of Au, Pt, or Ru layer on CZT shows a modification of morphology and roughness on the surface with deposition time. At a critical thickness, micro-cracks appear at the surface of Pt or Ru layer, whereas the Au layer does not present any micro-cracks or peeling off. For Ru, the deposition rate is much slower than Au or Pt. The Pt layers deposited on CZT are polycrystalline, while Ru layers are monocrystalline.
- The annealing step presents a decrease of the leakage current with sputtering method but an increase with the evaporation method as the annealing holding time in air

increases. With the electroless Au contact, the annealing treatment under air displays insignificant variation of leakage current for a long annealing time.

Various types of contacts have been deposited on the CdTe/CZT samples by using electroless deposition method such as Au, Pt, Ru and Rh.

- The contacts have been successfully identified on the samples by TXRF technique. By RBS depth profiles, a significant concentration of Te oxide appears in the interfacial layers for four metallisation process.
- For the deposition on CdTe material, the contacts show quasi ohmic behaviours, and Pt contact gives better performance than the other contacts.For the deposition on CZT material, the I-V characteristics exhibited Schottky contact behaviours for different metal contacts, Au contact has shown the best detector performance than the other contacts.

The study of the feasibility to deposit nanometric multi-layers on CZT by electroless method has been investigated.

- The capability of deposited double and triple layers onto CZT material has been identified by TXRF. The quantities of Cd (and Te) rejected in Ru solution can be identified, but not with Au or Pd solutions. The inter-diffusion phenomena between layers are also clearly demonstrated by RBS.
- The detector performance of the structure single layer on one side and double-layer on the other side is better than the double layers contacts on both sides.

Samples prepared with different crystal growth processes have been characterized. All the commercial detectors show clean and smooth surface with minimal scratches, Pt electrodes were found on the detectors. The comparison between the different commercial samples from eV product show a slight difference of detector performance, putting in evidence the good reproducibility of the manufacturer process. One commercial detector has been reprocessed by our home-made process and compare with the as-received one. The detector performance is slightly lower than the commercial samples.

Two different ways of crystal growth preparation by using CZT uncompounded materials or compounded materials have been investigated.

- The concentration of Zn gradually decreases with the solidified fraction having lower Te inclusions concentration in the bottom region than in the top region for both ingots.

- The detectors obtained from the ingot grown by CZT uncompounded materials display higher leakage current than the detectors achieved from the ingot grown by compounded materials. The performance of the detectors harvested from the bottom of the ingot grown with uncompounded materials is better than the detectors harvested from the ingot grown by compounded material. Both ingots harvested non-uniform materials, but a significant difference was observed with the ingot grown by uncompounded material. For the ingot grown by compounded materials, high quality materials can be achieved at the first half region of the ingot with a good homogeneity between detectors.

The twin structures have been investigated in order to understand the effect of twins on the quality of the materials. High density of more closely spaced Te inclusions is present in the twinned region, while the twin-free region displays larger diameter but lower density of Te inclusions. The PL intensity of the twin-free sample is higher than the sample which displays twinning behaviour. The sample with twinned structure has lower leakage current than the one without twin feature.

CONCLUSIONES GENERALES

En esta Tesis se ha investigado en la preparación y desarrollo de detectores basados en CdTe/CZT para aplicaciones de radiación de rayos gamma, obteniéndose los siguientes resultados.

Para la preparación del detector, se ha demostrado un proceso completo de corte, lapping y pulido mecánico, siendo el ataque químico extremadamente importante antes de la deposición del electrodo dado que mejora la cristalinidad y disminuye la corriente de fuga. Se ha demostrado la importancia del tratamiento de los bordes laterales de los detectores y el proceso de pasivación con el objeto de mejorar el rendimiento de los detectores.

Se investigaron tres métodos diferentes de deposición de electrodo: sputtering, evaporación, y electrolítico, con el fin de encontrar el método de deposición óptimo.

- La deposición de los electrodos Au en CZT reduce el efecto de las vacantes de Cd actuando como donantes Au.
- Mediante el método de electroless deposition, aparece un fuerte intercambio entre Au, TeO_2, y CZT. El método de sputtering muestra la capa más gruesa de Te óxido, mientras que el método de evaporación muestra la capa más delgada de óxido.
- Los contactos depositados por el método electroless muestran el mejor comportamiento del detector en comparación con los métodos de depósito de sputtering y evaporación.

Se investigaron diferentes parámetros críticos de la deposición de capa única sobre CZT por método electroless, incluyendo la influencia del tiempo de deposición y la adición de una etapa de recocido después de la deposición.

- La deposición de capa Au, Pt, or Ru sobre CZT muestra una modificación de la morfología y la rugosidad de la superficie con el tiempo de deposición. Para un espesor crítico, aparecen micro-grietas en la superficie de la capa de Pt o Ru, mientras que la capa de Au no presenta micro-grietas. Para Ru, la velocidad de deposición es mucho más lenta que Au o Pt. Las capas de Pt depositadas en CZT son policristalinas, mientras que las capas de Ru son monocristalinas.

- El proceso de recocido presenta una disminución de la corriente de fuga con el método sputtering, pero aumenta con el tiempo en el método de evaporación. En el proceso de contacto de Au mediante electroless, el tratamiento de recocido bajo aire muestra la variación insignificante de corriente de fuga para tiempos largos de recocido.

Se han depositado varios tipos de contactos sobre en las muestras de CdTe/CZT mediante el método de deposición electroless tal como Au, Pt, Ru, y Rh.

- Los contactos han sido correctamente identificados en las muestras por la técnica TXRF. Mediante Perfiles de profundidad RBS, aparece una concentración importante de TeO_2 en las capas interfaciales.
- Para la deposición sobre materiales CZT, las características I-V exhiben comportamiento de contactos Schottky para distintos contactos metálicos, mostrando el contacto Au el mejor rendimiento. Para la deposición sobre material CdTe, los contactos muestran comportamientos cuasi óhmicos, y el contacto de Pt ofrece el mejor rendimiento.

Se ha investigado la viabilidad para depositar multicapas nanométricas en CZT por método electroless.

- Se ha identificado la capacidad de de depositar capas dobles y triples sobre CZT mediante TXRF. Las cantidades de Cd (y Te) rechazados en solución Ru pueden ser identificadas, pero no en soluciones Au o Pd. Los fenómenos inter-difusión entre las capas se demuestra también por RBS.
- El funcionamiento del detector de la capa única de estructura en un lado u doble capa en el otro lado es mejor que los contados de capas dobles en ambos lados.

Se han caracterizado muestras preparadas con diferentes procesos de crecimiento de cristales Todos los detectores comerciales presentan contactos de Pt presentando una superficie limpia y lisa con rasguños mínimos. La comparación entre las diferentes muestras comerciales de productos eV muestra una ligera diferencia de funcionamiento como detector, poniendo en evidencia la buena reproducibilidad del proceso del fabricante. Un detector comercial ha sido reprocesado por nuestro proceso de fabricación y comparado con uno tal como se recibió. El funcionamiento del detector es ligeramente inferior a las muestras comerciales recibidas.

Se han investigado la influencia del proceso de crecimiento en las características como detector:

- La concentración de Zn disminuye gradualmente con la fracción solidificada con menor concentración de inclusiones de Te en la región solidificada en primer lugar en comparación con la región superior de los lingotes.
- Los detectores obtenidos a partir del lingote crecido con material CZT preparado a partir de los productos elementales, muestran mayor corriente de fuga que los detectores obtenidos a partir del lingote crecido con materiales compuestos. El rendimiento de los detectores obtenidos de la parte inferior del lingote crecido con materiales no compuestos es mejor que los detectores obtenidos del lingote crecido con material compuesto. Los dos lingotes resultaron en material no uniforme, y se observaron diferencias significativas con el lingote crecido por material compuesto. Para el lingote crecido con materiales compuestos, se pueden obtener materiales de alta calidad en la primera mitad de lingote con buena homogeneidad entre los detectores.

Se han investigado las estructuras tipo twin con el fin de comprender su efecto en la calidad de los materiales. Una alta densidad de inclusiones Te están presentes en la región de twin, mientras que la región libre de twins muestra inclusiones Te de mayor diámetro pero de menor densidad. La intensidad de PL de la muestra libre de twins es mayor que la muestra que muestra con twins. La muestra con twins tiene corriente de fuga menor que una sin twins.

LIST OF PUBLICATIONS AND CONFERENCES

Publications list:

1. Q. Zheng, F. Dierre, V. Corregidor, J. Crocco, H. Bensalah, J.L. Plaza, E. Alves, E. Dieguez, "Electroless Deposition of Au, Pt, or Ru Metallic Film Layer on CdZnTe", ***Thin Solid Films***, submitted, (2012).
2. Q. Zheng, J. Crocco, P. Wellmann, A. Osvet, U. Künecke, F. Dierre, H. Bensalah, A. Black, O. Vela, J.M. Perez, E. Dieguez, "Influence of Crystal Growth Process on CZT Radiation Detectors", submitted, (2012).
3. Q. Zheng, P. Wellmann, A. Osvet, J. Crocco, F. Dierre, H. Bensalah, E. Dieguez, "Photoluminescence Characterization of In doped CdZnTe Grown by Vertical Gradient Freeze Method", submitted, (2012).
4. Q. Zheng, F. Dierre, J. Franc, J. Crocco, H. Bensalah, V. Corregidor, E. Alves, E. Ruiz, O. Vela, J.M. Perez, E. Dieguez, "Investigation of Generation of Defects due to Metallisation on CdZnTe Detectors", ***J. Phys. D: Appl. Phys.***, 45, 175102 (2012).
5. Q. Zheng, F. Dierre, V. Corregidor, R. Fernández-Ruiz, J. Crocco, H. Bensalah, E. Alves, E. Diéguez, "Deposition of Nanometric Double Layers Ru/Au, Ru/Pd, and Pd/Au onto CdZnTe by the Electroless Method", ***J. Cryst. Growth.***, In press, doi:10.1016/j.jcrysgro.2011.04.014, (2011).
6. Q. Zheng, F. Dierre, M. Ayoub, J. Crocco, H. Bensalah, V. Corregidor, E. Alves, R. Fernandez-Ruiz, J. M. Perez, and E. Dieguez, "Comparison of the Detector Performance for Different Metal Contacts on Cd(Zn)Te for Radiation Applications", ***Cryst. Res. Technol.***, 46, No. 11, 1131-1136 (2011).
7. Q. Zheng, F. Dierre, J. Crocco, V. Carcelen, H. Bensalah, J.L. Plaza, E. Dieguez, "Influence of Surface Preparation on CdZnTe Nuclear Radiation Detectors", ***Appl. Surf. Sci.***, 257, 8742– 8746 (2011).
8. J. Crocco, Q. Zheng, H. Bensalah, D. Cavalcoli, B. Fraboni, A. Cavallini, P. Hidalgo, G.C. Camarda, G. Yang, V. Babentsov, A.E. Bolotnikov, A. Hossain, K.H. Kim, R.B. James, E. Dieguez, "Crystallographic Twinning in Cd(Zn)Te", submitted, 2012.
9. J. Crocco, H. Bensalah, Q. Zheng, V. Corregidor, A. Castaldini, B. Fraboni, D. Cavalcoli, A. Cavallini, O. Vela, E. Dieguez, "Investigation of Asymmetries of Cd(Zn)Te Detectors Investigated Using PICTS, RBS, SPS, and Gamma Ray Spectroscopies", submitted, 2012.
10. J. Crocco, A. Castaldini, B. Fraboni, D. Cavacoli, H. Bensalah, Q. Zheng, A. Cavallini, E. Dieguez, "Influence of Dynamic Temperature Adjustments During Growth on the Material Properties of Cd(Zn)Te Radiation Detectors", ***J. Crystal. Growth.***, In press, doi:10.1016/j.jcrysgro.2012.07.036, (2012).
11. H. Bensalah, J. Crocco, V. Carcélen, A. Black, Q. Zheng, J.L. Plaza, E. Diéguez, "Effect of Superheating and Fast Cooling on Te Inclusions of $Cd_{0.9}Zn_{0.1}Te$:In Crystals Grown by Vertical Gradient Freezing", ***J. Cryst. Growth.***, In press, doi:10.1016/j.jcrysgro.2012.07.012, (2012).

12. H. Bensalah, V. Hortelano, J.L. Plaza, O. Martínez, J. Crocco, Q. Zheng, V. Carcelen, E.Dieguez, "Characterization of CdZnTe after Argon Ion Beam Bombardment", ***Journal of Alloys and Compounds,*** In press, doi:10.1016/j.jallcom.2012.07.109, 2012.
13. J. Crocco, A. Black, H. Bensalah, Q. Zheng, V. Carcélen, E. Dieguez, "Investigation of Crystal Growth of 50mm CZT Using SiC Pedestal and pBN Crucible", ***J. Cryst. Growth.***, 355, 46-51 (2012).
14. J. Crocco, Q. Zheng, H. Bensalah, E. Dieguez, "Detector Surface Preparation of $Cd_{0.9}Zn_{0.1}Te$ for Electrode Patterning", ***Appl. Surf. Sci.***, 258, 2948-2952 (2012).
15. J. Crocco, V. Carcelen, B. Methven, I. Gallardo, H. Bensalah, Q. Zheng, I. Rivas, F. Moreno, O. Vela, E. Dieguez, "Influence of Carbon pBN Crucible on Crystal Growth of $Cd_{0.9}Zn_{0.1}Te$ for Radiation Detector Applications", ***J. Cryst. Growth.***, 349, 61-67 (2012).
16. J. Crocco, H. Bensalah, Q. Zheng, V. Carcelén, E. Diéguez, "Influence of SiC Pedestal in the Growth of 50 mm CZT by Vertical Gradient Freeze Method", ***J. Cryst. Growth.***, In press, doi:10.1016/j.jcrysgro.2011.11.047, (2011).
17. J. Crocco, H. Bensalah, Q. Zheng, F. Dierre, P. Hidalgo, J. Carrascal, O. Vela, J. Piqueras, E. Diéguez, "Study of the Effects of Edge Morphology on Detector Performance by Leakage Current and Cathodoluminescence", ***IEEE Trans. Nucl. Sci.***, 58(4), 1935-1941 (2011).
18. H. Bensalah, J. Crocco, V. Carcélen, J. L. Plaza, Q. Zheng, L. Marchini, M. Zanichelli, G. Domínguez, L. Soriano, and E. Diéguez, "Study of Ammonium Fluoride Passivation Time on CdZnTe Bulk Crystal Wafers", ***Cryst. Res. Technol.***, 46, No. 7, 659 - 663 (2011).
19. H. Bensalah, J.L. Plaza, J. Crocco, Q. Zheng, V. Carcelen, A. Bensouici, E. Dieguez, "The Effect of Etching Time on the CdZnTe Surface", ***Appl. Surf. Sci.***, 257, 4633-4636 (2011).

Conference participations list:

1. Q. Zheng, J. Crocco, P. Wellmann, A. Osvet, U. Künecke, F. Dierre, H. Bensalah, A. Black, O. Vela, J.M. Perez, E. Dieguez, "Influence of Crystal Growth Process on CZT Radiation Detectors", Poster presentation, ***IEEE 19th Room Temperature Semiconductor Detector Workshop***, October 29 – November 3, 2012, Anaheim, California, (USA).
2. Q. Zheng, F. Dierre, V. Corregidor, J. Crocco, H. Bensalah, J.L. Plaza, E. Alves, and E. Dieguez, "Electroless Plating of Au, Pt, or Ru Thin Film Layers on CdZnTe", Oral presentation, ***IEEE 18th Room Temperature Semiconductor Detector Workshop***, October 23-29, 2011, Valencia, (Spain).
3. Q. Zheng, F. Dierre, J. Crocco, H. Bensalah, O. Vela, J. M. Perez, E. Dieguez, "Spectral Characterization of CdZnTe Detectors with a Planar, Hemispherical, or Single Pixel Geometry", Poster presentation, ***IEEE 18th Room Temperature Semiconductor Detector Workshop***, October 23-29, 2011, Valencia, (Spain).
4. Q. Zheng, F. Dierre, J. Franc, J. Crocco, H. Bensalah, V. Corregidor, E. Alves, E. Ruiz, O. Vela, J.M. Perez, E. Dieguez, "Investigation of Generated Defects due to Processes of Metallisation on CdZnTe Detectors", Poster presentation, ***IEEE 18th Room Temperature Semiconductor Detector Workshop***, October 23-29, 2011, Valencia, (Spain).
5. Q. Zheng, F. Dierre, M. Ayoub, J. Crocco, H. Bensalah, V. Corregidor, E. Alves, R. Fernandez-Ruiz,J. M. Perez, and E. Dieguez, "Comparison of the Detector Performance for Different Metal Contacts on Cd(Zn)Te for Radiation Applications", Poster presentation, ***IEEE 17th Room Temperature Semiconductor Detector Workshop***, October 30 – November 6 , 2010, Knoxville, Tennessee (USA).
6. Q. Zheng, F. Dierre, V. Corregidor, R. Fernández-Ruiz, J. Crocco, H.Bensalah, E. Alves, E. Diéguez, "Deposition of Nanometric Double layers Ru/Au, Ru/Pd, and Pd/Au onto CdZnTe by the Electroless Method", Poster presentation, ***European Materials Reserch Society (E-MRS) 2010 Fall Meeting***, September 13-17, 2010, Warsaw (Poland).
7. J. Crocco, H. Bensalah, Q. Zheng, A. Black, B. Fraboni, D. Cavalcoli, A. Castaldini, A. Cavallini, E. Alves, V. Corregidor, P. Hidalgo, O. Vela, E. Dieguez, " Asymmetries of CZT Detectors Used for Gamma Ray Spectroscopy", Oral presentation, ***IEEE 19th Room Temperature Semiconductor Detector Workshop***, October 29 – November 3, 2012, Anaheim, California, (USA).
8. H. Bensalah, J. Crocco, A. Black, Q. Zheng, O. Vela, J.L. Plaza, E. Dieguez, "Reduction of Te Inclusions in CdZnTe Crystals by Growth Process and Annealing Steps in Order to Improve the Detector Performance", Oral presentation, ***IEEE 19th Room Temperature Semiconductor Detector Workshop***, October 29 – November 3, 2012, Anaheim, California, (USA).
9. H. Bensalah, A. Medvids, J. Crocco, A. Michko, E. Dauksta, V. Ivanov, Q. Zheng, J.L. Plaza, E. Dieguez, "Improvement of the Quality of CdZnTe Detectors after Laser Irradiation", Poster presentation, ***IEEE 19th Room Temperature Semiconductor Detector Workshop***, October 29 – November 3, 2012, Anaheim, California, (USA).

10. J. Crocco, H. Bensalah, Q. Zheng, E. Dieguez, "Crystal Growth of CZT using SiC Pedestal and pBN Crucible", Oral presentation, ***IEEE 18th Room Temperature Semiconductor Detector Workshop***, October 23-29, 2011, Valencia, (Spain).
11. J.D. Crocco, H. Bensalah, Q. Zheng, I. Gallardo, E. Dieguez, "Vaccum Carbon Coating of Quartz and pBN Crucibles Applied to VGF Growth of Cadimum Zinc Telluride", Poster presentation, ***IEEE 18th Room Temperature Semiconductor Detector Workshop***, October 23-29, 2011, Valencia, (Spain).
12. H. Bensalah, J. Crocco, J. L. Plaza, Q. Zheng, E. Dieguez, "Effect of Different Superheating Temperature on Te Inclusions of $Cd_{0.9}Zn_{0.1}Te$:In Crystals Grown by Vertical Gradient Freezing", Poster presentation, ***IEEE 18th Room Temperature Semiconductor Detector Workshop***, October 23-29, 2011, Valencia, (Spain).
13. H. Bensalah, J. L. Plaza, V. Hortelano, O. Martnez, J. Crocco, Q. Zheng, V. Carcelen, E. Dieguez, "Characterization of CdZnTe after Argon Ion Beam Bombardment", Poster presentation, ***IEEE 18th Room Temperature Semiconductor Detector Workshop***, October 23-29, 2011, Valencia, (Spain).
14. J. Crocco, H. Bensalah, Q. Zheng, I. Gallardo, E. Dieguez, "Challenges for Improving the Growth of Bulk CZT Crystals", Poster presentation, ***5th International Workshop on Crystal Growth Technology (IWCGT-5)***, June 26-30, 2011, Berlin, Germany.
15. J. D. Crocco, F. Dierre, H. Bensalah, Q. Zheng, P. Hidalgo, J. Piqueras, E. Dieguez, "Effects of Surface Morphology on CZT Detectors Studied by I-V and Cathode Luminescence", Oral presentation, ***IEEE 17th Room Temperature Semiconductor Detector Workshop***, October 30 – November 6 , 2010, Knoxville, Tennessee (USA).
16. H. Bensalah, J. Crocco, V. D. Carcelen, J. L. Plaza, Q. Zheng, G. Rodriguez, L. Soriano, E. Dieguez, "Study of Passivation with Time on CdZnTe Bulk Crystal by XPS and I-V", Poster presentation, ***IEEE 17th Room Temperature Semiconductor Detector Workshop***, October 30 – November 6 , 2010, Knoxville, Tennessee (USA).
17. H. Bensalah, J.L. Plaza, J. Crocco, Q. Zheng, V. Carcelen, A. Bensouici, E. Dieguez, "The Effect of Etching Time on the CdZnTe Surface", Poster presentation, ***European Materials Reserch Society (E-MRS) 2010 Fall Meeting***, September 13-17, 2010, Warsaw (Poland).